NOBLE GAS CHEMISTRY DERIVED FROM $N{\equiv}SF_3$ AND RELATED SULFUR-NITROGEN-FLUORINE CHEMISTRY

By

GREGORY L. SMITH

A Thesis

Submitted to the School of Graduate Studies

in Partial Fulfillment of the Requirements

for the Degree

Doctor of Philosophy

McMaster University

DOCTOR OF PHILOSOPHY — McMaster University

(Chemistry) — Hamilton, Ontario

TITLE: NOBLE GAS CHEMISTRY DERIVED FROM $N{\equiv}SF_3$ AND RELATED SULFUR-NITROGEN-FLUORINE CHEMISTRY

AUTHOR: Gregory L. Smith, B. Sc. (McMaster University)

SUPERVISOR: Professor Gary J. Schrobilgen

NUMBER OF PAGES: 320, xxv

ABSTRACT

The chemistry of xenon(II) has been significantly extended by the syntheses and characterizations of new examples of xenon bound to nitrogen having formal sp, sp^2, and sp^3 hybridization, namely the $F_3S{\equiv}NXeF^+$, $F_4S{=}NXe^+$, and $F_5SN(H)Xe^+$ cations. The $F_4S{=}NXe{---}N{\equiv}SF_3^+$ adduct-cation is the first example of an N–Xe–N linkage to be structurally characterized by X-ray crystallography. Until recently, all of the known compounds containing xenon bound to formally sp-hybridized nitrogen have been prepared using organic nitrogen bases. The inorganic nitrogen Lewis base thiazyl trifluoride, $N{\equiv}SF_3$, was reacted with the AsF_6^- salt of the Lewis-acidic XeF^+ cation at –20 °C to synthesize the donor-acceptor adduct $[F_3S{\equiv}NXeF][AsF_6]$. Displacement of XeF_2 from $[FXeOXeFXeF][AsF_6]$ by $N{\equiv}SF_3$ at –60 °C led to the formation of the $FXeOXe{---}N{\equiv}SF_3^+$ adduct-cation, providing a rare example of a xenon(II) oxide fluoride, which was characterized by Raman spectroscopy of natural abundance and ^{18}O-enriched salts. The solid-state rearrangement of $[F_3S{\equiv}NXeF][AsF_6]$ at 22 °C yielded $[F_4S{=}NXe][AsF_6]$, which was characterized by Raman spectroscopy. This is the first example of xenon bonded to an imido-nitrogen and the first example of the $F_4S{=}N$- group bonded to a noble gas. The HF solvolysis of $[F_3S{\equiv}NXeF][AsF_6]$ at –20 °C in aHF or BrF_5 solvents generated $[F_5SN(H)Xe][AsF_6]$, which, in addition to $F_5TeN(H)Xe^+$, provides the only other example of xenon bonded to an sp^3-hybridized nitrogen centre.

Through further study of the HF solvolysis of $[F_3S{\equiv}NXeF][AsF_6]$ in aHF or BrF_5 solutions, it was shown that the $F_4S{=}NXe^+$ cation was also formed, and may be

understood in terms of an HF-catalyzed mechanism. The $F_4S{=}NXe^+$ cation subsequently underwent HF solvolysis, forming $F_4S{=}NH_2^+$, XeF_2, and $F_5SN(H)Xe^+$. Both cations underwent further HF solvolyses to form the $F_5SNH_3^+$ cation. The $F_4S{=}NXe^+$ and $F_4S{=}NH_2^+$ cations were characterized by NMR spectroscopy and single-crystal X-ray diffraction, and exhibit high barriers to rotation about their S=N double bonds. They are the first cations known to contain the $F_4S{=}N$- group, significantly extending the chemistry of this ligand. The rearrangement of $[F_3S{\equiv}NXeF][AsF_6]$ in $N{\equiv}SF_3$ solution at 0 °C yielded $[F_4S{=}NXe{---}N{\equiv}SF_3][AsF_6]$, which was characterized by Raman spectroscopy and X-ray crystallography.

Solvolysis of $N{\equiv}SF_3$ in aHF is known to give the primary amine, F_5SNH_2, whereas solvolysis in the superacid medium AsF_5/aHF results in amine protonation to give $[F_5SNH_3][AsF_6]$. Until recently, definitive structural characterizations were not known for either of these fundamental species. Isolation of $F_5SNH_2{\cdot}n$HF from the reaction of $N{\equiv}SF_3$ with HF has provided a structural characterization of F_5SNH_2 by Raman spectroscopy. Crystal growth by sublimation of $F_5SNH_2{\cdot}n$HF at –30 to –40 °C provided single crystals of $F_5SNH_2{\cdot}2[F_5SNH_3][HF_2]{\cdot}4HF$, and recrystallization of $[F_5SNH_3][AsF_6]$ from $N{\equiv}SF_3$ solution at –70 °C afforded crystalline $[F_5SNH_3][AsF_6]{\cdot}2N{\equiv}SF_3$ and resulted in the structural characterization of these salts by X-ray crystallography. The redox decomposition of $[F_4S{=}NXe{---}N{\equiv}SF_3][AsF_6]$ in $N{\equiv}SF_3$ at 0 °C generated Xe, *cis*-N_2F_2, and $[F_3S(N{\equiv}SF_3)_2][AsF_6]$ which was characterized by Raman spectroscopy and single-crystal X-ray diffraction. These X-ray crystal structure determinations, in themselves, represent a significant extension of sulfur-nitrogen-

fluorine chemistry, providing the first definitive characterizations of F_5SNH_2 and $F_5SNH_3^+$, only the second known example of unadducted $N{\equiv}SF_3$, and rare examples of main-group coordination compounds of $N{\equiv}SF_3$.

The $F_5SNH_3^+$ cation protonated CH_3CN to CH_3CNH^+ which is proposed to initiate the cyclotrimerization of CH_3CN, generating F_5SNH_2 and $[s\text{-}C_3(CH_3)_3N_3H][AsF_6]$, as characterized by NMR spectroscopy at −10 °C in CH_3CN solvent. Crystal growth from CH_3CN at −10 to −35 °C enabled the determination of the X-ray crystal structure of $[s\text{-}C_3(CH_3)_3N_3H\text{---}NCCH_3][AsF_6]\cdot CH_3CN$. This represents the first known crystal structure of a *sym*-2,4,6-trialkyl-1,3,5-triazinium cation.

The final objective of this research was to extend the chemistry of krypton-nitrogen bonded species. The nitrile cations $RC{\equiv}NKrF^+$ (R = H, CF_3, C_2F_5, $n\text{-}C_3F_7$) are currently the only known examples containing Kr–N bonds. The syntheses of the $F_3S{\equiv}NKrF^+$ and $F_5SN(H)Kr^+$ cations as their AsF_6^- salts were attempted by the reaction of KrF_2 with $F_3S{\equiv}NAsF_5$ and $[F_5SNH_3][AsF_6]$, respectively, for characterization by NMR spectroscopy in BrF_5 solvent at −70 to −60 °C. No conclusive evidence for Kr–N bond formation was found, however, in each case, the fluorination and oxidation products SF_6, NF_3, NF_4^+ and AsF_6^- were observed instead.

ACKNOWLEDGEMENTS

I wish to sincerely thank Professor Gary J. Schrobilgen for providing me with interesting and exciting avenues of research, as well as for his insight, guidance, enthusiasm, patience, and confidence in me.

I would also like to thank the other members of my supervisory committee, Dr. Ignacio Vargas-Baca and Dr. David J. Emslie, for their support, useful discussions, and interest in my research projects.

A heartfelt thanks to Dr. Hélène P. A. Mercier for her expertise, advice, and encouragement throughout the course of this work, as well as for the numerous hours spent in helping solve various crystal structures and writing contributions for our publications together.

I am also very grateful to Dr. Matthew D. B. Moran as my primary mentor in learning the day-to-day operations of the laboratory, his humour, his advice, and for his friendship. Also special thanks to Dr. Bernard E. Pointner and Dr. John F. Lehmann for their expertise, advice, and support during my first years of graduate school.

Thanks also to other past and present members of the Schrobilgen research group, namely Michael Hughes, David Brock, Maria Ivanova, Rezwan Ashique, Jonathan Paxon, Babak Behnam-Azad, Dr. Kazuhiko Matumoto, Dr. Karsten Koppe, and Corey J. Lapierre for all of their help and encouragement. I am also grateful to Gregory J. Bahun, Dr. Matthew C. Parrott, and Dr. Jeff C. Landry for useful discussions, good times, and for their friendship.

For their help in their respective fields, I would like to thank Dr. Jim Britten (X-ray crystallographic facilities), Dr. Steve Kornic (NMR and Spectroscopy facilities), and Michael Palme (Chemistry Glassblowing Shop).

I would like to acknowledge the Ontario Ministry of Education and Training - Ontario Graduate Scholarships in Science & Technology program (OGSST), the McMaster University Dependent and Spouse bursary program, and the McMaster University Department of Chemistry for financial support in the form of bursaries and scholarships over the years.

Finally, I would like to thank my soul mate, Jessica Pace, for her unwavering love, endless understanding, amazing support, and full confidence in my abilities, and give special thanks to my parents, Larry and Linda, my grandmothers Dorothy Smith and Dorothy Froud, and my brother and sister-in-law, Rob and Laurie Smith, for all of their financial and emotional support throughout my post-secondary education.

PREFACE

The following Chapters have been published, in part or in whole, by the American Chemical Society (ACS). All experimental and computational work was conducted by the author.

Chapter 3: Smith, Gregory L.; Mercier, H. P. A.; Schrobilgen, G. J. *Inorg. Chem.* **2007**, *46*, 1369-1378.

Chpater 4: Smith, Gregory L.; Mercier, H. P. A.; Schrobilgen, G. J. *Inorg. Chem.* **2008**, *47*, 4173-4184.

Chapter 5: Smith, Gregory L.; Mercier, H. P. A.; Schrobilgen, G. J. *J. Am. Chem. Soc.* **2009**, *131*, 7272-7286.

Chapter 6: Smith, Gregory L.; Schrobilgen, G. J. *Inorg. Chem.* **2009**, *48*, 7714-7728.

LIST OF ABBREVIATIONS AND SYMBOLS

General

aHF	anhydrous hydrofluoric acid
BDH	British Drug Houses
SAE	Society of Automotive Engineers
ax	axial
eq	equatorial
CCD	charge-coupled device
FT	Fourier transform
FEP	perfluoroethylene/perfluoropropylene copolymer
IR	infrared
Kel-F	chlorotrifluoroethylene polymer
PTFE	tetrafluoroethylene polymer
VSEPR	valence shell electron pair repulsion
N.A.	natural abundance (isotopic)

Raman Spectroscopy

$\Delta\nu$	frequency
cm^{-1}	wavenumber
ν	stretching mode
δ	in-plane bend
ρ_w	wagging mode

ρ_r	rocking mode
ρ_t	twisting mode
o.o.p.	out-of-plane
i.p.	in-plane

Nuclear Magnetic Resonance Spectroscopy

NMR	nuclear magnetic resonance
ppm	parts per million
δ	chemical shift
I	nuclear spin quantum number
J	scalar coupling constant, in Hz
Hz	Hertz, or cycles per second
FID	free induction decay
SF	spectral frequency
SW	sweep width
TD	time domain
PW	pulse width
$\Delta\nu_{1/2}$	line width at half height
WF	width factor

X-ray Crystallography

$a, b, c, \alpha, \beta, \gamma$	unit cell parameters

V	unit cell volume
λ	wavelength
Z	molecules per unit cell
mol. wt.	molecular weight
ρ	density
μ	absorption coefficient
F	structure factor
R_1	conventional agreement index
wR_2	weighted agreement index

Computational and Thermochemical

DFT	density functional theory
MP2	Møller-Plesset, second order perturbation
HF	Hartree-Fock
RLC	relative large core
NBO	natural bond orbital
NPA	natural population analysis
ΔH^{o}	standard enthalpy of reaction
ΔH_f^{o}	standard enthalpy of formation

TABLE OF CONTENTS

page

LIST OF TABLES

LIST OF FIGURES

CHAPTER 1

INTRODUCTION

1.1. Noble-Gas Chemistry

The chemistry of Group 18, the noble or rare gases, has been a subject of research interest since the discovery of noble-gas reactivity in 1962 by Neil Bartlett.[1] When Bartlett discovered that platinum hexafluoride, PtF_6, was able to oxidize molecular oxygen, O_2, to O_2^+,[1] it became evident that PtF_6 should also be capable of oxidizing xenon gas, because xenon and molecular oxygen have very similar first ionization potentials (12.13 and 12.2 eV, respectively). Bartlett confirmed his speculation by demonstrating that xenon gas was readily oxidized by PtF_6 at room temperature (eq 1.1)

$$Xe_{(g)} + PtF_{6\,(g)} \longrightarrow [Xe][PtF_6]_{(s)} \qquad (1.1)$$

to form a yellow-orange solid which was then formulated as $[Xe][PtF_6]$. Approximately forty years later, Bartlett reported that the reaction between xenon and PtF_6 yielded a mixture of $[XeF][PtF_6]$ and $[XeF][Pt_2F_{11}]$,[2] however, he continued to maintain that a pale yellow solid resulting from the reaction of a stoichiometric mixture of Xe and PtF_6 was indeed $[Xe][PtF_6]$, which is more properly formulated as $[XeF][PtF_5]$. Bartlett conjectured that the latter product was likely to be a $n XeF^+$ salt of the polymeric anion $(PtF_5^-)_n$.[2] The synthesis of a stable xenon compound soon led to other examples of binary xenon fluorides, namely, XeF_2,[3] XeF_4,[4] and XeF_6,[5] as well as XeO_3,[6] $XeOF_4$,[7] and KrF_2,[8] all within three years of Bartlett's initial discovery of noble-gas reactivity.

Although HArF has been stabilized in a solid argon matrix at extremely low temperature (7.5 K) and studied by infrared spectroscopy[9,10] and ArF^+ has been observed in the gas phase in a vacuum ultraviolet study in which argon/fluorine mixtures were irradiated at 79.1 nm,[11] no long-lived argon species have been synthesized in macroscopic amounts to date. Synthesis of radon compounds is rendered difficult because no stable isotopes of this element exist. When a mixture of trace amounts of radon-222 and fluorine gas are heated to approximately 400 °C, a non-volatile fluoride is formed.[12] Radon was also oxidized by halogen fluorides or NiF_6^{2-} to give stable solutions of radon fluoride, which were not analyzed because they were prepared at the radiotracer level owing to the radioactivity of ^{222}Rn ($t_{½}$ = 3.82 d). Comparison of the reactions of radon with those of krypton and xenon suggest that RnF_2 is formed,[13] and electromigration and ion-exchange studies show that the ionic radon species present in solutions of halogen fluorides in SbF_5 are likely RnF^+ and Rn^{2+}.[14] Thus, the only Group 18 elements which exhibit extensive chemistries are xenon and krypton.

Xenon has the most extensive chemistry among the noble gases, exhibiting oxidation states of +½, +2, +4, +6, and +8, of which all but +½ are stabilized by bonds to electronegative atoms such as fluorine, oxygen, and chlorine, as well as by electronegative ligands bonded through oxygen, carbon, and nitrogen. Krypton has a less extensive chemistry, exhibiting only the +2 oxidation state, which is stabilized by bonding to fluorine or to ligands bonded through oxygen or nitrogen. A number of comprehensive reviews covering the chemistry of the noble gases are available,[15-21] as

well as a historical account of the events leading up to the discovery of noble-gas reactivity and its impact on modern chemistry.[22]

1.2. Xenon(II) Chemistry

The compounds of xenon in the +2 oxidation state are the most widely studied of the noble gases, and are ultimately derived from XeF_2. Several synthetic routes to XeF_2 are known, with the most convenient, high-yield synthesis being the direct combination of the elements at high temperatures (ca. 300 °C) in the presence of an excess of Xe (eq 1.2).[23,24] The compound is a white, crystalline solid that is stable at room

$$Xe + F_2 \longrightarrow XeF_2 \qquad (1.2)$$

temperature ($\Delta H_f^o = -162.8 \pm 0.9$ kJ mol^{-1};[25] m.p., 129.03 ±0.05 °C;[26] vapour pressure at 298.15 K, 4.55 Torr[26]), and exhibits strong oxidant behaviour.

The bonding in XeF_2 can be described in terms of valence bond structures or by molecular orbital (MO) theory. The valence bond description maintains an octet of electrons around each atom, and retains the canonical 2-centre-2-electron model of a chemical bond, through the superposition of two resonance structures (Structures I and III) to describe an average Lewis structure denoted by Structure II. In an MO description,

$$F\text{–}Xe^{+}\ F^{-} \quad \leftrightarrow \quad F\text{---}Xe\text{---}F \quad \leftrightarrow \quad F^{-}\ {}^{+}Xe\text{–}F$$

I II III

the octet of electrons is again retained. Of the 22 electrons in XeF_2, all but four are placed in non-bonding atomic orbitals (AOs) to give an ns^2 np_x^2 np_y^2 np_z^0 electron configuration around each atom. The two unoccupied p_z orbitals of the fluorine atoms are mixed with the unoccupied p_z orbital of the noble-gas atom to generate three MOs; bonding(Ψ_1), non-bonding(Ψ_2), and anti-bonding(Ψ_3), respectively (Figure 1.1). The four

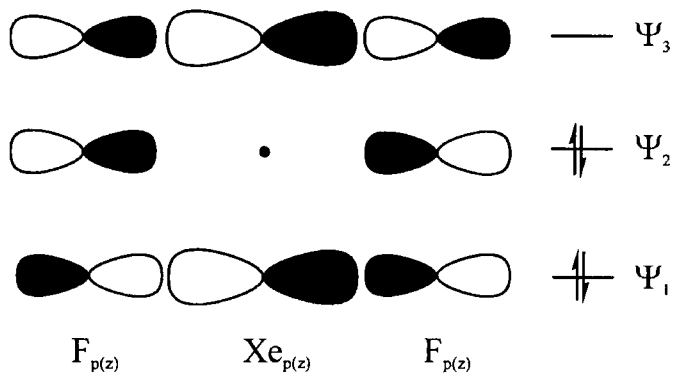

Figure 1.1. Partial MO description representing the σ-bonding in XeF_2.

non-AO electrons populate the bonding and non-bonding MOs, giving a bond order of 0.5 for the two Xe–F interactions. The molecule is said to possess a 3-centre-2-electron model of bonding (or alternatively, a 3-centre-4-electron model if one includes the electrons in the non-bonding MO). Since the non-bonding MO is localized mainly over the two fluorine atoms, the Xe–F bond is significantly polarized, which is in agreement with the valence bond description. As a consequence, XeF_2 tends to be a fluoride ion donor (Lewis base), and can either coordinate to a Lewis acid centre of appropriate strength through a fluorine atom, or transfer a fluoride ion to form XeF^+ and the corresponding fluoro-anion derived from the Lewis acid.

The reactivity of XeF_2 has been extensively explored, resulting in Xe–O, Xe–C, Xe–N, and Xe–Cl bonded species. Derivatives of xenon(II) are typically prepared (1) by fluoride ion abstraction from XeF_2, (2) by metathesis (ligand exchange) reactions involving XeF_2 and a suitable ligand transfer reagent, (3) by HF displacement in the reaction of XeF_2 with a strong protic acid, or (4) by reaction of the Lewis acid, XeF^+, with an oxidatively resistant base. This reactivity will be further explored in the ensuing discussion in this chapter.

There are two general classes of ligands which are suitable for stabilizing xenon in its positive oxidation states; protonic acids which also exist as stable anions, and neutral Lewis bases. In each case, the ligand must be resistant to redox degradation and withstand the high electron affinity associated with the positive formal oxidation state of the noble gas to which it is bonded. The anion of the ligand must (1) have a high effective group electronegativity and first adiabatic ionization potential, (2) exist as a moderate to strong monoprotic acid, (3) exist as a stable anion in alkali metal salts, and (4) form a positive chlorine derivative. Neutral Lewis base ligands must (1) posess a first adiabatic ionization potential greater than the electron affinity of the strongly oxidizing noble-gas cation, and (2) be basic enough to donate an electron lone pair to the noble-gas cation Lewis acid.

1.2.1. Fluoride Ion Donor Properties of XeF_2

Xenon difluoride reacts with strong fluoride ion acceptors such as AsF_5 and SbF_5 to form adducts having the formulations $XeF_2 \cdot MF_5$, $XeF_2 \cdot 2MF_5$, and $2XeF_2 \cdot MF_5$, which

are best described as salts of the XeF^+ and $Xe_2F_3^+$ cations (eqs 1.3–1.5).[27-29] The XeF^+ cation interacts strongly with the MF_6^- anion by means of a fluorine bridge

$$XeF_2 + MF_5 \longrightarrow [XeF][MF_6] \ (M = As, Sb) \quad (1.3)$$

$$XeF_2 + 2MF_5 \longrightarrow [XeF][M_2F_{11}] \ (M = As, Sb) \quad (1.4)$$

$$XeF_2 + [XeF][MF_6] \longrightarrow [Xe_2F_3][MF_6] \ (M = As, Sb) \quad (1.5)$$

between xenon and a fluorine atom of the anion,[29] while the $Xe_2F_3^+$ cation does not fluorine bridge to the anion.[28] The $Xe_2F_3^+$ cation can be regarded as a fluoride ion bridged to two XeF^+ cations, forming a symmetric, planar, V-shaped cation having C_{2v} symmetry, which also exhibits slightly bent F–Xe---F bond angles (Structure IV).[28]

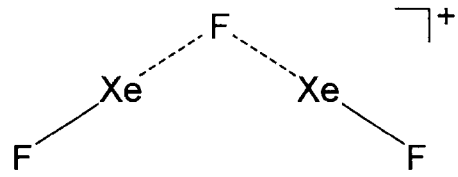

IV

The propensity of the XeF^+ cation to form fluorine bridges attests to its strong Lewis acid character.[18]

The ionic character of the Xe---F interaction in the $[XeF][MF_6]$ salts is dependent on the fluorobasicity of the anion, i.e., the ability of the MF_6^- anion to partially donate a fluoride ion to the XeF^+ cation. Decreasing the fluoride ion basicity of the anion (or increasing the Lewis acidity of the Lewis acid fluoride) leads to a more ionic Xe---F bridge interaction. For example, the weaker fluoride ion donor properties of $Sb_2F_{11}^-$

relative to AsF_6^- leads to a more ionic interaction between the bridging Xe---F in $[XeF][Sb_2F_{11}]$ (Xe---F distance, 2.343(4) Å)[30] than in $[XeF][AsF_6]$ (Xe---F distance, 2.208(3) Å).[30] Because these bonds are not purely ionic, they are significantly shorter than the sum of the xenon and fluorine van der Walls radii (3.63 Å).[31] The difference in fluoride ion donor properties for these anions does not, however, significantly affect the terminal Xe–F bond lengths of $[XeF][Sb_2F_{11}]$ (1.888(4) Å)[30] and $[XeF][AsF_6]$ (1.888(3) Å).[30]

A simple valence bond description for XeF_2 and $[XeF][MF_6]$ accounts for the behaviour of the F–Xe bond of XeF^+ salts with the fluorobasicity of the anion. The interactions can be represented in terms of three competing resonance structures which serve to describe the 3-centre-2-electron bonding in their structures (Structures V–VII).

$$\underset{\text{V}}{F\text{–}Xe^+\ F\text{–}MF_5^-} \leftrightarrow \underset{\text{VI}}{F\text{–}Xe^+\ F^-\ MF_5} \leftrightarrow \underset{\text{VII}}{F^-\ {}^+Xe\text{–}F\ MF_5}$$

When a fluoride ion acceptor is introduced to XeF_2, it is able to effectively stabilize the ionic resonance structures (Structures II and IV, vide supra). As the interaction between xenon and the bridging fluorine becomes more ionic in character (Structure VI), the bridging fluorine donates less electron density to $F\text{–}Xe^+$, increasing the bond order between xenon and the terminal fluorine. Conversely, a more covalent interaction between xenon and the bridge fluorine (Structure VII) donates more electron density to $F\text{–}Xe^+$, decreasing the bond order between xenon and the terminal fluorine.

1.2.2. The Lewis Acid Properties of the XeF^+ Cation

The Lewis acidity of the XeF^+ cation, as seen from the propensity of XeF^+ to form fluorine bridges with the anions of its salts[18] and by its ability to form the $Xe_2F_3^+$ cation (eq 1.5),[28] has been exploited to form Xe(II)–N bonded cations by the reaction of oxidatively resistant electron pair donors with XeF^+.[32] The electron affinity of XeF^+ has been estimated to be 10.9 eV,[33] allowing one to predict which ligands, based on their first adiabatic ionization potentials, are likely to be stable to redox degradation by this noble-gas cation. Reactions of XeF^+ with neutral organic nitrogen bases in HF, or reactions of XeF_2 with protonated nitrogen base salts in BrF_5 accompanied by HF elimination, have led to cations in which XeF^+ is adducted to formally sp- and sp^2-hybridized nitrogen centers. These include hydrogen cyanide,[34,35] alkylnitriles,[34] pentafluorobenzene-nitrile,[34] perfluoroalkylnitriles,[34,36] perfluoropyridines,[37] and *s*-trifluorotriazine.[36] With the exception of the *s*-trifluorotriazine adduct-cation, *s*-$C_3F_3N_2NXeF^+$, all of the adduct-cations decompose below room temperature.

1.3. Compounds Containing Xenon-Nitrogen Bonds

Known species containing xenon-nitrogen bonds can be divided into three classes; those in which xenon is bound to nitrogen having formal sp-, sp^2-, or sp^3-hybridization. Prior to this work, examples exhibiting sp-hybridization were limited to the XeF^+ adducts of organic nitriles, and exhibition of formal sp^3-hybridization at nitrogen was solely represented by $F_5TeN(H)Xe^+$. Species containing xenon bound to formally sp^2-hybridized nitrogen include the XeF^+ adducts of *s*-trifluorotriazine and several perfluoropyridines, as

well as species derived from the $-N(SO_2F)_2$ and $-N(SO_2CF_3)_2$ groups. The ensuing discussion will more fully describe these three classes of Xe–N bonded species.

1.3.1. Xenon Bound to Formally sp-Hybridized Nitrogen

The majority of xenon-nitrogen bonded species that contain formally sp-hybridized nitrogen have been synthesized by addition of stoichiometric amounts of the XeF^+ or $Xe_2F_3^+$, cations as their AsF_6^- salts, to neutral organic nitriles, RC≡N, in anhydrous HF (aHF) and/or BrF_5 (eqs 1.6 and 1.7). The cations generated have been characterized by

$$[XeF][AsF_6] + RC{\equiv}N \longrightarrow [RC{\equiv}NXeF][AsF_6] \quad (1.6)$$

$$[Xe_2F_3][AsF_6] + RC{\equiv}N \longrightarrow [RC{\equiv}NXeF][AsF_6] + XeF_2 \quad (1.7)$$

multi-NMR and Raman spectroscopy as their AsF_6^- salts, and include $RC{\equiv}NXeF^+$ (R = H,[34,35,38] CH_3,[34,38] CH_2F,[34] CH_2Cl,[39] CF_3,[36] C_2H_5,[34] CH_2FCH_2,[39] C_2F_5,[34,36] *n*-C_3H_7,[39] $CH_2FCH_2CH_2$,[39] CH_3CHFCH_2,[39] $CHF_2CH_2CH_2$,[39] $CH_3CF_2CH_2$,[39] *n*-C_3F_7,[34,36] *n*-C_4H_9,[39] $CH_3CHFCH_2CH_2$,[39] $(CH_3)_2CH$,[39] $(CH_3)_3C$,[38,39] $CH_2FC(CH_3)H$,[39] $CH_2ClC(CH_3)H$,[39] or C_6F_5[34]). In addition, single-crystal X-ray structures have been determined for $[HC{\equiv}NXeF][AsF_6]$, $[CH_3C{\equiv}NXeF][AsF_6]{\cdot}HF$ and $[(CH_3)_3CC{\equiv}NXeF][AsF_6]$ (Figure 1.2),[38] providing Xe–N bond lengths of 2.235(3), 2.179(7), and 2.212(4) Å, respectively. The NMR chemical shifts, Raman frequencies, and X-ray diffraction-determined geometries support a bonding description in which the Xe–N bonds in the $RC{\equiv}NXeF^+$ cations are regarded as Lewis acid-base donor-acceptor bonds. This interpretation is also supported by Atoms in Molecules (AIM) analysis.[33] This donor-acceptor bond can be viewed as

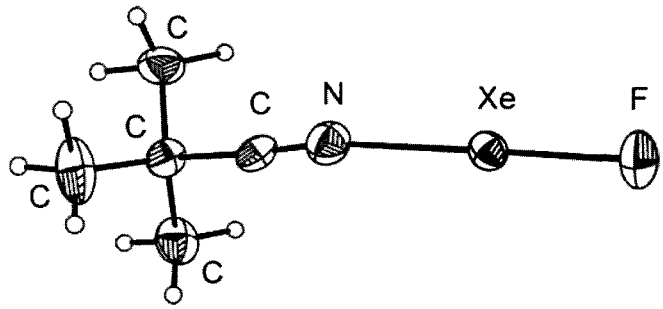

Figure 1.2. X-ray Crystal Structure of the $(CH_3)_3CCNXeF^+$ cation in $[(CH_3)_3CCNXeF][AsF_6]$; thermal ellipsoids are shown at the 50% probability level.[38]

the inter-penetration of the outer diffuse closed shell (nonbonded) densities of the Xe and N atoms. The xenon atom electron lone pairs form a torus of electron density which exposes the positively charged xenon atom core opposite the F ligand in XeF^+,[40] resulting in considerable electro-static character for the Xe–N bond.

A second group of cations containing xenon bound to formally sp-hybridized nitrogen atoms are the salts of the $C_6F_5Xe^+$ cation in which $C_6F_5Xe^+$ is coordinated to CH_3CN. Crystallization of these salts as adducts of CH_3CN is a consequence of their high solubilities in CH_3CN, but lower solubilities in weakly-coordinating solvents such as CH_2Cl_2. When XeF_2 was allowed to react with $B(C_6F_5)_3$ in CH_2Cl_2 solution at –40 °C, sparingly soluble $[C_6F_5Xe][(C_6F_5)_2BF_2]$ precipitated (eq 1.8),[41] which readily dissolved in CH_3CN to give a solution from which the CH_3CN adduct, $[C_6F_5Xe{---}NCCH_3][(C_6F_5)_2BF_2]$, was crystallized (eq 1.9).[41] This difference in solubilities was also employed in metathesis reactions in CH_3CN between soluble $[C_6F_5Xe][BF_4]$ and $[M][BY_4]$ (Y = CF_3, CN, or C_6F_5; M = K or Cs) salts which precipitated sparingly soluble

$$XeF_2 + B(C_6F_5)_3 \longrightarrow [C_6F_5Xe][(C_6F_5)_2BF_2] \quad (1.8)$$

$$[C_6F_5Xe][(C_6F_5)_2BF_2] + CH_3CN \longrightarrow [C_6F_5Xe{-}{-}{-}NCCH_3][(C_6F_5)_2BF_2] \quad (1.9)$$

$[M][BF_4]$, thereby generating $C_6F_5Xe^+$ salts of the BY_4^- anions.[42] Of these salts, crystallization yielded two more structures in which $C_6F_5Xe^+$ was adducted to CH_3CN, namely the $C_6F_5Xe{-}{-}{-}NCCH_3^+$ salts of $B(CF_3)_4^-$ and $B(C_6F_5)_4^-$.[42] Compared to the nitrile adducts of XeF^+ (vide supra), these salts contain considerably longer Xe---N contacts (2.681(8), 2.640(6), and 2.610(11) Å, respectively). Interestingly, the $[C_6F_5Xe][B(CN)_4]$ salt can be considered as an ion-pair formulated as $C_6F_5Xe{-}{-}{-}NCB(CN)_3$, because of the short Xe---N contact (2.716(3) Å) to a cyanide ligand of the anion, that is also considerably less than the sum of the xenon and nitrogen van der Waals radii (3.71 Å).[31]

1.3.2. Xenon Bound to Formally sp^2-Hybridized Nitrogen

Three distinct synthetic approaches have been used to synthesize species containing xenon bound to formally sp^2-hybridized nitrogen atoms; (1) the use of XeF^+ as a Lewis acid to adduct to a neutral nitrogen base, (2) the reaction of XeF_2 with a protonic acid which also exists as a stable anion, liberating HF, and (3) fluorine-ligand exchange with XeF_2 by use of an appropriate ligand transfer reagent.

The former approach was used in the neat, room-temperature reaction of XeF^+ with *s*-trifluorotriazine to form the *s*-$C_3F_3N_2NXeF^+$ cation (eq 1.10). The [*s*-$C_3F_3N_2NXeF$][AsF_6] salt has been characterized by multi-NMR spectroscopy (in HF

$$[XeF][AsF_6] + s\text{-}C_3F_3N_3 \longrightarrow [s\text{-}C_3F_3N_2NXeF][AsF_6] \quad (1.10)$$

and BrF_5 solutions) and Raman spectroscopy.[36] The single-crystal X-ray structure of $[s\text{-}C_3F_3N_2NXeF][AsF_6]\cdot 2.5BrF_5$ has also been determined.[38] Reaction of the nitrogen bases RC_5F_4N [R = F, *n*-CF_3 (*n* = 2, 3, 4)] with XeF^+ in aHF at –30 to –20 °C proceeds through a base protonation reaction (eq 1.11) and two equilibria involving XeF_2 (eqs 1.12 and 1.13) to generate $RC_5F_4NXeF^+$. Reaction 1.13 also proceeds in BrF_5 solution with the

$$RC_5F_4N + (n+2)HF \longrightarrow [RC_5F_4NH][HF_2\cdot nHF] \quad (1.11)$$

$$[RC_5F_4NH][HF_2\cdot nHF] + [XeF][AsF_6] \rightleftharpoons [RC_5F_4NH][AsF_6] + XeF_2 + (n+1)HF \quad (1.12)$$

$$[RC_5F_4NH][AsF_6] + XeF_2 \rightleftharpoons [RC_5F_4NXeF][AsF_6] + HF \quad (1.13)$$

Xe–N bonded cation being more strongly favoured in this aprotic medium. The $[C_5F_5NXeF][AsF_6]$ salt has been characterized by multi-NMR (in HF and BrF_5 solutions) and Raman spectroscopy[37] and by the single-crystal X-ray structure of $[C_5F_5NXeF][AsF_6]\cdot 2.5BrF_5$.[38] The *n*-$CF_3C_5F_4NXeF^+$ (*n* = 2,[39] 3,[39] 4[37]) cations have been characterized by multi-NMR (in HF and BrF_5 solutions) and by Raman spectroscopy of their AsF_6^- salts.

The studies in which salts of $C_6F_5Xe^+$ have been prepared in CH_3CN solvent led to adducts bonded through the sp-hybridized nitrogen of this base (vide supra). Adducts of $C_6F_5Xe^+$ to nitrogen atoms having formal sp^2-hybridization, in the form of a series of pyridines, have been studied by multi-NMR spectroscopy.[43] The crystal structure of one such adduct, $[2,6\text{-}C_5H_3F_2N\text{---}XeC_6F_5][AsF_6]$, has been determined and exhibits a long

Xe---N contact, 2.694(5) Å,[43] which is still considerably less than the sum of the xenon and nitrogen van der Waals radii (3.71 Å).[31]

A further example of xenon bonded to sp^2-hybridized nitrogen is the first xenon-nitrogen bonded compound, $FXeN(SO_2F)_2$. This compound was synthesized by reaction of the acid, $HN(SO_2F)_2$, with XeF_2 in CF_2Cl_2 solvent at 0 °C for 4 d (eq 1.14),[44] and was characterized by multi-NMR and Raman spectroscopy,[44-46] as well as by single-crystal X-ray diffraction (Figure 1.3).[46] A two-fold increase in the stoichiometric amount of the

$$HN(SO_2F)_2 + XeF_2 \longrightarrow FXeN(SO_2F)_2 + HF \qquad (1.14)$$

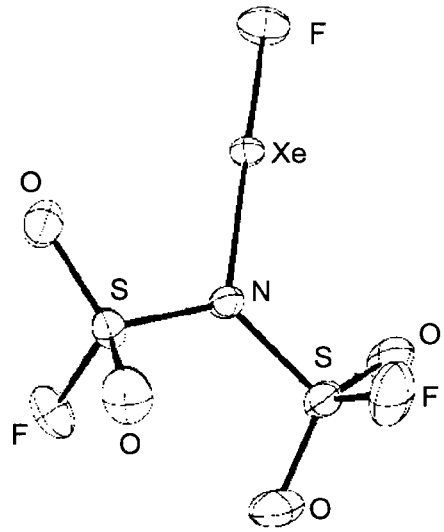

Figure 1.3. X-ray Crystal Structure of $FXeN(SO_2F)_2$; thermal ellipsoids are shown at the 50% probability level.[46]

acid resulted in the *bis*-derivative, $Xe[N(SO_2F)_2]_2$ (eq 1.15)[45,47] and, in the case of the trifluoromethyl analogue, $Xe[N(SO_2CF_3)_2]_2$, improved yields were obtained when the

trimethylsilyl derivative was allowed to react with XeF_2 in CF_2Cl_2 solvent at 0 °C (eq 1.16).[48] The related cationic species, $F[XeN(SO_2F)_2]_2^+$, was generated by fluoride ion

$$2HN(SO_2F)_2 + XeF_2 \longrightarrow Xe[N(SO_2F)_2]_2 + 2HF \quad (1.15)$$

$$2(CH_3)_3SiN(SO_2CF_3)_2 + XeF_2 \longrightarrow Xe[N(SO_2CF_3)_2]_2 + 2(CH_3)_3SiF \quad (1.16)$$

abstraction from $FXeN(SO_2F)_2$ using half an equivalent of neat AsF_5 at −78 to −5 °C over 36 h to generate the AsF_6^- salt. (eq 1.17)[45,47,49] Fluoride abstraction with one equivalent of AsF_5 (neat liquid, −78 °C) gave $[XeN(SO_2F)_2][AsF_6]$ (eq 1.18).[49] In addition, $[XeN(SO_2F)_2][AsF_6]$ was also generated by pumping on the latter salt under dynamic vacuum at 23 °C, liberating AsF_5 (eq 1.19). The $XeN(SO_2F)_2^+$ cation was obtained as its $Sb_3F_{16}^-$ salt by careful reaction of $F[XeN(SO_2F)_2]_2^+AsF_6^-$ with excess liquid SbF_5, which evolved AsF_5 (eq 1.20). The crystal structure of the product, $[XeN(SO_2F)_2][Sb_3F_{16}]$, was determined (Figure 1.4).[49]

$$2FXeN(SO_2F)_2 + AsF_5 \longrightarrow F[XeN(SO_2F)_2]_2^+AsF_6^- \quad (1.17)$$

$$FXeN(SO_2F)_2 + AsF_5 \longrightarrow [XeN(SO_2F)_2][AsF_6] \quad (1.18)$$

$$2[XeN(SO_2F)_2][AsF_6] \longrightarrow F[XeN(SO_2F)_2]_2^+AsF_6^- + AsF_5 \quad (1.19)$$

$$F[XeN(SO_2F)_2]_2^+AsF_6^- + 3SbF_5 \longrightarrow 2[XeN(SO_2F)_2][Sb_3F_{16}] + AsF_5 \quad (1.20)$$

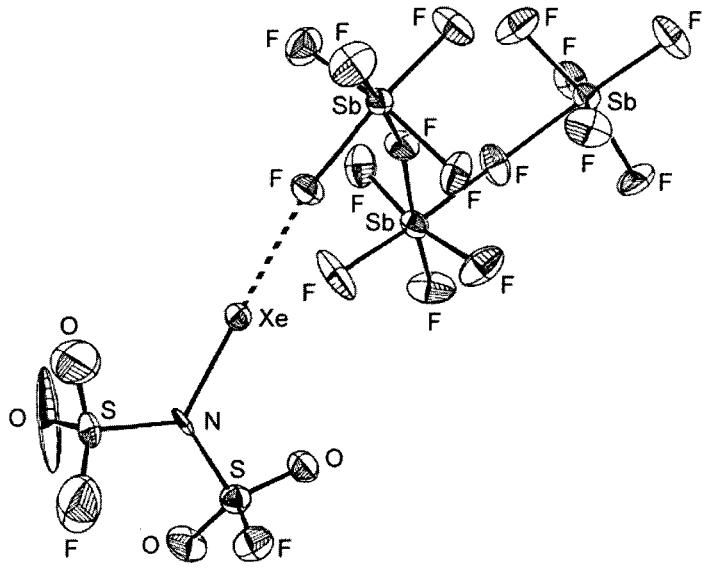

Figure 1.4. X-ray Crystal Structure of $[XeN(SO_2F)_2][Sb_3F_{16}]$; thermal ellipsoids are shown at the 50% probability level.[49]

1.3.3. Xenon Bound to Formally sp^3-Hybridized Nitrogen

Prior to this work, only one example of xenon bound to formally sp^3-hybridized nitrogen was known, namely, $F_5TeN(H)Xe^+$, which was synthesized as its AsF_6^- salt by reaction of F_5TeNH_2 with $[XeF][AsF_6]$ in aHF at –45 to –35 °C (eqs 1.21–1.24), and in the equilibrium reaction of $F_5TeNH_3^+$ with XeF_2 in HF (–45 to –35 °C) or BrF_5 (–62 to –45 °C) solvents (eq 1.24). The cation has been characterized by multi-NMR and Raman

$$[XeF][AsF_6] + HF \rightleftharpoons XeF_2 + [H_2F][AsF_6] \quad (1.21)$$

$$F_5TeNH_2 + [H_2F][AsF_6] \longrightarrow [F_5TeNH_3][AsF_6] + HF \quad (1.22)$$

$$F_5TeNH_2 + (n + 2)HF \longrightarrow [F_5TeNH_3][HF_2 \cdot nHF] \quad (1.23)$$

$$[F_5TeNH_3][AsF_6] + XeF_2 \rightleftharpoons [F_5TeN(H)Xe][AsF_6] + 2HF \quad (1.24)$$

spectroscopy, and by single-crystal X-ray diffraction (Figure 1.5).[50] The ^{129}Xe chemical shift of $F_5TeN(H)Xe^+$ indicates the xenon atom is highly shielded (–2902 ppm, BrF_5 solvent, –48 °C) and the Xe–N bond is among the shortest known (2.044(4) Å), making this one of the most covalent Xe–N bonds formed by xenon.

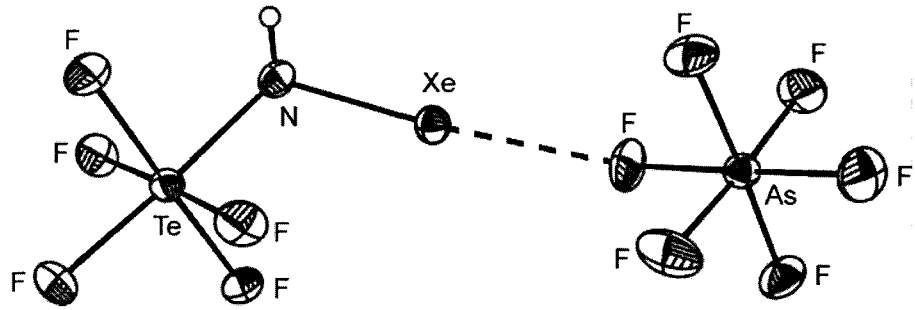

Figure 1.5. X-ray Crystal Structure of $[F_5TeN(H)Xe][AsF_6]$; thermal ellipsoids are shown at the 50% probability level.[50]

1.4. Krypton(II) Chemistry

The chemistry of krypton has been reviewed,[21] and in many ways is analogous to that of xenon, however, far fewer krypton compounds are known because of their lower thermodynamic stabilities and stronger oxidant properties. The only known neutral krypton fluoride, KrF_2, has an endothermic heat of formation, but can be produced in macroscopic quantities at low temperature. The endothermic nature of this compound makes it a better low-temperature source of F· atoms than F_2. This is exemplified by the mean thermochemical bond energies for F_2, XeF_2, and KrF_2, which are 154.6(6),[51] 81.4,[52] and –30.1(1.7) kJ mol^{-1},[53,54] respectively. Methods used to generate the fluorine atoms that are required for reaction with krypton include high-voltage glow discharge,[8,55,56]

small particle (e^-, p^+) bombardment,[57,58] UV irradiation,[59-63] and thermal dissociation using a hot-wire reactor.[63-65] The highly reactive fluorine radicals (eq 1.25) react with krypton to form the metastable KrF$^\bullet$ radical (eq 1.26), which forms KrF_2 by combination with a fluorine radical, or by combination with KrF$^\bullet$, liberating Kr (eqs 1.27, 1.28).

$$F_2 \longrightarrow 2F^\bullet \quad (1.25)$$

$$F^\bullet + Kr \longrightarrow KrF^\bullet \quad (1.26)$$

$$KrF^\bullet + F^\bullet \longrightarrow KrF_2 \quad (1.27)$$

$$KrF^\bullet + KrF^\bullet \longrightarrow KrF_2 + Kr \quad (1.28)$$

1.4.1. Fluoride Ion Donor Properties of KrF_2

Krypton difluoride exhibits fluoride ion donor behaviour that is similar to that established for XeF_2. Reactions of KrF_2 with strong fluoride acceptors such as AsF_5 and SbF_5 to form KrF^+ and $Kr_2F_3^+$ salts (eqs 1.29–1.31) in the absence of a solvent and in

$$KrF_2 + MF_5 \longrightarrow [KrF][MF_6] \ (M = As, Sb) \quad (1.29)$$

$$KrF_2 + 2MF_5 \longrightarrow [KrF][M_2F_{11}] \ (M = As, Sb) \quad (1.30)$$

$$KrF_2 + [KrF][MF_6] \longrightarrow [Kr_2F_3][MF_6] \ (M = As, Sb) \quad (1.31)$$

aHF or BrF_5 solvents have been well studied.[21] Unlike their xenon analogues, the KrF^+ and $Kr_2F_3^+$ cations are extremely potent oxidizers and are thermodynamically unstable with respect to redox decomposition. As in the case of the XeF^+ cation, the KrF^+ cation interacts strongly with the anion by means of a fluorine bridge between krypton and a fluorine atom of the anion,[21] whereas the $Kr_2F_3^+$ cation does not strongly interact with the

anion. The $Kr_2F_3^+$ cation has a V-shaped geometry analogous to that of the $Xe_2F_3^+$ cation (Structure I).

1.4.2. Lewis Acid Properties of the KrF^+ Cation

As is the case for XeF^+, the Lewis acidity of the KrF^+ cation is manifested by its tendency to form fluorine bridges with the anions of its salts,[21] and by its ability to form the dinuclear $Kr_2F_3^+$ cation in preference to bridging to MF_6^-.[21] The Lewis acidity of KrF^+ has been exploited to form the first Kr–N bonded species by the reaction of protonated or AsF_5-adducted oxidatively resistant electron pair donors with KrF^+.[36,66] Despite the strong oxidizing properties of the KrF^+ cation, a limited number of nitriles having first adiabatic ionization potentials that are comparable with or exceed the estimated electron affinity of the KrF^+ cation (13.2 eV),[66] are resistant to oxidation by the KrF^+ cation at low temperatures. These adducts are thermally and kinetically unstable above ca. –60 °C and are currently the only known examples of krypton bonded to nitrogen.

1.5. Krypton-Nitrogen Bonds

The known chemistry of compounds containing krypton-nitrogen bonds is restricted to the series of four cations generated by the low-temperature reaction of KrF_2 with the protonated hydrogen cyanide cation, $HC{\equiv}NH^+$ (eq 1.32),[66] and the Lewis acid-base adducts, $R_FC{\equiv}NAsF_5$ ($R_F = CF_3$, C_2F_5, n-C_3F_7) (eq 1.33)[36] in BrF_5 or aHF

$$[HC{\equiv}NH][AsF_6] + KrF_2 \longrightarrow [HC{\equiv}NKrF][AsF_6] + HF \qquad (1.32)$$

$$R_FC{\equiv}NAsF_5 + KrF_2 \longrightarrow [R_FC{\equiv}NKrF][AsF_6] \quad (1.33)$$

solvent at ca. –60 °C to give the corresponding KrF^+ adducts. This synthetic strategy differs from that used to generate the analogous xenon cations; by direct reaction of XeF^+ with the nitrile (eq. 1.6). The KrF^+ cation is a much more potent oxidizer than XeF^+, which results in oxidative attack and fluorination of the base with the rapid evolution of Kr, NF_3, and CF_4 gases at higher temperature. Such reactions are likely to be accompanied by detonations. Although these cations were found to be far less stable than their xenon analogues, they have been unambiguously characterized by low-temperature multi-NMR spectroscopy despite their short (1–2 h) lifetimes at ca. –60 °C,[36,66] which precluded their study by other means.

1.6. Sulfur-Nitrogen-Fluorine Chemistry

The first reported compounds containing only the elements sulfur, nitrogen, and fluorine were $S_4N_4F_4$, SN_2F_2, and N≡SF, which were synthesized by reaction of S_4N_4 with AgF_2.[67] Shortly thereafter, N≡SF was oxidized with two equivalents of AgF_2 to give $N{\equiv}SF_3$ (eq 1.34).[68] In addition to N≡SF and $N{\equiv}SF_3$, several other neutral NSF_x

$$N{\equiv}SF + 2AgF_2 \longrightarrow N{\equiv}SF_3 + 2AgF \quad (1.34)$$

(x = 1, 3, 5, 7) compounds are known, including FNS,[69,70] $FN{=}SF_2$,[71,72] $FN{=}SF_4$,[73,74] and F_2NSF_5.[75-77]

The field of sulfur-nitrogen-fluorine chemistry has, over the past fifty years, grown significantly, and several reviews are now available on this diverse topic.[78-81] Only the chemistry of $N{\equiv}SF_3$, which has a direct bearing on the experimental work described in this thesis, is summarized in the ensuing discussion.

1.6.1. The Structure and Chemistry of Thiazyl Trifuoride, $N{\equiv}SF_3$

The geometry of thiazyl trifluoride has been determined by NMR,[82] infrared,[82,83] Raman,[84] and microwave spectroscopy,[85] and most recently by single-crystal X-ray diffraction.[86] Like isoelectronic SO_2F_2, $N{\equiv}SF_3$ has a distorted tetrahedral geometry (Figure 1.6), with a formal N≡S triple bond and an electron lone pair on nitrogen.

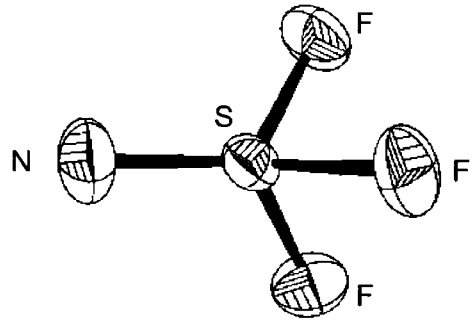

Figure 1.6. X-ray crystal structure of $N{\equiv}SF_3$; thermal ellipsoids are shown at the 50% probability level.[86]

The chemistry of $N{\equiv}SF_3$ has been reviewed,[78] and embraces three major areas of study; (1) reactions with Lewis acids, which occur by donation of the electron lone pair on nitrogen to a Lewis-acid centre to form a donor-acceptor adduct, (2) addition reactions

involving the π-system of the formal N≡S triple bond, and (3) reactions with nucleophiles that result from the partial positive charge at the coordinatively unsaturated sulfur atom.

The stability of $N{\equiv}SF_3$ towards the strong fluoride ion acceptors BF_3, AsF_5, and SbF_5 results in Lewis acid-base adduct formation to give $F_3S{\equiv}NBF_3$,[82,87] $F_3S{\equiv}NAsF_5$,[78,88] and $F_3S{\equiv}NSbF_5$.[88] Thiazyl trifluoride is also sufficiently stable to act as a main-group element ligand, as in $[(CF_3)_nSF_{3-n}{\cdot}N{\equiv}SF_3][AsF_6]$,[89] and as a transition-metal ligand,[78,90-95] e.g., $[M(N{\equiv}SF_3)_4][AsF_6]_2$ (M = Mn, Fe, Co, Ni, Cu).[94] Protonation of $N{\equiv}SF_3$ occurs in the superacidic medium HSO_3F/SbF_5 (eq 1.35), but above –80 °C, the equilibrium favours adduct formation (eq 1.36).[78] Although cations of the type $XN{\equiv}SF_3^+$ are expected

$$N{\equiv}SF + HSO_3F/SbF_5 \longrightarrow [F_3S{\equiv}NH][SbF_5OSO_2F] \quad (1.35)$$

$$[F_3S{\equiv}NH][SbF_5OSO_2F] + N{\equiv}SF_3 \rightleftharpoons F_3S{\equiv}NSbF_5 + HSO_3F{\cdot}N{\equiv}SF_3 \quad (1.36)$$

as intermediates in reactions that involve XF (X = H, Cl) addition to the N≡S triple bond of $N{\equiv}SF_3$, none have been isolated.[96,97] If, however, alkyl groups (R = CH_3, C_2H_5) are used to lower the electrophilicities of the cationic addition products, salts can be isolated (eq 1.37).[98-101]

$$N{\equiv}SF_3 + [ROSO][SbF_6] \longrightarrow [F_3S{\equiv}NR][SbF_6] + SO_2 \quad (1.37)$$

All known reactions of XF (X = H, Cl) with $N{\equiv}SF_3$ result in addition of two equivalents of XF across the N≡S triple bond, yielding F_5SNX_2 (eq 1.38),[96] but no

intermediates have been isolated. In the superacidic medium aHF/AsF_5, addition of HF to the AsF_5 adduct of $N{\equiv}SF_3$ gives the ammonium cation, $F_5SNH_3^+$ (eq 1.39).[101]

$$N{\equiv}SF_3 + 2XF \longrightarrow F_5SNX_2 \quad (1.38)$$

$$F_3S{\equiv}NAsF_5 + 3HF \longrightarrow [F_5SNH_3][AsF_6] \quad (1.39)$$

Thiazyl trifluoride also undergoes reactions with nucleophiles. Reaction with elemental fluorine in the presence of CsF (eq 1.40), and with HgF_2 and elemental chlorine (eq 1.41), gives products that are highly suggestive of the as yet unconfirmed

$$N{\equiv}SF_3 + CsF \longrightarrow \{[Cs][N{\equiv}SF_4]\} + F_2 \longrightarrow F_5SNF_2 + CsF \quad (1.40)$$

$$N{\equiv}SF_3 + HgF_2 \longrightarrow \{Hg(N{\equiv}SF_4)_2\} + Cl_2 \longrightarrow F_5SNCl_2 + HgF_2 \quad (1.41)$$

anion intermediate, $N{=}SF_4^-$,[78] which is isoelectronic with the well-known $O{=}SF_4$ molecule. Products which retain the formal N≡S triple bond are generated when $N{\equiv}SF_3$ is allowed to react with secondary amines ($HN(C_2H_5)_2$, HNC_5H_{10}, eq 1.42)[102,103] or C_6H_5OH (eq 1.43),[103] and undergo substitution at sulfur. Reactions with cesium perfluoroalkyl reagents [Cs][R_FF] (e.g., R_F = C_3F_6, eq 1.44)[104,105] or organolithium reagents (e.g., LiC_6H_5, eq 1.45)[106] lead to sulfur-carbon bond formation.

$$N{\equiv}SF_3 + 2R_2NH \longrightarrow N{\equiv}SF_2NR_2 + R_2NH{\cdot}HF \quad (1.42)$$

$$N{\equiv}SF_3 + C_6H_5OH + (CH_3)_3N \longrightarrow N{\equiv}SF_2OC_6H_5 + (CH_3)_3N{\cdot}HF \quad (1.43)$$

$$N{\equiv}SF_3 + [Cs][R_FF] \longrightarrow N{\equiv}SF_2R_F + CsF \quad (1.44)$$

$$N{\equiv}SF_3 + LiC_6H_5 \longrightarrow N{\equiv}SF_2C_6H_5 + LiF \quad (1.45)$$

Nucleophilic attack at the sulfur atom in $N{\equiv}SF_3$ by hydroxide ion is also likely, as evidenced by the generation of the intermediate, $HN{=}SOF_2$, in hot aqueous alkali (eq 1.46). The presence of $HN{=}SOF_2$ was inferred by precipitation of the

$$N{\equiv}SF_3 + KOH \longrightarrow HN{=}SOF_2 + KF \qquad (1.46)$$

$[P(C_6H_5)_4][N{=}SOF_2]$ salt.[107] Substitution reactions such as these have formed the basis for a large body of continuing work in the field of sulfur-nitrogen-fluorine chemistry.[86,108]

1.7. Purpose and Scope of the Present Work

The present work will expand upon the known chemistry of the noble gases, and in particular, it will explore avenues that may lead to new examples of xenon-nitrogen and krypton-nitrogen bonds in which the noble gas atom is bonded to an inorganic main-group ligand. Currently only Xe(II) and Kr(II) form bonds to nitrogen, and the majority of the known species involve organic nitrogen Lewis base ligands adducted to XeF^+ or KrF^+, or xenon bound to the bisfluorosulfurylamine ligand, $-N(SO_2F)_2$. The use of $N{\equiv}SF_3$ as an inorganic nitrogen Lewis base has potential to significantly expand this chemistry because of the demonstrated reactivity of the $S{\equiv}N$ bond. Structural characterization by multi-NMR and Raman spectroscopy and by single-crystal X-ray structure determinations of new Xe(II) and Kr(II) compounds are goals of the present work. The geometries and bonding of these new noble-gas species will also be studied by use of quantum-chemical calculations.

Another facet of the present research concerns the absence from the literature of full characterizations for the HF addition products of $N{\equiv}SF_3$, namely, F_5SNH_2 and $F_5SNH_3^+$, which renders further work on these fundamental sulfur-nitrogen-fluorine species important. The mechanism of HF solvolysis is unknown, and no intermediates arising from addition of only one molecule of HF have been isolated or characterized. The pentafluorosulfanyl species F_5SNH_2 and $F_5SNH_3^+$ may also provide avenues to new noble-gas species in reactions similar to those of their known tellurium analogues, and would significantly expand the chemistry of noble gases bonded to formally sp^3-hybridized nitrogen, of which there was only one example known prior to this work, namely, $F_5TeN(H)Xe^+$. Studies of the solvolytic behaviours of noble-gas compounds derived from $N{\equiv}SF_3$ could lead to new noble-gas species, as well as to a better understanding of the mechanism of the HF solvolysis of the S–N triple bond of $N{\equiv}SF_3$.

The aforementioned synthetic goals will broaden and deepen our understanding of the chemistry of the noble gases, the synthetic scope of $N{\equiv}SF_3$ and its derivatives, and enhance our understanding of sulphur-nitrogen-fluorine chemistry. The fundamental nature of the molecules under investigation will make it possible to validate geometries predicted by bonding models such as the VSEPR rules and by quantum-chemical calculations.

CHAPTER 2

EXPERIMENTAL SECTION

2.1. Standard Techniques

2.1.1. Dry Box and Vacuum Line Techniques

The compounds used and prepared during the course of this work were moisture- and temperature-sensitive, and were handled under rigorously anhydrous conditions on glass and metal vacuum line systems or in an inert atmosphere (N_2 gas) dry box (Vacuum Atmospheres Model DLX, oxygen and moisture <0.1 ppm) equipped with a glass cryowell. Preparative work inside the dry box requiring low temperatures was accomplished using a metal Dewar filled with 4.5 mm copper-plated spheres that had previously been cooled to ca. –140 °C in the glass cryowell (–196 °C) of the dry box.

Preparative work involving volatile fluorides that attack glass (e.g., HF) were carried out on metal vacuum lines constructed primarily from 316 stainless steel and nickel and fitted with 316 stainless steel valves (Autoclave Engineers, Inc., Figure 2.1). Pressures were measured at ambient temperatures using MKS Model PDR-5B pressure transducers having wetted surfaces constructed of Inconel. The pressure transducer possessed a range of 0–1150 Torr, which was accurate to ±0.5 Torr.

Reactions that did not involve transfer of materials that attack glass were carried out on Pyrex glass vacuum lines equipped with grease-free 6-mm J. Young PTFE/glass stopcocks outfitted with PTFE barrels (Figure 2.2). Pressures inside the glass manifold were monitored using a mercury manometer.

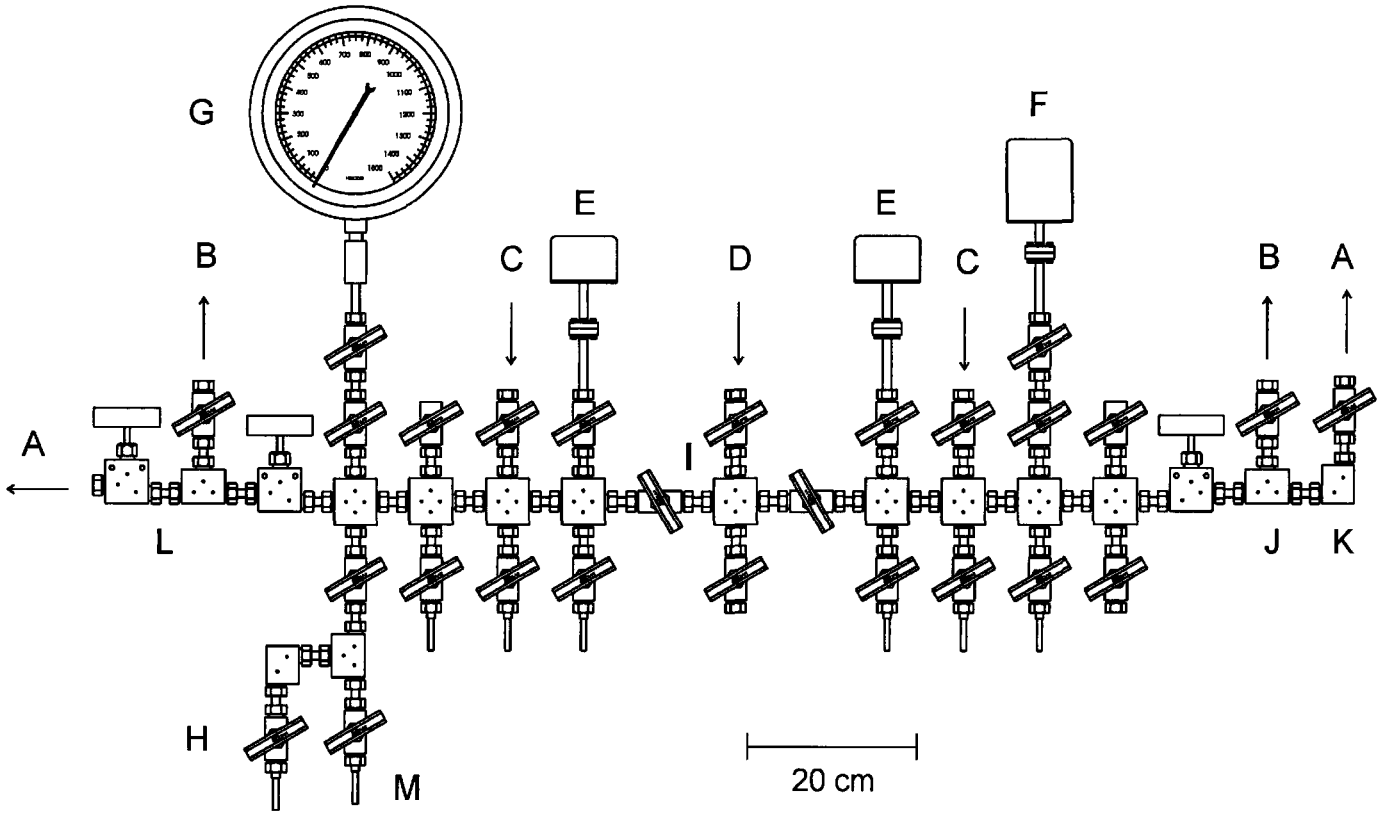

Figure 2.1. Schematic Diagram of Metal Vacuum Line System: (A) outlet to liquid nitrogen and charcoal (Norit) traps followed by a two-stage direct-drive rotary vacuum pump (Edwards, E2M8) – hard vacuum, (B) outlet to soda lime and liquid nitrogen traps followed by a two-stage direct-drive rotary vacuum pump (Edwards, E2M8) – rough vacuum, (C) dry nitrogen inlet, (D) fluorine inlet, (E) MKS Model PDR-5B pressure transducer (0 –1000 Torr), (F) MKS Model PDR-5B pressure transducer (0 – 10 Torr), (G) Bourdon pressure gauge (0 – 1500 Torr), (H) $^{3}/_{8}$-in. 316 stainless steel high pressure valve (Autoclave Engineers, 30BM6071), (I) 316 stainless steel cross, (J) 316 stainless steel T-piece, (K) 316 stainless steel L-piece, (L) nickel connectors, (M) ¼-in. o.d., $^{1}/_{8}$-in. i.d. nickel tube.

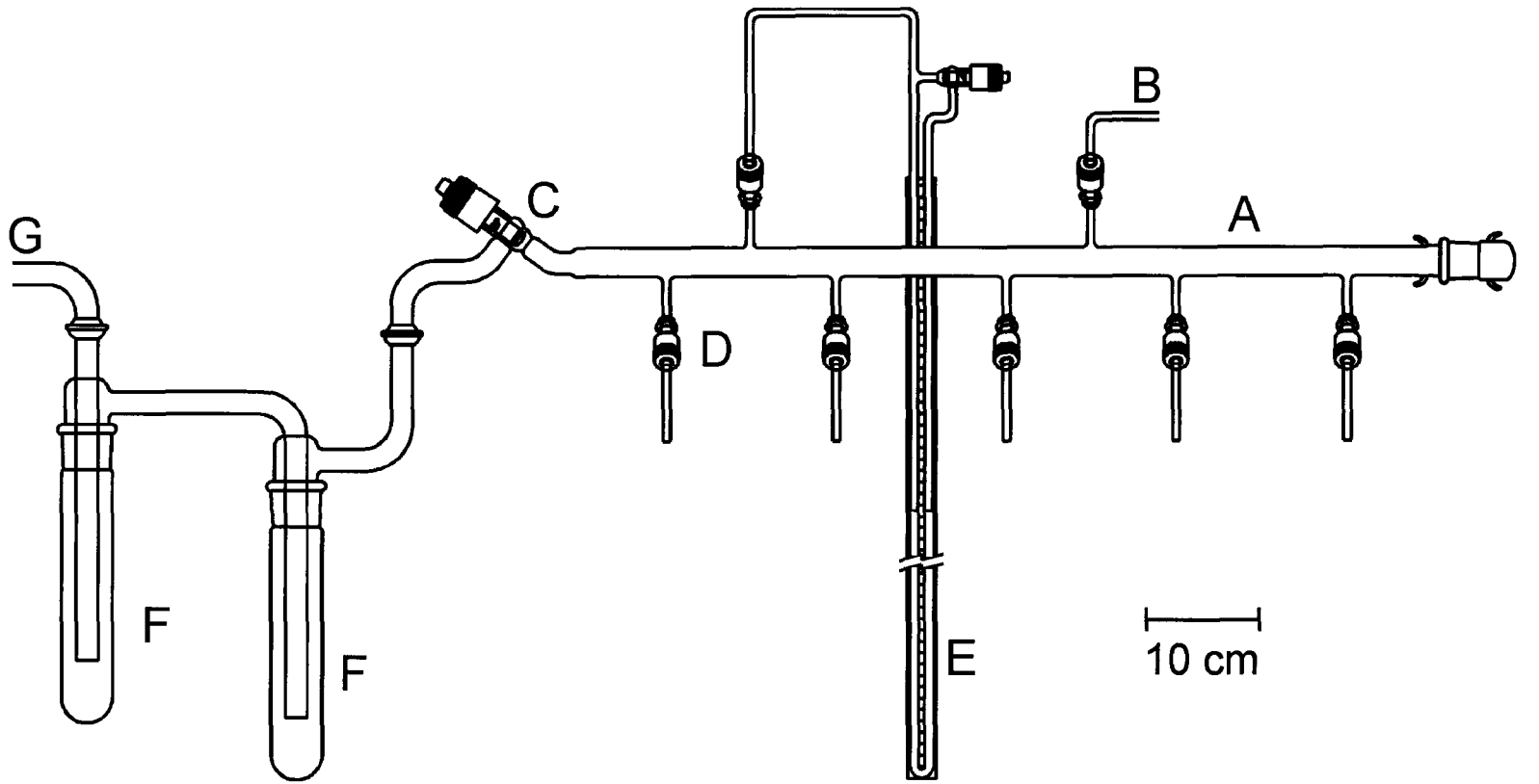

Figure 2.2. Glass vacuum line used for the manipulation of non-corrosive volatile materials. (A) Main vacuum manifold. (B) Dry N_2 inlet. (C) 15-mm greaseless J. Young valve with PTFE barrel. (D) 6-mm greaseless J. Young valve with PTFE barrel. (E) Mercury manometer. (F) Liquid N_2 cold trap. (G) Outlet to vacuum pump.

Glass vacuum lines were equipped with Edwards two-stage internal vane E2M8 direct-drive vacuum pumps which produced manifold pressure of ca. 10^{-3}–10^{-4} Torr. Vacuum was maintained on the metal vacuum line by use of two E2M8 vacuum pumps; the first, a roughing pump, was used primarily for the removal of volatile reactive fluoride and oxide fluoride compounds. The rough pump was used to pump reactive, volatile fluorine compounds through a fluoride/fluorine trap consisting of a stainless steel tube (ca. 60 cm, 15 cm dia.) packed with soda lime absorbent (Fisher Scientific, 4–8 mesh), followed by a final trapping procedure, utilizing a glass liquid nitrogen trap to remove CO_2 and water formed by reaction of fluoride materials with soda lime and other volatile materials that were unreactive towards soda lime. The second vacuum pump provided the high vacuum (ca. 10^{-4} Torr) source for the manifold and was fitted with a glass liquid nitrogen trap. The Edwards rough and high vacuum pumps also had activated charcoal (Norit) beds installed on their intakes to remove any trace of F_2 that may still be present after cold or chemical trapping.

Materials of low volatility were transferred under a dry nitrogen atmosphere (<0.1 ppm H_2O) of a Vacuum Atmospheres dry box. Temperature sensitive materials were transported into the dry box through a glass cryowell immersed in liquid nitrogen. These materials could be safely handled at temperatures as low as ca −140 °C for extended periods (ca 1 h) in a stainless steel Dewar filled with pre-cooled metal spheres (Copperhead, Airgun Shot, Steel BB Cal. 4.5-mm, Model #0757).

2.1.2. Sample Vessels

All synthetic work was carried out in reactors constructed from lengths of ¼-in. o.d. FEP tubing which were heat-sealed at one end and heat-flared (45° SAE) at the other. The tubing was connected to Kel-F valves, encased in aluminum housings, using brass flare fittings. All vessels were then connected to a glass vacuum line using ¼-in. i.d. stainless steel Swagelok Ultra-Torr unions fitted with Viton O-rings and were rigorously dried by pumping (a minimum of 6 h) under dynamic vacuum. Vessels were then connected to the metal vacuum line using a PTFE Swagelok union and passivated with ca. 1000 Torr of F_2 for ca. 12 h. Once passivated, vessels were evacuated under dynamic vacuum to remove all volatile impurities and back-filled with dry N_2 (ca. 1000 Torr) prior to use. Similarly, connections made to the metal vacuum line manifold were dried under dynamic vacuum and passivated with F_2 gas overnight. Connections made to a glass vacuum line were dried under dynamic vacuum overnight. Glass vessels used to handle less corrosive materials were dried under dynamic vacuum for a minimum of 8 hr and were periodically flamed out with a Bunsen burner.

Nuclear magnetic resonance spectra were acquired using sample tubes prepared from ¼-in. o.d. FEP tubing. One end of each tube was heat-sealed using the end of a heated thin-walled 10-mm o.d. glass NMR tube, while the other end was fused to ca. 5 cm of ¼-in. o.d. thick-walled tubing. The end was subsequently heat-flared (45° SAE) for connection to a Kel-F valve. Prior to acquisition of the NMR data, the sample tubes were heat-sealed under dynamic vacuum using a nichrome wire resistance furnace of appropriate diameter. Otherwise, NMR samples were prepared in 5-mm o.d. thin wall

precision glass NMR tubes (Wilmad) fused to ¼-in. o.d. lengths of glass tubing which were, in turn, attached to 4-mm J. Young PTFE/glass stopcocks by use of ¼-in. i.d. stainless steel Swagelok Ultra-Torr unions fitted with Viton O-rings. The NMR tubes were then vacuum dried for 8–12 h prior to use, and once sample and solvent were added, the tubes were frozen at –196 °C, evacuated, and heat-sealed under dynamic vacuum.

Low-temperature Raman spectra of solids (ca. –160 °C) were recorded on samples prepared in thin-walled ¼-in. FEP tubing as well as 5-mm o.d. glass tubes fused to ¼-in. o.d. lengths of glass tubing which were in turn attached to 4-mm J. Young PTFE/glass stopcocks by use of ¼-in. i.d. stainless steel Swagelok Ultra-Torr unions fitted with Viton O-rings. The Raman sample tubes were then vacuum-dried for 8–12 h before use, and once the sample was added, the tube was cooled to –196 °C and heat-sealed under dynamic vacuum.

All connections to vacuum lines were made using thick-walled ¼-in. FEP tubing in conjunction with either a ¼-in. PTFE Swagelok unions outfitted with PTFE compression fittings (front and back ferrules) or ¼-in. i.d. stainless steel Swagelok Ultra-Torr connectors outfitted with stainless steel compression fittings and Viton rubber O-rings.

2.2. Preparation and Purification of Starting Materials

2.2.1. Sources and Purification of Gases; N_2, Ar, F_2, Xe, and Kr

House nitrogen gas was generated by boiling off liquid nitrogen (Air Liquide) which was further dried by passage through a freshly regenerated bed of type 4Å

molecular sieves. High purity argon gas (Air Liquide, 99.998% (excluding nitrogen)), also employed for the back pressuring of reaction vessels, was used without further purification. Technical grade fluorine gas (Air Products) and ultra-high purity Xe (Air Products, 99.995%) and Kr (Air Products, 99.995%) were used without further purification.

2.2.2. Purification of Solvents; Anhydrous HF, BrF_5, SO_2ClF, CH_3CN, and SO_2

Anhydrous hydrogen fluoride, HF (Harshaw Chemical Co.), was purified by addition of ca. 5 atm of fluorine gas to a commercial HF sample contained in a nickel can for a period of ca. 48 h prior to use, converting residual water to HF and O_2. The HF was then distilled into a Kel-F storage vessel equipped with a Kel-F valve and stored at room temperature for future use. Transfer of HF was accomplished by vacuum distillation from the Kel-F storage vessel, on a metal vacuum line, through connections constructed from FEP, as shown in Figure 2.3.

Bromine pentafluoride (Ozark-Mahoning Co.) was purified (ca. 150 mL) in a 1.25-in. o.d. FEP vessel equipped with a Kel-F valve and loaded with 20 g of KF (to sequester HF as $[K][HF_2 \cdot nHF]$). Bromine and BrF_3 impurities were eliminated by the direct fluorination of these species to BrF_5 at ambient temperature as previously described.[109] The product was stored in the purification vessel under 1000 Torr of a 2:1 mixture of N_2 and F_2 at –78 °C and transferred under static vacuum when required.

Sulfuryl chloride fluoride (Allied Chemical Co., Baker and Adams Division, >90%, ca. 100 g crude material) was purified by fractional distillation through two FEP

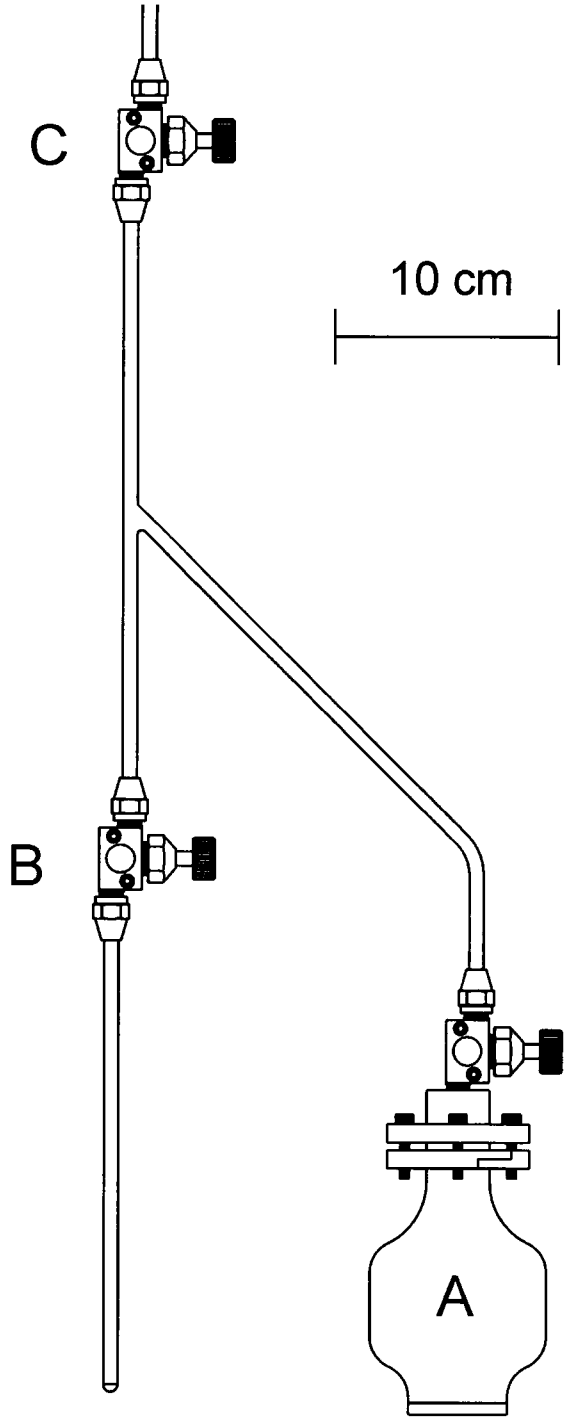

Figure 2.3. Hydrogen fluoride distillation apparatus. (A) Kel-F storage vessel containing HF. (B) FEP reaction vessel fitted with a Kel-F valve. (C) Kel-F valve connected to vacuum manifold.

U-tube traps cooled to –78 and –90 °C, respectively, effectively removing the inert impurity SO_2F_2. The remaining SO_2ClF was then condensed into an FEP U-tube containing ca. 80 g of SbF_5 at –78 °C and slowly warmed to room temperature with vigorous mixing to remove SO_2 by formation of the $SO_2{\cdot}(SbF_5)_n$ complex. Sulfur dioxide rapidly reduces xenon(II) species. The purified SO_2ClF was then transferred to an FEP U-tube cooled to –78 °C and containing dried KF. Again, the mixture was slowly warmed to room temperature with vigorous mixing and allowed to stand with periodic mixing at room temperature for ca. 2 h to remove any residual SbF_5. The sample was again cooled to –78 °C and condensed into a 1.25-in. o.d. FEP reaction vessel containing XeF_2 (1.7 g) for 24 h to ensure all impurities with reducing properties (i.e., SO_2) had been removed. Finally, the liquid was distilled under static vacuum at –78 °C into a glass vessel, outfitted with a 6-mm J. Young all-glass stopcock, and containing ca. 10 g of dry KF. The purity of the sample was assessed by recording the ^1H, ^{17}O, and ^{19}F NMR spectra of a neat sample at –80 °C. Only trace amounts of inert SO_2F_2 (2.2 mol%) were found. Sulfuryl chloride fluoride was transferred under static vacuum by use of a glass vacuum line and was distilled through a sub-manifold comprised of a Y-shaped glass connection to the reaction vessel (Figure 2.4). The sample was stored at room temperature until used. Acetonitrile (Caledon, HPLC Grade) was purified according to the literature method,[110] stored over previously vacuum dried 3Å molecular sieves in a glass vessel, outfitted with a grease-free 6-mm J. Young PTFE/glass stopcock, and was transferred under static vacuum using a glass vacuum line and a glass Y-piece configuration similar to that in Figure 2.4.

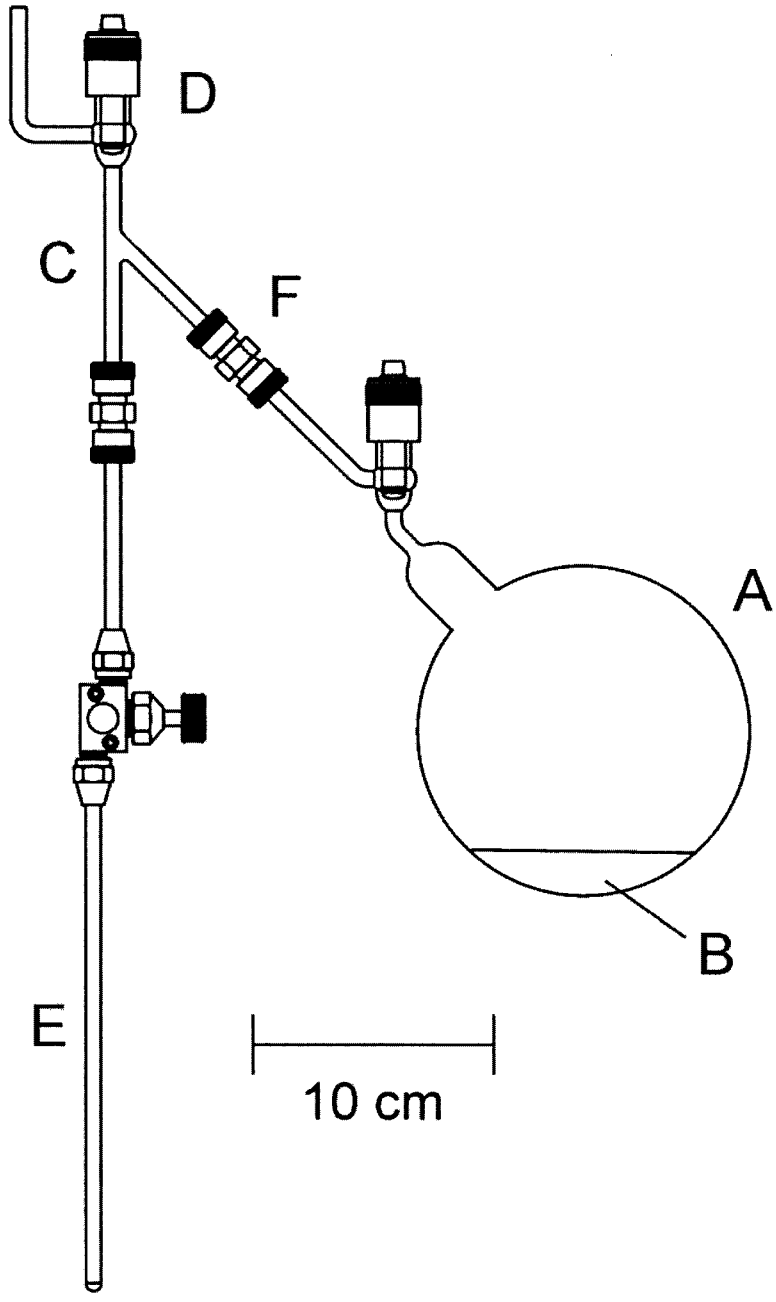

Figure 2.4. Apparatus used for the vacuum transfer of SO_2ClF solvent; (A) 250-mL glass vessel equipped with a grease-free 6-mm J. Young PTFE/glass stopcock, (B) bed of dry, powdered KF, (C) glass Y-connector, (D) 6-mm J. Young PTFE/glass valve, (E) FEP reaction vessel fitted with a Kel-F valve, (F) stainless steel Swagelok Ultra-Torr union.

Sulfur dioxide (Aldrich) was stored over P_4O_{10} in a thick-walled glass vessel, outfitted with a grease-free 6-mm J. Young PTFE/glass stopcock. Transfers were carried out under static vacuum using a glass vacuum line and a glass Y-piece configuration similar to that in Figure 2.4.

2.2.3. KF

Finely ground potassium fluoride (J. T. Baker Chemical Co., 99%) was dried under dynamic vacuum at ca. 250 °C in a glass vessel for a minimum of 3 days. The solid was stored in the glass drying vessel in a dry box until used.

2.2.4. Preparation of Reagents; AsF_5, XeF_2, and $[XeF][AsF_6]$

Arsenic pentafluoride was prepared as previously described[52,111] by direct fluorination of purified AsF_3 with purified F_2 in a nickel can. The AsF_5 was used from the reaction can without further purification.

Xenon difluoride was prepared according to the literature method[52] and stored in a Kel-F tube inside a dry box until needed.

The salt, $[XeF][AsF_6]$, was prepared by the reaction of XeF_2 with AsF_5, as previously described.[112] In a typical preparation, anhydrous HF was condensed into an FEP vessel containing a pre-weighed amount of XeF_2 (2.7798 g, 16.42 mmol). A stoichiometric excess of AsF_5 (18.95 mmol, ca. 15% excess) was condensed into the vessel and the contents were warmed to ambient temperature with agitation. On cooling the sample to −78 °C a large amount of pale yellow solid precipitated from the HF

solution. The solvent, and residual AsF_5, were then removed by pumping the sample at −78 °C for ca. 8 h through an FEP U-tube cooled to −196 °C. The sample, free of HF, was then back pressured to ca. 1 atm with dry nitrogen and stored inside a drybox. Samples of $[XeF][AsF_6]$ must be pumped at −78 °C to remove HF in order to prevent the liberation of AsF_5 and formation of $[Xe_2F_3][AsF_6]$. The purity of the sample was verified by Raman spectroscopy to verify the absence of $[Xe_2F_3][AsF_6]$. All subsequent transfers of $[XeF][AsF_6]$ were carried out in the drybox.

2.2.5. Preparation of KrF_2

Krypton difluoride was prepared by use of a 316 stainless steel hot-wire reactor (Figure 2.5) equipped with a nickel filament, similar to that originally described[64] and subsequently modified.[63] The filament was fabricated from a $^1/_{16}$-in nickel rod tightly wound about a second length of $^1/_{16}$-in rod that was, in turn, coiled and stretched into a helix. In a typical preparation, the hot-wire reactor was pressurized with 1000 Torr (50 mmol) of krypton and then cooled to −196 °C in a 20-L Dewar. After reaching thermal equilibrium, the reactor was pressurized with 25 Torr of F_2 and the DC power supply for the nickel filament was adjusted to *ca.* 6 V and 30 A (the filament was dull red in colour under these conditions). The F_2 pressure increased to ca. 45 Torr after the power supply was turned on and was regulated between 25 and 45 Torr by the periodic addition of F_2 during the synthesis. The decline in F_2 pressure was used to monitor the production of KrF_2, and additional Kr (1.0 to 2.0 mmol) was condensed into the reactor when the rate of KrF_2 production slowed or ceased. Upon completion of the reaction (ca. 12 h), excess

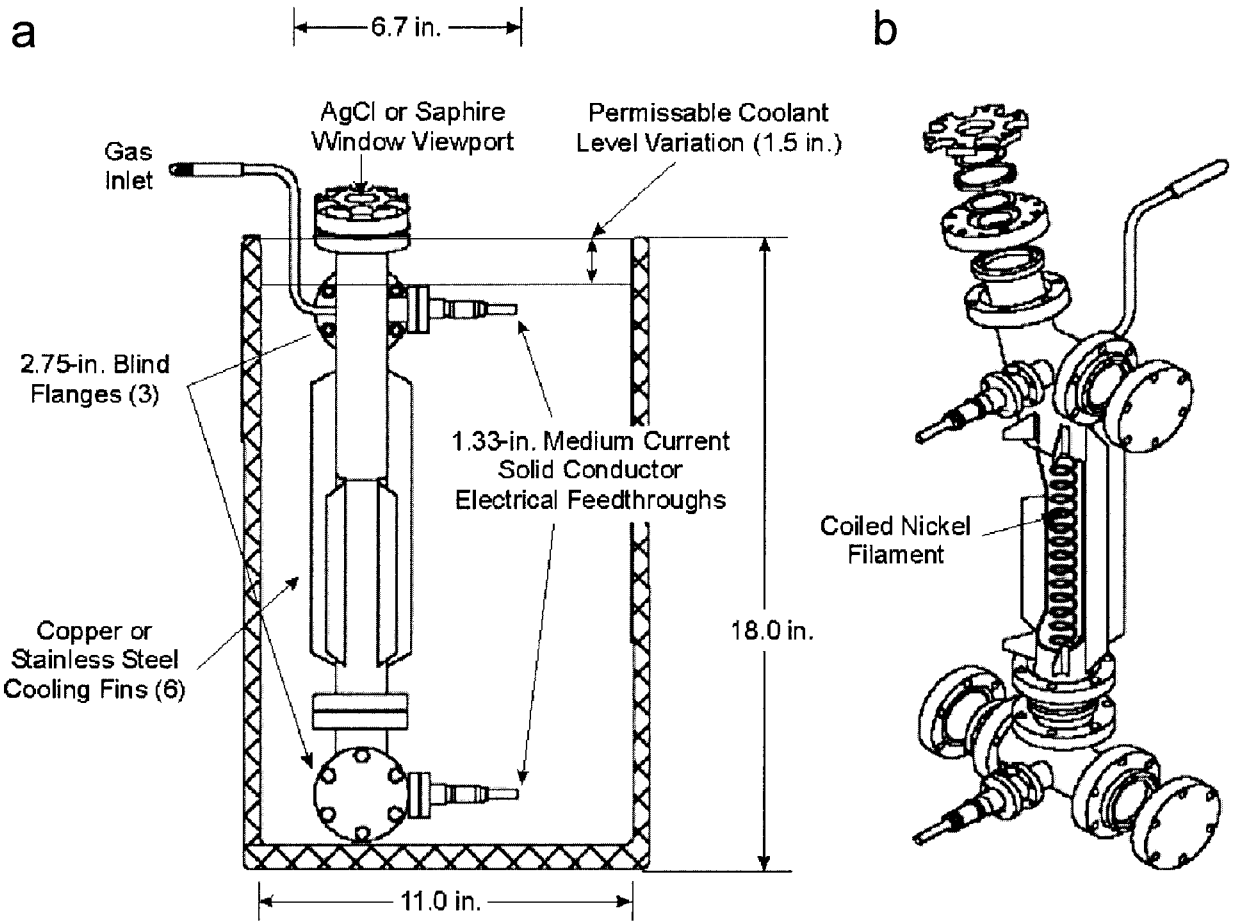

Figure 2.5. The stainless steel hot-wire reactor used for the preparation of KrF_2. (a) An external view and dimensions of a hot-wire reactor submerged in a liquid nitrogen coolant bath. (b) A perspective drawing of the hot-wire reactor showing the flange assembly and nickel filament (cut away region). Reproduced with permission from ref 63.

F_2 was removed under dynamic vacuum at –196 °C. The excess Kr and crude KrF_2 were recovered as a pink solid (the colouration arises from chromium oxide fluoride contamination; likely mostly CrO_2F_2) by allowing the reactor to slowly warm to room temperature while dynamically pumping the volatile contents through a ½-in o.d. FEP U-trap (–196 °C). The Kr/KrF_2 mixture was then warmed to –78 °C under dynamic vacuum to remove the unreacted Kr. The crude KrF_2 was purified by briefly warming the sample to 0 °C and flash distilling off the more volatile chromium oxide fluorides. The remaining colourless KrF_2 was finally warmed to room temperature and rapidly sublimed into a $^3/_8$-in o.d. FEP tube equipped with a Kel-F valve, where it was stored under 1000 Torr of N_2 or Ar at –78 °C until used. This synthesis is very reliable with typical yields of 2.5 to 3.0 g of purified KrF_2 over a 12 h period.

2.2.6. Synthesis and Preparation of $N{\equiv}SF_3$ Starting Materials

2.2.6.1. KOCN

Finely ground potassium cyanate (Aldrich, >97%) was dried under dynamic vacuum at ca. 250 °C in a glass vessel for a minimum of 3 days. The solid was stored in the glass drying vessel in a dry box until used.

2.2.6.2. $SiCl_4$

Silicon tetrachloride (Aldrich, 99%) was purified by distillation and stored in a glass vessel outfitted with a grease-free 6-mm J. Young PTFE/glass stopcock. Transfers

were carried out under static vacuum using a glass vacuum line and a glass Y-piece configuration similar to that in Figure 2.4.

2.2.6.3. SF_4

Sulfur tetrachloride (Air Products, Technical Grade) was used without further purification.

2.2.6.4. AgF_2

Silver difluoride was prepared in a 500-mL Monel vessel equipped with a removable lid and knife-edge flanges. The flanges were sealed by means of a copper gasket, and the lid was fitted with a high-pressure ⅛-in. i.d. 316 stainless steel valve (Autoclave Engineers, 30BM6071). Approximately 85 g of a mixture of recovered AgF and AgF_2 was added to the vessel in the dry box. The vessel was connected directly to the metal vacuum manifold through the valve. A ca. 5 mol% excess of fluorine (assuming the entire sample is AgF) was condensed into the vessel at −196 °C and the vessel was warmed to ca. 250 °C for a period of 24 h. The fluorination was repeated until the drop in fluorine pressure after heating was less than 100 Torr, and the sample was stored in this reactor under ca. 900 Torr of F_2 at room temperature until used in the $N{\equiv}SF_3$ synthesis.

2.2.6.5. $Si(NCO)_4$

Tetraisocyanatosilane was prepared by a procedure using a modification of the literature method.[113] The synthetic apparatus (Figure 2.6) consisted of two 250 mL round-

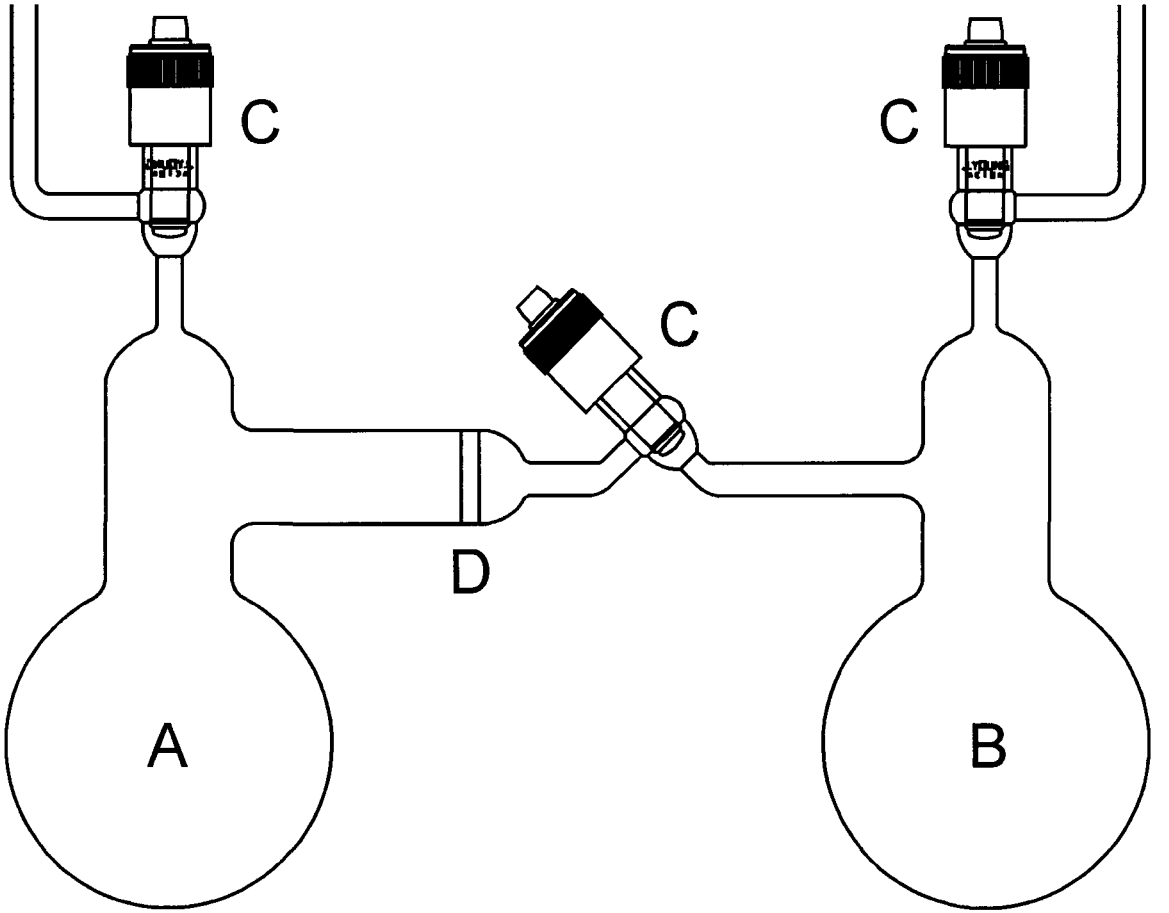

Figure 2.6. Reactor used for the synthesis of $Si(NCO)_4$; (A) flask A (250 mL round bottom flask); (B) flask B (250 mL round bottom flask); (C) 6-mm greaseless glass J. Young valve with PTFE barrel. (D) 25-mm diameter coarse glass frit (porosity 3).

bottom flasks, each outfitted with a grease-free 6-mm J. Young PTFE/glass stopcock, joined by means of a 7.5-cm length of 3.5-in o.d. Pyrex glass tubing fused to a 25-mm diameter course glass frit (porosity 3). In a typical reaction, the apparatus was dried under dynamic vacuum for ca. 24 h and was periodically flamed out with a Bunsen burner. Dried KOCN (81.0402 g, 0.9991 mol) and a Teflon-coated magnetic stirring bar were added to flask A of the apparatus described above in an inert atmosphere glovebox. The apparatus was then connected to a glass Y-piece with a grease-free 6-mm J. Young PTFE/glass stopcock along with a glass vessel containing purified $SiCl_4$. The latter were connected to a glass vacuum manifold and flask A was dried overnight under dynamic vacuum. Approximately 100 mL SO_2 solvent was condensed onto the KOCN in flask A at –78 °C, forming a pale yellow solution. At –196 °C, ca. 2 mL of $SiCl_4$ was distilled onto the frozen KOCN solution, which was then warmed to –50 °C, at which point an off-white solid was formed. Additions of small amounts of $SiCl_4$ by distillation at –196 °C were repeated, with intermittent warming to –30 °C to effect reaction, until all $SiCl_4$ (23.722 g, 0.1396 mol) was added to the reactor. At several points during the addition, the apparatus was disconnected from the glass Y-piece (while flowing dry N_2 gas to maintain dryness) and the reactor was agitated to ensure mixing. The reactor was then stored at –78 °C overnight, followed by warming to –15 °C for 6 h with occasional mixing, which resulted in a significant amount of a fine white powder and a yellow viscous liquid. The reactor was again stored at –78 °C overnight. To facilitate separation of the two solid products, $Si(NCO)_4$ and KCl, flask A was warmed to 25 °C and flask B was maintained at –78 °C while the reactor was positioned so that the reaction mixture

could gravity filter through the glass frit. The SO_2 was then distilled out of flask B and condensed into flask A –78 °C for a second wash with shaking at 0 °C followed by a repetition of the filtration process. The SO_2 was finally distilled from bulb B as described above and flask A was then warmed to 0 °C and pumped overnight to remove any remaining solvent. This purified $Si(NCO)_4$ was a colourless glass at 25 °C and was stored at that temperature in flask B under 1 atm of dry N_2 gas. The yield was 13.97 g (0.0712 mol), or 51.0 %.

2.2.6.6. $FC(O)N=SF_2$

The procedure for the synthesis of $FC(O)N=SF_2$ is a modified version of the procedure described in the literature.[114] In a typical synthesis, $Si(NCO)_4$ (13.97 g, 0.0712 mol) was melted inside the dry box by gentle warming of flask A (see above and Figure 2.6) to ca. 26 °C and poured, by means of a glass funnel, into a 155-mL stainless steel Hoke cylinder fitted with a Whitey valve. The cylinder was attached to a metal vacuum line through a metal sub-manifold and was degassed at 0 °C using several freeze-pump-thaw cycles. Sulfur tetrafluoride (0.2920 mol; a 4.10:1 molar ratio) was condensed into the cylinder at –196 °C in several aliquots from a 0.848 L nickel measuring vessel of known pressure. The reactor was then placed in a 0 °C ice-water bath and was allowed to warm to 22 °C. After 24 h, the reactor was removed from the submanifold and was connected to a series of three dried and passivated ½-in o.d. FEP U-traps fitted with Kel-F valves and connected by lengths of ¼-in o.d., ⅛-in. i.d. FEP tubing. The U-traps were cooled to –25, –78, and –196 °C, respectively. With the reactor cooled to –85 °C in an

ethyl acetate/dry ice bath spiked with liquid nitrogen, the volatile SiF_4 byproduct and unreacted SF_4 were removed by distillation into the –196 °C trap, which was then pumped and trapped onto the soda lime trap of the metal vacuum line. The reactor was then slowly warmed to 25 °C under dynamic vacuum, with the product, $FC(O)N{=}SF_2$, condensing in the –78 °C trap. Several freeze-pump-thaw cycles, and switching of the –25 and –78 °C traps removed trace SiF_4 and SF_4 impurities. The purified $FC(O)N{=}SF_2$ was a colourless liquid at 25 °C and was stored at –78 °C in a ½-in o.d. FEP storage vessel backfilled with N_2 gas. The yield was 36.44 g (0.2780 mol), or 98.16 %.

2.2.6.7. Synthesis of $N{\equiv}SF_3$

The final step in the procedure for the synthesis of $N{\equiv}SF_3$ is a modified version of that found in the literature.[115] In a typical synthesis, $FC(O)N{=}SF_2$ (36.1979 g, 0.2762 mol) was distilled, at –196 °C, onto AgF_2 (87.51 g, 0.5999 mol) which had been prepared in situ in a 500-mL Monel vessel equipped with a removable lid and knife-edge flanges. The flanges were sealed by means of a copper gasket, and the lid was fitted with a high-pressure ⅛-in. i.d. 316 stainless steel valve (Autoclave Engineers, 30BM6071). The reactor was then placed in a –78 °C bath for ca. 1 h, and was allowed to warm to 0 °C over ca. 12 h and held at that temperature overnight. The cylinder was then warmed to 22 °C over ca. 12 h, and after an additional 12 h, the reactor was connected to a series of three dried and passivated ½-in o.d. FEP U-traps fitted with Kel-F valves and connected by ¼-in o.d., ⅛-in. i.d. FEP tubing. The U-traps were cooled to –78, –131 (*n*-pentane/liquid N_2), and –196 °C, respectively. With the reactor at –78 °C, the volatile

contents were slowly metered out into the series of traps, which were then pumped on by dynamic vacuum with the valve of the reactor closed at first, until the volatiles were removed. This process was continued with warming of the reactor to –30 °C until the most volatile reaction products, COF_2 and SOF_2, had distilled into the –196 °C trap. These products were then pumped onto the soda lime trap of the metal vacuum line. The trap-to-trap distillation process was continued while the reactor was slowly warmed to –10 °C, with $N{\equiv}SF_3$ and unreacted $FC(O)N{=}SF_2$ co-condensing in the –78 and –131 °C traps. The $FC(O)N{=}SF_2$ was separated and recovered from the $N{\equiv}SF_3$ by distillation at –85 °C. The crude $N{\equiv}SF_3$ product was a colourless solid at –78 °C and was stored at that temperature in a ½-in o.d. FEP U-tube backfilled with N_2 gas until further purified.

2.2.6.8. Purification of $N{\equiv}SF_3$

The crude $N{\equiv}SF_3$ generated above contained ca. 4 mol% SF_4 as assayed by ^{19}F NMR and low-temperature Raman spectroscopy. Purification of $N{\equiv}SF_3$ followed a procedure based on that in the literature.[115] Purified $N{\equiv}SF_3$ was distilled into a 30 mL 316 stainless steel Hoke vessel with a 316 stainless steel Whitey (SS-ORM2) valve for storage.

2.2.7. $F_3S{\equiv}NAsF_5$

In a typical synthesis, a ¼-in. o.d. FEP tube, fitted with a Kel-F valve, was connected to an FEP submanifold that was, in turn, connected to a stainless steel cylinder containing $N{\equiv}SF_3$. The cylinder was fitted with two 316 stainless steel Whitey (SS-

ORM2) valves separated by a ca. 5-cm length of ¼-in o.d. stainless steel tubing to produce a volume (ca. 1.4 mL) which could be filled with an autogenous pressure of $N{\equiv}SF_3$. Condensation of successive 1.4 mL aliquots of gaseous $N{\equiv}SF_3$ allowed for a total of ca. 0.18 g, 1.7 mmol of $N{\equiv}SF_3$ to be metered into the reaction vessel. The reactor was then moved to a metal vacuum line that was, in turn, connected to a nickel vessel containing AsF_5. Excess AsF_5 (2.0 mmol) was condensed into the reaction vessel from the calibrated volume of the vacuum manifold at –196 °C, and the reaction mixture was warmed to –78 °C. The reaction was allowed to proceed, with occasional mixing, for ca. 1 h at –78 °C, forming $F_3S{\equiv}NAsF_5$ as a friable white solid. After removal of excess AsF_5 by pumping at –78 °C for ca. 1 h, the sample was stored at that temperature until characterized by Raman spectroscopy.

2.3. Synthesis and Characterization of $[F_3S{\equiv}NXeF][AsF_6]$

2.3.1. Synthesis of $[F_3S{\equiv}NXeF][AsF_6]$

In a typical synthesis, $[XeF][AsF_6]$ (0.1004 g, 0.2959 mmol) was loaded into a ¼-in. o.d. FEP tube, fitted with a Kel-F valve, and connected to an FEP submanifold that was, in turn, connected to a stainless steel cylinder containing $N{\equiv}SF_3$. The cylinder was fitted with two 316 stainless steel Whitey (SS-ORM2) valves separated by a ca. 5-cm length of ¼-in o.d. stainless-steel tubing to produce a volume (ca. 1.4 mL) which was pressurized with $N{\equiv}SF_3$. Condensation of successive aliquots of gaseous $N{\equiv}SF_3$ allowed controlled metering of $N{\equiv}SF_3$ into the reaction vessel. Frozen $N{\equiv}SF_3$, which accumulated at the top of the reaction vessel at –196 °C, was warmed to –78 °C whereupon it melted

and reacted, on contact, with $[XeF][AsF_6]$ upon warming (–25 to –15 °C). During the first hour, the solid changed from very pale yellow to white under a layer of liquid $N{\equiv}SF_3$. The reaction was allowed to proceed, with occasional mixing for ca. 6 h. The product and excess $N{\equiv}SF_3$ were then characterized by Raman spectroscopy to ensure that no unreacted $[XeF][AsF_6]$ remained. Excess $N{\equiv}SF_3$ was then removed under dynamic vacuum at –50 °C, yielding a white powder, which was characterized by Raman spectroscopy and stored at –78 °C until it could be characterized by NMR spectroscopy or used for crystal growth.

2.3.2. $[F_3S{\equiv}NXeF][AsF_6]$ Crystal Growth

Anhydrous HF (ca. 1 mL) was condensed onto $[F_3S{\equiv}NXeF][AsF_6]$ (0.1309 g, 0.2959 mmol) at –196 °C that had been synthesized in situ in one arm of a ¼-in o.d. FEP T-shaped reactor fitted with a Kel-F valve. The reactor was warmed to –40 °C, to effect dissolution, and initially gave a colorless solution. The general crystal growth procedure was followed (see Section 2.10.1). The temperature was lowered over a period of 3 h to –45 °C, whereupon colorless crystals of $[F_3S{\equiv}NXeF][AsF_6]$ began to grow on the walls of the FEP vessel as the supernatant changed to a very pale yellow color. The solution was then cooled, over a period of 30 min, to –55 °C where it was held for 30 min, and then cooled over a period of 15 min to –60 °C where it was again held for a further 30 min to allow for more complete crystallization. Colorless, blade-shaped crystals were then isolated. A crystal having the dimensions 0.32 x 0.18 x 0.10 mm^3 was selected at –105 ±3 °C for low-

temperature X-ray structure determination on the Siemens P4 diffractometer (see Section 2.10.3.1).

2.4. HF Solvolysis of $[F_3S{\equiv}NXeF][AsF_6]$

2.4.1. Synthesis of $[F_5SN(H)Xe][AsF_6]$

In a typical synthesis, ca. 1 mL aHF was condensed onto $[F_3S{\equiv}NXeF][AsF_6]$ (0.1309 g, 0.2959 mmol) in a ¼-in. o.d. FEP reaction tube, fitted with a Kel-F valve, at –196 °C. The reaction vessel was initially warmed to –78 °C, then to –20 °C and was allowed to stand, with occasional mixing, for ca. 6 h. Over this time period, the white solid slowly dissolved to form a yellow solution, from which a deep yellow microcrystalline solid deposited. After removal of the solvent under dynamic vacuum at –78 °C, the sample was stored at that temperature until characterized by Raman spectroscopy.

2.4.2. Synthesis of $[F_5SNH_3][AsF_6]$

In a typical synthesis, anhydrous HF (ca 1 mL) was condensed at –196 °C onto $F_3S{\equiv}NAsF_5$ (0.0881 g, 0.3226 mmol) which had been synthesized in situ in a ¼-in. o.d. FEP reaction tube fitted with a Kel-F valve. The reaction vessel was warmed to –78 °C whereupon the HF liquified. The vessel was warmed to 0 °C the affect reaction, and the reaction mixture was allowed to stand, with occasional mixing, for ca. 6 h, over which time the white solid dissolved and colorless feather-like crystals of $[F_5SNH_3][AsF_6]$

deposited. After removal of aHF under dynamic vacuum at –78 °C, the sample was stored at that temperature until characterized by Raman spectroscopy.

2.4.3. Synthesis of $[F_5SN(H)Xe][AsF_6]$ from $[F_5SNH_3][AsF_6]$ for NMR spectroscopy

The $F_5SN(H)Xe^+$ cation was also synthesized in a 4-mm o.d. FEP tube, fused to a ¼-in. FEP tube to connect with a Kel-F valve, that contained $[F_5SNH_3][AsF_6]$ (0.0502 g, 0.1501 mmol) and a 2-fold molar excess of XeF_2 (0.0508 g, 0.3003 mmol). Anhydrous HF or BrF_5 (ca. 0.5 mL) was statically distilled onto the sample at –196 °C, and the reaction vessel was initially warmed to –78 °C and then to –20 °C just prior to characterization by low-temperature multi-NMR spectroscopy.

2.4.4. $[F_5SN(H)Xe][AsF_6]$ Crystal Growth

Anhydrous HF (ca. 1 mL) was condensed onto $[F_3S{\equiv}NXeF][AsF_6]$ (0.1186 g, 0.2681 mmol) at –196 °C that had been synthesized in situ in one arm of a ¼-in o.d. FEP T-shaped reactor fitted with a Kel-F valve. The general crystal growth and isolation procedures outlined in Section 2.10.1 were followed. The reactor was warmed to –20 °C and the reaction was allowed to proceed for ca. 4 h, over which time the white solid slowly dissolved and the solution became deep yellow in color. Transparent yellow plates subsequently grew as the supernatant became colourless again. The temperature was lowered over a period of 1 h to –50 °C, where it was held for a further 30 min to allow for more complete crystallization. Transparent yellow plate-shaped crystals were then isolated. A crystal having the dimensions 0.28 × 0.24 × 0.10 mm^3 was selected at –105 ±3 °C for

low-temperature X-ray structure determination on the Siemens P4 diffractometer (see Section 2.10.3.1.).

2.4.5. $[F_5SNH_3][AsF_6]$ Crystal Growth

Anhydrous HF (ca. 1 mL) was condensed onto $[F_5SNH_3][AsF_6]$ (0.245 g, 1.70 mmol) at –196 °C that had been synthesized in situ in one arm of a ¼-in o.d. FEP T-shaped reactor fitted with a Kel-F valve. The reactor was warmed to 0 °C to effect dissolution and initially gave a colorless solution. The general crystal growth and isolation procedures were followed as outlined in Section 2.10.1. This temperature was maintained, and over a period of 10 h, colorless plates slowly deposited that were isolated and transferred to a goniometer head for low-temperature X-ray structure determination on the Siemens P4 diffractometer (see Section 2.10.3.1.).

Crystals of $[F_5SNH_3][AsF_6]$ were shown by inspection under a stereomicroscope to have striations in one plane that are associated with multiple crystal growth. This was confirmed by a low-angle data set collection as described below. Although unit cell parameters were reproducibly determined from six multiple crystals: a = 5.752(1) Å, b = 5.761(1) Å, c = 11.733(2) Å, α = 89.81(1)°, β = 89.93(1)°, γ = 89.74(1)°, only a preliminary solution could be obtained in which bond length uncertainties exceeded 0.02 Å. This preliminary solution confirmed the expected gross structural features of the $F_5SNH_3^+$ cation and AsF_6^- anion and clearly indicated that one bond of the cation (S–N) was longer than the remaining five bonds. A further crystallization attempt from SO_2 solvent also yielded multiple crystals that gave the same unit cell parameters. Attempts to

characterize $[F_5SNH_3][AsF_6]$ by single-crystal X-ray diffraction have also proven unsuccessful in the hands of other workers.[116]

2.5. HF Solvolysis Pathway Intermediates of $[F_3S{\equiv}NXeF][AsF_6]$

2.5.1. Formation of $[F_4S{=}NXe][AsF_6]$ and $[F_4S{=}NH_2][AsF_6]$ in aHF and BrF_5 Solvents

Samples containing $[F_4S{=}NXe][AsF_6]$ and $[F_4S{=}NH_2][AsF_6]$ were typically prepared in 4-mm o.d. FEP tubes fused to lengths of ¼-in. FEP tubing fitted with Kel-F valves, which contained $[F_3S{\equiv}NXeF][AsF_6]$ (ca. 0.048 g) prepared in situ (see Section 2.3.1.). The samples were connected to an FEP submanifold that was, in turn, connected through a Kel-F valve to a Kel-F vessel containing aHF or to an FEP vessel containing BrF_5 stored over anhydrous KF. The FEP submanifold was connected to a metal vacuum line, and ca. 0.5 mL of aHF or BrF_5 was statically distilled onto $[F_3S{\equiv}NXeF][AsF_6]$ at –196 °C. For samples containing catalytic aHF in BrF_5 solvent, after BrF_5 had been condensed onto the solute, ca. 0.05 mL of aHF was condensed onto the mixture at –196 °C. The sample was then warmed to –20 °C and over ca. 30 min, the colourless $[F_3S{\equiv}NXeF][AsF_6]$ solution converted to a uniformly bright yellow solution containing $[F_4S{=}NXe][AsF_6]$ and $[F_4S{=}NH_2][AsF_6]$ which was monitored by ^{19}F NMR spectroscopy at this temperature.

2.5.2. $[F_4S{=}NH_2][AsF_6]$ Crystal Growth

Anhydrous HF (ca. 1 mL) was condensed at –196 °C onto $[F_3S{\equiv}NXeF][AsF_6]$ (0.1186 g, 0.2681 mmol) that had been synthesized in situ in one arm of a ¼-in o.d. FEP T-

shaped reactor fitted with a Kel-F valve. The reactor was warmed to –20 °C to effect dissolution and reaction, giving a colorless solution. The reaction was allowed to proceed for ca. 30 min at –20 °C, over which time the white solid dissolved, yielding a yellow solution. The crystal growth and isolation procedures described in Section 2.10.1 were used. The temperature was lowered over a period of 5 min to –60 °C, whereupon crystals of several solvolysis products grew. The sample was maintained at –60 °C for a further 10 min to allow for more complete crystallization. Transparent colorless and yellow crystals having four discernable morphologies were isolated. Colorless needles, transparent yellow plates, and colorless plates were present which were identified, by determination of their known unit cells, as $[F_3S{\equiv}NXeF][AsF_6]$, $[F_5SN(H)Xe][AsF_6]$, and $[F_5SNH_3][AsF_6]$, respectively. In addition, colourless blades of $[F_4S{=}NH_2][AsF_6]$ were present, and one such crystal, having the dimensions 0.24 x 0.10 x 0.06 mm^3, was selected at –104 ±2 °C for a low-temperature X-ray structure determination on the Siemens P4 diffractometer (see Section 2.10.3.1.).

2.5.3. Solid-state Synthesis of $[F_4S{=}NXe][AsF_6]$

Samples of $[F_4S{=}NXe][AsF_6]$ were synthesized by solid-state rearrangement of $[F_3S{\equiv}NXeF][AsF_6]$ (eq 2). In a typical synthesis, $[F_3S{\equiv}NXeF][AsF_6]$ (0.1309 g, 0.2959 mmol) was prepared in a ¼-in. o.d. FEP tube, fitted with a Kel-F valve. The sample was then warmed to 22 °C for a total of ca. 70 min for periods not exceeding 45 min, with periodic cooling to –78 °C for ca. 5 min, to minimize decomposition of $[F_4S{=}NXe][AsF_6]$. Over this time period, conversion of solid white $[F_3S{\equiv}NXeF][AsF_6]$ to

a uniformly bright yellow solid occurred which was monitored by low-temperature (–160 °C) Raman spectroscopy. The conversion of $[F_3S{\equiv}NXeF][AsF_6]$ into $[F_4S{=}NXe][AsF_6]$ reached a maximum after a total of ca. 70 min of warming, after which time no further rearrangement was detected by Raman spectroscopy. The sample was stored at –78 °C for several weeks with no sign of further reaction or decomposition.

2.5.4. $[F_4S{=}NXe][AsF_6]$ Crystal Growth

Anhydrous HF (ca. 1 mL) was condensed at –196 °C onto $[F_4S{=}NXe][AsF_6]$ (0.0889 g, 0.2010 mmol), synthesized in situ by solid state rearrangement of $[F_3S{\equiv}NXeF][AsF_6]$ (see Section 2.3.1.), in one arm of a ¼-in o.d. FEP T-shaped reaction vessel fitted with a Kel-F valve. The reactor was warmed to –40 °C, to effect dissolution, giving a yellow solution, and the general crystal growth and isolation procedures were followed as outlined in Section 2.10.1. The temperature was lowered over a 15 min period to –50 °C and yellow needle-shaped crystals began to grow, but with accompanying xenon gas evolution indicative of decomposition). Over the subsequent 15 min period, the temperature was lowered to –67 °C whereupon xenon evolution ceased. More complete crystallization occurred over a further 30 min, after which time the crystals were isolated. A transparent yellow needle, having the dimensions 0.18 x 0.06 x 0.02 mm^3, was selected at –104 ±2 °C for low-temperature X-ray structure determination on the Bruker ApexII diffractometer (see Section 2.10.3.2.).

2.6. Reactivity of $[F_3S{\equiv}NXeF][AsF_6]$ with $N{\equiv}SF_3$

2.6.1. Synthesis of $[F_4S{=}NXe{---}N{\equiv}SF_3][AsF_6]$

In a typical $[F_4S{=}NXe{---}N{\equiv}SF_3][AsF_6]$ synthesis, $[F_3S{\equiv}NXeF][AsF_6]$ (0.1309 g, 0.2959 mmol) was prepared in a ¼-in. o.d. FEP reaction tube fitted with a Kel-F valve. The reactor was connected to an FEP submanifold that was, in turn, connected to a stainless steel cylinder containing $N{\equiv}SF_3$. The cylinder was fitted with two 316 stainless steel Whitey (SS-ORM2) valves separated by a ca. 5-cm length of ¼-in o.d. stainless steel tubing that afforded a volume (ca. 1.4 mL) which was pressurized to the autogenous pressure of $N{\equiv}SF_3$ at room temperature. Successive 1.4 mL aliquots of gaseous $N{\equiv}SF_3$ were metered into the reaction vessel by condensation at –196 °C to give a total of ca. 0.18 g (1.7 mmol) of $N{\equiv}SF_3$. The reaction vessel was initially warmed to –78 °C, followed by warming to –20 °C for ca. 6 h with occasional mixing. The white solid corresponding to $[F_3S{\equiv}NXeF][AsF_6]$ slowly dissolved in excess liquid $N{\equiv}SF_3$ to form a yellow solution from which a deep yellow microcrystalline solid deposited. With gradual warming to 0 °C over an additional 15 h period, the solid redissolved and two liquid phases separated, a colorless upper layer and a deep yellow lower layer. Excess $N{\equiv}SF_3$ was removed under dynamic vacuum at –50 °C over a period of ca. 30 min, yielding a bright yellow powder, $[F_4S{=}N{-}Xe{---}N{\equiv}SF_3][AsF_6]$, which was stored at –78 °C until characterized by Raman spectroscopy.

2.6.2. Synthesis of $[F_3S(N{\equiv}SF_3)_2][AsF_6]$

The synthesis of $[F_3S(N{\equiv}SF_3)_2][AsF_6]$ follows the procedure described for $[F_4S{=}N{-}Xe{---}N{\equiv}SF_3][AsF_6]$ above up to the point of solvent removal. At that point, the solution was maintained in liquid $N{\equiv}SF_3$ at 0 °C for an additional 6 h, over which time the solution slowly changed from yellow to colorless. Excess $N{\equiv}SF_3$ was then removed under dynamic vacuum at –50 °C over a period of ca. 5 min, yielding a friable white solid that was a mixture of $[F_3S(N{\equiv}SF_3)_2][AsF_6]$ and *cis*-N_2F_2, which was stored at –78 °C until characterized by Raman spectroscopy. Further pumping at –45 °C for ca. 15 min, removed the *cis*-N_2F_2 and remaining $N{\equiv}SF_3$, yielding $[SF_3][AsF_6]$, a known salt, which was confirmed by Raman spectroscopy.

2.6.3. $[F_4S{=}N{-}Xe{---}N{\equiv}SF_3][AsF_6]$ and $[F_3S(N{\equiv}SF_3)_2][AsF_6]$ Crystal Growth

Thiazyl trifluoride ($N{\equiv}SF_3$, ca. 1 mL) was condensed onto $[F_3S{\equiv}NXeF][AsF_6]$ (0.1186 g, 0.2681 mmol) at –196 °C that had been synthesized in situ in one arm of a ¼-in o.d. FEP T-shaped reactor fitted with a Kel-F valve. The reactor was warmed to –78 °C and pressurized to 1 atm with dry nitrogen before warming to –20 °C, and then to 0 °C, as described under the syntheses of these compounds. The general crystal growth procedure was then followed (see Section 2.10.1). The temperature was lowered over a period of 1 h from 0 to –10 °C, where it was held for a further 30 min to allow for more complete crystallization. The resulting crystalline material was isolated. A pale yellow, block-shaped crystal of $[F_4S{=}N{-}Xe{---}N{\equiv}SF_3][AsF_6]$, having the dimensions 0.22 x 0.20 x 0.16 mm^3, and

a colorless, blade-shaped crystal of $[F_3S(N{\equiv}SF_3)_2][AsF_6]$, having the dimensions 0.28 x 0.12 x 0.06 mm^3, were selected at –104 ±2 °C for a low-temperature X-ray structure determination on the Bruker ApexII diffractometer (see Section 2.10.3.2.).

2.7. [FXeOXe---N≡SF$_3$][AsF$_6$]

In a typical synthesis, $[Xe_3OF_3][AsF_6]$ (0.3389 g, 0.5168 mmol) was prepared in a ¼-in. o.d. FEP reaction tube, fitted with a Kel-F valve, as previously described.[117] The reactor was then connected to an FEP submanifold that was, in turn, connected to a stainless steel cylinder containing $N{\equiv}SF_3$. The cylinder was fitted with two 316 stainless steel Whitey (SS-ORM2) valves separated by a ca. 5-cm length of ¼-in o.d. stainless steel tubing to produce a volume (ca. 1.4 mL) which could be filled with an autogenous pressure of $N{\equiv}SF_3$. Condensation of successive 1.4 mL aliquots of $N{\equiv}SF_3$ allowed for a total of ca. 0.18 g, 1.7 mmol of $N{\equiv}SF_3$ to be metered into the reaction vessel by distillation at –196 °C. The reaction vessel was initially warmed to –78 °C, then was warmed to and allowed to stand at –60 °C with occasional mixing for ca. 6 h, over which time the deep red-brown solid slowly changed to a deep orange-yellow solid, under completely colorless $N{\equiv}SF_3$. After removal of excess $N{\equiv}SF_3$ under dynamic vacuum at –60 °C for ca. 1 h, an orange-yellow powder remained, and the sample was stored at –78 °C until characterized by Raman spectroscopy.

2.8. Characterization and Reactivity of $F_5SNH_3^+$

2.8.1. $[F_5SNH_3][AsF_6]\cdot 2N{\equiv}SF_3$ Crystal Growth

Thiazyl trifluoride (ca. 0.5 mL) was condensed onto $[F_5SNH_3][AsF_6]$ (0.245g, 1.70 mmol) at –196 °C that had been synthesized[118] in situ in one arm of a ¼-in. o.d. FEP T-shaped reactor fitted with a Kel-F valve. The reactor was warmed to –60 °C to effect dissolution and initially gave a pale yellow solution. The general crystal growth procedure was then followed (see Section 2.10.1). As the temperature was lowered to –70 °C over a period of 3 h and then held at that temperature for an additional 4 h, pale yellow blade-shaped crystals slowly grew from the transparent yellow solution. The crystals were isolated and stored at –78 °C. A pale yellow blade-shaped crystal of $[F_5SNH_3][AsF_6]\cdot 2N{\equiv}SF_3$, having the dimensions 0.22 x 0.14 x 0.04 mm^3, was selected at –104 ±2 °C for a low-temperature X-ray structure determination on the Bruker ApexII diffractometer (see Section 2.10.3.2.).

2.8.2. Synthesis of $F_5SNH_2\cdot nHF$

In a typical synthesis, a ¼-in. o.d. FEP tube, fitted with a Kel-F valve, was connected to an FEP submanifold that was, in turn, connected to a stainless steel cylinder containing $N{\equiv}SF_3$. The cylinder was fitted with two Whitey valves separated by a ca. 5-cm length of ¼-in o.d. stainless steel tubing to produce a volume (ca. 1.4 mL) which could be filled with an autogenous pressure of $N{\equiv}SF_3$. Condensation of successive 1.4 mL aliquots of $N{\equiv}SF_3$ allowed for a total of ca. 0.18 g, 1.7 mmol of $N{\equiv}SF_3$ to be metered into the reaction vessel. The reactor was then connected to an FEP submanifold that was,

in turn, connected to a Kel-F vessel containing aHF. Anhydrous HF was condensed onto $N{\equiv}SF_3$ at –196 °C and the reaction vessel was warmed to 0 °C whereupon it liquified. The reaction mixture was allowed to stand, with occasional mixing, for ca. 8 h, over which time the solution remained colorless. After careful removal of excess aHF solvent under dynamic vacuum at –65 °C, a friable white powder remained. The sample was stored at –78 °C until characterized by Raman spectroscopy.

2.8.3. $F_5SNH_2{\cdot}2[F_5SNH_3][AsF_6]{\cdot}4HF$ Crystal Growth

Crystals of $F_5SNH_2{\cdot}2[F_5SNH_3][AsF_6]{\cdot}4HF$ were obtained by sublimation of $F_5SNH_2{\cdot}n$HF within a ¼-in. o.d. FEP reactor fitted with a Kel-F valve containing ca. 1 atm of dry N_2 over a period of 8 h at –30 to –40 °C. The colorless crystals were then stored at –78 °C. A Colourless needle-shaped crystal of $[F_5SNH_3][AsF_6]{\cdot}0.5F_5SNH_2{\cdot}2HF$, having the dimensions 0.22 x 0.06 x 0.02 mm^3, was selected at –104 ±2 °C for a low-temperature X-ray structure determination on the Bruker D8 diffractometer (see Section 2.10.3.3.).

2.8.4. Synthesis of $[s\text{-}C_3(CH_3)_3N_3H][AsF_6]$

In a typical synthesis, 0.325 g (2.26 mmol) of $[F_5SNH_3][AsF_6]$ was added, inside a drybox, to a ¼-in. o.d. FEP reaction tube, fitted with a Kel-F valve. The reaction vessel was then connected to a glass submanifold that was, in turn, connected to a glass bulb containing dry CH_3CN. Approximately 1 mL of CH_3CN was statically condensed into the reaction vessel at –196 °C. The vessel was warmed to –10 °C and the reaction was allowed to proceed, with occasional mixing, for ca. 30 min, forming a precipitate of

yellow microcrystals after the solution turned from colorless to transparent yellow. The sample was stored at –78 °C until used for crystal growth.

2.8.5. [*s*-$C_3(CH_3)_3N_3H$---$NCCH_3$][AsF_6]·CH_3CN Crystal Growth

Samples of [F_5SNH_3][AsF_6] in CH_3CN were prepared as described above, but in ¼-in. T-shaped FEP tubes. With the reactor at –10 °C, the general crystal growth and isolation procedure was followed as outlined in Section 2.10.1. As the temperature was lowered to –35 °C over a period of 8 h, yellow blade-shaped crystals slowly grew from the transparent yellow solution. When crystal growth was deemed complete, the temperature was maintained at −35 °C while the reactor was quickly cut cleanly through ca. 15 cm from the bottom end and capped with a Kel-F plug and $^1/_{16}$-in. Teflon tube with a slow flow of argon. A second Teflon capillary tube was inserted through the outlet hole of the Kel-F cap while maintaining the argon flow. Lowering the outlet tube into the solution expelled the yellow supernatant through the capillary tube into a second ¼-in. o.d. FEP tube cooled to –78 °C. When the transfer was complete, the Kel-F valve assembly was replaced, and the vessel was connected, by means of a ¼-in. i.d. stainless steel Swagelok Ultra-Torr union fitted with Viton O-rings, to a glass vacuum manifold, and the crystals were dried under dynamic vacuum at −45 °C, and then stored at –78 °C until a suitable crystal could be selected and mounted on the diffractometer. A yellow blade-shaped crystal of [*s*-$C_3(CH_3)_3N_3H$---$NCCH_3$][AsF_6]·CH_3CN, having the dimensions 0.26 x 0.16 x 0.06 mm^3, was selected at –104 ±2 °C for a low-temperature X-ray structure determination on the Bruker D8 diffractometer (see Section 2.10.3.3.).

2.9. Attempted syntheses of New Kr–N bonded species

2.9.1. $[F_5SN(H)Kr][AsF_6]$

In a typical reaction, $[F_5SNH_3][AsF_6]$ (0.0502 g, 0.1501 mmol) was prepared in a 4-mm o.d. FEP NMR tube fused to a length of ¼-in. FEP tubing which was, in turn, fitted with a Kel-F valve. Using an FEP submanifold, ca. 0.5 mL of BrF_5 was statically distilled onto the sample at –196 °C. The reactor was warmed to –60 °C to melt the BrF_5 and to allow mixing and dissolution of $[F_5SNH_3][AsF_6]$. When the undissolved solid had settled to the bottom of the sample tube, the reactor was cooled to –78 °C to freeze the BrF_5. A stoichiometric excess of KrF_2 (ca. 50 mol%) was then distilled on top of the BrF_5 at –196 °C, and the reactor was maintained at –78 °C or lower to maintain a barrier of frozen BrF_5 between the two reactants. The tube was heat-sealed off under dynamic vacuum at –196 °C, and was then warmed to –70 to –65 °C to allow for dissolution of KrF_2 and mixing of the reactants in super-cooled BrF_5 at its low-temperature limit just prior to characterization at the same temperature by multi-NMR spectroscopy.

2.9.2. $[F_3S{\equiv}NKrF][AsF_6]$

In a typical reaction, $F_3S{\equiv}NAsF_5$ (0.0511 g, 0.1872 mmol) was prepared in a 4-mm o.d. FEP NMR tube fused to a length of ¼-in. FEP tubing which was, in turn, fitted with a Kel-F valve. Using an FEP submanifold, ca. 0.5 mL of BrF_5 was statically distilled onto the sample at –196 °C. The reactor was warmed to –60 °C to melt the BrF_5 and to allow mixing and dissolution of $F_3S{\equiv}NAsF_5$. From this point on, low-temperature sample handling and KrF_2 addition procedures were followed as described above. The tube was

heat-sealed off under dynamic vacuum at –196 °C, and was then warmed to –70 to –65 °C to allow for dissolution of KrF_2 and mixing of the reactants in super-cooled BrF_5 at its low-temperature limit just prior to characterization at the same temperature by multi-NMR spectroscopy.

2.10. X-ray Crystallography

2.10.1. Crystal Growth and Isolation

The majority of the crystals grown for structure determination by X-ray crystallography were grown in the low-temperature crystal growing apparatus depicted in Figure 2.7. The following procedure summarizes the general approach used to grow crystals from solutions using the temperature gradient method.

Solvent (ca. 1 mL) was condensed onto the compound (ca. 0.3 mmol) at –196 °C that had been synthesized in situ in one arm of a ¼-in o.d. FEP T-shaped reactor fitted with a Kel-F valve. The reactor was warmed so as to just effect dissolution, and while maintained at that temperature, the reactor was attached to a vacuum line and pressurized to ca. 1 atm with dry nitrogen. The arm containing the solution was inclined at ca. 5° from horizontal inside the glass dewar of a crystal growing apparatus[65] that had been previously adjusted to the same temperature. The temperature was then lowered over a period of time, usually several hours, whereupon crystals began to grow on the walls of the FEP vessel. The reactor was then held for a further period of time to allow for more complete crystallization. Crystals were isolated by decanting the solvent under dry nitrogen into the side arm of the FEP vessel which was immersed in liquid nitrogen, followed by evacuation and vacuum

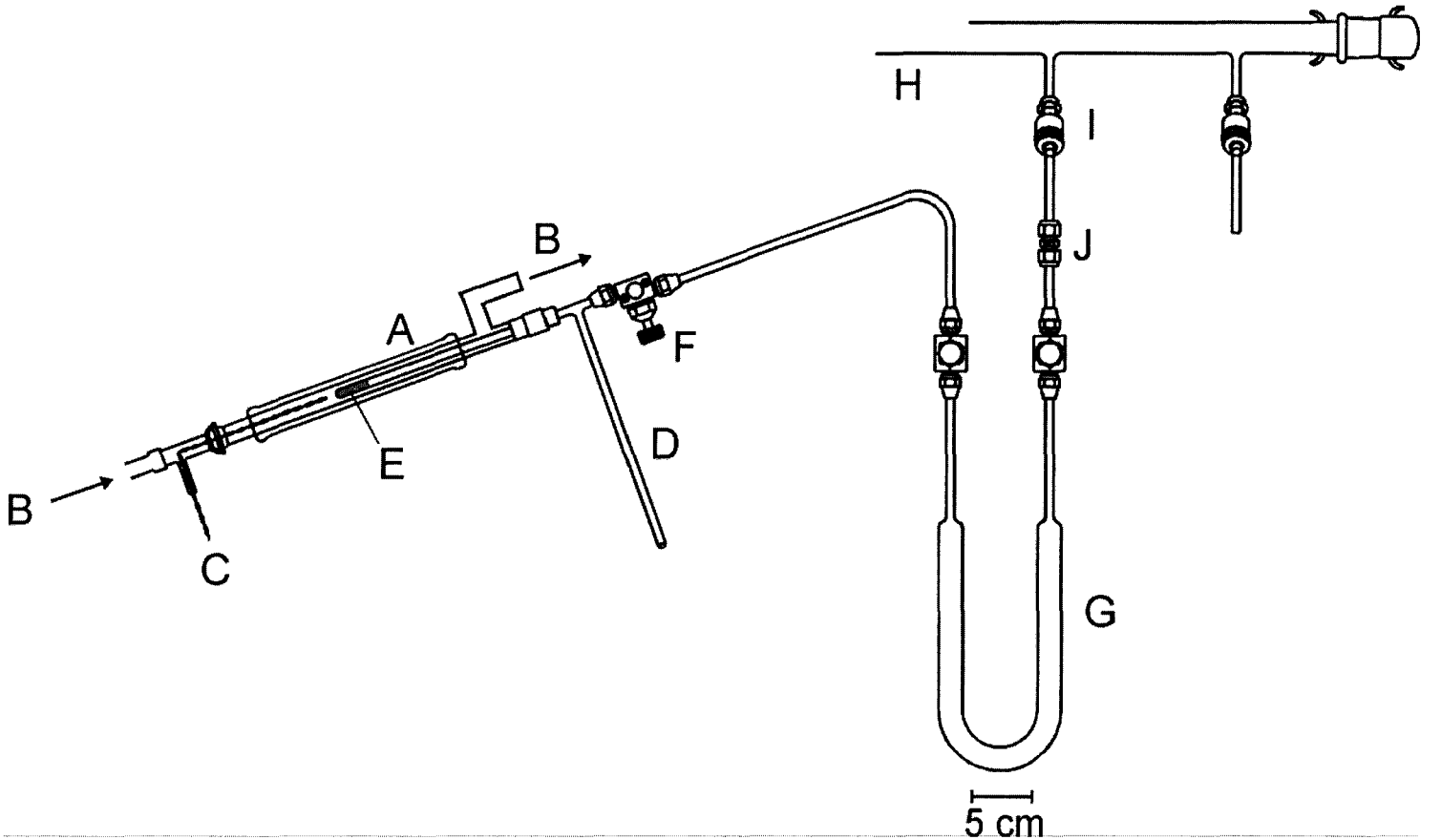

Figure 2.7. Low-temperature crystal growing apparatus; (A) glass-jacketed dewar, (B) nitrogen cold flow, (C) thermocouple lead, (D) T-shaped FEP reaction vessel with side arm, (E) sample region, (F) Kel-F valve, (G) FEP U-trap, (H) glass vacuum manifold, (I) greaseless J. Young valve with PTFE barrel, amd (J) PTFE Swagelok or stainless steel Swagelok Ultra-Torr union.

drying of the crystalline product under dynamic vacuum at –80 °C before the side-arm containing the supernatant was heat-sealed off. A crystal having dimensions less than 0.35 x 0.35 x 0.35 mm^3 was selected at –104 ±2 °C for low-temperature X-ray structure determination and was mounted in a cold stream (–173 °C) on a goniometer head as described in the next section.[119]

2.10.2. Low-Temperature Crystal Mounting

Because most of the samples investigated in this work were thermally unstable and/or moisture sensitive, all of the samples investigated were mounted at low temperature using the apparatus depicted in Figures 2.8 and 2.9. The reaction vessels containing the samples were first cut open below the Kel-F valve under a flow of dry argon gas, using an inverted glass funnel, while maintaining the sample at –78 °C. The sample was then quickly dumped into the aluminum trough of the crystal mounting apparatus under a stream of dry argon, precooled (–104 ±2 °C) by the regulated passage of dry nitrogen gas flow through a 5-L dewar filled with liquid N_2 (Figure 2.8). The temperature inside the trough was measured using a copper-constantan thermocouple positioned in the sample region of the trough. Using an additional glass sleeve, which was fitted into a concentric position around the silvered cold-flow dewar, an ambient nitrogen gas flow was slowly passed through the sleeve in order to maintain a laminar flow, thereby reducing atmospheric moisture build up in the trough. Crystals were then selected using a stereo-zoom microscope and mounted on a glass fibre (0.05 to 0.1-mm o.d.) using perfluorinated polyether oil (Ausimont Inc., Fomblin Z15 or Z25) which

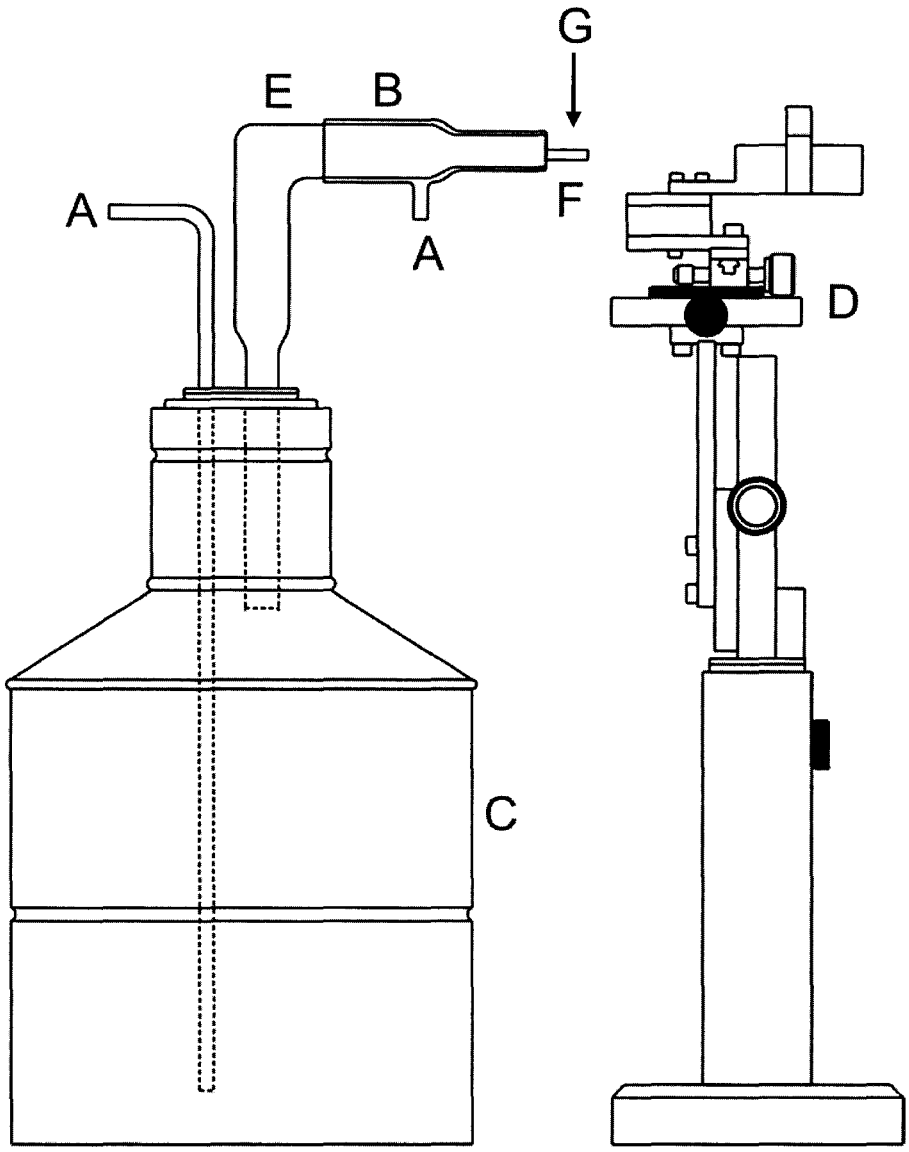

Figure 2.8. Low-temperature crystal mounting apparatus; (A) nitrogen inlet, (B) glass sleeve for ambient nitrogen flow (optional), (C) liquid N_2 dewar, (D) adjustable support stage, (E) silvered dewar (glass), (F) aluminum trough, (G) stereo-zoom microscope.

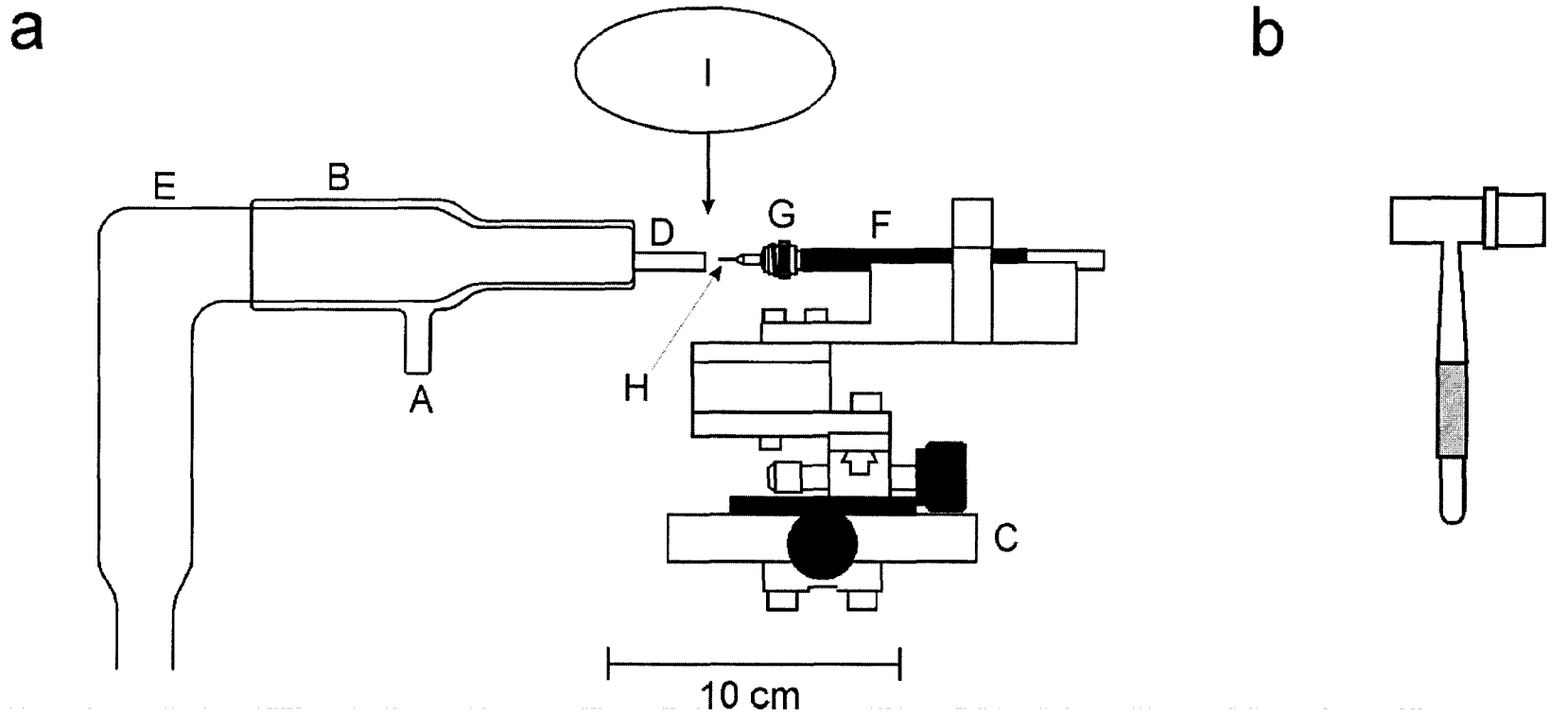

Figure 2.9. (a) Enlarged view of the crystal mounting apparatus; (A) ambient nitrogen gas flow inlet, (B) glass sleeve for ambient nitrogen gas flow, (C) adjustable support stage, (D) aluminum trough, (E) silvered glass jacketed dewar, (F) magnetic-tipped wand affixed to (G) the magnetic-based copper pin-fibre assembly, (H) glass fibre. (I) stereo-zoom microscope, (b) cryotongs employed in the transfer of the copper pin-fibre assembly with adhered crystal from the support stage to the goniometer head.

served as an adhesive upon freezing at low temperature. The glass fibre was previously mounted with epoxy cement to a copper pin fitted to a magnetic base and affixed to the end of a magnetic wand (Hampton Research). The magnetic wand could be fastened to an adjustable support stage such that samples could be inspected under the stereo-zoom microscope once affixed to the glass fibre. The mounted crystal and magnetic pin were quickly (ca. 5 s) transferred from the crystal mounting apparatus to the magnetic mount of the goniometer by means of cryotongs (Hampton Research) which were precooled in liquid N_2 prior to use. The crystals were maintained at low temperature on the goniometer head by a cold N_2 gas flow provided by a Molecular Structure Corporation cryostat system.

2.10.3. Data Collections

The crystallographic data acquired during the course of this Thesis were collected using three different diffractometers, which are each described in detail in the subsequent sections. All three instruments were equipped with Oxford Cryosystems low-temperature cryostream accessories that provided a stream of cold, gaseous N_2 for low-temperature data collection. Both molybdenum instruments were controlled by a Cryostream Controller 700 (Oxford Cryosystems), whereas the copper instrument was controlled by a Cyrojet 98 system (Oxford Instruments).

2.10.3.1. Siemens P4 Diffractometer

The Siemens diffractometer was equipped with a Siemens 1K CCD area detector

controlled by SMART[120] and a rotating anode (molybdenum) emitting Kα radiation monochromated (λ = 0.71073 Å) by a graphite crystal. Diffraction data collection (–173 °C) consisted of a full φ-rotation at χ = 0° using 0.3° (1040 + 30) frames, followed by a series of short (80 frames) ω scans at various φ and χ settings to fill the gaps. The crystal-to-detector distance was 4.970–5.020 cm, and the data collection was carried out in a 512 × 512 pixel mode using 2 × 2 pixel binning. Processing of the raw data was completed using SAINT+,[121] which applied Lorentz and polarization corrections to three-dimensionally integrated diffraction spots.

2.10.3.2. Bruker SMART APEX II Diffractometer

The Bruker SMART APEX II diffractometer was equipped with an APEX II 4K CCD area detector and a 3-axis goniometer, controlled by the APEX2 Graphical User Interface (GUI) software,[122] and a sealed tube X-ray source (Mo target) emitting Kα radiation monochromated (λ = 0.71073 Å) by a graphite crystal. Diffraction data collection was typically at –173 °C consisted of a full φ-rotation at a fixed χ = 54.74° with 0.36° (1010) frames, followed by a series of short (250 frames) ω scans at various φ settings to fill the gaps. The crystal-to-detector distance was 4.969–4.999 cm, and the data collection was carried out in a 512 × 512 pixel mode using 2 × 2 pixel binning. Processing of the raw data was completed using the APEX2 GUI software,[122] which applied Lorentz and polarization corrections to three-dimensionally integrated diffraction spots.

2.10.3.3. Bruker D8 Diffractometer

The Bruker D8 diffractometer was equipped with a Siemens SMART 6K charge-coupled device (CCD) area detector that used the program SMART,[120] and a Rigaku rotating anode using parallel-focused cross-coupled Cu-Kα radiation (λ = 1.54178 Å). The diffraction data collection consisted of a series of ω scans using 360 (0.5°) frames at various φ settings to achieve good coverage. The crystal-to-detector distance was 4.190 cm, and the data collection was carried out in a 1024 × 1024 pixel mode using 4 × 4 pixel binning. Processing was carried out by using the program SAINT+,[121] which applied Lorentz and polarization corrections to three-dimensionally integrated diffraction spots.

2.10.4. Solution and Refinement of Structures

The program SADABS[121] was used for the scaling of diffraction data, the application of a decay correction, and an empirical absorption correction based on the intensity ratios of redundant reflections. The XPREP program was used to confirm the unit cell dimensions and the crystal lattices. The final refinements were obtained by introducing anisotropic parameters for all the atoms, an extinction parameter, and the recommended weight factor. The maximum electron densities in the final difference Fourier maps were located around the heavy atoms. All calculations were performed using the SHELXTL package for the structure determination, refinement, and molecular graphics.[123] Structure solutions were obtained by direct methods which located the Xe and/or As atoms. Successive difference Fourier syntheses revealed the positions of the fluorine, nitrogen, and sulfur atoms.

The position of the hydrogen atoms in the crystal structures of $[F_4S{=}NH_2][AsF_6]$, $F_5SNH_2{\cdot}2[F_5SNH_3][AsF_6]{\cdot}4HF$, $[F_5SNH_3][AsF_6]{\cdot}2N{\equiv}SF_3$, and $[F_5SN(H)Xe][AsF_6]$, were located on the difference map, and then were calculated (d(N–H) ≈ 0.82 to 1.01 Å; U(H) fixed to –1.2 to –1.5 U(N) as appropriate) and were refined using DFIX restraints. For the [s] structure, the methyl-group hydrogen atoms were calculated (d(C–H) = 0.980 Å; ∠(C–C–H) = ∠(H–C–H) = 109.5; U(H) fixed to $-1.2U$(N)) and were refined using AFIX restraints.

2.11. Raman Spectroscopy

All Raman spectra were recorded on a Bruker RFS 100 Fourier transform Raman spectrometer employing a quartz beam splitter and a liquid-nitrogen cooled Ge diode detector. The 1064-nm line of a Nd-YAG laser was used for excitation with a laser spot of <0.1 mm at the sample and configured such that only the 180°-backscattered radiation was detected. The scanner velocity was 5 kHz and the wavelength range was 5894 to 10394 cm^{-1} relative to the laser line at 9394 cm^{-1}, resulting in a spectral range of 3501 to –999 cm^{-1}. Fourier transformations were processed using a Blackman Harris 4-term apodization and a zero-filling factor of 2. Typical acquisitions used 1.0 cm^{-1} resolution, 300–350 mW power, and involved 600 scans for strongly scattering samples and 1200–1600 scans for weakly scattering samples. The very weakly scattering $[F_5SN(H)Xe][AsF_6]$ and $F_5SNH_2{\cdot}2[F_5SNH_3][HF_2]{\cdot}4HF$ samples required 10,000 scans. Low-temperature spectra were acquired using a Bruker I0121 low-temperature accessory which provided temperatures ranging of –30 to –50 °C for the long run times needed for

very weakly scattering samples, to –160 °C for routine samples, with an estimated error of ±1 °C.

2.12. Nuclear Magnetic Resonance Spectroscopy

High-field nuclear magnetic resonance spectra were recorded unlocked (field drift < 0.1 Hz h^{-1}) on a Bruker DRX-500 (11.744 T) spectrometer using XWINNMR. The spectrometer was equipped with a Bruker 5-mm combination $^{1}H/^{19}F$ probe, or a Bruker 5-mm broad band inverse probe. Low-temperature spectra were acquired using a cold nitrogen gas flow and a variable temperature controller (BV-T 3000). The ^{1}H, ^{13}C, ^{14}N, ^{19}F, and ^{129}Xe were referenced externally at 30 °C using neat samples of TMS (^{1}H and ^{13}C), CH_3NO_2, $CFCl_3$, and $XeOF_4$, respectively. The chemical shift convention used is that a positive (negative) sign indicates a chemical shift to high (low) frequency of the reference compound. A summary of typical spectroscopic parameters used for the spectra acquired for this Thesis are provided in Table 2.1.

Spectral simulations were performed on a PC using the program ISOTOPOMER.[124] The program provides a full heteronuclear simulation that takes into account natural abundances and second-order effects. Spectra in the present study were not iterated. In addition, Gaussian multiplication was often used to enhance spectral resolution.

Table 2.1. Summary of Typical Spectroscopic Parameters Used for NMR Spectroscopy

Acquisition Parameter[a]	^{1}H	^{13}C	^{14}N	^{19}F	^{129}Xe
B_o = 11.744 T					
SF (MHz)	500.130	125.758	36.141	470.592	138.857
TD (K)	32	32	16	64	32
SW (kHz)	7	29	29	25 to 100	100
Hz/pt	0.207	0.885	1.765	0.380	3.051
PW (μs)	2.5	6.0	6.0	8.5	10.0
RD (s)	2.5	2 to 5	0.05	0.1	0.1
NS	100	10000	16,000	500 to 5000	32,000

[a] The abbreviations denote: B_o, external magnetic field; SF, spectral frequency; TD, time domain; SW, sweep width; PW, pulse width; RD, relaxation delay; NS, number of scans

2.13. Quantum-Chemical Calculations

All calculations were performed using the Gaussian 03[125] or Gaussian 09[126] software packages. Geometries were fully optimized using density functional theory (B3LYP, SVWN, and/or PBE1PBE) and Møller-Plesset (MP2) methods using (SDB-)cc-pVTZ and/or aug-cc-pVTZ(-PP) basis sets. The standard all-electron cc-pVTZ or aug-cc-pVTZ basis sets, as implemented in the Gaussian program, were utilized for all elements except Xe and As, for which the semirelativistic large core (RLC) pseudopotential basis set SDB-cc-pVTZ (with cc-pVTZ) or aug-cc-pVTZ-PP (with aug-cc-pVTZ) were used.[127] The combined uses described are indicated by (SDB-)cc-pVTZ and aug-cc-pVTZ(-PP), respectively. Basis sets were obtained online from the EMSL Basis Set Exchange (https://bse.pnl.gov/bse/portal).[128,129] Fundamental vibrational frequencies were calculated along with Raman intensities, and Natural Bond Orbital (NBO) analyses were obtained for the optimized local minima. The program GaussView[130] was used to visualize the vibrational displacements that form the basis of the vibrational mode descriptions presented.

CHAPTER 3

SYNTHESIS OF $[F_3S{\equiv}NXeF][AsF_6]$ AND STRUCTURAL STUDY BY MULTI-NMR AND RAMAN SPECTROSCOPY, ELECTRONIC STRUCTURE CALCULATIONS, AND X-RAY CRYSTALLOGRAPHY

3.1. Introduction

The first example of xenon bonded to nitrogen, $FXeN(SO_2F)_2$, was synthesized[44] and characterized in the solid state by Raman[45,46] and EPR spectroscopy,[45] by a single-crystal X-ray structure determination,[46] and by solution ^{19}F,[45,46] ^{15}N,[46] and ^{129}Xe[45,46] NMR spectroscopy. Other imidodisulfurylfluoride species containing Xe(II)–N bonds have since been characterized by multi-NMR and Raman spectroscopy, and include $Xe[N(SO_2F)_2]_2$,[45,47] $F[XeN(SO_2F)_2]_2^+$,[45,47,49] $XeN(SO_2F)_2^+$,[49] and $Xe[N(SO_2CF_3)_2]_2$.[48] Additionally, $[XeN(SO_2F)_2][Sb_3F_{16}]$ was also characterized by a single-crystal X-ray structure determination.[49] In these species, xenon is bonded to sp^2-hybridized nitrogen atoms which derive their stabilities from the high electronegativity[44,45,47-49,131] and oxidative resistance of the imidodisulfurylfluoride ligand. Most recently, the synthesis and detailed structural characterization of $[F_5TeN(H)Xe][AsF_6]$, the first example of a noble gas bonded to a formally sp^3-hybridized nitrogen center, has been reported from this laboratory.[50]

The Lewis acidity of the XeF^+ cation, as seen from the propensity of XeF^+ to form fluorine bridges with the counteranions of its salts,[15] has been exploited in this laboratory to form Xe(II)–N bonded cations by the reaction of oxidatively resistant electron pair donors

with XeF^+.[32] Reactions of XeF^+ with neutral organic nitrogen bases in HF, or XeF_2 with protonated nitrogen base salts in BrF_5, accompanied by HF elimination, have led to cations in which XeF^+ is adducted to formally sp-and sp^2-hybridized nitrogen centers. These include hydrogen cyanide,[34,35] alkylnitriles,[34] pentafluorobenzenenitrile,[34] perfluoroalkylnitriles,[34,36] perfluoropyridines,[37] and *s*-trifluorotriazine.[36] With the exception of the *s*-trifluorotriazine adduct cation, *s*-$C_3F_3N_2NXeF^+$, all of the adduct cations decompose below room temperature. The krypton(II) cations, $HC{\equiv}NKrF^+$ [66] and $R_FC{\equiv}NKrF^+$ (R_F = CF_3, C_2F_5, *n*-C_3F_7),[36] characterized in this laboratory as their AsF_6^- salts, are unstable above ca. –50 °C.

The basicity of $N{\equiv}SF_3$ was previously demonstrated by reaction of $N{\equiv}SF_3$ with BF_3, AsF_5, and SbF_5 in SO_2 to give the Lewis acid-base adducts, $F_3S{\equiv}NBF_3$,[82,87] $F_3S{\equiv}NAsF_5$,[78,88] $F_3S{\equiv}NSbF_5$,[88] and by the formation of $[(CF_3)_nSF_{3-n}{\cdot}N{\equiv}SF_3][AsF_6]$[89] and transition metal complexes,[78,90-95] e.g., $[M(N{\equiv}SF_3)_4][AsF_6]_2$ (M = Mn, Fe, Co Ni, Cu).[94] In view of the established Lewis basicity and anticipated resistance to oxidation (first adiabatic ionization potential, 12.50 eV)[132] of $N{\equiv}SF_3$, its reaction with the Lewis acid cation XeF^+ was investigated, providing the first synthesis and detailed structural characterization of a noble-gas compound in which the noble-gas atom is bonded to an inorganic sp-hybridized nitrogen center.

3.2. Results and Discussion

3.2.1. Synthesis of $[F_3S{\equiv}NXeF][AsF_6]$

The salt, $[F_3S{\equiv}NXeF][AsF_6]$, was synthesized by reaction of $[XeF][AsF_6]$ and liquid $N{\equiv}SF_3$ at –25 to –15 °C for ca. 6 h according to eq 3.1, forming a colorless, micro-

crystalline solid which was identified by Raman spectroscopy at –160 °C.

$$N{\equiv}SF_3 + [XeF][AsF_6] \xrightarrow[-25 \text{ to } -15\ ^{\circ}C]{N{\equiv}SF_3} [F_3S{\equiv}NXeF][AsF_6] \quad (3.1)$$

3.2.2. X-ray Crystal Structure of $[F_3S{\equiv}NXeF][AsF_6]$

A summary of the refinement results and other crystallographic information is provided in Table 3.1. Important bond lengths and angles for $[F_3S{\equiv}NXeF][AsF_6]$ are listed in Table 3.2 along with calculated values for the $F_3S{\equiv}NXeF^+$ cation.

The structure of $[F_3S{\equiv}NXeF][AsF_6]$ (Figure 3.1a) consists of well-separated $F_3S{\equiv}NXeF^+$ cations and AsF_6^- anions. The anion shows no significant distortion from octahedral geometry, with As–F bonds ranging from 1.711(3) to 1.718(3) Å, in good agreement with previously reported values.[28,50] The Xe–N and Xe–F bond lengths, (2.236(4) and (1.938(3) Å), are equal, within experimental error, to those in $[HC{\equiv}NXeF][AsF_6]$ (2.235(3) and (1.936(2) Å),[38] and are comparable to those observed in $[CH_3C{\equiv}NXeF][AsF_6]{\cdot}HF$ (2.179(7) and (1.947(5) Å)[38] and $[(CH_3)_3CC{\equiv}NXeF][AsF_6]$ (2.212(4) and 1.952(3) Å).[38] The Xe–N bond in $F_3S{\equiv}NXeF^+$ is significantly shorter than the Xe–N bonds in $CH_3C{\equiv}N{---}XeC_6F_5^+$ (2.681(8) Å)[41] and $[2,6\text{–}C_5H_3F_2N{---}XeC_6F_5][AsF_6]$ (2.694(5) Å).[43] The Xe–F bond length of $F_3S{\equiv}NXeF^+$ is significantly longer than the terminal Xe–F bond length in $[XeF][AsF_6]$ (1.888(3),[30] 1.873(6)[133] Å) and other XeF^+ salts,[30,134] but shorter than those in XeF_2 (2.010(6),[135] 1.999(4)[30] Å). The relationship between the relative strength of the donor-acceptor interactions in XeF^+ salts, i.e., $FXe^+{---}F\text{–}MF_5^-$ and $FXe^+{---}F\text{–}MF_{10}^-$, and Xe–F bond length is well established and

Table 3.1. Summary of Crystal Data and Refinement Results for $[F_3S{\equiv}NXeF][AsF_6]$

empirical formula	$F_{10}SNXeAs$
space group (No.)	*Pbca* (61)
a (Å)	8.7844(3)
b (Å)	12.3857(4)
c (Å)	16.2550(5)
V (Å^3)	1768.56(5)
molecules/unit cell	8
mol. wt. (g mol^{-1})	442.29
calcd. density (g cm^{-3})	3.322
T (°C)	–173
μ (mm^{-1})	7.97
R_1[a]	0.0438
wR_2[b]	0.0679

[a] R_1 is defined as $\Sigma||F_o|-|F_c||/\Sigma|F_o|$ for $I > 2\sigma(I)$.
[b] wR_2 is defined as $[\Sigma[w(F_o^2 - F_c^2)^2]/\Sigma w(F_o^2)^2]^{1/2}$ for $I > 2\sigma(I)$.

Table 3.2. Experimental Geometries for $[F_3S{\equiv}NXeF][AsF_6]$ and Calculated Geometries for $F_3S{\equiv}NXeF^+$, $N{\equiv}SF_3$, and XeF^+

		Bond Lengths (Å)					
		calcd[a]					
		$F_3S{\equiv}NXeF^+$ (C_1)		$N{\equiv}SF_3$ (C_{3v})		XeF^+ ($C_{\infty v}$)	
	exptl	MP2	SVWN	MP2	SVWN	MP2	SVWN
Xe(1)–N(1)	2.236(4)	2.295	2.242				
Xe(1)–F(1)	1.938(3)	1.916	1.933			1.874	1.878
S(1)–N(1)	1.397(5)	1.418	1.416	1.437	1.449		
S(1)–F(2)	1.503(3)	1.528	1.532	1.574	1.616		
S(1)–F(3)	1.503(3)	1.528	1.532	1.574	1.616		
S(1)–F(4)	1.496(3)	1.528	1.532	1.574	1.616		
As(1)–F(5)	1.713(3)						
As(1)–F(6)	1.715(3)						
As(1)–F(7)	1.711(3)						
As(1)–F(8)	1.716(3)						
As(1)–F(9)	1.717(3)						
As(1)–F(10)	1.718(3)						
N(1)···F(1A)	3.097(6)						
N(1)···F(10A)	3.076(5)						
N(1)···F(6B)	3.133(5)						
N(1)···F(5A)	3.201(6)						

		Bond Angles (°)			
		calcd[a]			
		$F_3S{\equiv}NXeF^+$ (C_1)		$N{\equiv}SF_3$ (C_{3v})	
	exptl	MP2	SVWN	MP2	SVWN
F(1)–Xe(1)–N(3)	179.6(2)	180.0	180.0		
Xe(1)–N(1)–S(3)	142.6(3)	180.0	180.0		
N(1)–S(1)–F(2)	115.2(2)	120.3	120.0	123.8	123.0
N(1)–S(1)–F(3)	120.7(2)	120.3	120.0	123.8	123.0
N(1)–S(1)–F(4)	123.4(2)	120.3	120.0	123.8	123.0
F(2)–S(1)–F(3)	97.1(2)				
F(2)–S(1)–F(4)	97.7(2)				
F(3)–S(1)–F(4)	97.3(2)				
F(5)–As(1)–F(6)	179.1(2)				
F(5)–As(1)–F(7)	90.3(2)				
F(5)–As(1)–F(8)	89.7(2)				
F(5)–As(1)–F(9)	90.0(2)				
F(5)–As(1)–F(10)	90.2(2)				
F(6)–As(1)–F(7)	89.9(2)				
F(6)–As(1)–F(8)	89.4(2)				
F(6)–As(1)–F(9)	90.8(2)				
F(6)–As(1)–F(10)	89.6(2)				
F(7)–As(1)–F(8)	90.0(2)				
F(7)–As(1)–F(9)	90.8(2)				
F(7)–As(1)–F(10)	179.4(2)				
F(8)–As(1)–F(9)	179.2(2)				
F(8)–As(1)–F(10)	89.6(2)				
F(9)–As(1)–F(10)	89.6(2)				

[a] (SDB-)cc-pVTZ basis set.

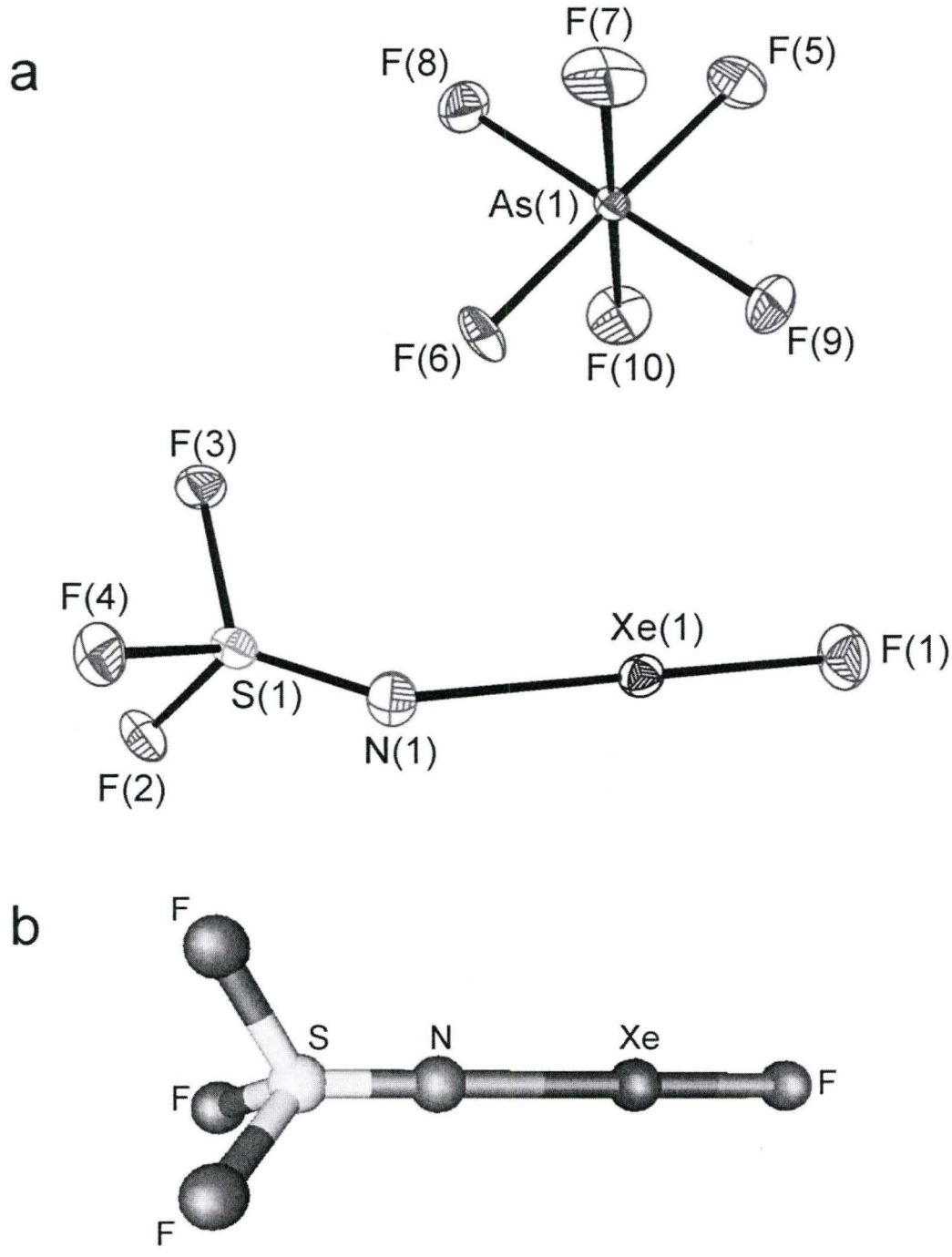

Figure 3.1. (a) X-ray crystal structure of $[F_3S{\equiv}NXeF][AsF_6]$; thermal ellipsoids are shown at the 50% probability level. (b) Calculated geometry of the $F_3S{\equiv}NXeF^+$ cation. The atom numbering scheme corresponds to that given in Table 3.2 where the values of experimental and calculated geometric parameters are provided.

leads to Xe–F bond strengthening with decreasing fluoro-basicity and a corresponding increase in ν(XeF).[112,136] Of the crystallographically characterized N–Xe–F bonded cations having formal sp-hybridization at N, the Xe–N and Xe–F bond lengths in the $F_3S{\equiv}NXeF^+$ cation are most similar to those of $HC{\equiv}NXeF^+$ [38] and to the terminal Xe–F bond length in $[Xe_2F_3][AsF_6]$ (1.90(3),[137] 1.915(8)[28] Å), thus placing the XeF^+ adducts of $N{\equiv}SF_3$ and $HC{\equiv}N$ toward the most ionic end of the scale.

The N≡S and S–F bonds of $[F_3S{\equiv}NXeF][AsF_6]$ (1.397(5) Å and 1.503(3) Å) are shorter than those in $N{\equiv}SF_3$ (1.415(3) and 1.547(1) Å, respectively).[86] Similar bond length contractions occur in other $N{\equiv}SF_3$ complexes, i.e., $F_3S{\equiv}NAsF_5$ (1.383 Å and 1.439 Å),[78] $[Mn(N{\equiv}SF_3)_4][AsF_6]_2$ (1.365(11) Å and 1.506(5) Å),[90] $[Zn(N{\equiv}SF_3)_4][AsF_6]_2$ (1.365(7) Å and 1.496(6) Å),[92] $[Re(CO)_5N{\equiv}SF_3][AsF_6]$ (1.384(14) Å and 1.499(10) Å),[93] and $[CpFe(CO)_2N{\equiv}SF_3][AsF_6]$ (1.376(3) Å and 1.515(3) Å).[91]

Although quantum-chemical calculations predict a linear structure (Figure 3.1b, also see Section 3.3.1.), the Xe–N–S angle (142.6(3)°) is significantly more distorted from linearity than the Xe–N–C angles in the crystal structures of $[HC{\equiv}NXeF][AsF_6]$ (177.7(3)°),[38] $[CH_3C{\equiv}NXeF][AsF_6]{\cdot}HF$ (175.0(8)°),[38] and $[(CH_3)_3CC{\equiv}NXeF][AsF_6]$ (166.9(4)°),[38] however, no explanations were given. Other bent E–N–C (E = In, Tl, Sn, Pb) arrangements have been encountered in the solid state.[138-141] In the present instance, the bent Xe–N–S angle appears to result from several close N---F contacts within the crystal lattice, three from anions (3.076(5), 3.133(5), 3.201(6) Å) and one from the fluorine ligand bonded to xenon (3.097(6) Å) in a neighboring $F_3S{\equiv}NXeF^+$ cation. These contacts

are at the limit of the sum of nitrogen and fluorine van der Waals radii (3.02 Å),[31] and form a distorted square planar arrangement about nitrogen (Figure 3.2) with the cation bent towards the longest, most open edge.

The N–S–F and F–S–F angles in $[F_3S{\equiv}NXeF][AsF_6]$ average 119.8(2)° and 97.4(2)°, respectively, comprising a distorted tetrahedral arrangement about sulfur that is similar to those of $N{\equiv}SF_3$ (122.2(1)° and 94.2(1)°)[86], $F_3S{\equiv}NAsF_5$ (122.2° and 94.3°),[78] and $[CpFe(CO)_2N{\equiv}SF_3][AsF_6]$ (120.9(2)° and 96.0(2)°).[91]

3.2.3. NMR Spectroscopy

The ^{14}N, ^{19}F, and ^{129}Xe NMR parameters for $[F_3S{\equiv}NXeF][AsF_6]$ recorded in anhydrous HF solvent at –20 °C and BrF_5 solvent at –60 °C (NMR parameters obtained from BrF_5 solutions are given in parentheses) are listed in Table 3.3.

The ^{19}F spectrum consists of two resonances at 51.2 (53.3) and –185.5 (–180.5) ppm, corresponding to the fluorine-on-sulfur (Figure 3.3a) and fluorine-on-xenon (Figure 3.3b) environments, respectively. The latter singlet is accompanied by natural abundance ^{129}Xe (26.44%) satellites resulting from $^1J(^{129}Xe–^{19}F)$ = 6265 (6248) Hz. The $^4J(^{19}F_{Xe}–^{19}F_S)$ coupling cannot be observed in HF solvent, which may be a consequence of line broadening (F-on-S, $\Delta\nu_{1/2}$ = 47 Hz and F-on-Xe, $\Delta\nu_{1/2}$ = 150 Hz) arising from slow chemical exchange between HF and $F_3S{\equiv}NXeF^+$ (eq 3.2). A diminished fluorine

$$F_3S{\equiv}NXeF^+ + 2HF \rightleftharpoons XeF_2 + N{\equiv}SF_3 + H_2F^+ \qquad (3.2)$$

exchange rate in BrF_5 and a greatly enhanced rate of quadrupolar relaxation of residual

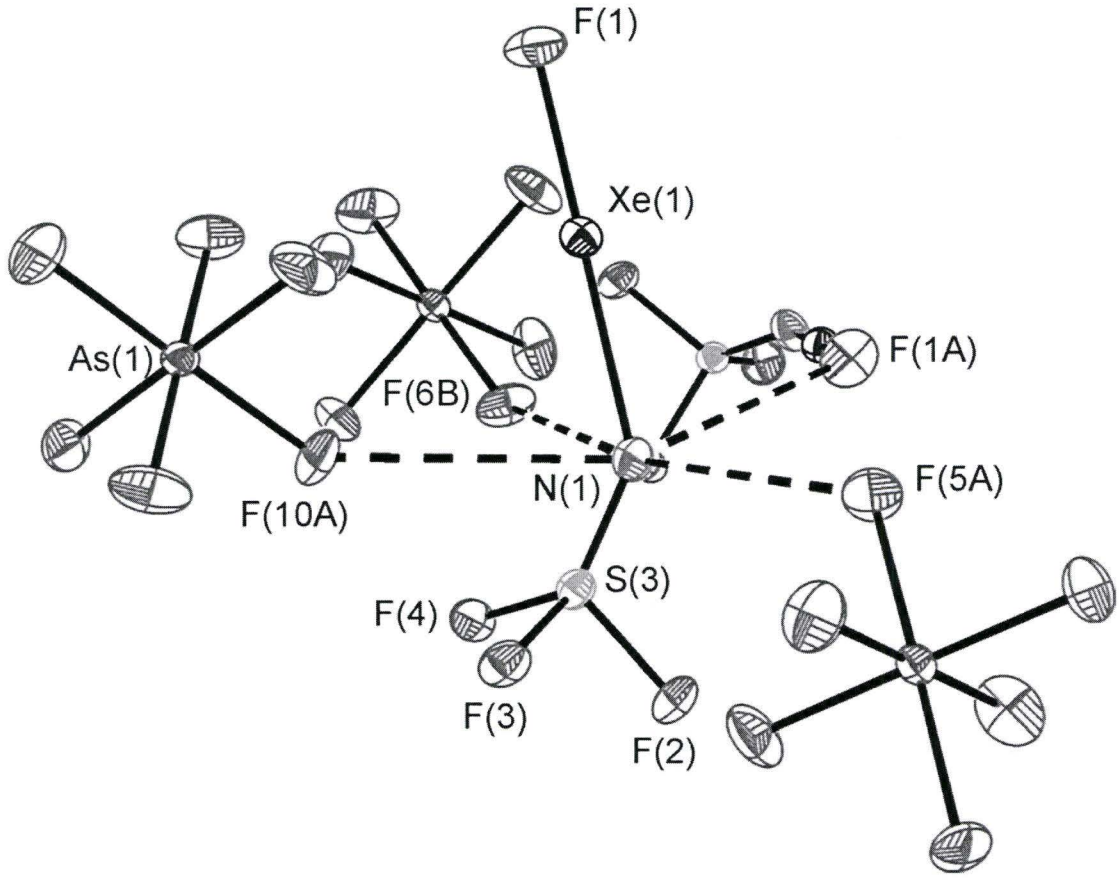

Figure 3.2. View of the $F_3S{\equiv}NXeF^+$ cation showing the closest N---F contacts with three neighboring AsF_6^- anions and the fluorine on xenon of a neighboring $F_3S{\equiv}NXeF^+$ cation.

Table 3.3. NMR Chemical Shifts and Spin-Spin Coupling Constants for $[F_3S{\equiv}NXeF][AsF_6]$[a]

species	chemical shifts, ppm			coupling constants, Hz		
	$\delta(^{129}Xe)$	$\delta(^{19}F)$	$\delta(^{14}N)$	$^{1}J(^{129}Xe{-}^{19}F)$	$^{1}J(^{129}Xe{-}^{14}N)$	$^{n}J(^{19}F{-}^{19}F)$
$F_3S{\equiv}NXeF^{+}$ [b]	–1652 (–1661)	–185.5 (–180.5), F_{Xe} 51.2 (53.3), F_S	–278.0	6265 (6248)	350	(15.1), $n = 4$
AsF_6^{-} [c]		–69 (–62)				
HF		–197				
BrF_5 [d]		(136.4), F_{eq} (274.4), F_{ax}				(77.0), $n = 2$

[a] The values in parentheses have been measured in BrF_5 solvent at –60 °C; all other values have been measured in HF solvent at –20 °C. The secondary isotope effect of $^{32/34}S$ on ^{19}F, $^{1}\Delta^{19}F(^{34/32}S) = -0.066$ ppm, was observed in both HF and BrF_5 solvents. [b] The fluorines bonded to Xe and S are denoted by F_{Xe} and F_S, respectively. [c] The ^{19}F resonance of AsF_6^{-} was a broad, saddle-shaped feature, $\Delta\nu_{1/2} = 2860$ (2500) Hz, as a result of partial quadrupole-collapse of the $^{1}J(^{75}As{-}^{19}F)$ coupling. [d] The axial (quintet) and equatorial (doublet) ^{19}F environments, denoted by F_{ax} and F_{eq}, respectively, exhibited bromine secondary isotope shifts: $^{1}\Delta^{19}F_{ax}(^{79/81}Br) = -0.012$ ppm and $^{1}\Delta^{19}F_{eq}(^{79/81}Br) = -0.029$ ppm.

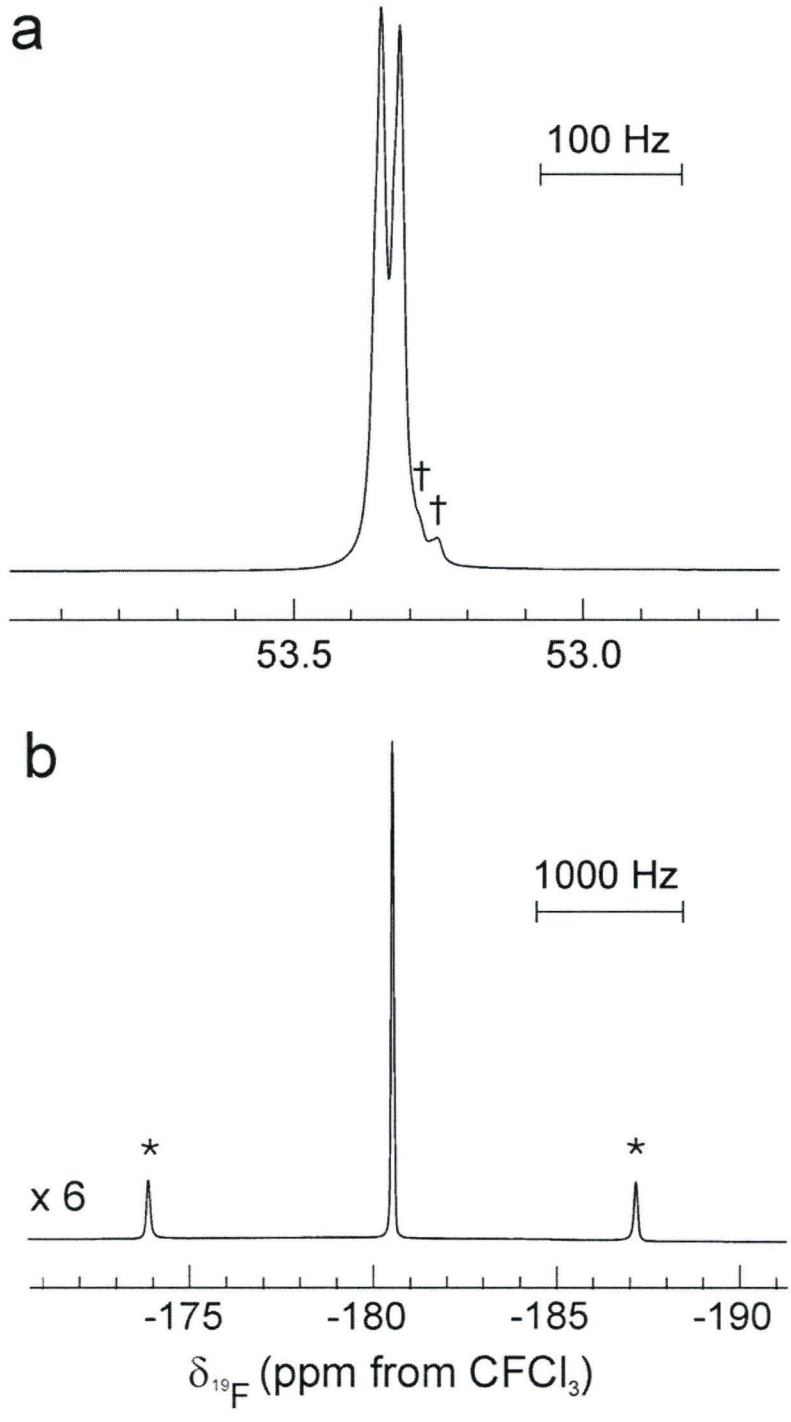

Figure 3.3. ^{19}F NMR spectrum (470.592 MHz) of $[F_3S{\equiv}NXeF][AsF_6]$ in BrF_5 solvent at –60 °C showing the cation resonances; (a) the F-on-S environment; daggers (†) denote the $^{1}\Delta^{19}F_S(^{34/32}S)$ secondary isotope shift, and (b) the F-on-Xe environment; asterisks (*) denote ^{129}Xe satellites.

$^2J(^{19}F_S–^{14}N)$ and $^2J(^{19}F_{Xe}–^{14}N)$ couplings that result from the higher viscosity of BrF_5 at –60 °C are apparently responsible for the line narrowing[142] that permits observation of the $^4J(^{19}F_{Xe}–^{19}F_S)$ coupling (doublet, 15.1 Hz, $\Delta\nu_{½}$ = 26 Hz) on the F-on-S environment (vide infra). The anticipated 1:3:3:1 quartet corresponding to the F-on-Xe environment could only be partially resolved in BrF_5 solvent ($\Delta\nu_{½}$ = 45 Hz).

The ^{129}Xe spectrum (Figure 3.4) consists of a doublet arising from $^1J(^{129}Xe–^{19}F)$ = 6265 (6248) Hz, which, in turn, is split into a 1:1:1 triplet ($^1J(^{129}Xe–^{14}N)$ = 350 Hz) in anhydrous HF solvent. The outer transitions of the triplets are broader than the central transition owing to partial quadrupolar relaxation of ^{14}N (I = 1) in the presence of the small electric field gradient at ^{14}N in this axially symmetric cation. Similar $^1J(^{129}Xe–^{14}N)$ couplings have been observed for the HC≡N and alkyl nitrile adducts of XeF^+ when recorded in HF solvent (cf. $HC{\equiv}NXeF^+$, $^1J(^{129}Xe–^{19}F)$ = 6161 Hz and $^1J(^{129}Xe–^{14}N)$ = 332 Hz at –10 °C).[38] The ^{129}Xe NMR chemical shift, $\delta(^{129}Xe)$ = –1652 (–1661) ppm, is consistent with that expected for an Xe–F moiety bound to an sp-hybridized nitrogen (cf. $HC{\equiv}NXeF^+$, $\delta(^{129}Xe)$ = –1552 (–1570) ppm in HF (BrF_5) solvent at –10 (–50) °C).[38] When the ^{129}Xe NMR spectrum was recorded in BrF_5 solvent, the $^1J(^{129}Xe–^{14}N)$ coupling was quadrupole collapsed to a doublet corresponding to $^1J(^{129}Xe–^{19}F)$. Complete collapse of the $^1J(^{129}Xe–^{14}N)$ coupling in BrF_5 solvent is attributed to fast quadrupolar relaxation of ^{14}N that is mainly a consequence of the high viscosity[142] of BrF_5 at –60 °C. The ^{14}N spectrum of $F_3S{\equiv}NXeF^+$ recorded in HF at –20 °C consisted of a quadrupole broadened resonance ($\Delta\nu_{½}$ = 750 Hz) at −278.0 ppm, which obscured the expected ^{129}Xe satellites.

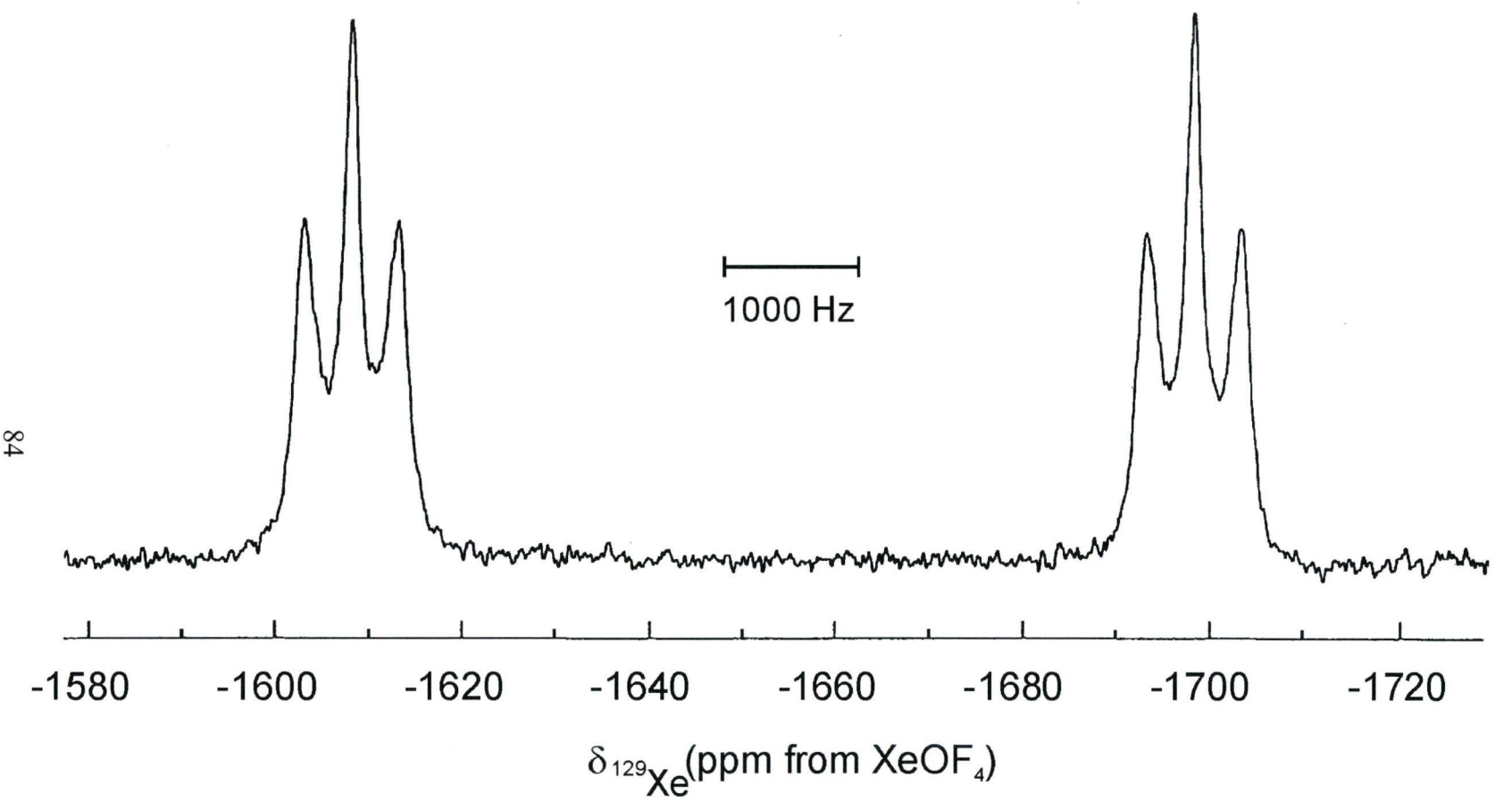

Figure 3.4. ^{129}Xe NMR spectrum (138.086 MHz) of $[F_3S{\equiv}NXeF][AsF_6]$ in anhydrous HF solvent at –20 °C.

Other than an early ^{19}F NMR study of $N{\equiv}SF_3$, which only reported the $^2J(^{19}F{-}^{14}N)$ coupling constant (27 Hz),[143] the NMR spectroscopic characterization of $N{\equiv}SF_3$ appears to be surprisingly incomplete. In the present study, the following NMR parameters for $N{\equiv}SF_3$ have been determined in SO_2ClF solvent at 30 °C: $\delta(^{19}F)$ = 68.3 ppm, $\delta(^{14}N)$ = –245.8 ppm, $^1J(^{19}F{-}^{14}N)$ = 26.6 Hz, $^1\Delta^{19}F^{(34/32)}S$ = 0.058 ppm. The ^{19}F and ^{14}N chemical shifts of $N{\equiv}SF_3$ and $F_3S{\equiv}NXeF^+$ have been measured in different solvents at different temperatures because $N{\equiv}SF_3$ undergoes HF solvolysis to yield F_5SNH_2[96] and because $[F_3S{\equiv}NXeF][AsF_6]$ is insoluble in SO_2ClF. The complexation shifts $\delta(^{19}F_S)_{F_3S{\equiv}NXeF^+} - \delta(^{19}F_S)_{N{\equiv}SF_3}$ = –17.1 [–15.0] ppm and $\delta(^{14}N)_{F_3S{\equiv}NXeF^+} - \delta(^{14}N)_{N{\equiv}SF_3}$ = –32.2 ppm indicate that both the $^{19}F_S$ and ^{14}N environments are more shielded in the cation. The individual shielding tensors that contribute to the isotropic shielding would need to be determined for a fuller understanding of the complexation shifts. It is noteworthy, however, that the increased shielding of ^{14}N in $F_3S{\equiv}NXeF^+$ parallels its increased charge and valency, whereas the charges of the more highly shielded fluorine ligands bonded to sulfur have diminished, but their valencies have also increased relative to those of $N{\equiv}SF_3$ (see Section 3.3.2.).

3.2.4. Raman Spectroscopy

The Raman spectrum of $[F_3S{\equiv}NXeF][AsF_6]$ was assigned by comparison with that of solid $N{\equiv}SF_3$, recorded during the course of this study, and previously published

vibrational assignments for $N{\equiv}SF_3$[78,83,84,143] and AsF_6^-,[50] and by electronic structure calculations (see Section 3.3.).

The $F_3S{\equiv}NXeF^+$ cation (C_1 symmetry) possesses 15 Raman- and infrared-active fundamental vibrational modes belonging to the A irreducible representations. The 15 vibrational modes of AsF_6^- belong to the irreducible representations $A_{1g} + E_g + T_{2g} + 2T_{1u} + T_{2u}$ under O_h symmetry, where the A_{1g}, E_g, and T_{2g} modes are Raman active and the T_{1u} modes are infrared active. The eight cations and anions occupy C_1 sites in its crystallographic unit cell. Factor-group analyses for the cation and anion are provided in Table 3.4 and predict that each gas phase Raman- and infrared-active vibrational mode of $F_3S{\equiv}NXeF^+$ and AsF_6^- is split, as a result of site symmetry lowering, into a maximum of four Raman-active (A_g, B_{1g}, B_{2g}, B_{3g}) and infrared-active (A_u, B_{1u}, B_{2u}, B_{3u}) components. Anion bands, under O_h symmetry, corresponding to the $\nu_1(A_{1g})$, $\nu_2(E_g)$, and $\nu_3(T_{1u})$ modes were split into two components and $\nu_4(T_{1u})$ was split into three components (Figure 3.5). The cation splittings were only resolved for the vibrational modes associated with adducted $N{\equiv}SF_3$, i.e., the $\delta_s(SF_3)$ mode (four components), the $\nu(SN)$, $\nu_{as}(SF_3)$, and $\nu_s(SF_3)$ modes (three components each), and the $\delta(NSF_2)$ and $\delta_{as}(NSF_3)$ modes (two components each).

Vibrational frequencies calculated at the MP2 and SVWN levels of theory reproduced all the experimental frequency trends, although $\nu(SN)$ and $\nu(XeF)$ are both predicted to be ca. 60 cm^{-1} higher than the experimental frequencies (Table 3.5). The XeF stretching mode of $F_3S{\equiv}NXeF^+$ (550 cm^{-1}) is characteristically intense, having a frequency that is intermediate with respect to those of $FXeN(SO_2F)_2$ (506 cm^{-1})[45] and $[XeF][AsF_6]$ (608, 610 cm^{-1}),[144] and very similar to that of $HC{\equiv}NXeF^+$ (561, 569 cm^{-1}).[38]

Table 3.4. Correlation Diagrams and Selection Rules for the Vibrational Modes of $[F_3S{\equiv}NXeF][AsF_6]$

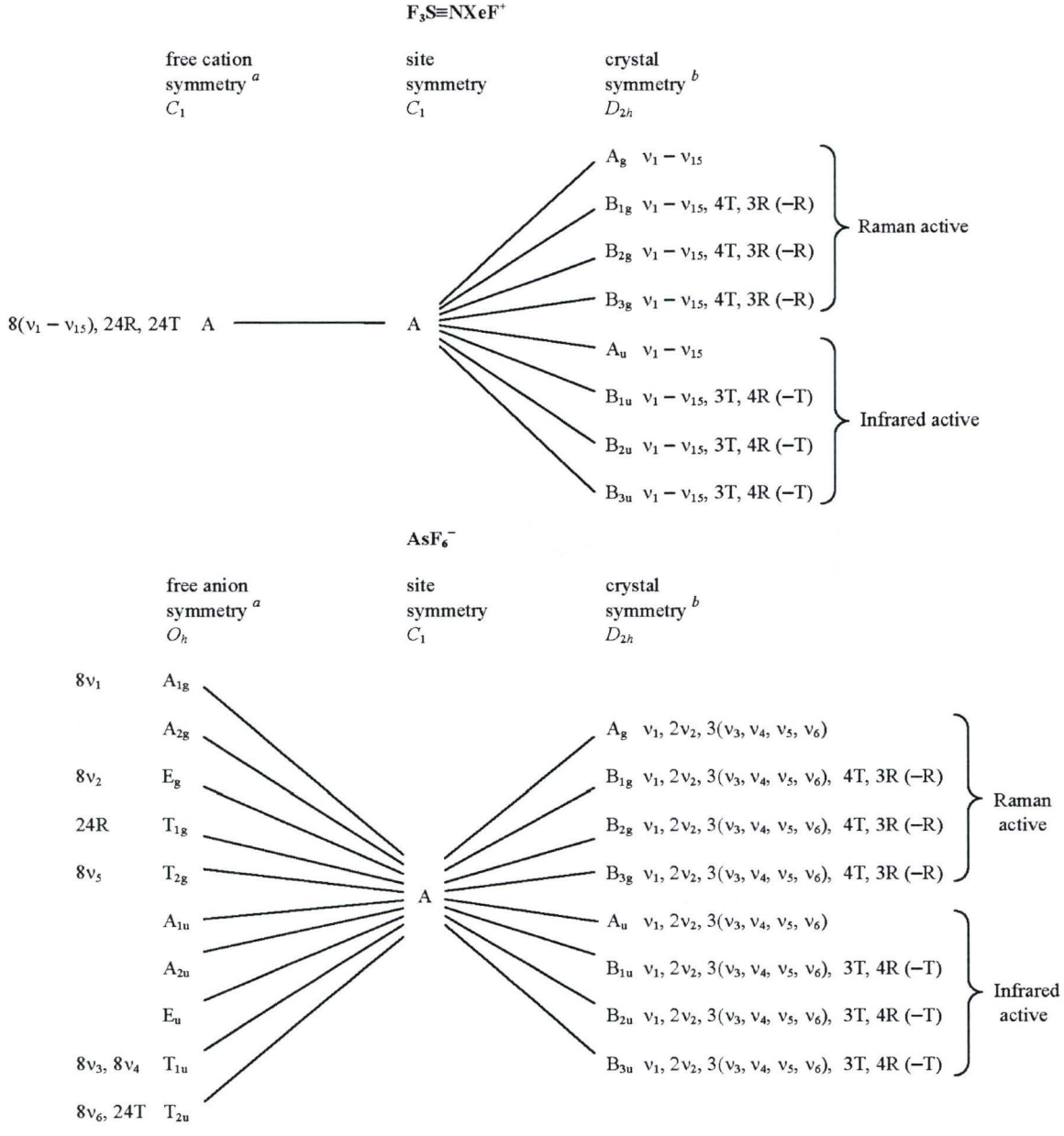

[a] The irreducible representations are $\Gamma = 15A$ (C_1) for the bent $F_3S{\equiv}NXeF^+$ cation and $\Gamma = A_{1g} + E_g + T_{2g} + 2T_{1u} + T_{2u}$ (O_h) for the AsF_6^- anion in the gas phase. [b] The crystallographic space group is *Pbca* with $Z = 8$ molecules.

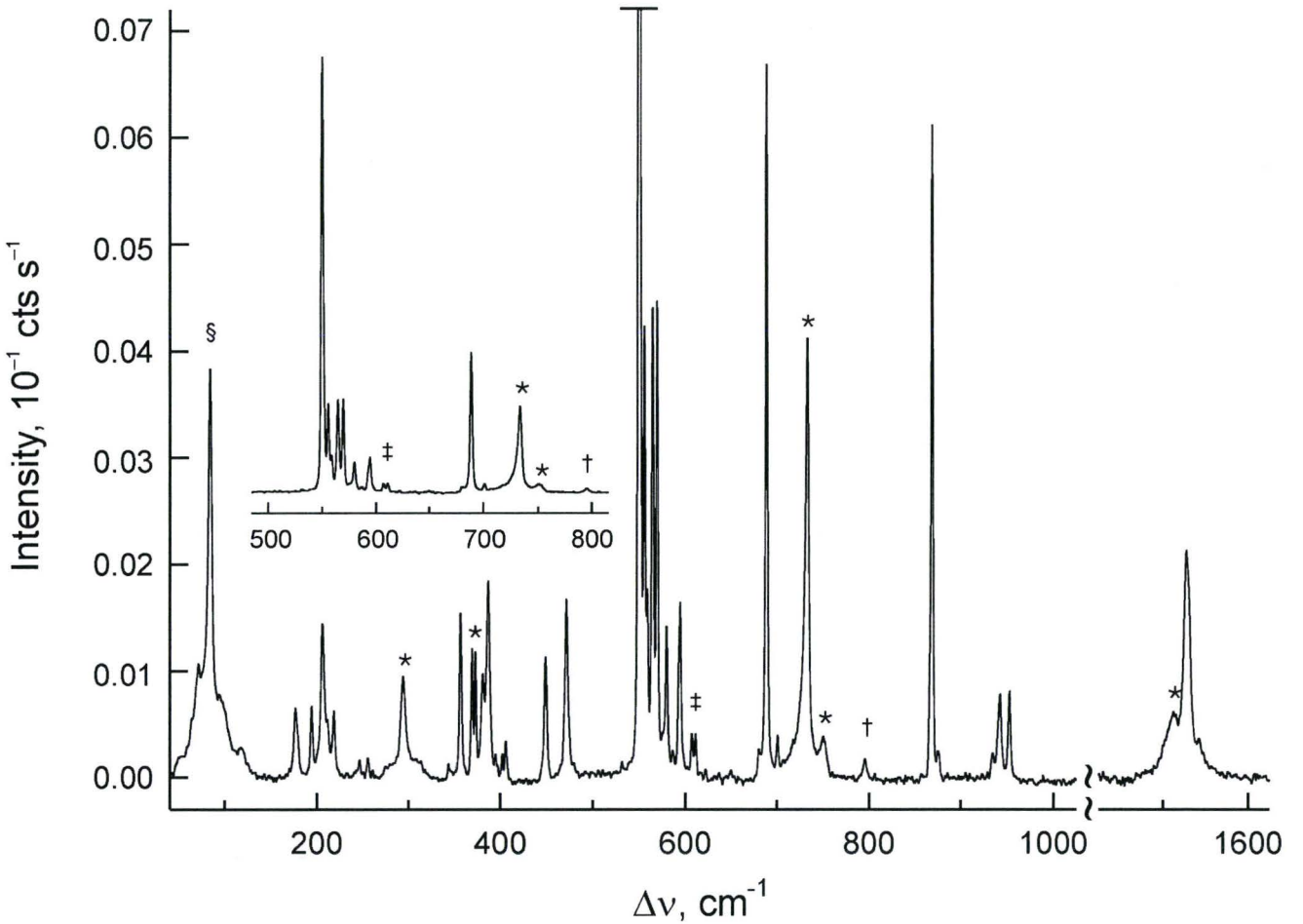

Figure 3.5. Raman spectrum of $[F_3S{\equiv}NXeF][AsF_6]$ recorded at –150 °C using 1064-nm excitation; the symbols denote FEP sample tube lines (*), $\nu_s(SF_3)$ of unreacted $N{\equiv}SF_3$ (†), ν(XeF) of unreacted $[XeF][AsF_6]$ (‡), and an instrumental artifact (§).

Table 3.5. Raman Vibrational Frequencies and Intensities for $N{\equiv}SF_3$ and $[F_3S{\equiv}NXeF][AsF_6]$, and Calculated Vibrational Frequencies, Intensities, and Assignments for $N{\equiv}SF_3$, $F_3S{\equiv}NXeF^+$, and XeF^+ [a]

freq, cm^{-1} [b]						assignts	
$N{\equiv}SF_3$			$F_3S{\equiv}NXeF^+$			$F_3S{\equiv}NXeF^+$	AsF_6^-
exptl	calcd[c]		exptl[d]	calcd[c]		(C_1)	(O_h)
	MP2	SVWN		MP2	SVWN		
1524 (7) 1519 (39) 1503 (3)	1503 [68] (16)	1466 [73] (9)	1548 (1) 1542 sh 1527 (10)	1619 [475] (84)	1607 [459] (86)	ν(SN)	
855 (3) 851 (13) 811 (7) 809 (5)	809 [211] (3)	751 [194] (5)	952 (4) 942 (4) 934 (1)	941 [193] (3)	924 [179] (4)	$\nu_{as}(SF_3)$	
779 (100)	759 [149] (23)	714 [122] (24)	876 (1) 875 (1) 869 (28)	873 [89] (36)	846 [98] (56)	$\nu_s(SF_3)$	
			724 sh 717 sh				$\nu_3(T_{1u})$
			701 (2) 689 (31)				$\nu_1(A_{1g})$
			594 (8) 580 (5)				$\nu_2(E_g)$
530 (10) 526 (2)	511 [27] (2)	443 [14] (2)	570 (22) 565 (21) 558 sh 556 sh	547 [10] (1)	518 [11] (1)	$\delta_s(SF_3)$	
			550 (100)	610 [98] (63)	604 [114] (44)	ν(XeF)	
445 (21) 438 (14)	419 [7] (4)	376 [6] (4)	471 (8) 448 (6)	440 [20] (4)	407 [16] (3)	$\delta(NSF_2)$	

Table 3.5. (continued…)

			406 (3)			
			402 (2)			$\nu_4(T_{1u})$
			395 (2)			
			373 (6)			$\nu_5(T_{2g})$
355 (21)	337 [2] (4)	295 [1] (3)	369 (6)	345 [5] (3)	318 [5] (2)	$\delta_{as}(NSF_3)$
349 (30)			357 (8)			
			246 (1)			$\nu_6(T_{2u})$
			218 (3)			
			211 sh			
			206 (7)			
			194 (3)	161 [47] (1)	177 [31] (2)	ν(XeN)
			177 (4)	175 [5] (1)	171 [5] (1)	δ(NXeF)
			118 (1) br			
			95 (3)			
			n.o.	32 [<1] (1)	15 [<1] (1)	torsion about Xe

[a] The calculated stretching frequency of gas-phase XeF^+ occurs at 665 (MP2) and 667 (SVWN) cm^{-1}. The experimental frequency of XeF^+ in its salts occurs at 608, 610 (AsF_6^-, this work), 615 (SbF_6^-, ref. 112), 602, 608 (BiF_6^-, ref. 136), 619 ($Sb_2F_{11}^-$, ref. 112), and 605, 609 ($Bi_2F_{11}^-$) ref. 136) cm^{-1}. [b] Values in parentheses denote experimental Raman intensities. [c] Infrared intensities (in km mol^{-1}) are given in brackets, calculated Raman intensities (in $Å^4$ amu^{-1}) are given in parentheses. [d] Abbreviations denote shoulder (sh), broad (br), and not observed (n.o.).

The XeF stretching frequency trend correlates with the Xe–F bond lengths of these species and with donor atom base strength, decreasing with increasing base strength,[33,112] affirming the highly ionic characters of the Xe–N bonds in $F_3S{\equiv}NXeF^+$ and $HC{\equiv}NXeF^+$. The experimental shift of ν(XeF) in $F_3S{\equiv}NXeF^+$, 59 cm^{-1} to lower frequency relative to that of $[XeF][AsF_6]$, is in accord with the calculated gas-phase complexation shifts of 55/63 (MP2/SVWN) cm^{-1} for XeF^+ and $F_3S{\equiv}NXeF^+$.

Correspondingly, the ν(XeN) stretch occurs at low frequency and is assigned to the band at 194 cm^{-1}, which is slightly higher than that observed in $(CH_3)_3CC{\equiv}NXeF^+$ (188 cm^{-1}),[38] but significantly lower than those observed in $CH_3C{\equiv}NXeF^+$ (280 cm^{-1}),[38] $HC{\equiv}NXeF^+$ (331 cm^{-1}),[38] and $FXeN(SO_2F)_2$ (422 cm^{-1}).[45] The NXeF bend is assigned to the band at 177 cm^{-1}, which is comparable to those of $CH_3C{\equiv}NXeF^+$ (160, 170 cm^{-1})[38] and $HC{\equiv}NXeF^+$ (181 cm^{-1}).[38]

All $N{\equiv}SF_3$ modes of $F_3S{\equiv}NXeF^+$ exhibit complexation shifts to higher frequency relative to those of solid $N{\equiv}SF_3$. The highest-frequency mode, assigned to ν(SN), occurs 20 cm^{-1} to higher frequency with respect to that of $N{\equiv}SF_3$, but is much less than the calculated shifts of 116/141 cm^{-1}. The average $\nu_{as}(SF_3)$ and $\nu_s(SF_3)$ frequencies increase 111 (132/173) cm^{-1} and 94 (114/132) cm^{-1}, respectively, upon complexation, and the bending modes, $\delta_s(SF_3)$, $\delta(NSF_2)$, and $\delta_{as}(NSF_3)$, shift to higher frequency by 34, 26, and 11 (36/75, 21/31, 8/23) cm^{-1}, respectively. The high-frequency shifts are in accord with the N–S and S–F bond length contractions that result upon adduct formation with XeF^+. Bands below 220 cm^{-1}, that are not otherwise explicitly assigned, are attributed to lattice modes.

The lowest frequency mode, torsion about Xe, was calculated at 32/15 cm^{-1}, but could not be observed.

3.3. Computational Results

Quantum-chemical calculations were carried out at the MP2 and DFT (SVWN) levels using cc-pVTZ or (SDB-)cc-pVTZ basis sets for $F_3S{\equiv}NXeF^+$ and XeF^+ to support the vibrational assignments (see Raman Spectroscopy) and to gain insight into the structure and bonding of $F_3S{\equiv}NXeF^+$ (Table 3.2). The energy-minimized geometries and vibrational frequencies of $N{\equiv}SF_3$ and XeF^+ were also calculated and served as benchmarks. The MP2 calculations provided vibrational frequencies that were in better agreement with the experimental frequencies and better reproduced their trends, while the SVWN calculations (values given in parentheses) provided geometrical parameters that were in better agreement with the experimental values.

3.3.1. Calculated Geometries

Although close to C_{3v} symmetry, both the MP2 and SVWN energy-minimized structures of $F_3S{\equiv}NXeF^+$ had C_1 symmetry. Both levels of theory reproduced the experimentally observed decreases in the S–N and S–F bond lengths upon complex formation with XeF^+, and the Xe–F bond elongation [0.04 (0.06) Å] with respect to that calculated for gas-phase XeF^+. The Xe–N–S angle, found to be bent by low-temperature X-ray diffraction (vide supra), was linear in the calculated geometry. The calculated MP2 energy difference (7.9 kJ mol^{-1}) between the experimental bent and calculated linear

geometries indicates that the Xe–N–S angle is very deformable, and is most likely the result of crystal lattice packing.

Because the valence electron lone pair on the nitrogen atom of $N{\equiv}SF_3$ is formally sp-hybridized, Xe–N donor-acceptor bond formation directly influences the S–N σ bond by strengthening and shortening this bond through removal of charge density from S. Enhancement of the sulfur positive charge, in turn, leads to shorter, more covalent S–F bonds. This agrees with the trend in the calculated bond lengths for $N{\equiv}SF_3$ and $F_3S{\equiv}NXeF^+$ where the N–S bond shortens by 0.019 (0.033) Å and the S–F bond shortens by 0.046 (0.084) Å upon cation formation.

3.3.2. Charges, Valencies and Bond Orders

The natural bond orbital (NBO) charges, valencies, and bond orders calculated at the MP2 and SVWN levels of theory (SVWN values are given in parentheses) for $N{\equiv}SF_3$ and $F_3S{\equiv}NXeF^+$ are listed in Table 3.6. The experimental and calculated contraction of the S–F and S–N bond lengths, elongation of the Xe–F bond, and formation of the Xe–N bond upon complexation are corroborated by the NBO analyses. The positive charges in $F_3S{\equiv}NXeF^+$ occur on Xe and S with the charge on Xe decreasing only slightly from 1.32 (1.33) in gas-phase XeF^+ to 1.29 (1.25) in $F_3S{\equiv}NXeF^+$. The small xenon valency increase from 0.47 (0.45) in XeF^+ to 0.62 (0.66) in the adduct cation is matched by the increase in the nitrogen valency from 1.57 (1.46) to 1.74 (1.69), and is indicative of a weak bonding interaction with nitrogen, which is corroborated by the low Xe–N bond order [0.24 (0.27)]. The negative charge on the fluorine atom of XeF^+ [–0.32 (–0.33)] increases upon

Table 3.6. Natural Bond Orbital (NBO) Charges, Valencies, and Bond Orders for $F_3S{\equiv}NXeF^+$, $N{\equiv}SF_3$, and XeF^+ [a]

	$F_3S{\equiv}NXeF^+$				$N{\equiv}SF_3$				XeF^+			
atom	charges		valencies		charges		valencies		charges		valencies	
	MP2	SVWN	MP2	SVWN	MP2	SVWN	MP2	SVWN	MP2	SVWN	MP2	SVWN
F_{Xe}	–0.46	–0.46	0.38	0.39					–0.32	–0.33	0.47	0.45
Xe	1.29	1.25	0.62	0.66					1.32	1.33	0.47	0.45
N	–1.09	–1.04	1.74	1.69	–0.82	–0.75	1.57	1.46				
S	2.45	2.35	3.84	3.62	2.19	2.06	3.68	3.34				
F_S	–0.40	–0.37	0.64	0.59	–0.46	–0.44	0.56	0.50				

bond orders

bond	$F_3S{\equiv}NXeF^+$		$N{\equiv}SF_3$		XeF^+	
	MP2	SVWN	MP2	SVWN	MP2	SVWN
F–Xe	0.38	0.39			0.47	0.45
Xe–N	0.24	0.27				
N–S	1.62	1.54	1.69	1.57		
S–F	0.74	0.69	0.66	0.59		

[a] (SDB-)cc-pVTZ basis set.

adduct formation [–0.46 (–0.46)], consistent with a longer more polar Xe–F bond (Table 3.2.) and a correspondingly lower F valency and Xe–F bond order. Contraction of the S–F bonds in $F_3S{\equiv}NXeF^+$ is in accord with the increased S–F bond order and valency, and the greater difference between the S and F charges. Interestingly, the N atom has a greater negative charge in the cation [–1.09 (–1.04)] when compared with that in $N{\equiv}SF_3$ [–0.82 (–0.75)], with the negative charge increase on N being matched by the positive charge increase on S [$N{\equiv}SF_3$, 2.19 (2.06); $F_3S{\equiv}NXeF^+$, 2.45 (2.35)].

Among the plausible contributions to a valence bond description of $F_3S{\equiv}NXeF^+$ (VIII–XVII), the calculated increase in electron density on N of the cation, relative to that of the free base, suggests that valence structures XII and XV are significant contributors.

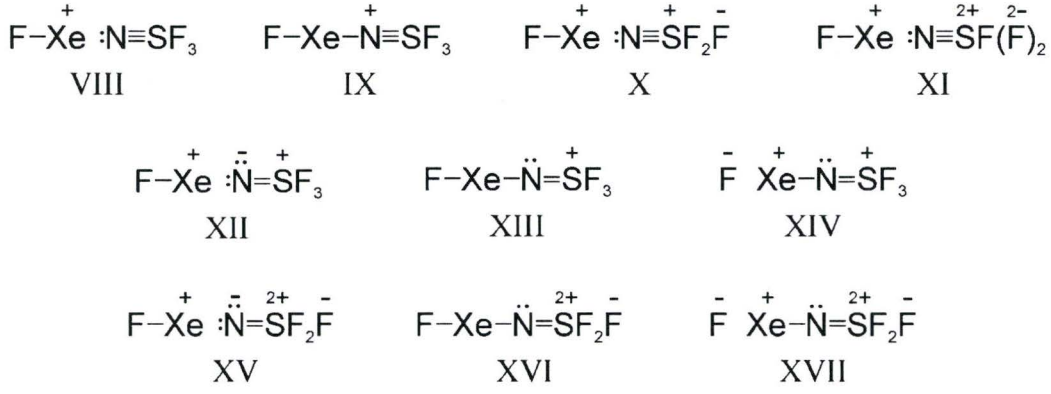

The negative charge on nitrogen in these structures is presumably stabilized, through polarization, by the positive charge on Xe. Structures XII and XV also account for the high positive charges on Xe and S and appear to best represent the calculated charge distributions. A prior computational study of $N{\equiv}SF_3$ concluded that any withdrawal of

electron density from nitrogen results in a marked stabilization of the S–N and S–F bonds and in their contraction.[78,145]

3.3.3. Nature of the Xenon-Nitrogen Bond.

The gas-phase reaction energies corresponding to xenon-ligand dissociation were calculated at the MP2 level of theory for $F_3S{\equiv}NAsF_5$, $HC{\equiv}NAsF_5$, $F_3S{\equiv}NXeF^+$, $HC{\equiv}NXeF^+$, $(FO_2S)_2NXeF$, and XeF_2 and are listed in Scheme 3.1. The donor-acceptor adduct dissociation energies of $F_3S{\equiv}NXeF^+$ and $HC{\equiv}NXeF^+$ are remarkably similar. These donor-acceptor interactions are decidedly weaker than those of XeF^+ with the F^- or $N(SO_2F)_2^-$ ions, but notably stronger than the As–N dissociation energies of $HC{\equiv}NAsF_5$ and $F_3S{\equiv}NAsF_5$. Under gas-phase conditions, it is clear that XeF^+ is a significantly stronger Lewis acid towards both bases. These findings are consistent with a valence bond description of $F_3S{\equiv}NXeF^+$ that is dominated by the non-bonded structures XII and XV (vide supra) and with the spectroscopic and structural findings, i.e., correlations of Xe–F bond length and vibrational frequency with base strength,[33,112] placing the Xe–N interactions of $F_3S{\equiv}NXeF^+$ and $HC{\equiv}NXeF^+$ toward the most ionic end of the scale. The similar changes in XeF stretching frequencies and bond length for $HC{\equiv}N$ and $N{\equiv}SF_3$ upon complexation with XeF^+, as well as similar charge distribution changes for $HC{\equiv}N$ and $HC{\equiv}NXeF^+$,[33] yields a picture of adduct formation between XeF^+ and $N{\equiv}SF_3$ that is similar to that of XeF^+ and $HC{\equiv}N$. In this depiction, mutual penetration of outer diffuse non-bonded densities of the Xe and N atoms which, unlike a covalent interaction,

produces no substantial shared density as reflected in the low Xe–N bond order and small changes in Xe and N valencies (Table 3.6.). Instead, the final density and bond strength of the interaction are primarily determined by the extent of interpenetration of their closed shell densities, which leads to little modification of the Xe charge but polarization of, and increased negative charge on, the N donor atom (vide supra).

Scheme 3.1. Donor-Acceptor Adduct Dissociation Energies (kJ mol^{-1}) for Selected Species Calculated at the MP2/(SDB-)cc-pVTZ Level of Theory.

$F_3S{\equiv}NAsF_5 \rightarrow F_3S{\equiv}N: + AsF_5$	27.8
$HC{\equiv}NAsF_5 \rightarrow HC{\equiv}N: + AsF_5$	38.6
$HC{\equiv}NXeF^+ \rightarrow HC{\equiv}N: + XeF^+$	157.1
$F_3S{\equiv}NXeF^+ \rightarrow F_3S{\equiv}N: + XeF^+$	157.2
$(FO_2S)_2NXeF \rightarrow (FO_2S)_2N:^- + XeF^+$	628.5
$XeF_2 \rightarrow F^- + XeF^+$	1000.8

3.4. Conclusions

The synthesis and structural characterization of the $F_3S{\equiv}NXeF^+$ cation provides, in addition to the $HC{\equiv}NXeF^+$ cation, a further example of xenon bound to a formally sp-hybridized nitrogen atom of an inorganic nitrogen base, and affirms that $N{\equiv}SF_3$ is stable to oxidative attack by the highly electrophilic XeF^+ cation. Raman and NMR spectroscopic studies and an X-ray crystallographic study of $[F_3S{\equiv}NXeF][AsF_6]$ demonstrate that the $F_3S{\equiv}NXeF^+$ cation possesses among the longest Xe–N bonds known. This is corroborated

by the deformation of the Xe–N–S angle from its linear gas-phase geometry to the severely bent arrangement that results from crystal packing in the solid state structure of $[F_3S{\equiv}NXeF][AsF_6]$. These experimental findings, complimented by quantum-chemical calculations, reveal that $F_3S{\equiv}NXeF^+$ is among the weakest donor-acceptor adducts of XeF^+ and has an Xe-N donor-acceptor bond strength that is very similar to that of $HC{\equiv}NXeF^+$, but significantly greater than those of the AsF_5 adducts of $HC{\equiv}N$ and $N{\equiv}SF_3$. Despite the low dissociation energy of the donor-acceptor bond in $F_3S{\equiv}NXeF^+$, solution ^{129}Xe, ^{19}F, and ^{14}N NMR studies reveal that the $F_3S{\equiv}NXeF^+$ cation is nonlabile at low temperatures in HF and BrF_5 solvents.

CHAPTER 4

$F_5SN(H)Xe^+$; A RARE EXAMPLE OF XENON BONDED TO sp^3-HYBRIDIZED NITROGEN; SYNTHESIS AND STRUCTURAL CHARACTERIZATION OF $[F_5SN(H)Xe][AsF_6]$

4.1. Introduction

Until recently, the only known Xe–N bonded compounds were those containing sp^2- or sp-hybridized nitrogen centers, namely, $FXeN(SO_2F)_2$,[44-46] $Xe[N(SO_2F)_2]_2$,[45,47] $F[XeN(SO_2F)_2]_2^+$,[45,47,49] $XeN(SO_2F)_2^+$,[49] $Xe[N(SO_2CF_3)_2]_2$,[48] and the XeF^+ adducts of hydrogen cyanide,[34,35] alkylnitriles,[34] pentafluorobenzenenitrile,[34] perfluoroalkylnitriles,[34,36] perfluoropyridines,[37] and *s*-trifluorotriazine.[36] Until the present work, the only example of a noble gas bonded to a formally sp^3-hybridized nitrogen atom was $[F_5TeN(H)Xe][AsF_6]$ which was recently reported from this laboratory.[50] The $F_5TeN(H)Xe^+$ cation represents the most covalent Xe–N bonded species reported to date and was synthesized by reaction of the XeF^+ cation with F_5TeNH_2 in anhydrous HF (aHF), and by reaction of $F_5TeNH_3^+$ and XeF_2 in aHF and BrF_5 solvents. Most recently, the synthesis and structural characterization of the $F_3S{\equiv}NXeF^+$ cation, a rare example of a noble-gas compound in which the noble-gas atom is bonded to an inorganic sp-hybridized nitrogen center, was reported by the author (see Chapter 3).[146] In the latter study, the previously demonstrated Lewis basicity of thiazyl trifluoride, $N{\equiv}SF_3$,[78] was exploited by reaction of the Lewis acidic XeF^+ cation,[32] as its AsF_6^- salt, with $N{\equiv}SF_3$ to form $[F_3S{\equiv}NXeF][AsF_6]$.[146]

In view of the solvolytic behavior of $N{\equiv}SF_3$ in aHF, which gives rise to F_5SNH_2[96] and to $[F_5SNH_3][AsF_6]$,[101] in the superacidic medium AsF_5/aHF, and the basicity of F_5SNH_2 which forms the room-temperature stable Lewis acid-base adducts, $F_5SNH_2{\cdot}BF_3$ and $F_5SNH_2{\cdot}PF_5$,[97] two synthetic approaches to the formation of the $F_5SN(H)Xe^+$ cation were developed that are described in this chapter: (1) the reaction of $[F_5SNH_3][AsF_6]$ with XeF_2 in aHF and BrF_5 solvents, and (2) the HF solvolysis of $[F_3S{\equiv}NXeF][AsF_6]$, providing avenues to the second example of xenon bound to a formally sp^3-hybridized nitrogen center.

4.2. Results and Discussion

4.2.1. Syntheses of $[F_5SNH_3][AsF_6]$ and $[F_5SN(H)Xe][AsF_6]$

The solvolytic reactions leading to the $F_5SNH_3^+$ and $F_5SN(H)Xe^+$ cations and their further solvolyses were monitored by ^1H, ^{19}F, and ^{129}Xe NMR spectroscopy in both aHF and BrF_5 solvents. The NMR parameters reported in this section (parameters obtained in BrF_5 are given in parentheses) are for previously known species and are not further discussed. Those of the title species are discussed in section 4.2.2.

4.2.1.1. $[F_5SNH_3][AsF_6]$

The donor-acceptor adduct, $F_3S{\equiv}NAsF_5$, was prepared as previously described,[88] by reaction of $N{\equiv}SF_3$ with AsF_5 at –78 °C for ca. 1 h, forming a friable white solid. The ammonium salt, $[F_5SNH_3][AsF_6]$, was synthesized as previously described[101] by reaction of $F_3S{\equiv}NAsF_5$ with aHF at 0 °C for ca. 6 h (eq 4.1), forming colourless, feather-like

crystals. In both instances, the products were characterized by Raman spectroscopy at –160 °C.

$$F_3S{\equiv}NAsF_5 + 3HF \xrightarrow[HF]{0\ ^\circ C} [F_5SNH_3][AsF_6] \quad (4.1)$$

4.2.1.2. $[F_5SN(H)Xe][AsF_6]$

The solvolysis of $[F_3S{\equiv}NXeF][AsF_6]$[146] in aHF over a period of ca. 4 h at –20 °C led to $[F_5SN(H)Xe][AsF_6]$ formation according to eq 4.2. The salt was obtained as transparent yellow plates and was characterized by Raman spectroscopy at –45 °C. The $F_5SN(H)Xe^+$ cation was also formed by reaction of $[F_5SNH_3][AsF_6]$ with XeF_2 in aHF and BrF_5 solvents (eq 4.3) at –30 °C for ca. 30 min and was characterized by ^{19}F NMR

$$[F_3S{\equiv}NXeF][AsF_6] + HF \xrightarrow[HF]{-20\ ^\circ C} [F_5SN(H)Xe][AsF_6] \quad (4.2)$$

$$[F_5SNH_3][AsF_6] + XeF_2 \underset{BrF_5}{\overset{HF\ or}{\rightleftharpoons}} [F_5SN(H)Xe][AsF_6] + 2HF \quad (4.3)$$

spectroscopy (at –20 °C and supercooled to –70 °C, respectively). In both synthetic approaches, $F_5SNH_3^+$ and $F_5SN(H)Xe^+$ were observed in equilibrium with XeF_2 and HF, so that eq 4.3 is best described as a solvent- and temperature-dependent equilibrium. In BrF_5 and aHF solutions below –20 °C, this equilibrium lies to the right, while in aHF above –20 °C, no $F_5SN(H)Xe^+$ is observed.

4.2.1.3. Decomposition of $[F_5SNH_3][AsF_6]$ and $[F_5SN(H)Xe][AsF_6]$ in aHF

The decompositions of $[F_5SNH_3][AsF_6]$ and $[F_5SN(H)Xe][AsF_6]$ in aHF at 0 °C

were monitored by ^{19}F NMR spectroscopy. The $F_5SN(H)Xe^+$ cation underwent solvolysis in aHF to form $F_5SNH_3^+$ and XeF_2 [$\delta(^{19}F)$ = –194.5 (–185.0) ppm, $^1J(^{19}F–^{129}Xe)$ = 5652 (5611) Hz] according to the reverse of eq 4.3. The $F_5SNH_3^+$ cation underwent further solvolysis (eq 4.4) to form SF_6 [$\delta(^{19}F)$ = 54.1 (56.0) ppm, $^1J(^{19}F–^{33}S)$ = 251.9 Hz], and

$$[F_5SNH_3][AsF_6] + HF \xrightarrow[HF]{\text{–20 to 0 °C}} SF_6 + [NH_4][AsF_6] \qquad (4.4)$$

the NH_4^+ cation [$\delta(^1H)$ = 5.54 ppm, $^1J(^1H–^{14}N)$ = 51 Hz]. Small amounts of F_5SNF_2 also formed in the course of $F_5SN(H)Xe^+$ decomposition. The $[F_5SNH_3^+]/[F_5SN(H)Xe^+]/[F_5SNF_2]/[SF_6]$ molar ratios at –20 °C in BrF_5 and aHF were 1.00:0.17:0.02:0.47 and 1.00:0.01:0.01:0.44, respectively.

The formation of F_5SNF_2 likely results from a series of reactions (eqs 4.5 – 4.10) analogous to those leading to F_5TeNF_2, a minor product in the decomposition of the $F_5TeN(H)Xe^+$ cation.[50] The decomposition of $F_5SN(H)Xe^+$ to form F_5SNF_2 is consistent with nucleophilic fluorination of $F_5SN(H)Xe^+$ accompanied by liberation of xenon gas and formation of the nitrenium ion, F_5SNF^+, as in intermediate (eq 4.5). Nucleophilic attack by the F^- ion leads to the known fluoramine, F_5SNHF, according to eq 4.6.[74] The enhanced fluoroacidity that results from fluorination of the nitrenium cation (eq 4.6), also results in the formation of the strong oxidant cations, XeF^+ and $Xe_2F_3^+$ (eqs 4.7 and 4.8), which may be expected to fluorinate F_5SNHF to $F_5SNHF_2^+$ (eq 4.9). The $F_5SNHF_2^+$ cation is expected to readily deprotonate (eq 4.10) by analogy with NF_3, which is too weakly basic to be protonated in the AsF_5/HF solution.[147] The NMR parameters determined for F_5SNF_2 in HF at –20 °C in this work [$\delta(^{19}F_{eq})$ = 31.5 ppm (doublet of triplets), $\delta(^{19}F_N)$ = 66.3 ppm

(quintet), $^2J(^{19}F_{ax}–^{19}F_{eq})$ = 157.1 Hz and $^3J(^{19}F_N–^{19}F_{eq})$ = 13.8 Hz] are in good agreement with the previously reported parameters [$\delta(^{19}F_{ax})$ = 48.5 ppm (quintet),[77] $\delta(^{19}F_{eq})$ = 36.5 ppm (doublet of triplets),[77] $\delta(^{19}F_N)$ = 66.3 ppm (quintet),[77] $^2J(^{19}F_{ax}–^{19}F_{eq})$ = 153.2 Hz,[76] and $^3J(^{19}F_N–^{19}F_{eq})$ = 19 Hz[77]]. In the present study, the axial fluorine resonance was obscured by overlap with the axial fluorine resonance of $F_5SNH_3^+$ (49.9 ppm, aHF, –20 °C). The $^3J(^{19}F_N–^{19}F_{ax})$ coupling was not resolved in the present and prior studies, in accordance with the general inability to resolve three-bond couplings to the axial fluorine of F_5Te moiety.[50] The $^3J(^{19}F_N–^{19}F_{ax})$ coupling also was not resolved in F_5TeNF_2.[50]

$$F_5SN(H)Xe^+ \longrightarrow [F_5SNH^+] + Xe \quad (4.5)$$

$$[F_5SNH^+] + 2HF/AsF_6^- \longrightarrow F_5SNHF + H_2F^+/AsF_5 \quad (4.6)$$

$$AsF_5 + XeF_2 \rightleftharpoons [XeF][AsF_6] \quad (4.7)$$

$$[XeF][AsF_6] + XeF_2 \rightleftharpoons [Xe_2F_3][AsF_6] \quad (4.8)$$

$$F_5SNHF + XeF^+ (Xe_2F_3^+) \longrightarrow F_5SNHF_2^+ + Xe\ (Xe + XeF_2) \quad (4.9)$$

$$F_5SNHF_2^+ + HF \longrightarrow F_5SNF_2 + H_2F^+ \quad (4.10)$$

4.2.2. NMR Spectroscopy

The ^1H, ^{19}F, and ^{129}Xe NMR parameters for $[F_5SNH_3][AsF_6]$ and $[F_5SN(H)Xe][AsF_6]$, recorded in aHF solvent at –20 °C or BrF_5 supercooled to –70 °C, are listed in Table 4.1 (NMR parameters obtained in BrF_5 are given in parentheses). The chemical shifts and coupling constants are in accord with those of other F_5S-derivatives,[101,148] $F_5TeNH_3^+$,[50] and $F_5TeN(H)Xe^+$.[50]

Table 4.1. NMR Chemical Shifts and Spin-Spin Coupling Constants for $[F_5SNH_3][AsF_6]$ and $[F_5SN(H)Xe][AsF_6]$[a]

species	chemical shifts, ppm			coupling constants, Hz
	$\delta(^{129}Xe)$	$\delta(^{19}F)$	$\delta(^{1}H)$	$^{2}J(^{19}F_{ax}-^{19}F_{eq})$
$F_5SNH_3^{+}$ [b]		50.1 (50.0), F_{ax} 71.7 (73.8), F_{eq}	8.92 (7.74)	152.6 (154.7)
$F_5SN(H)Xe^{+}$	–2897 (–2956)	59.0 (59.6), F_{ax} 71.3 (73.0), F_{eq}	(9.57)	152.9 (154.7)
AsF_6^{-} [c]		–69 (–64)		
SF_6 [d]		54.1 (56.0)		
NH_4^{+} [e]			5.54	
XeF_2 [f]		–194.5 (–185.0)		
HF		–197 (–192)	8.26 (7.39)	
BrF_5		(134.5), F_{eq} (272.0), F_{ax}		(76.3)

[a] The values in parentheses were measured in supercooled BrF_5 solvent at –70 °C; all other values were measured in aHF solvent at –20 °C. The axial and equatorial fluorines are denoted by F_{ax} and F_{eq}, respectively. The secondary isotope shifts arising from $^{32/34}S$ were measured in the ^{19}F NMR spectra of $F_5SNH_3^{+}$ and $F_5SN(H)Xe^{+}$ in aHF solvent: $^{1}\Delta^{19}F_{ax}(^{34/32}S)$ = –0.058 and –0.060 ppm and $^{1}\Delta^{19}F_{eq}(^{34/32}S)$ = –0.056 and –0.056 ppm, respectively. [b] Also measured in SO_2 solvent at 30 °C: $\delta(^{19}F_{ax})$ = 52.4 ppm, $\delta(^{19}F_{eq})$ = 76.4 ppm, $^{2}J(^{19}F_{ax}-^{19}F_{eq})$ = 156.5 Hz, $\delta(^{1}H)$ = 8.8 ppm. [c] The ^{19}F resonance of the AsF_6^{-} anion was broad and saddle-shaped in aHF ($\Delta\nu_{1/2}$ = 2860 [700] Hz) as a result of the partial quadrupole collapse of the 1:1:1:1 quartet arising from $^{1}J(^{75}As-^{19}F)$. [d] The secondary isotope effect of $^{32/34}S$ on ^{19}F, $^{1}\Delta^{19}F_{ax}(^{34/32}S)$ = –0.052 ppm, and $^{1}J(^{19}F-^{33}S)$ = 251.9 Hz were observed in aHF solvent at –20 °C. [e] $^{1}J(^{1}H-^{14}N)$ = 51 Hz. [f] $^{1}J(^{19}F-^{129}Xe)$ = 5652 [5611] Hz.

4.2.2.1. $[F_5SNH_3][AsF_6]$

The ^{19}F NMR spectrum of the $F_5SNH_3^+$ cation (Figure 4.1) is an AX_4 spin coupling pattern, occurring at 71.7 (73.8) [doublet, F_{eq}] and 50.1 (50.0) [quintet, F_{ax}] ppm with $^2J(^{19}F_{ax}–^{19}F_{eq})$ = 152.6 (154.7) Hz., that arises from the pseudo-octahedral F_5SN group. These parameters are in good agreement with those previously reported in SO_2; 76.37 and 52.43 ppm and 156.5 Hz (–40 °C), respectively.[101]

The ^1H NMR spectrum of $[F_5SNH_3][AsF_6]$ consists of a broad singlet at 8.92 (7.74) ppm ($\Delta\nu_{½}$ = 23.0 (54.2) Hz). This chemical shift is in agreement with that reported in SO_2; 8.8 ppm (–40 °C).[101] The line broadening and absence of resolved couplings results from quadrupolar relaxation by the directly bonded ^{14}N atom (I = 1).

4.2.2.2. $[F_5SN(H)Xe][AsF_6]$

The NMR spectra are consistent with eqs 4.2 and 4.3 in which resonances arising from the $F_5SNH_3^+$ cation, SF_6, and NH_4^+ (vide supra) (eqs 4.3 and 4.4) were also observed.

The ^{19}F NMR spectrum of the $F_5SN(H)Xe^+$ cation (Figure 4.2) consists of an AB_4 spin-coupling pattern at 71.3 (73.0) [doublet, F_{eq}] and 59.0 (59.6) [quintet, F_{ax}] ppm, with $^2J(^{19}F_{ax}–^{19}F_{eq})$ = 152.9 (154.7) Hz that arises from the pseudo-octahedral F_5SN group. These parameters are very similar to those of the $F_5SNH_3^+$ cation (vide supra), except for the equatorial fluorine chemical shift, which is significantly more deshielded in the xenon cation, a trend that was also observed for the $F_5TeN(H)Xe^+$ and $F_5TeNH_3^+$ analogues.[50] The additional fine structure observed on the quintet results from second-order transitions, which were confirmed by spectral simulation.

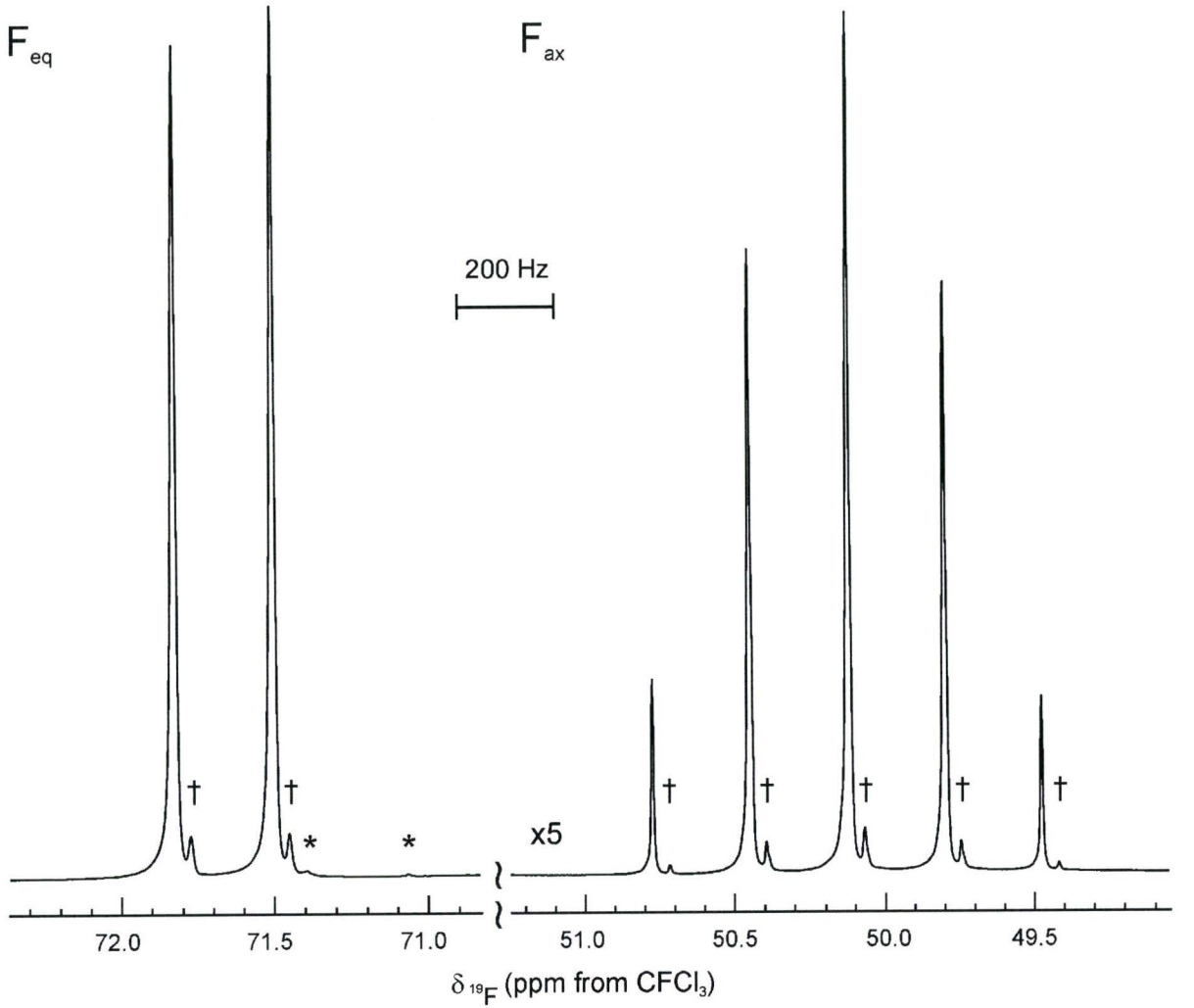

Figure 4.1. ^{19}F NMR spectrum (470.592 MHz) of $F_5SNH_3^+$ in HF solvent at –20 °C; symbols denote the $^1\Delta^{19}F_S(^{34/32}S)$ secondary isotope shift (†), and F_{eq} of $F_5SN(H)Xe^+$ (*).

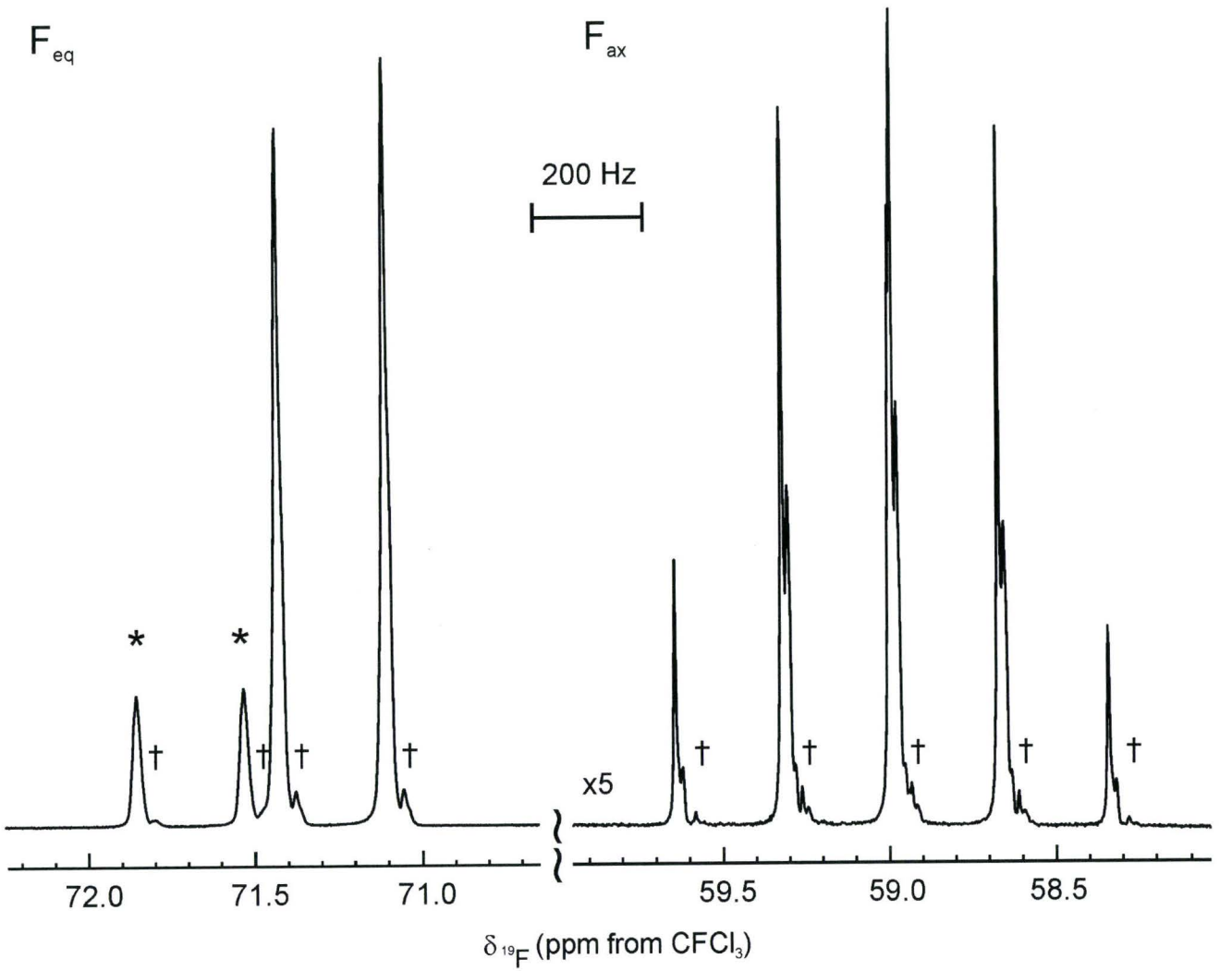

Figure 4.2. The ^{19}F NMR spectrum (470.592 MHz) of $F_5SN(H)Xe^+$ in HF solvent at –20 °C. Symbols denote the secondary isotope shifts, $^1\Delta^{19}F(^{34/32}S)$, on F_{eq} and F_{ax} (†), and on F_{eq} of $F_5SNH_3^+$ (*).

The ^{129}Xe NMR spectrum of $F_5SN(H)Xe^+$ is a singlet [$\Delta\nu_{1/2}$ = 128 (150) Hz] at –2897 (–2956) ppm. The high ^{129}Xe shielding places the Xe–N bond among the most covalent Xe–N bonds,[19] but is considerably less shielded than ^{129}Xe in $C_6F_5Xe^+$ (–3831 ppm, HF solvent, –40 °C).[149] The ^{129}Xe shielding is very similar to that in $F_5TeN(H)Xe^+$ (–2841 ppm, HF solvent, –45 °C, –2902 ppm, BrF_5 solvent, –48 °C),[50] and both $F_5TeN(H)Xe^+$ and $F_5SN(H)Xe^+$ are considerably more shielded than the ^{129}Xe resonances of $(SO_2F)_2NXe^+$ (–1943 ppm, SbF_5 solvent, 25 °C),[49] $F_3S{\equiv}NXeF^+$ (–1652 ppm, HF solvent, –20 °C; –1661 ppm, BrF_5 solvent, –60 °C),[146] isovalent F_5TeOXe^+ (–1472 ppm, SbF_5 solvent, 5 °C),[150] and XeF^+ (–574 ppm, SbF_5 solvent, 25 °C).[151] As in the case of $F_5TeN(H)Xe^+$,[50] the ^{129}Xe shielding may be used as a gauge of L-group electronegativity and Xe–E bond covalency (L is an electronegative ligand and E is a second row ligand atom), and the shielding increases (group electronegativity decreases) with Xe–E bond covalency for the series of LXe^+ cations, that is, Xe–C > Xe–N > Xe–O > Xe–F. The ^{129}Xe–^{14}N coupling is not observed in $F_5SN(H)Xe^+$ because of quadrupolar relaxation of ^{14}N resulting from the low symmetry (high electric field gradient) at the nitrogen nucleus. The broad ^{129}Xe line widths of $F_5SN(H)Xe^+$ recorded at 11.7440 T precluded observation of the long-range couplings to xenon, namely, $^2J(^{129}Xe–^1H)$, $^3J(^{129}Xe–^{19}F_{ax})$, and $^3J(^{129}Xe–^{19}F_{eq})$, which are presumably, in large measure, attributable to relaxation of ^{129}Xe by shielding anisotropy (SA), and also were not observed for $F_5TeN(H)Xe^+$.[50]

The ^{1}H NMR spectrum of $F_5SN(H)Xe^+$ consisted of a singlet at 9.57 ppm in BrF_5 supercooled to –70 °C but the coupling to ^{14}N was not observed, as a result of quadrupolar relaxation. Failure to observe the $^2J(^{129}Xe–^1H)$ coupling is also attributed to broadening of

the ^{129}Xe satellites as a result of a significant SA contribution to T_1 at the high external field strength used to obtain the ^1H NMR spectra.

4.2.3. X-ray Crystal Structure of $[F_5SN(H)Xe][AsF_6]$

A summary of the refinement results and other crystallographic information is provided in Table 4.2. Important bond lengths and angles for $[F_5SN(H)Xe][AsF_6]$ are listed in Table 4.3 along with calculated values for the $F_5SN(H)Xe^+$ and $F_5SNH_3^+$ cations. The $[F_5SN(H)Xe][AsF_6]$ unit cell is isomorphous with that of $[F_5TeN(H)Xe][AsF_6]$[50] and belongs to the $P\bar{1}$ space group. The sulfur analogue has a unit cell volume that is 27.6(6) $Å^3$ smaller than that of the tellurium analogue.

The $F_5SN(H)Xe^+$ cation and the AsF_6^- anion form an ion pair by interaction through a Xe---F–As fluorine bridge (Figure 4.3a) in which the AsF_6^- anion is distorted from O_h to approximate C_{4v} local symmetry. The symmetry lowering experienced by the anion is shown in the crystal structure to be very close to an axial distortion in which the four equatorial As–F bonds are equal to within ±3σ and the As–F bond trans to the elongated bridging As---F bond is equal to the equatorial As–F bonds within ±3σ, thus preserving the 4-fold principal axis. In $[F_5SN(H)Xe][AsF_6]$, the Xe–N (2.069(4) Å) and Xe---F(6) (2.634(4) Å) bond lengths are somewhat longer than their counterparts in $[F_5TeN(H)Xe][AsF_6]$ (2.044(4) and 2.580(3), respectively), while the Xe–N–H, N–Xe---F(6), and S/Te–N–Xe angles are all equal within experimental error, and the As–F(6) bond lengths (1.759(4) Å and 1.740(4) Å, respectively) are similar. The longer Xe–N and Xe---F(6) bond lengths in the sulfur analogue are offset by the expected shorter S–N

Table 4.2. Summary of Crystal Data and Refinement Results for $[F_5SN(H)Xe][AsF_6]$

	$[F_5SN(H)Xe][AsF_6]$
empirical formula	$HAsF_{11}NSXe$
space group (No.)	$P\bar{1}$ (*2*)
a (Å)	5.3248(9)
b (Å)	7.100(1)
c (Å)	11.877(2)
α (deg)	87.551(5)
β (deg)	83.398(5)
γ (deg)	86.278(6)
V (Å^3)	444.8(1)
molecules/unit cell	2
mol. wt. (g mol^{-1})	462.275
calcd. density (g cm^{-3})	3.452
T (°C)	−173
μ (mm^{-1})	7.95
R_1[a]	0.0218
wR_2[b]	0.0481

[a] R_1 is defined as $\Sigma||F_o|-|F_c||/\Sigma|F_o|$ for $I > 2\sigma(I)$
[b] wR_2 is defined as $[\Sigma[w(F_o^2 - F_c^2)^2]/\Sigma w(F_o^2)^2]^{1/2}$ for $I > 2\sigma(I)$.

Table 4.3. Experimental Geometry for $[F_5SN(H)Xe][AsF_6]$ and Calculated Geometries for $F_5SN(H)Xe^+$ and $F_5SNH_3^+$ [a]

	Bond Lengths (Å)				
	$F_5SN(H)Xe^+$ (C_1)			$F_5SNH_3^+$ (C_1)	
		calcd[b]		calcd[c]	
	exptl	MP2	SVWN	MP2	SVWN
Xe(1)–N(1)	2.069(4)	2.065	2.095		
N(1)–S(1)	1.761(4)	1.822	1.805	1.853	1.853
N(1)–H(1)	0.801[d]	1.028	1.042	1.023	1.045
N(1)–H(2)				1.023	1.044
N(1)–H(3)				1.022	1.044
S(1)–F(1)	1.559(3)	1.544	1.548	1.531	1.561
S(1)–F(2)	1.565(3)	1.578	1.589	1.567	1.595
S(1)–F(3)	1.578(3)	1.578	1.583	1.567	1.594
S(1)–F(4)	1.578(3)	1.591	1.596	1.567	1.594
S(1)–F(5)	1.571(3)	1.561	1.569	1.567	1.594
Xe(1)---F(6)	2.634(3)		2.251		

	Bond Angles (°)				
	$F_5SN(H)Xe^+$ (C_1)			$F_5SNH_3^+$ (C_1)	
		calcd[b]		calcd[c]	
	exptl	MP2	SVWN	MP2	SVWN
Xe(1)–N(1)–S(1)	115.3(2)	115.0	113.5		
Xe(1)–N(1)–H(1)	107.2[d]	101.2	101.1		
S(1)–N(1)–H(1)	106.9[d]	104.9	104.5	110.0	109.0
S(1)–N(1)–H(2)				109.2	108.8
S(1)–N(1)–H(3)				109.4	108.7
N(1)–S(1)–F(1)	176.7(2)	177.4	176.6	179.2	179.2
N(1)–S(1)–F(2)	87.4 (2)	86.1	85.7	87.9	88.0
N(1)–S(1)–F(3)	94.0 (2)	89.8	90.3	86.2	86.5
N(1)–S(1)–F(4)	88.5 (2)	91.6	92.2	87.2	87.0
N(1)–S(1)–F(5)	90.7 (2)	86.4	85.9	87.0	87.4
F(1)–S(1)–F(2)	89.6 (2)	92.1	92.0	92.9	92.8
F(1)–S(1)–F(3)	89.0 (2)	91.9	92.1	92.9	92.8
F(1)–S(1)–F(4)	90.2 (2)	90.3	90.4	92.9	92.8
F(1)–S(1)–F(5)	90.5 (2)	91.6	91.6	92.9	92.8
F(2)–S(1)–F(3)	178.4 (2)	175.9	175.9	174.1	174.4
F(2)–S(1)–F(4)	89.2 (2)	89.8	89.9	89.7	89.8
F(2)–S(1)–F(5)	90.5 (2)	90.1	89.9	89.7	89.7
F(3)–S(1)–F(4)	90.0 (2)	89.6	89.8	90.0	90.0
F(3)–S(1)–F(5)	90.2 (2)	90.2	90.3	90.0	89.9
F(4)–S(1)–F(5)	179.2 (2)	178.0	178.1	174.1	174.4

[a] The labels correspond to those used in Figures 4.3a and 4.3b. [b] (SDB-)cc-pVTZ basis set. [c] cc-pVTZ basis set. [d] The hydrogen position was calculated and a riding model was used; therefore no error is given.

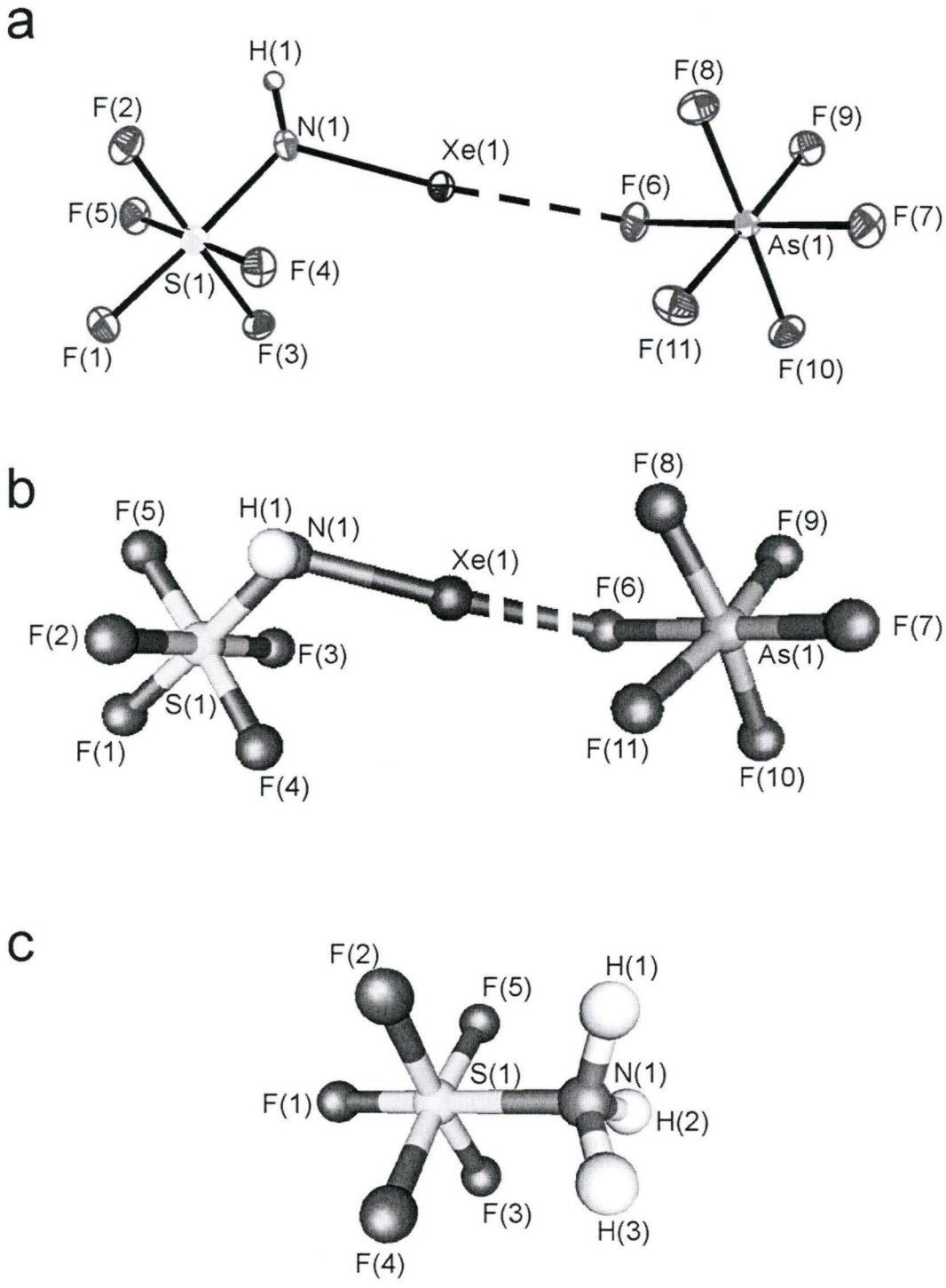

Figure 4.3. (a) X-ray crystal structure of $[F_5SN(H)Xe][AsF_6]$; thermal ellipsoids are shown at the 50% probability level. (b) Calculated geometry of $[F_5SN(H)Xe][AsF_6]$. (c) Calculated geometry of the $F_5SNH_3^+$ cation.

(1.761(4) Å), S–F_{ax} (1.559(3) Å), and average S–F_{eq} (1.573(4) Å) bond lengths when compared with the Te–N (1.982(5) Å), Te–F_{ax} (1.791(4) Å), and average Te–F_{eq} (1.811(5) Å) bond lengths of $[F_5TeN(H)Xe][AsF_6]$ and account for the smaller unit cell volume of the sulfur analogue.

The contributions to the total bond valency of xenon in $[F_5SN(H)Xe][AsF_6]$ and $[F_5TeN(H)Xe][AsF_6]$ have been determined for the Xe–N bond, the Xe---F contact to the AsF_6^- anion of the ion pair, and all long Xe---F contacts that fall within the sum of the xenon and fluorine van der Waals radii (3.63 Å)[31] according to the method described by Brown[152,153] (Table 4.4). The xenon atom in $[F_5SN(H)Xe][AsF_6]$ has six long Xe---F contacts [Xe---F(6A) (3.342 Å), Xe---F(6B) (3.387 Å), Xe---F(5A) (3.271 Å), Xe---F(2A) (3.267 Å), Xe---F(1A) (3.376 Å), and Xe---F(1B) (3.225 Å), (Figure 4.4)], compared to four Xe---F contacts in the tellurium salt, which in the latter case, are somewhat shorter in order to achieve a similar total bond valency at Xe. The longer Xe–N and Xe---F bridge bonds of the sulfur analogue have a bond valency sum at Xe (1.675 v.u.) that is 0.140 bond valence units less than that of the tellurium analogue (1.815 v.u.). The six long Xe---F contacts in the sulfur salt, however, have a bond valency sum that is 0.038 bond valency units greater than the sum for the four long Xe---F contacts of the tellurium analogue (0.148 v.u.). The two additional long contacts in $[F_5SN(H)Xe][AsF_6]$ partly compensate for the loss of bond valency that results from the longer Xe---F bridge and Xe–N bonds. Thus, the total bond valency of Xe in $F_5SN(H)Xe^+$ (1.861 v.u.) is only 0.102 bond valence units less than that of the tellurium salt (1.963 v.u.). These additional long contacts also correlate with closer packing in the $F_5SN(H)Xe^+$ salt, which is manifested by the smaller crystallographic unit

Table 4.4. Calculated Bond Valencies[a] at Xenon in $[F_5SN(H)Xe][AsF_6]$ and $[F_5TeN(H)Xe][AsF_6]$

	$[F_5SN(H)Xe][AsF_6]$		$[F_5TeN(H)Xe][AsF_6]$	
bond	bond length (Å)	bond valence	bond length (Å)	bond valence
Xe–N	2.069	1.485	2.044	1.595
Xe---F_b	2.634	0.190	2.580	0.220
Xe---F_{lc}	3.225	0.039	3.169	0.045
	3.267	0.034	3.260	0.035
	3.271	0.034	3.265	0.035
	3.342	0.028	3.281	0.033
	3.376	0.026		
	3.387	0.025		
Total Bond Valence		1.861		1.963

[a] Values calculated as described in Appendix 1 of ref 152 using the Bond Valence Calculator program (Hormillosa, C.; Healy, S.; Stephen, T., *Bond Valence Calculator*, version 2.00; McMaster University; Hamilton, ON, 1993.) with empirical parameters R_0 = 2.02 and 2.2075, and B = 0.37 and 0.35, for Xe---F and Xe–N, respectively. Empirical parameters for Xe–N were calculated as described in ref 153, using R_0 = 2.05 for Xe–O. Fluorine atom contacts considered in the bond valence calculations for xenon are F_b of the Xe---F–As fluorine bridge and those making long contacts with xenon, denoted by F_{lc}.

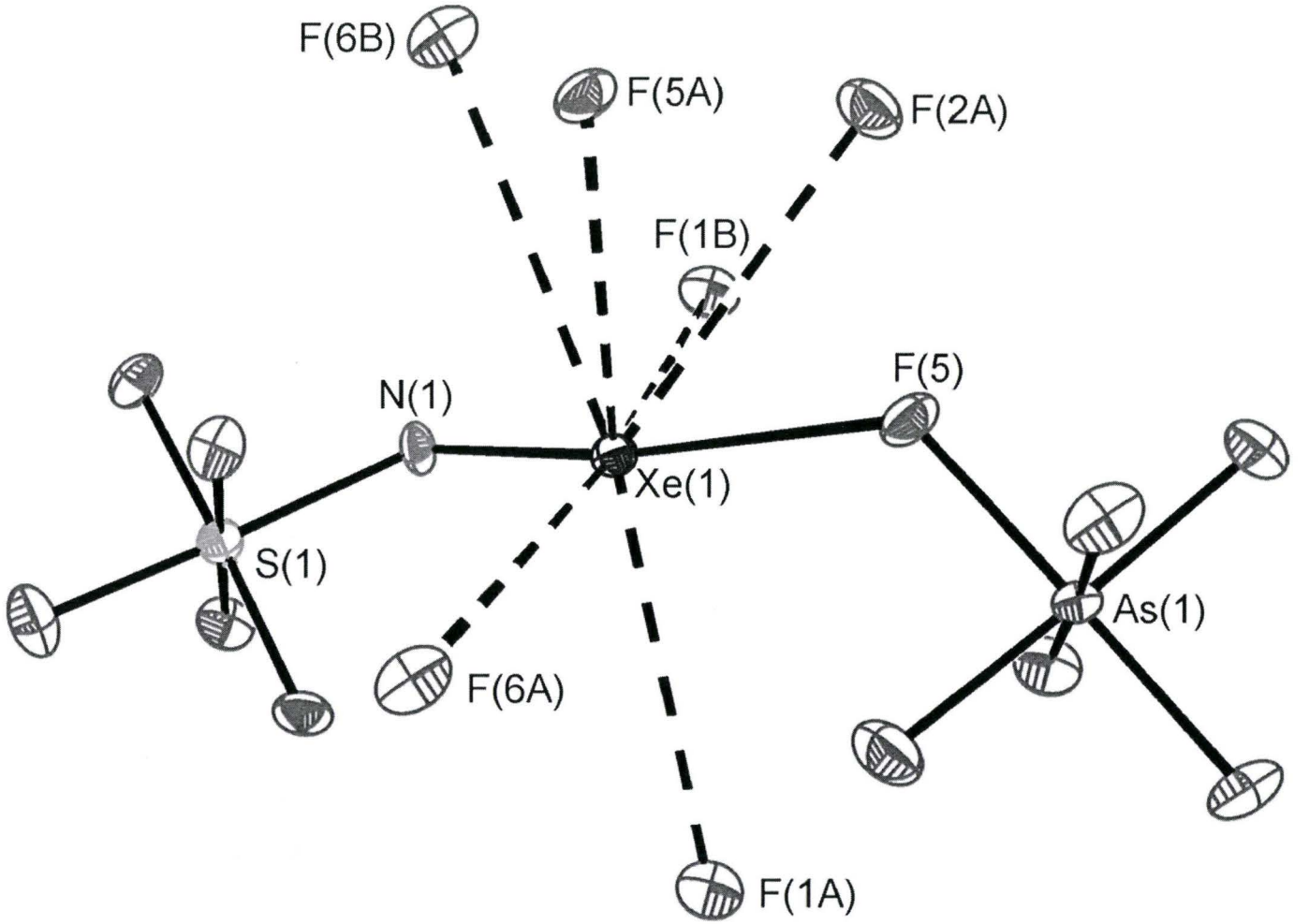

Figure 4.4. View of $[F_5SNH_3][AsF_6]$ showing the closest Xe---F contacts with neighbouring AsF_6^- anions, which were considered in the bond valence calculations.

cell volume observed for this salt. The fluorine contacts to xenon in $F_5SN(H)Xe^+$ avoid the torus of electron density around xenon(II).[40] These contacts may also contribute to distortion of the N–Xe---F angle from the expected linear AX_2E_3 VSEPR arrangement; however, a similar deviation from linearity was obtained in the energy-minimized gas-phase geometries (Table 4.5, see section 4.2.5.), and for F–Ng---F (Ng = Xe, Kr) in $Kr_2F_3^+$,[65] $Xe_2F_3^+$,[28] and $[KrF][MF_6]$ (M = As, Sb, or Bi)[65] and therefore may not be wholly attributable to crystal packing. The Xe---F(6)–As bridge bond angle (127.2(1)°) is comparable to that in $[F_5TeN(H)Xe][AsF_6]$ (128.1(2)°),[50] and is consistent with the bent geometry predicted by the VSEPR model and with the observed range of Ng---F–As (Ng = Xe, Kr) angles in $[XeF][AsF_6]$ (134.8(2)°),[133] $HF{\cdot}[HO\text{-}TeF_4\text{-}OXe][AsF_6]$ (133.0(4)°),[154] $[KrF][AsF_6]$ (133.7(1)°),[65] $[Kr_2F_3][AsF_6]{\cdot}[KrF][AsF_6]$ (127.5(3)°),[65] and $[C_6F_5Xe][AsF_6]$ (128.7(3)° and 126.4(3)°).[155]

4.2.4. Raman Spectroscopy

The Raman spectra of $[F_5SNH_3][AsF_6]$ (Figure 4.5) and $[F_5SN(H)Xe][AsF_6]$ (Figure 4.6) were assigned by comparison with those of $F_5TeNH_3^+$,[50] $F_5TeN(H)Xe^+$,[50] F_5TeOXe^+,[150,156] SF_6,[157,158] and F_5SCl[159] (Tables 4.6 and 4.7), and by comparison with the calculated frequencies derived for the gas-phase energy-minimized geometries of $F_5SNH_3^+$, $F_5SN(H)Xe^+$, and the $[F_5SN(H)Xe][AsF_6]$ ion pair (see section 4.2.5.). The vibrational modes of the uncoordinated AsF_6^- anion were assigned by comparison with those of $[O_2][AsF_6]$,[160] $[HC{\equiv}NXeF][AsF_6]$,[35] $[F_3S{\equiv}NXeF][AsF_6]$,[146] and $[F_5TeNH_3][AsF_6]$[50] and the modes of the distorted fluorine-bridged AsF_6^- anion were assigned by comparison with

Table 4.5. Experimental and Calculated (C_1) Geometries for the $[F_5SN(H)Xe][AsF_6]$ Ion Pair[a]

Bond Lengths (Å)		
	exptl	calcd[b]
Xe(1)--F(6)	2.634(3)	2.251
Xe(1)–N(1)	2.069(4)	2.111
N(1)–S(1)	1.761(4)	1.723
N(1)–H(1)[c]	0.801	1.032
S(1)–F(1)	1.559(3)	1.578
S(1)–F(2)	1.565(3)	1.601
S(1)–F(3)	1.578(3)	1.592
S(1)–F(4)	1.578(3)	1.611
S(1)–F(5)	1.571(3)	1.583
As(1)–F(6)	1.759(3)	1.919
As(1)–F(7)	1.716(3)	1.689
As(1)–F(8)	1.733(3)	1.734
As(1)–F(9)	1.722(3)	1.736
As(1)–F(10)	1.715(3)	1.699
As(1)–F(11)	1.713(3)	1.699

Bond Angles (°)					
	exptl	calcd[b]		exptl	calcd[b]
Xe(1)–N(1)–S(1)	115.3(2)	115.5	F(6)--Xe(1)–N(1)	171.6(1)	175.3
Xe(1)–N(1)–H(1)[c]	107.2	103.8	Xe(1)--F(6)–As(1)	127.2 (1)	112.7
S(1)–N(1)–H(1)[c]	106.9	105.7	F(6)–As(1)–F(7)	178.7 (1)	177.1
N(1)–S(1)–F(1)	176.7(2)	178.2	F(6)–As(1)–F(8)	88.0 (1)	83.7
N(1)–S(1)–F(2)	87.4 (2)	89.4	F(6)–As(1)–F(9)	89.3 (1)	83.6
N(1)–S(1)–F(3)	94.0 (2)	90.9	F(6)–As(1)–F(10)	89.3 (1)	86.0
N(1)–S(1)–F(4)	88.5 (2)	93.9	F(6)–As(1)–F(11)	88.6 (1)	86.0
N(1)–S(1)–F(5)	90.7 (2)	89.5	F(7)–As(1)–F(8)	90.8 (1)	94.2
F(1)–S(1)–F(2)	89.6 (2)	89.8	F(7)–As(1)–F(9)	91.3 (1)	94.2
F(1)–S(1)–F(3)	89.0 (2)	89.9	F(7)–As(1)–F(10)	91.9 (1)	96.0
F(1)–S(1)–F(4)	90.2 (2)	87.8	F(7)–As(1)–F(11)	90.8 (1)	96.1
F(1)–S(1)–F(5)	90.5 (2)	88.8	F(8)–As(1)–F(9)	89.2 (1)	87.2
F(2)–S(1)–F(3)	178.4 (2)	179.7	F(8)–As(1)–F(10)	177.2 (1)	169.5
F(2)–S(1)–F(4)	89.2 (2)	89.8	F(8)–As(1)–F(11)	89.7 (1)	89.8
F(2)–S(1)–F(5)	90.5 (2)	89.9	F(9)–As(1)–F(10)	91.3 (1)	89.8
F(3)–S(1)–F(4)	90.0 (2)	90.0	F(9)–As(1)–F(11)	177.6 (1)	169.5
F(3)–S(1)–F(5)	90.2 (2)	90.3	F(10)–As(1)–F(11)	90.9 (1)	91.4
F(4)–S(1)–F(5)	179.2 (2)	176.6			

[a] The labels correspond to those used in Figure 4.3. [b] SVWN/(SDB-)cc-pVTZ level of theory. [c] The bond length and angles do not have an error because the hydrogen position was calculated and a riding model was used.

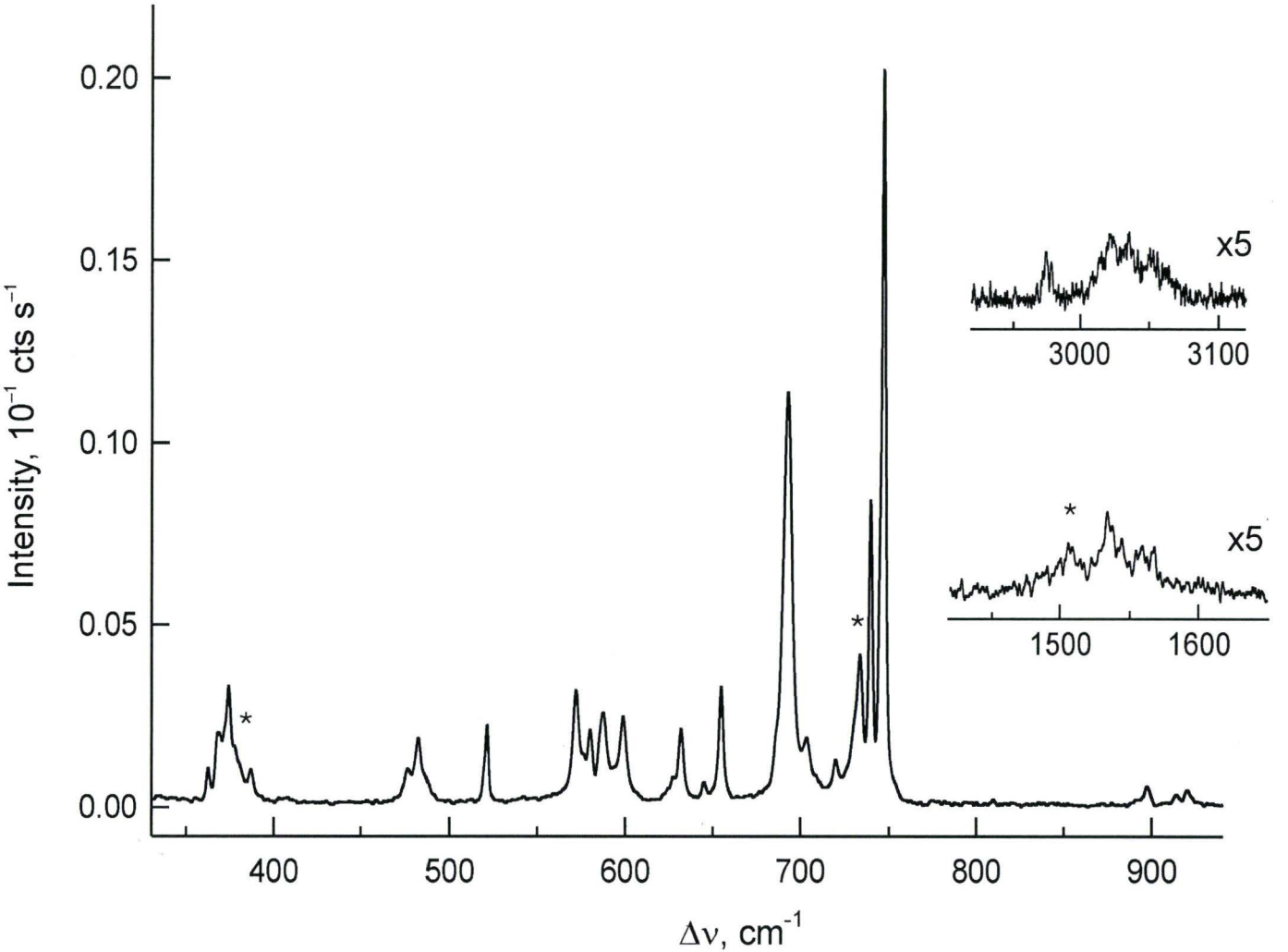

Figure 4.5. Raman spectrum of $[F_5SNH_3][AsF_6]$ recorded at –160 °C using 1064-nm excitation; symbols denote FEP sample tube lines (*).

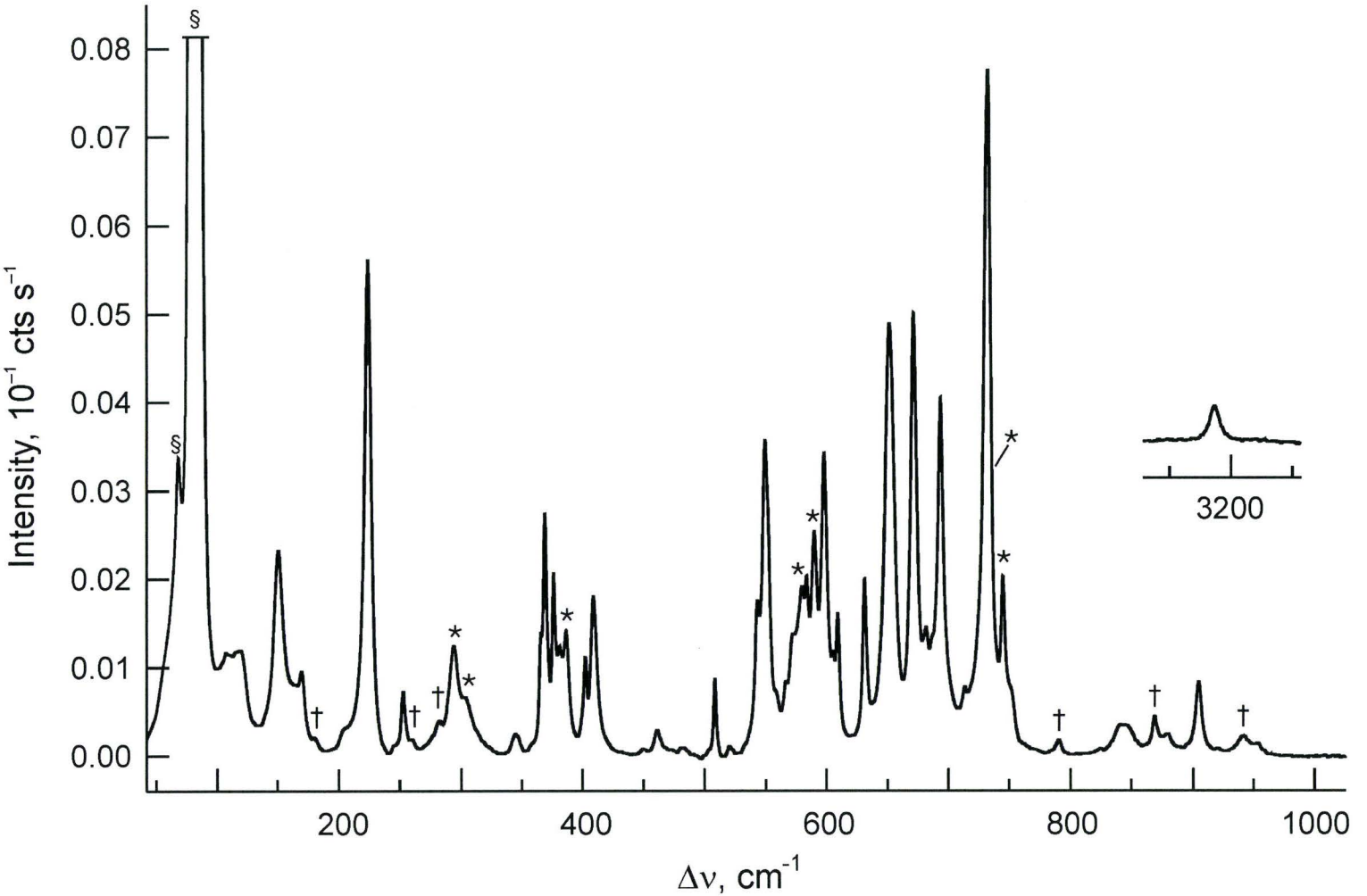

Figure 4.6. Raman spectrum of $[F_5SN(H)Xe][AsF_6]$ recorded at –45 °C using 1064-nm excitation; symbols denote FEP sample tube lines (*) and an instrumental artifact (§).

Table 4.6. Raman Vibrational Frequencies, Intensities, and Assignments for $[F_5SNH_3][AsF_6]$, and Calculated Vibrational Frequencies and Intensities for $F_5SNH_3^+$

freq, cm^{-1}							
$[F_5SNH_3][AsF_6]$	$F_5SNH_3^+$ calcd[b]				assgnts[c]		
exptl[a]	MP2		SVWN		$F_5SNH_3^+$ (C_1)	AsF_6^- (O_h)	
3138 (2) br	3524	(20) [163]	3310	(26) [178]	ν(NH2 – NH3)		
3072 (2) br	3521	(20) [163]	3307	(27) [178]	ν(NH2 + NH3) – ν(NH1)		
2939 (2) br	3402	(60) [103]	3191	(64) [110]	ν(NH1 + NH2 + NH3)		
1560 (2) br	1641	(3) [40]	1569	(4) [43]	ρ_t(H2NH3) + δ(NH1) wag – o.o.p.		
1535 (3) br	1633	(3) [42]	1552	(4) [43]	δ(H2NH3) + δ(NH1) wag – i.p.		
n.o.	1449	(<1) [163]	1360	(<1) [169]	δ(NH_3) inv		
n.o.	1066	(<1) [261]	1023	(<1) [256]	ν(SF4 – SF5) – NH_3 rock		
n.o.	1064	(<1) [261]	1022	(<1) [256]	ν(SF2 – SF3) – NH_3 rock		
920 (2)	970	(<1) [345]	924	(1) [295]	ν(SF1)		
914 (2)	914	(1) [115]	870	(1) [91]	ν(SF4 – SF5) + NH_3 rock		
898 (3)	914	(1) [114]	868	(1) [90]	ν(SF2 – SF3) + NH_3 rock		
747 (100)							
745 sh	757	(14) [5]	697	(19) [1]	ν(SF2 + SF3) + ν(SF4 + SF5) + ν(SN)		
739 (42)							
720 (7)							
704 (10)						ν_1 (A_{1g})	
693 (57)							
655 (16)							
645 (3)	669	(3) [<1]	642	(4) [<1]	ν(SF2 + SF3) – ν(SF4 + SF5)		
632 (11)							
628 sh	613	(1) [94]	563	(4) [50]	δ(SF_{4eq}) o.o.p.		
599 (12)							
587 (13)						ν_2 (E_g)	
580 (11)							
576 sh	574	(<1) [19]	508	(4) [23]	ν(SN) + δ(F2SF3) + δ(F4SF5)		
572 (16)	574	(<1) [19]	505	(<1) [14]	δ(F1SN) + δ(F2SF3)		
521 (11)	527	(2) [<1]	504	(2) [18]	δ(F1SN) + δ(F4SF5)		

Table 4.6. (continued…)

518 sh		518	(8) [1]	464	(2) [<1]	δ(F3SF4) + δ(F2SF5)	
487 sh 482 (10) 476 (3)	}	458 456	(1) [<1] (1) [<1]	404 402	(1) [1] (1) [1]	δ(F1SF5) + δ(F4SN) δ(F1SF2) + δ(F5SN)	
387 (5)							ν_4 (T_{1u})
378 sh 374 (17)	}						ν_5 (T_{2g})
368 sh 362 (5)	}	330 320 316	(<1) [<1] (<1) [9] (<1) [10]	293 286 282	(<1) [<1] (<1) [10] (1) [10]	δ(F2SF3) – δ(F4SF5) δ(F1SN) o.o.p. δ(F1SN) i.p.	
n.o.		4	(<1) [1]	18	(<1) [1]	NH_3 torsion	

[a] Values in parentheses denote experimental relative Raman intensities, abbreviations denote broad (br), shoulder (sh) and not observed (n.o.). [b] cc-pVTZ basis set. Calculated infrared intensities (in km mol^{-1}) are given in brackets, calculated Raman intensities (in $Å^4$ amu^{-1}) are given in parentheses. [c] The atom numbering corresponds to that used in Figure 2c, abbreviations denote out of plane (o.o.p.) and in plane (i.p.), where the plane is defined by the S, N, H1 atoms; inversion (inv); twist (ρ_t); and four equatorial fluorines (F_{4eq}).

Table 4.7. Raman Vibrational Frequencies, Intensities and Assignments for $[F_5SN(H)Xe][AsF_6]$, and Calculated Vibrational Frequencies and Intensities for $F_5SN(H)Xe^+$

freq, cm^{-1}						
$[F_5SN(H)Xe][AsF_6]$	$F_5SN(H)Xe^+$					
	calcd[b]				assgnts[c]	
exptl[a]	MP2		SVWN		$F_5SN(H)Xe^+$ (C_1)	AsF_6^- (C_{4v})
3186 (7)	3421	(38) [92]	3287	(40) [103]	ν(NH)	
n.o.	1328	(<1) [25]	1230	(1) [28]	δ(NH) wag – i.p.	
954 (2) br	980	(1) [277]	946	(5) [227]	δ(SNH)	
904 (14)	952	(2) [253]	921	(3) [261]	ν(SF4 – SF5) + ν(SF1)	
879 (4)	936	(2) [395]	902	(11) [303]	ν(SF2 – SF3) + ν(SF1)	
844 (6) br	888	(2) [145]	856	(5) [135]	δ(NH) wag – o.o.p.	
732 (58)	737	(7) [8]	701	(8) [5]	ν(SF2 + SF3) + ν(SF4 + SF5) + ν(SN)	
714 (10)						ν_8 (E)
693 (69)						
681 (22)						ν_1 (A_1)
671 (86)	661	(16) [10]	627	(4) [2]	ν(SF2 + SF3) – ν(SF4 + SF5)	
651 (83)	650	(4) [3]	586	(37) [>1]	ν(XeN) – ν(SN)	
631 (32)	606	(1) [130]	577	(4) [134]	$\delta(SF_{4eq})$ o.o.p.	
609 (26)						ν_2 (A_1)
598 (59)						ν_5 (B_1)
549 (61)	595	(2) [12]	566	(1) [13]	δ(F2SF3) + δ(NSF4) – δ(F1SF5)	
543 (29)	574	(<1) [18]	538	(1) [14]	δ(F1SF4) – δ(F3SF5)	
520 (4) br	535	(5) [13]	512	(3) [10]	ν(XeN) + ν(SN) + δ(F1SF4) + δ(F3SF4) – δ(F2SF5)	
508 (17)	511	(1) [<1]	479	(2) [<1]	δ(F3SF5) + δ(F2SF4)	
461 (4) br			420	(17) [109][d]	ν(Xe--F6)[d]	
409 (33)	446	(1) [6]	415	(<1) [6]	ρ_t(F1SN) + ρ_w(F2SF4) – ρ_w(F3SF5)	ν_4 (A_1)
402 (20)						ν_3 (A_1)
376 (37)						ν_7 (B_2)
369 (49)						ν_9 (E)
366 (24)	407	(2) [3]	382	(2) [4]	δ(F1SN) + ρ_w(F2SF5) – ρ_w(F3SF4)	
345 (4) br	338	(<1) [1]	316	(<1) [1]	ρ_t(F2SF5) – ρ_t(F3SF4)	
252 (13)	285	(1) [4]	254	(1) [4]	δ(F1SN) o.o.p.	

Table 4.7. (continued…)

224 (100)	222	(3) [<1]	207	(4) [<1]	ν(XeN) + $\rho_r(SF_5)$
169 (14)			156	(1) [8][d]	coupled deformation mode of $[F_5SN(H)Xe][AsF_6]$[d]
151 (37)	136	(1) [1]	125	(2) [1]	δ(XeNS)
119 (14)			105	(1) [1][d]	coupled deformation modes of $[F_5SN(H)Xe][AsF_6]$[d]
108 (14)			76	(1) [1][d]	
n.o.	56	(1) [1]	45	(2) [1]	torsion about Xe

[a] Values in parentheses denote experimental relative Raman intensities, abbreviations denote broad (br) and not observed (n.o.). [b] (SDB-)cc-pVTZ basis set. Calculated infrared intensities (in km mol^{-1}) are given in brackets, calculated Raman intensities (in $Å^4$ amu^{-1}) are given in parentheses. [c] Atom numbering corresponds to that used in Figure 2b, abbreviations denote in plane (i.p.) and out of plane (o.o.p.), where the plane is defined by Xe, N, S atoms; twist (ρ_t); wag (ρ_w); rock (ρ_r); and four equatorial fluorines (F_{4eq}). [d] Values and mode descriptions are from the calculated ion pair; see Table S3 for a full frequency listing and assignments.

those of $[F_5TeN(H)Xe][AsF_6]$,[50] $[F_5TeOXe][AsF_6]$,[156] $[XeF][AsF_6]$,[112] and $KrF][AsF_6]$.[109] Calculated frequencies appearing in parentheses were obtained at the MP2/SVWN levels, respectively, except for the ion pair, which could only be optimized at the SVWN level (Table 4.8). The vibrational frequencies of SF_6 and F_5SCl were chosen as benchmarks for the F_5S-group frequencies of $F_5SNH_3^+$ and $F_5SN(H)Xe^+$ (Table 4.9, see section 4.2.5.).

4.2.4.1. $[F_5SNH_3][AsF_6]$.

In the absence of a refined crystal structure, it was not possible to carry out a factor-group analysis which might account for the splittings observed on the majority of the cation and anion Raman bands. The 24 vibrational modes of $F_5SNH_3^+$ were assigned under C_1 point symmetry and belong to A irreducible representations, all of which are Raman- and infrared-active. The 15 vibrational modes of AsF_6^- were assigned under O_h symmetry and belong to the irreducible representations $A_{1g} + E_g + T_{2g} + 2T_{1u} + T_{2u}$, where the A_{1g}, E_g, and T_{2g} modes are Raman active and the T_{1u} modes are infrared active. The formally Raman inactive T_{1u} mode was, however, observed in the Raman spectrum as a weak band at 387 cm^{-1}.

The asymmetric NH_3 stretches at 3138 (3524/3310) and 3072 (3521/3307) cm^{-1}, the symmetric NH_3 stretch at 2939 (3402/3191) cm^{-1}, and the NH_3 bends at 1560 (1641/1569) and 1535 (1633/1552) cm^{-1} were overestimated by the calculations, which was also observed for $F_5TeNH_3^+$.[50] The S–N stretch couples with the equatorial SF_4 in-phase breathing mode at 739, 745, 747 cm^{-1} (757/697 cm^{-1}) and with the equatorial SF_4 out-of-phase, out-of-plane bend at 576 cm^{-1} (574/508 cm^{-1}), contrasting with the Te–N

Table 4.8. Experimental (Raman) and Calculated Vibrational Frequencies, Intensities, and Assignments for the $[F_5SN(H)Xe][AsF_6]$ Ion Pair

freq, cm^{-1}		assgnts		
exptl[a]	calcd[b]	$F_5SN(H)Xe^+AsF_6^-$ (C_1)[c]		
3186 (7)	3384 (56) [79]	ν(NH)		
n.o.	1247 (2) [38]	NH wag i.p.		
954 (2) br	912 (19) [368]	δ(SNH)		
904 (14)	889 (3) [246]	ν(SF4 – SF5) + ν(SF3 – SF2)		
879 (4)	871 (10) [376]	ν(SF1) + ν(SF2 – SF3)		
844 (6) br	794 (8) [124]	NH wag o.o.p.		
732 (58)	713 (14) [26]	ν(SF2 + SF3) + ν(SF4 + SF5) + ν(SN) + ν(SF1) small		
714 (10) 693 (69)	752 (7) [137]	ν(AsF9 – AsF11) + ν(AsF8 – AsF10) + ν(AsF7)	}	[ν_3 (T_{1u})]
	749 (3) [131]	ν(AsF9 – AsF11) + ν(AsF10 – AsF8)		
	745 (7) [190]	ν(AsF7)		
681 (22)	655 (14) [40]	ν(AsF_{4eq})		[ν_1 (A_{1g})]
671 (86)	606 (3) [6]	ν(SF2 + SF3) – ν(SF4 + SF5)		
651 (83)	629 (75) [15]	ν(XeN) – ν(SN)		
631 (32)	580 (1) [78]	δ(SF_{4e}) o.o.p.		
609 (26)	590 (2) [11]	ν(AsF9 + AsF11) – ν(AsF8 + AsF10)	}	[ν_2 (E_g)]
598 (59)	410 (2) [7]	ν(As--F6)		
549 (61)	574 (8) [12]	δ(NSF4) + δ(F2SF3) – δ(F1SF5)		
543 (29)	539 (1) [12]	δ(F1SF2) – δ(F2SF3)		

Table 4.8. (continued…)

520 (4) br	522 (7) [1]	ν(XeN) + ν(SN) + δ(F1SF4) + δ(F3SF4) – δ(F2SF5)	
508 (17)	463 (1) [<1]	δ(F3SF5) + δ(F2SF4)	
461 (4) br	420 (17) [109]	ν(Xe--F6)	
409 (33)	432 (1) [22]	ρ_t(F1SN) + ρ_w(F2SF4) – ρ_w(F3SF5)	
402 (20)	374 (1) [41] 371 (6) [29] 363 (1) [25]	AsF_6^- deformation modes	[ν_4 (T_{1u})]
376 (37) 369 (49)	341 (1) [257] 321 (1) [<1] 268 (2) [48]	AsF_6^- deformation modes	[ν_5 (T_{2g})]
366 (24)	377 (12) [30]	δ(F1SFN) + ρ_w(F2SF5) – ρ_w(F3SF4)	
345 (4) br	327 (1) [3]	ρ_t(F2SF5) – ρ_t(F3SF4)	
252 (13)	284 (1) [4]	δ(F1SN) o.o.p. + ρ_r(F2SF5) – ρ_r(F3SF4)	
n.o. 224 (100) n.o.	227 (<1) [<1] 217 (13) [20] 196 (<1) [<1]	ν(XeN) + $\rho_r(SF_5)$ + AsF_6^- deformation modes	[ν_6 (T_{2u})]
169 (14)	156 (1) [8]	coupled deformation modes of $F_5SN(H)Xe^+$ and AsF_6^-	
151 (37)	124 (5) [3]	δ(XeNS)	

Table 4.8. (continued…)

119 (14)	105 (1) [1]	coupled deformation modes of $F_5SN(H)Xe^+$ and AsF_6^-
108 (14)	76 (1) [1]	
n.o.	60 (1) [2]	
n.o.	35 (<1) [1]	
n.o.	29 (<1) [1]	
n.o.	8 (<1) [1]	

[a] Values in parentheses denote experimental Raman intensities, abbreviations denote broad (br) and not observed (n.o.). [b] SVWN/(SDB-)cc-pVTZ level of theory. Calculated infrared intensities (in km mol^{-1}) are given in brackets, calculated Raman intensities (in $Å^4$ amu^{-1}) are given in parentheses. [c] Abbreviations denote in plane (i.p.), out of plane (o.o.p.) where the plane is defined by Xe, N, S atoms, twist (ρ_t), wag (ρ_w) and rock (ρ_r), and four equatorial fluorines (F_{4eq}); atom numbering corresponds to Figure 4.3; anion mode assignments in brackets indicate those corresponding to an octahedral geometry.

Table 4.9. Experimental and Calculated Geometrical Parameters, Vibrational Frequencies and NBO Parameters for SF_6 (O_h) and SF_5Cl (C_{4v})

SF_6	exptl	MP2[a]	SVWN[a]		
Bond Lengths (Å)[b]					
S–F	1.5622(7)	1.572	1.578		
Frequencies (cm^{-1})[c]				assgnts[d]	
	940 (n.o.) [n.o.]	971 (0) [430]	941 (0) [405]	$\nu_{as}(SF - SF)$	(T_{1u})
	773.5 (vs) [n.o.]	778 (15) [0]	746 (16) [0]	$\nu_s(SF_6)$	(A_{1g})
	641.7 (s) [n.o.]	655 (3) [0]	632 (3) [0]	$\nu_{as}(SF_2) - \nu(SF_4)$	(E_g)
	615 (n.o.) [n.o.]	613 (0) [29]	577 (0) [25]	$\nu(SF_4)$ o.o.p.	(T_{1u})
	525 (s) [n.o.]	519 (2) [0]	488 (2) [0]	$\delta(SF_2) + \delta(SF_2)$	(T_{2g})
	347 (n.o.) [n.o.]	346 (0) [0]	326 (0) [0]	$\rho_w(SF_2) - \rho_w(SF_2)$	(T_{2u})
Charges					
S		2.69	2.58		
F		–0.45	–0.43		
Valencies					
S		3.63	3.88		
F		0.48	0.54		
Bond Orders					
S–F		0.61	0.65		

Table 4.9. (continued…)

SF_5Cl	exptl	MP2 [a]	SVWN [a]		
Bond Lengths (Å)[e]					
$S–F_a$	1.588(9)	1.576	1.581		
$S–F_e$	1.566(3)	1.582	1.588		
S–Cl	2.047(3)	2.059	2.064		
Frequencies (cm^{-1})[e]				assgnts	
	909.0	935 (<1) [356]	907 (<1) [337]	$\nu_{as}(SF_{4eq})$	E
	854.6	871 (1) [455]	842 (1) [421]	$\nu(SF_a)$	A_1
	707.1	716 (14) [19]	688 (15) [11]	$\nu_s(SF_{4eq})$	A_1
	625	639 (3) [<<1]	617 (3) [<<1]	$\nu(SF_{4eq})$	B_1
	601.9	603 (1) [86]	572 (1) [84]	$\delta(SF_{4eq})$ o.o.p.	A_1
	579.0	577 (<1) [16	544 (<1) [14]	$\rho_w(SF_{4eq})$	E
	505	501 (2) [0]	471 (2) [0]	$\delta(SF_{4eq})$ i.p.	B_2
	441.0	440 (2) [1]	413 (2) [1]	$\rho(SF_{4eq})$ i.p.	E
	401.7	411 (9) [5]	387 (9) [5]	$\nu(SCl)$	A_1
	n.o.	338 (<<1) [0]	316 (<<1) [0]	$\rho(SF_{4eq})$ o.o.p.	B_1
	271	269 (1) [<<1]	250 (1) [<<1]	$\rho_w(SCl)$	E

Table 4.9. (continued…)

Charges		
S	2.43	2.33
F_a	–0.45	–0.44
F_e	–0.45	–0.43
Cl	–0.17	–0.15
Valencies		
S	3.56	3.79
F_a	0.47	0.52
F_e	0.46	0.52
Cl	0.50	0.52
Bond Orders		
S–F_a	0.60	0.64
S–F_e	0.59	0.63
S–Cl	0.62	0.64

[a] (SDB-)cc-pVTZ basis set. [b] Experimental value for the bond length is from *J. Chem. Phys.* **1981**, *75*, 5326–5328. [c] Experimental values for the Raman data are from ref 157, and for infrared data, from ref 158. [d] Abbreviations denote very strong (vs), strong (s), not observed (n.o.) and wag (ρ_w). [e] Experimental values for the bond lengths and for Raman data are from ref 159.

stretch of $F_5TeNH_3^+$, which is not significantly coupled. The out-of-phase trans equatorial SF_2 stretching modes are coupled to NH_3 rocking modes, whereas the axial S–F stretch is not coupled. All of the bands involving S–F stretches fall into the range 645–920 cm^{-1} (669–970/642–924 cm^{-1}) and those involving SF_5 bending modes fall into the range 362–632 cm^{-1} (316–613/282–563 cm^{-1}) which have frequencies similar to those of SF_6 (615–940 and 347–525 cm^{-1}) and F_5SCl (602–909 and 271–579 cm^{-1}).[159] The NH_3 torsion, predicted at (4/18 cm^{-1}), could not be observed.

4.2.4.2. $[F_5SN(H)Xe][AsF_6]$

The $F_5SN(H)Xe^+$ cation (calculated gas-phase and crystallographic symmetries optimized to C_1 symmetry) possesses 21 fundamental vibrational modes belonging to A irreducible representations which are both Raman- and infrared-active. The fluorine bridge interaction lowered the O_h symmetry of the anion (see section 4.2.3.) so that additional lines in the vibrational spectra were observed. Such symmetry lowering in hexafluoro anions of group 15 is oftentimes approximated as C_{4v} symmetry,[112] and the vibrational spectra are assigned under this or a lower symmetry (C_{2v}, C_s, or C_1). The distorted anion in the structural unit possesses 15 fundamental vibrational modes under approximate C_{4v} symmetry belonging to the irreducible representations, $4A_1 + 2B_1 + B_2 + 4E$, all of which are Raman-active and the A_1 and E modes are infrared-active. In practice, 9 of the 11 vibrational bands expected were observed (correlations to O_h symmetry are given in square brackets), namely, 681 (A_1) and 693, 714 (E) [T_{1u}], 598 (B_1) and 609 (A_1) [E_g], 402 (A_1) and 409 (A_1) [T_{1u}], and 369 (E) and 376 (B_2) [T_{2g}] cm^{-1}. Factor-group analyses correlating the

cation (C_1) and anion (C_{4v}) symmetries to their crystal site symmetries (C_1) and to the unit cell symmetry (C_i) are provided in Table 4.10. The A irreducible representations of the cation are maintained under C_1 site symmetry, while the doubly degenerate E modes of the anion are split as a result of site symmetry lowering. Both the cation and anion modes are split into Raman-active A_g and infrared-active A_u components under C_i crystal symmetry, giving the potential to observe 21 bands for the cation and 15 bands for the anion. As predicted, no additional splittings of the 19 observed cation bands and 11 observed anion bands occurred in the Raman spectrum under the crystal symmetry.

The calculated vibrational frequencies for the $[F_5SN(H)Xe][AsF_6]$ ion pair and for the isolated $F_5SN(H)Xe^+$ and AsF_6^- ions are generally in good agreement with the experimental frequencies. The ion pair calculation shows that the cation and anion modes are not coupled except for the low-frequency deformation modes. The modes associated with the Xe---F–As bridge are, however, deemed to be less reliable because the geometrical parameters of the Xe---F–As bridge are not well reproduced for the calculated ion pair (see section 4.2.5.).

Coupled ν(SN + XeN) and ν(SN – XeN) stretches were observed at 520 and 651 (535/512 and 650/586) cm^{-1}, respectively, compared with the coupled ν(TeN + XeN) and ν(TeN – XeN) stretches observed for $F_5TeN(H)Xe^+$ at 444 and 654 cm^{-1}.[50] The most intense band in the Raman spectrum of $[F_5SN(H)Xe][AsF_6]$ occurs at 224 (222/207) cm^{-1} and is assigned to the Xe–N stretch weakly coupled to a F_5S-group rock, whereas the corresponding low-frequency coupled mode was not observed for the tellurium analogue. Weak coupling between the Xe–N and a F_5S-group rock of $F_5SN(H)Xe^+$ may be the result

Table 4.10. Correlation Diagrams and Selection Rules for the Vibrational Modes of $[F_5SN(H)Xe][AsF_6]$

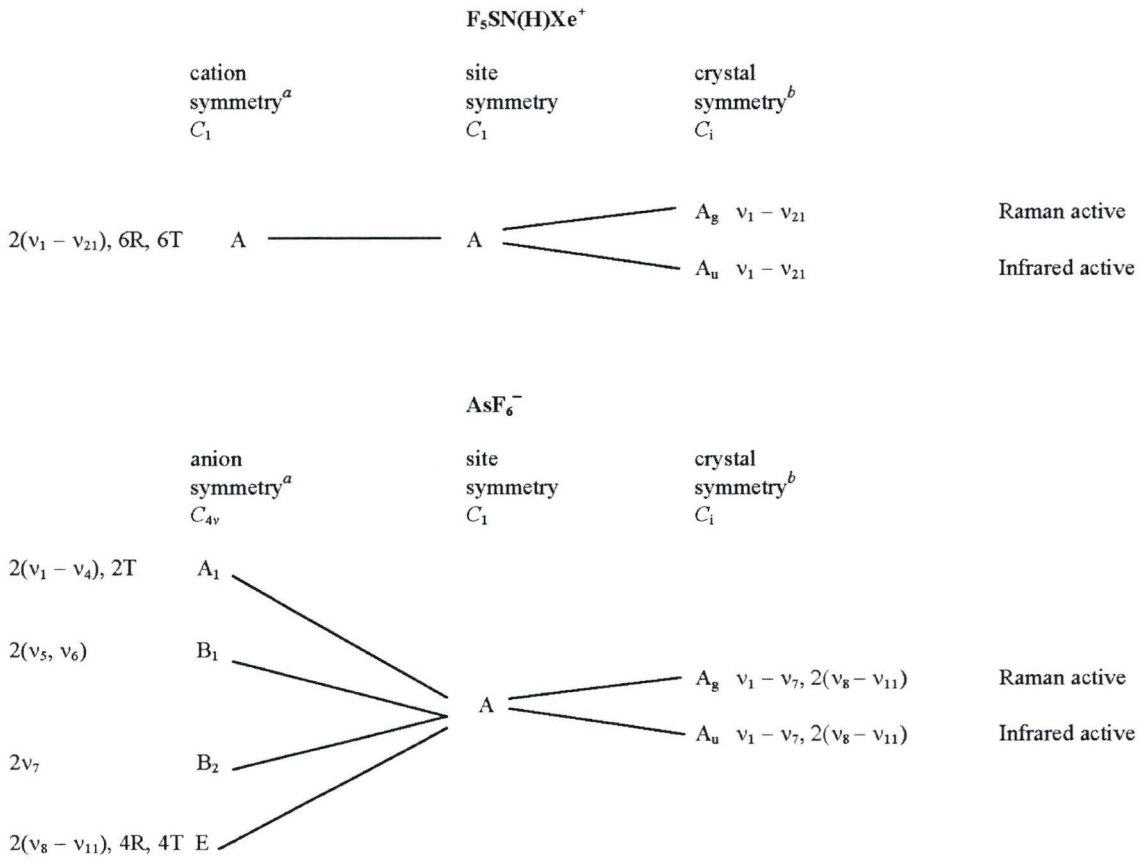

[a] The cation (C_1) and anion (C_{4v}) symmetries are local symmetries taken from the crystallographic structural unit. The modes associated with the Xe---F–As bridge interaction are not accounted for in this treatment. The irreducible representations are $\Gamma = 21A$ for the $F_5SN(H)Xe^+$ cation and $\Gamma = 4A_1 + 2B_1 + B_2 + 4E$ for the AsF_6^- anion. [b] The crystallographic space group is $P\bar{1}$ with $Z = 2$.

of the larger mass difference between xenon and sulfur than between xenon and tellurium. The equatorial SF_4 symmetric breathing mode is weakly coupled with the S–N stretch and occurs at 731 cm^{-1} (737/701 cm^{-1}), as observed in $F_5SNH_3^+$ (739, 745, 747 cm^{-1}). The broad band at 461 cm^{-1} could not be assigned by comparison with the modes calculated for the gas-phase $F_5SN(H)Xe^+$ cation, and consequently was assigned to ν(Xe---F) by comparison with the frequency calculated for the ion pair (420 cm^{-1}), with the difference attributed to the underestimated Xe---F distance. This frequency is higher than that assigned to ν(Xe---F) in $[XeN(SO_2F)_2][AsF_6]$ (317 cm^{-1}),[49] $[XeOTeF_5][AsF_6]$ (365 cm^{-1}),[150,156] and $[XeF][AsF_6]$ (417 cm^{-1}).[112] The Xe–N–S bend is assigned to the strong band at 151 (136/125) cm^{-1}, which is higher than that of the Xe–N–Te bend in $F_5TeN(H)Xe^+$ (113 cm^{-1}).[50] The highest frequency band, 3186 cm^{-1}, is assigned to ν(NH) (3421/3287 cm^{-1}) and is in good agreement with the N–H stretches in $F_5TeN(H)Xe^+$ (3146 cm^{-1}),[50] F_5TeNH_2 (symmetric, 3297 cm^{-1}; asymmetric, 3385 cm^{-1}),[50] $F_5TeNH_3^+$ (symmetric, 3018 cm^{-1}; asymmetric, 3110 cm^{-1}),[50] and $F_5SNH_3^+$ (symmetric, 2939 cm^{-1}; asymmetric, 3072, 3145 cm^{-1}).[144] The δ(SNH) bend, observed at 954 cm^{-1}, and δ(NH) wag, which was not observed, were calculated at 980/946 and 1328/1230 cm^{-1}, respectively, and are predicted to be weak. The experimental SF_5-group stretches (671-904 cm^{-1}) and bends (305-631 cm^{-1}) fall into ranges that are similar to those of $F_5SNH_3^+$ and the benchmarks, SF_6 and SF_5Cl (vide supra). The medium intensity modes at 108, 119, and 169 (76, 105, and 156) cm^{-1} are assigned to strongly coupled deformation modes associated with the ion pair, but the torsion about Xe, calculated at 56/45 cm^{-1}, could not be observed.

4.3. Computational Results

Electronic structure calculations were carried out for $F_5SNH_3^+$, $F_5SN(H)Xe^+$, and $[F_5SN(H)Xe][AsF_6]$ to aid in the vibrational assignments (see section 4.2.4.) and to gain insight into the structure and bonding of $F_5SNH_3^+$ and $F_5SN(H)Xe^+$. Comparisons of the calculated and experimental frequencies with those of the benchmarks, SF_6 and SF_5Cl, showed that the SVWN calculations provided vibrational frequencies that were in better agreement than the MP2 calculations for the highest-frequency modes, the asymmetric SF_6 and equatorial SF_4 stretches of SF_6 and F_5SCl, respectively, whereas the MP2 calculations better reproduced the symmetric stretches and all of the F–S–F bending frequencies (see Table 4.9).

4.3.1. Calculated Geometries

Although close to C_s symmetry, both the MP2 and SVWN energy-minimized structures of the $F_5SNH_3^+$ and $F_5SN(H)Xe^+$ cations optimized to C_1 symmetry, as did the SVWN energy-minimized structure of the $[F_5SN(H)Xe][AsF_6]$ ion pair. These calculations reproduced the experimental geometric parameters of the $F_5SN(H)Xe^+$ cation in the ion pair. The largest discrepancies occurred for the Xe---F–As fluorine bridge of the ion pair. The Xe---F(6) (2.251 Å) and As–F(6) (1.919 Å) fluorine-bridge bond lengths are under- and overestimated, respectively, when compared with the experimental values, 2.634(3) and 1.759(3) Å. The Xe---F–As angle, which was found to be bent in the low-temperature X-ray crystal structure (127.2(1)°) and is known to be influenced by crystal packing (see section 4.2.3.), was significantly more bent (112.7°) for the calculated

geometry. Similar differences were found for the $[F_5TeN(H)Xe][AsF_6]$ ion pair.[50] It is noteworthy that the calculated local symmetry of AsF_6^- in the $[F_5SN(H)Xe][AsF_6]$ ion pair is better approximated by C_{2v} symmetry than by the local C_{4v} symmetry used to assign the vibrational frequencies of AsF_6^- in the ion pair (see section 4.2.4.).

The calculated S–N bond length of $F_5SN(H)Xe^+$ is significantly shorter than that of $F_5SNH_3^+$ at both levels of theory. This trend was also observed for the experimental and calculated Te–N bond lengths in $F_5TeN(H)Xe^+$ and $F_5TeNH_3^+$,[50] whereas the S–F bond lengths of $F_5SN(H)Xe^+$ are slightly longer (MP2) or slightly shorter (SVWN) than in $F_5SNH_3^+$. It is not possible to discern significant differences in either the experimental or calculated Te–F bond lengths for the tellurium analogues.[50]

4.3.2. Charges, Valencies, and Bond Orders

The Natural Bond Orbital (NBO) charges, valencies, and bond orders calculated using the MP2 and SVWN methods (SVWN values are given in parentheses) for $F_5SNH_3^+$ and $F_5SN(H)Xe^+$ are listed in Table 4.11. The formal positive charge of both cations chiefly resides on S, H, and Xe, with positive charges on S and H in $F_5SN(H)Xe^+$ that are slightly lower than the corresponding charges in $F_5SNH_3^+$. The Xe–N bond order [0.58 (0.60)] in $F_5SN(H)Xe^+$ and the decrease in N valency from $F_5SNH_3^+$ [2.39 (2.52)] to $F_5SN(H)Xe^+$ [1.82 (1.90)] also indicate significant covalent bonding between xenon and nitrogen. Slight decreases in the absolute charges on sulfur [2.58 (2.48)] and nitrogen [–0.82 (–0.82)] correspond to the greater S–N bond order [0.64 (0.68)] for $F_5SN(H)Xe^+$ when compared with that of $F_5SNH_3^+$ [0.55 (0.56)] [S charge: 2.61, (2.51); N charge:

Table 4.11. Natural Bond Orbital (NBO) Charges, Valencies, and Bond Orders for $F_5SNH_3^+$ [a] and $F_5SN(H)Xe^+$ [b]

atom	$F_5SNH_3^+$				$F_5SN(H)Xe^+$			
	charges		valencies		charges		valencies	
	MP2	SVWN	MP2	SVWN	MP2	SVWN	MP2	SVWN
Xe					1.01	0.98	0.57	0.61
H	0.45	0.47	0.63	0.68	0.40	0.43	0.71	0.72
N	–0.85	–0.90	2.39	2.52	–0.82	–0.82	1.82	1.90
S	2.61	2.51	3.67	3.93	2.58	2.48	3.67	3.91
F1	–0.39	–0.37	0.55	0.61	–0.41	–0.38	0.53	0.59
F2	–0.43	–0.42	0.49	0.55	–0.43	–0.41	0.49	0.54
F3	–0.43	–0.41	0.49	0.54	–0.45	–0.44	0.47	0.54
F4	–0.43	–0.42	0.49	0.55	–0.46	–0.45	0.45	0.51
F5	–0.43	–0.41	0.49	0.54	–0.42	–0.38	0.50	0.54

bond	bond orders			
	$F_5SNH_3^+$		$F_5SN(H)Xe^+$	
	MP2	SVWN	MP2	SVWN
Xe–N			0.58	0.60
N–H	0.65	0.69	0.71	0.72
S–N	0.55	0.56	0.64	0.68
S–F1	0.67	0.72	0.65	0.70
S–F2	0.61	0.66	0.60	0.63
S–F3	0.61	0.66	0.59	0.64
S–F4	0.61	0.66	0.58	0.62
S–F5	0.61	0.66	0.62	0.65

[a] cc-pVTZ basis set, atom numbering corresponds to that used in Figure 4.3c. [b] (SDB-)cc-pVTZ basis set, atom numbering corresponds to that used in Figure 4.3b.

–0.85 (–0.90)]. The lower N–H bond order of $F_5SNH_3^+$ [0.65 (0.69)] compared with that of $F_5SN(H)Xe^+$ [0.71 (0.72)] and parallel decreases in absolute charges on H and N correspond to increased N–H bond covalency in $F_5SN(H)Xe^+$. There is little difference in the S–F bond orders, or in the charges and valencies at sulfur and fluorine in $F_5SNH_3^+$ and $F_5SN(H)Xe^+$. The S–F_{eq} bond orders and F_{eq} valencies of both cations differ little from those of the benchmarks, SF_6 and F_5SCl, whereas the S–F_{ax} bond orders and the F_{ax} valencies are slightly higher in both cations.

4.4. Conclusions

The $F_5SN(H)Xe^+$ cation has been synthesized by reaction of XeF_2 with $F_5SNH_3^+$ in BrF_5 and aHF solvents, and by HF solvolysis of the recently reported $F_3S{\equiv}NXeF^+$ cation. The $F_5SN(H)Xe^+$ cation provides, in addition to $F_5TeN(H)Xe^+$, an example of xenon bonded to an sp^3-hybridized nitrogen, and the second example of a synthetic route that makes use of an ammonium ($F_5ChNH_3^+$, Ch = S or Te) cation as the synthetic precursor to a Xe–N bonded compound. The Xe–N bond length, calculated Xe–N bond order derived from the NBO analyses, high shielding of the ^{129}Xe NMR resonance, and empirical Xe–N bond valency derived from the crystal structure of $[F_5SN(H)Xe][AsF_6]$ are consistent and place $F_5SNXe(H)^+$ among the most covalent Xe–N bonds presently known.

CHAPTER 5

SOLID-STATE AND SOLUTION REARRANGEMENTS OF $F_3S{\equiv}NXeF^+$ LEADING TO THE $F_4S{=}NXe^+$ CATION; SYNTHESES, HF SOLVOLYSES, AND STRUCTURAL CHARACTERIZATIONS OF $[F_4S{=}NXe][AsF_6]$ AND $[F_4S{=}NH_2][AsF_6]$

5.1. Introduction

Several xenon(II) species are known in which xenon is bound to nitrogen having formal sp-, sp^2-, and sp^3-hybridization. Most belong to a weakly bonded class of XeF^+ adducts with mainly organic nitrogen bases. Those exhibiting formal nitrogen sp-hybridization are represented by the XeF^+ adducts of thiazyl trifluoride,[146] hydrogen cyanide,[34,35] alkylnitriles,[34] pentafluorobenzenenitrile,[34] and perfluoroalkylnitriles.[34,36] Examples of XeF^+ adducts with sp^2-hybridized organic nitrogen bases are also known, namely, those with *s*-trifluorotriazine[36] and several perfluoropyridines.[37] The only examples in which xenon is bonded to sp^3-hybridized nitrogen are $F_5SN(H)Xe^+$ [118] and $F_5TeN(H)Xe^+$.[50] Until the present study, the only species bonded to sp^2-hybridized nitrogen atoms of inorganic ligands were those derived from the imidobis(sulfurylfluoride) group and included $FXeN(SO_2F)_2$,[44-46] $Xe[N(SO_2F)_2]_2$,[45,47] $F[XeN(SO_2F)_2]_2^+$,[45,47,49] and $XeN(SO_2F)_2^+$,[49] as well as the related imidobis(sulfuryltrifluoromethyl) group, which is solely represented by $Xe[N(SO_2CF_3)_2]_2$.[48]

Species containing the $F_4S{=}N$-group are presently limited to the neutral molecules $F_4S{=}NL$ (L = F,[73,74,161,162] CH_3,[98-101] CH_2CH_3,[99] CF_3,[163-165] CF_2CF_3,[166] SF_5,[167-169] SO_2F,[170,171]

$C(O)N(CH_2CH_3)_2$[172]) and $F_4S{=}N\cdot$.[173] The majority have been characterized by vibrational[74,98,99,163,166,167,170,172] and NMR[73,98-100,164-167,170,172] spectroscopy, and a number have been characterized by electron diffraction[74,100] and microwave spectroscopy.[74,100]

Solvolysis of $N{\equiv}SF_3$ in anhydrous HF (aHF) occurs by the addition of two molecules of HF across the sulfur-nitrogen triple bond to give the primary amine, F_5SNH_2,[96] whereas solvolysis of $N{\equiv}SF_3$ in the superacid medium, AsF_5/aHF, results in amine protonation to give $[F_5SNH_3][AsF_6]$.[101] Controlled solvolysis of $[F_3S{\equiv}NXeF][AsF_6]$ in aHF at –20 °C for 4 h has recently been shown to yield the $F_5SN(H)Xe^+$ and $F_5SNH_3^+$ cations,[118] but no intermediates were isolated.

In the current work, the intermediacy of $F_4S{=}NXe^+$ in the reaction pathways that lead to the $F_5SN(H)Xe^+$ and $F_4S{=}NH_2^+$ cations is documented, as well as the HF solvolyses of the $F_4S{=}NXe^+$, $F_4S{=}NH_2^+$, $F_5SN(H)Xe^+$, and $F_5SNH_3^+$ cations. The solid-state rearrangement of $[F_3S{\equiv}NXeF][AsF_6]$ to form $[F_4S{=}NXe][AsF_6]$ is also reported. The syntheses and detailed structural characterizations of the $F_4S{=}NXe^+$ and $F_4S{=}NH_2^+$ cations in the solid state and in solution significantly extend the chemistry of the $F_4S{=}N$-group, providing the only cationic derivatives of this ligand group that are presently known.

5.2. Results and Discussion

5.2.1. Syntheses of $[F_4S{=}NXe][AsF_6]$ and $[F_4S{=}NH_2][AsF_6]$

5.2.1.1. Rearrangement of $[F_3S{\equiv}NXeF][AsF_6]$ in aHF

The $F_4S{=}NXe^+$ cation was synthesized by reaction of the previously reported $[F_3S{\equiv}NXeF][AsF_6]$ salt[146] with HF for ca. 1 h at –20 °C in aHF or HF/BrF_5 solution (eq

5.1). The reaction likely proceeds via the HF-catalyzed rearrangement shown in Scheme

$$F_3S{\equiv}NXeF^+ \xrightarrow[HF \text{ or } HF/BrF_5]{-20\ ^\circ C} F_4S{=}NXe^+ \qquad (5.1)$$

5.1a. The $F_4S{=}NXe^+$ cation was shown by ^{19}F and ^{129}Xe NMR spectroscopy in both solvent media to be a major component and an intermediate leading to $F_5SN(H)Xe^+$ (see section 5.2.2.).

5.2.1.2. Solid State Rearrangement of $[F_3S{\equiv}NXeF][AsF_6]$

The $[F_4S{=}NXe][AsF_6]$ salt was also obtained by solid-state rearrangement of $[F_3S{\equiv}NXeF][AsF_6]$. Rearrangement occurred upon warming $[F_3S{\equiv}NXeF][AsF_6]$ to 22 °C (eq 5.2) and was monitored by periodically quenching the sample at –160 °C and

$$[F_3S{\equiv}NXeF][AsF_6] \xrightarrow{22\ ^\circ C} [F_4S{=}NXe][AsF_6] \qquad (5.2)$$

recording the Raman spectrum at this temperature. Monitoring of the most intense peaks in the Raman spectra [$F_3S{\equiv}NXeF^+$, ν(XeF) 550 cm^{-1}; $F_4S{=}NXe^+$, δ(XeNS) 178 cm^{-1}] showed that $F_4S{=}NXe^+$ formed as the only product as $F_3S{\equiv}NXeF^+$ was consumed, and that no further reaction occurred after ca. 70 min at 22 °C (see section 5.2.4.). The resulting bright yellow solid was also characterized by ^{19}F NMR spectroscopy at –20 °C in $N{\equiv}SF_3$ solvent.

The rationale for the rearrangement and for incomplete conversion of $F_3S{\equiv}NXeF^+$ to $F_4S{=}NXe^+$ is based upon the crystal packing of $[F_3S{\equiv}NXeF][AsF_6]$,[146] which shows that the shortest cation-anion contact (2.871(5) Å) occurs between a fluorine atom of

Scheme 5.1. Proposed (a) Solution and (b) Solid-State Rearrangements of $F_3S{\equiv}NXeF^+$ Leading to $F_4S{=}NXe^+$

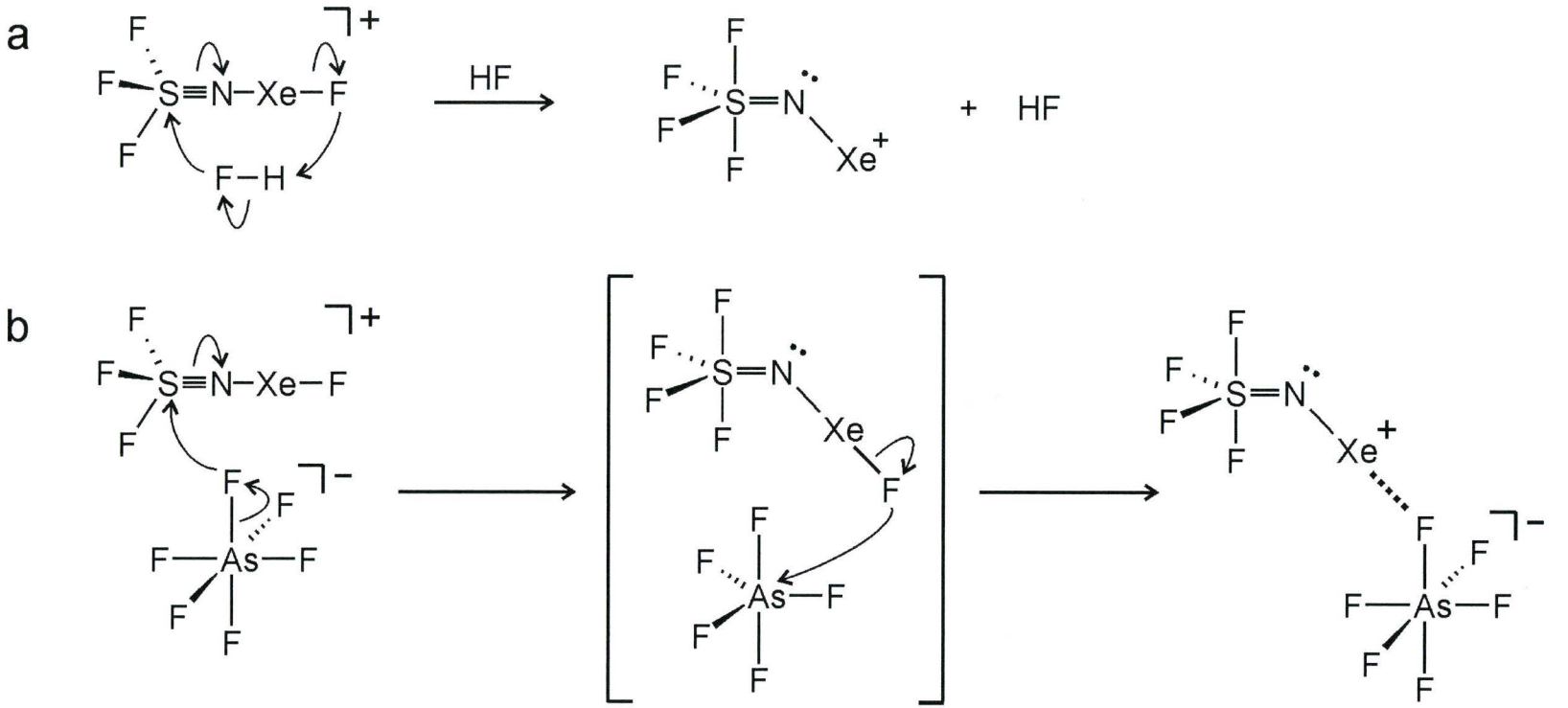

AsF_6^- and the sulfur atom of an adjacent $F_3S{\equiv}NXeF^+$ cation. This contact is significantly shorter than the sum of the fluorine and sulfur van der Waals radii (3.27 Å).[31] In the proposed solid-state reaction mechanism (Scheme 5.1b), a fluorine ligand of the AsF_6^- anion coordinates to the sulfur atom of an adjacent $F_3S{\equiv}NXeF^+$ cation, which leads to fluoride ion transfer and formation of the $[F_4S{=}NXe][AsF_6]$ ion pair. As the reaction proceeds, solid-state dilution of $F_3S{\equiv}NXeF^+$ and breakdown of the crystal lattice disrupt fluoride ion transfer and rearrangement, preventing the rearrangement from going to completion. Determination of a yield for this reaction was not possible because $F_3S{\equiv}NXeF^+$ [146] and $F_4S{=}NXe^+$ (see section 5.2.4.) share no directly comparable intense Raman bands. After rearrangement had ceased, the sample was stored at –78 °C for several weeks with no sign of further reaction. The proposed rearrangement pathway is also consistent with the optimized, zero-point-corrected energies of the $F_3S{\equiv}NXeF^+$ and $F_4S{=}NXe^+$ cations which show that $F_4S{=}NXe^+$ is 7.9 kJ mol^{-1} lower in energy than the $F_3S{\equiv}NXeF^+$ cation at the MP2/aug-cc-pVTZ(-PP) level of theory.

5.2.1.3. Synthesis of $[F_4S{=}NH_2][AsF_6]$

The $F_4S{=}NH_2^+$ cation was formed concurrently with $F_4S{=}NXe^+$ during the solvolysis of $F_3S{\equiv}NXeF^+$ in aHF at –20 °C. Reaction of $F_4S{=}NXe^+$ with 2 equiv of HF resulted in $F_4S{=}NH_2^+$ and XeF_2 formation according to eq 5.3, which were identified by

$$[F_4S{=}NXe][AsF_6] + 2HF \xrightarrow[HF \text{ or } BrF_5]{-20\ ^\circ C} [F_4S{=}NH_2][AsF_6] + XeF_2 \qquad (5.3)$$

^{19}F NMR spectroscopy (vide infra). Characterization by Raman spectroscopy was not attempted because it was not possible to isolate $[F_4S{=}NH_2][AsF_6]$ as a pure product from the complex admixture of solvolysis products comprised of $[F_4S{=}NXe][AsF_6]$, $[F_5SN(H)Xe][AsF_6]$, $[F_5SNH_3][AsF_6]$, $[NH_4][AsF_6]$, SF_6, and XeF_2.

5.2.1.4. Solvolytic Pathways and Thermodynamic Considerations

It has recently been shown that HF solvolysis of $F_3S{\equiv}NXeF^+$ led to the formation of the $F_5SN(H)Xe^+$ and $F_5SNH_3^+$ cations.[118] The identification and characterization of $F_4S{=}NXe^+$ and $F_4S{=}NH_2^+$ as intermediates provide a fuller understanding of the reaction pathways that lead to the aforementioned cations. Proposed reaction pathways that account for the products, along with their relative energies, are provided in Scheme 5.2.

The solvolysis of the $F_3S{\equiv}NXeF^+$ cation is likely initiated by HF-catalyzed rearrangement to $F_4S{=}NXe^+$ (Scheme 5.1a), which occurred at a much lower temperature (–20 °C) in HF or HF/BrF_5 solution than the fluoride ion-catalyzed solid-state rearrangement (22 °C, Scheme 5.1b). Moreover, $F_3S{\equiv}NXeF^+$ did not undergo rearrangement in BrF_5 solvent at –20 °C in the absence of HF.

Two pathways for the solvolysis of $F_4S{=}NXe^+$ are possible: (1) reaction with 2 equiv of HF to form $F_4S{=}NH_2^+$ and XeF_2 (eq 5.3), and (2) addition of HF across the S=N double bond of $F_4S{=}NXe^+$ to give $F_5SN(H)Xe^+$ (eq 5.4). Both cations may undergo

$$[F_4S{=}NXe][AsF_6] + HF \xrightarrow[HF \text{ or } BrF_5]{-20\ ^\circ C} [F_5SN(H)Xe][AsF_6] \qquad (5.4)$$

Scheme 5.2. Calculated Relative Gas-Phase Energies of Products Resulting from HF-Catalyzed Rearrangement of $F_3S{\equiv}NXeF^+$ and HF Solvolysis of $F_4S{=}NXe^+$ [kJ mol^{-1}; MP2/aug-cc-pVTZ(-PP)]

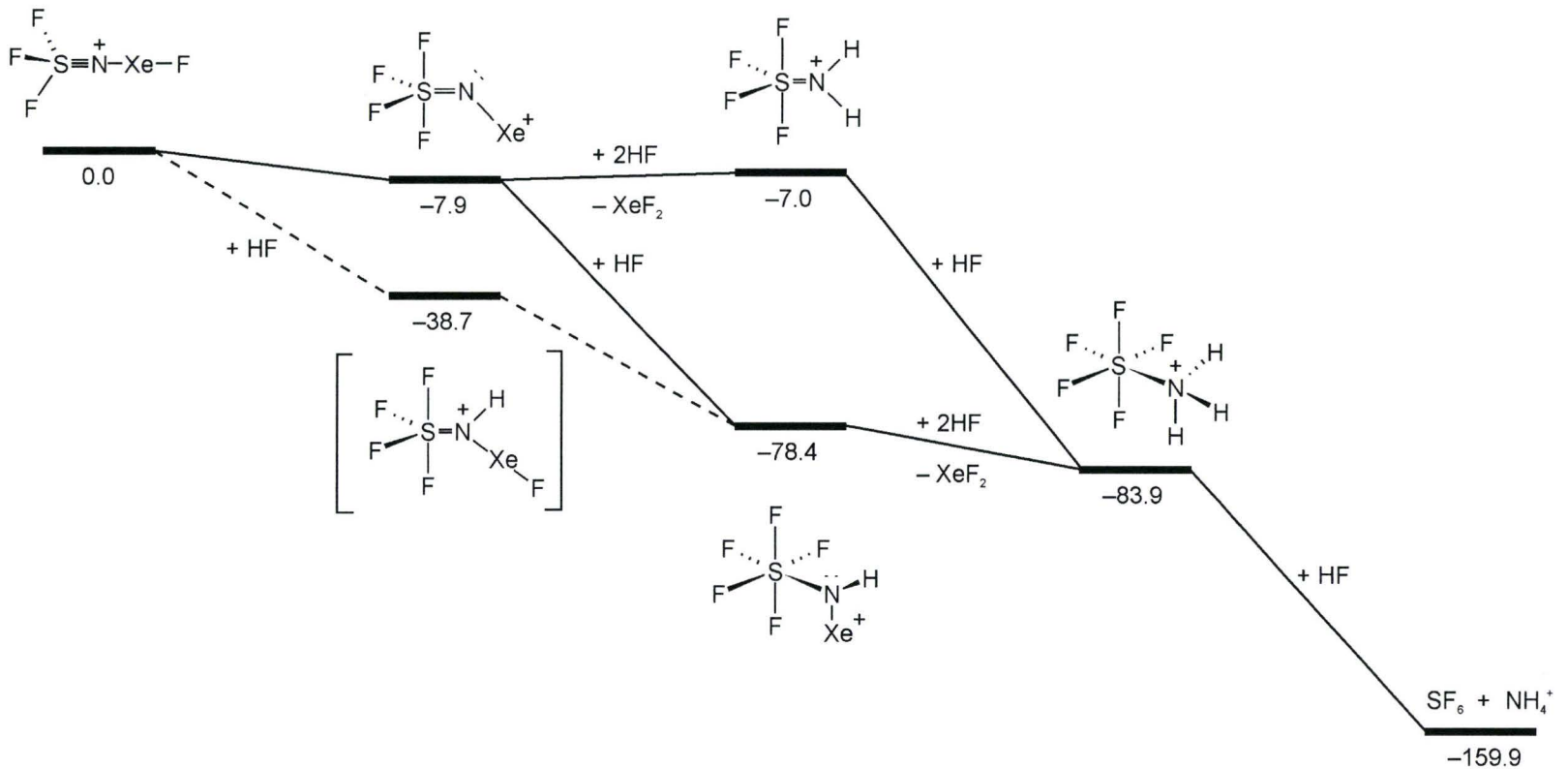

further HF attack by (1) reaction of $F_5SN(H)Xe^+$ with 2 equiv of HF to form the very stable $F_5SNH_3^+$ cation and XeF_2 according to equilibrium 5.5,[118] and/or (2) addition of HF across the S=N double bond of $F_4S{=}NH_2^+$ to form $F_5SNH_3^+$ (eq 5.6). Fluorine-19

$$[F_5SN(H)Xe][AsF_6] + 2HF \rightleftharpoons [F_5SNH_3][AsF_6] + XeF_2 \qquad (5.5)$$

$$[F_4S{=}NH_2][AsF_6] + HF \xrightarrow[HF \text{ or } BrF_5]{> 0\ ^\circ C} [F_5SNH_3][AsF_6] \qquad (5.6)$$

NMR spectroscopy showed that the $F_5SN(H)Xe^+$ cation was initially formed, along with $F_4S{=}NXe^+$ and $F_4S{=}NH_2^+$, at –20 °C. Initial formation of $F_5SN(H)Xe^+$ may arise from HF addition across the $F_3S{\equiv}NXeF^+$ triple bond to form $F_4S{=}N(H)XeF^+$ as an intermediate which subsequently undergoes rearrangement to form the known $F_5SN(H)Xe^+$ cation[118] (Scheme 5.2). Although the $F_4S{=}N(H)XeF^+$ cation was calculated to be thermodynamically favourable, it was not observed experimentally. When the reaction mixture was warmed to 0 °C, $F_5SNH_3^+$ formation was favoured while $F_4S{=}NXe^+$ was consumed and $F_4S{=}NH_2^+$ remained. Above 0 °C, the $F_5SNH_3^+$ cation dominated (eqs 5.5 and 5.6), along with increasing amounts of its solvolysis products, SF_6 and NH_4^+, and a trace amount of F_5SNF_2, which was presumably generated by a series of reactions that are analogous to those described for $F_5SN(H)Xe^+$ [118] and $F_5TeN(H)Xe^+$.[50] With careful temperature control, it was possible to record the ^{19}F NMR spectrum of the entire $F_3S{\equiv}NXeF^+$ solvolysis product mixture with the exception of F_5SNF_2 (Figure 5.1).

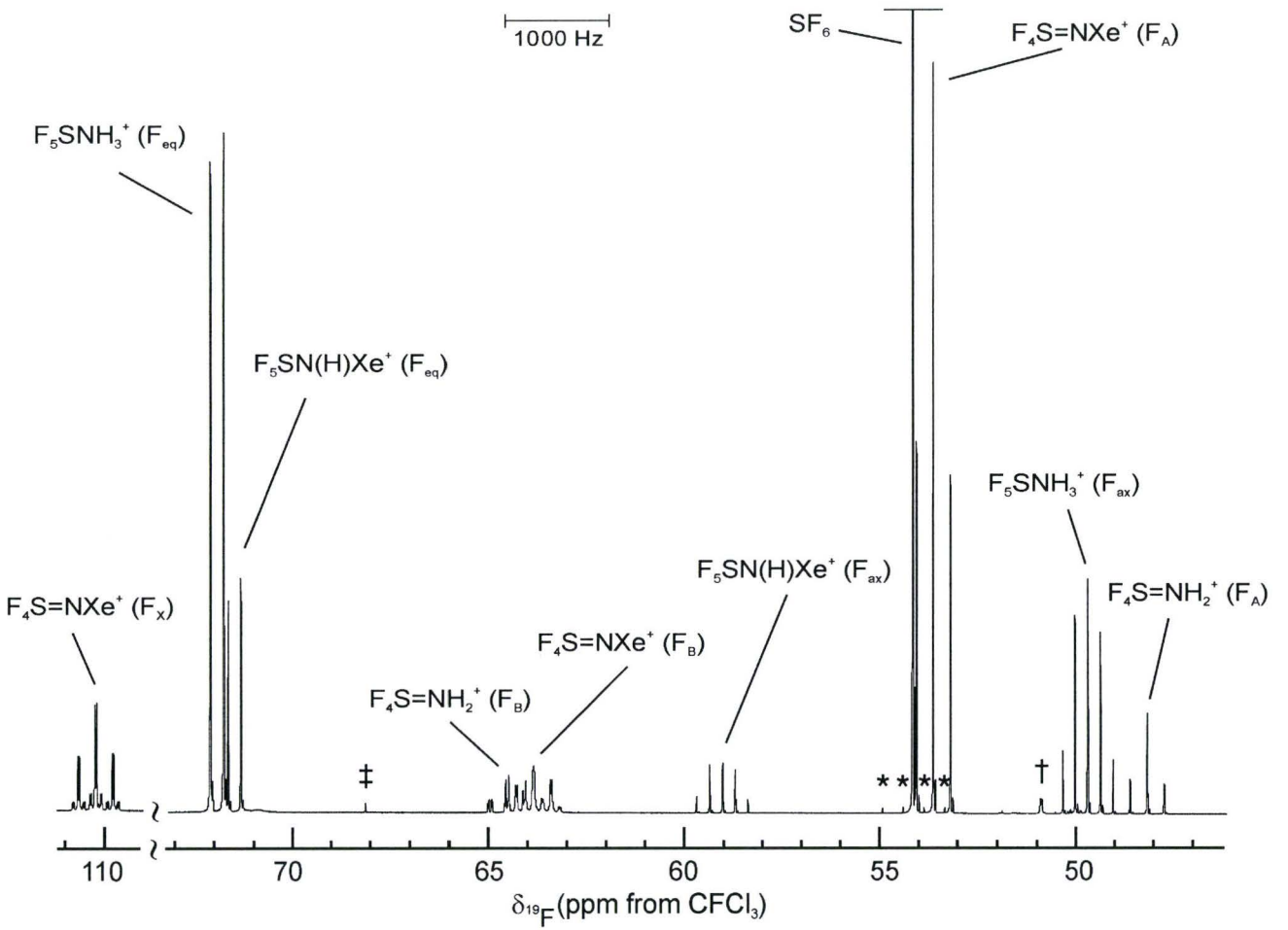

Figure 5.1. Fluorine-19 NMR spectrum (470.592 MHz) of a product mixture resulting from the solvolysis of $[F_3S{\equiv}NXeF][AsF_6]$ for 30 min in aHF solvent at –20 °C; symbols denote F-on-S of residual $F_3S{\equiv}NXeF^+$ (†), the 1:1:1:1 quartet arising from $^1J(^{19}F–^{33}S)$ of SF_6 (*), and a very weak unassigned resonance (‡). The XeF_2 resonance, not shown in the spectral trace, occurred at $\delta(^{19}F) = –194.5$ ppm with $^1J(^{19}F–^{129}Xe) = 5652$ Hz.

5.2.2. NMR Spectroscopy

The ^{19}F and ^{129}Xe NMR parameters for the AsF_6^- salt of the $F_4S{=}NXe^+$ cation (structure XVIII), recorded in aHF, BrF_5 containing a catalytic amount of HF (hereafter designated HF/BrF_5), and $N{\equiv}SF_3$ solvents, and the ^{19}F NMR parameters for the AsF_6^- salt of the $F_4S{=}NH_2^+$ cation (structure XIX), recorded in aHF and HF/BrF_5 solvents, are listed

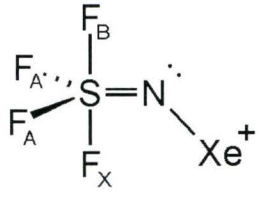

XVIII

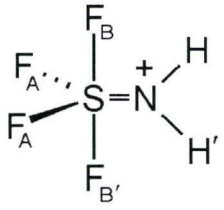

XIX

in Table 5.1. Only the ^{19}F and ^{129}Xe NMR spectra recorded in aHF at –20 °C (Figures 5.2–5.4) and their parameters are discussed in detail in this section. The ^{19}F chemical shift and coupling constants are similar to those of $F_4S{=}NF$,[73,74] $F_4S{=}NCH_3$,[99,100] and $F_4S{=}NCF_3$.[164] Spectral assignments were confirmed by use of the program ISOTOPOMER,[124] which provided simulated spectra for the $F_4S{=}NXe^+$ and $F_4S{=}NH_2^+$ cations that are in excellent agreement with their experimental ^{19}F (Figures 5.3 and 5.4) and ^{129}Xe (Figure 5.2) NMR spectra. As in the cases of $F_5SN(H)Xe^+$ and $F_5SNH_3^+$,[118] the ^{14}N resonances of $F_4S{=}NXe^+$ and $F_4S{=}NH_2^+$ were not observed, presumably because quadrupolar relaxation of ^{14}N (^{14}N, $I = 1$), resulting from the high electric field gradients at the ^{14}N nuclei that result from the low symmetries around nitrogen in these cations, resulted in broad ^{14}N resonances that could not be differentiated from the spectral baselines.

Table 5.1. ^{19}F and ^{129}Xe NMR Parameters for $[F_4S{=}NXe][AsF_6]$ and $[F_4S{=}NH_2][AsF_6]$ [a]

	chemical shifts, ppm				coupling constants, Hz					
cations	$\delta(^{129}Xe)$	$\delta(^{19}F_A)$	$\delta(^{19}F_B)$	$\delta(^{19}F_X)$	$^2J(^{19}F_A{-}^{19}F_B)$	$^2J(^{19}F_A{-}^{19}F_X)$	$^2J(^{19}F_B{-}^{19}F_X)$	$^3J(^{129}Xe{-}^{19}F_B)$	$^3J(^{129}Xe{-}^{19}F_X)$	$^3J(^{19}F_B{-}^{1}H)_{syn}$
$F_4S{=}NXe^+$ [b]	–2674	53.6	63.8	110.2	206.8	206.5	18.2	203.6	129.7	
	(–2588)	(55.1)	(64.7)	(113.3)	(212.3)	(210.2)	(18.0)	(208.7)	(126.7)	
	[–2510]	[58.6]	[c]	[110.6]	[206.3]	[209.6]	[21.6]	[208.9]	[102.0]	
$F_4S{=}NH_2^+$ [d]		48.1	64.5		205.4					42.5
		(49.6)	(66.5)		(203.5)					(38.2)

[a] The values in parentheses were measured in HF/BrF_5 solvent at –60 °C, and the values in square brackets were measured in $N{\equiv}SF_3$ solvent at 0 °C; all other values were measured in HF solvent at −20 °C. The AsF_6^- anion resonance in HF solvent was broad (saddle-shaped) [$\delta(^{19}F)$ = –69 (–64) ppm, $\Delta\nu_{½}$ = 2860 (700) Hz] and results from a partially quadrupole collapsed 1:1:1:1 quartet arising from $^1J(^{75}As{-}^{19}F)$. The NMR parameters for HF solvent are $\delta(^{19}F)$ = –197 (–192) ppm, $\delta(^1H)$ = 8.26 (7.39) ppm, and those for BrF_5 solvent are: $\delta(^{19}F_{eq})$ = 134.5 ppm, $\delta(^{19}F_{ax})$ = 272.0 ppm, $^2J(^{19}F_{ax}{-}^{19}F_{eq})$ = 76.3 Hz. [b] The fluorine atom labeling scheme is given by structure I. One-bond secondary isotope effects were observed for $F_4S{=}NXe^+$ in HF solvent; $^1\Delta^{19}F_A(^{34/32}S)$ = –0.064 ppm, $^1\Delta^{19}F_B(^{34/32}S)$ = –0.055 ppm, and $^1\Delta^{19}F_X(^{34/32}S)$ = –0.055 ppm. All coupling constants have positive signs based on the spectral simulations. The $^3J(^{129}Xe{-}^{19}F_A)$ coupling constant of $F_4S{=}NXe^+$ was too small to be resolved in all solvents. [c] The $^{19}F_B$ resonance in $N{\equiv}SF_3$ solvent was not observed because of overlap with the solvent. [d] The fluorine atom labeling scheme is given by structure II. Additional coupling constants obtained from spectral simulations are $^3J(^{19}F_B{-}^{1}H)_{anti}$ = –1.1 Hz, $^3J(^{19}F_A{-}^{1}H)$ = –3.6 Hz, $^2J(^1H{-}^1H)$ = 14.9 Hz. One-bond secondary isotope effects were observed for $F_4S{=}NH_2^+$ in HF solvent; $^1\Delta^{19}F_A(^{34/32}S)$ = –0.061 ppm and $^1\Delta^{19}F_B(^{34/32}S)$ = –0.049 ppm.

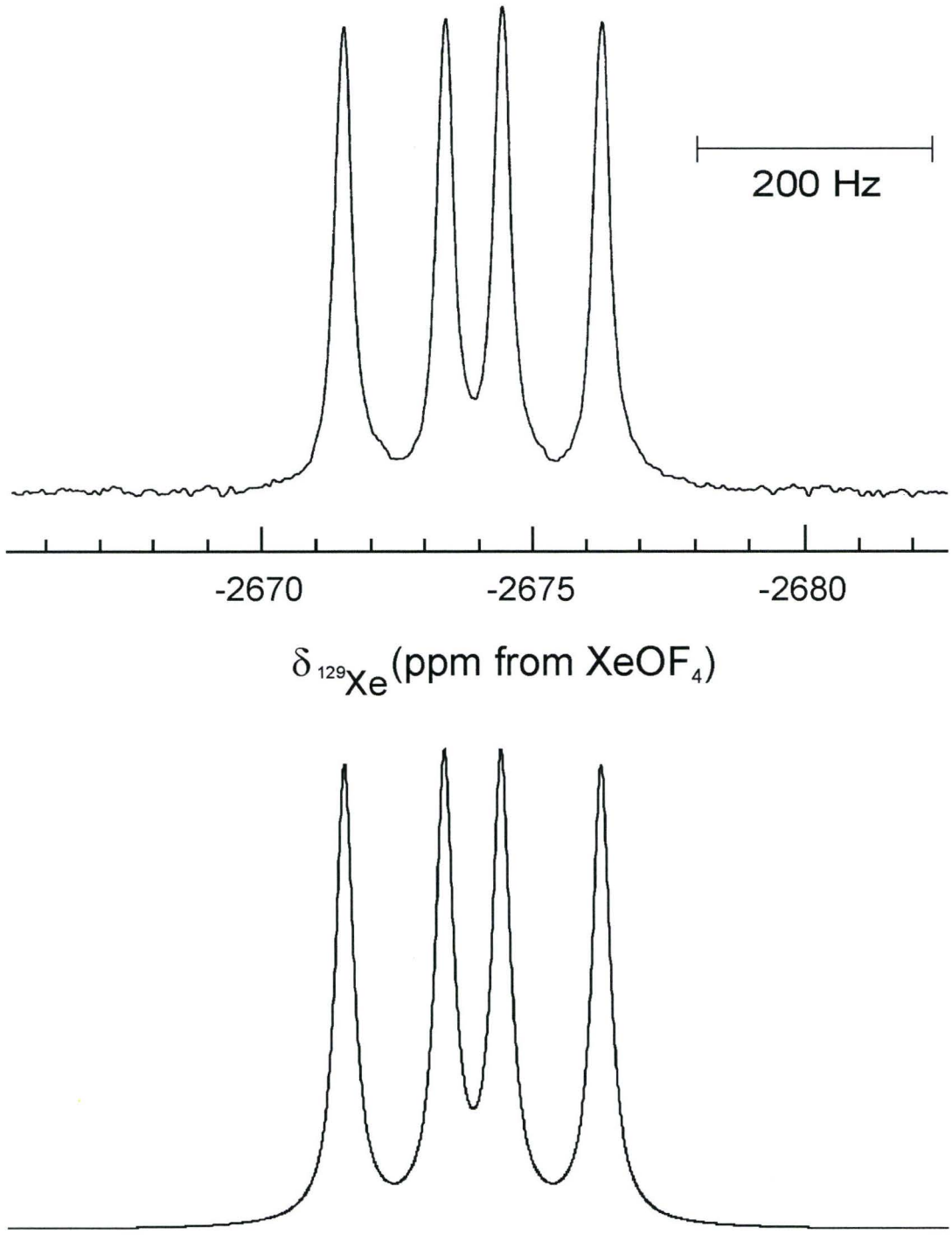

Figure 5.2. The ^{129}Xe NMR spectrum (138.086 MHz) of $F_4S{=}NXe^+$ in HF solvent at –20 °C (upper trace) and simulated spectrum (lower trace).

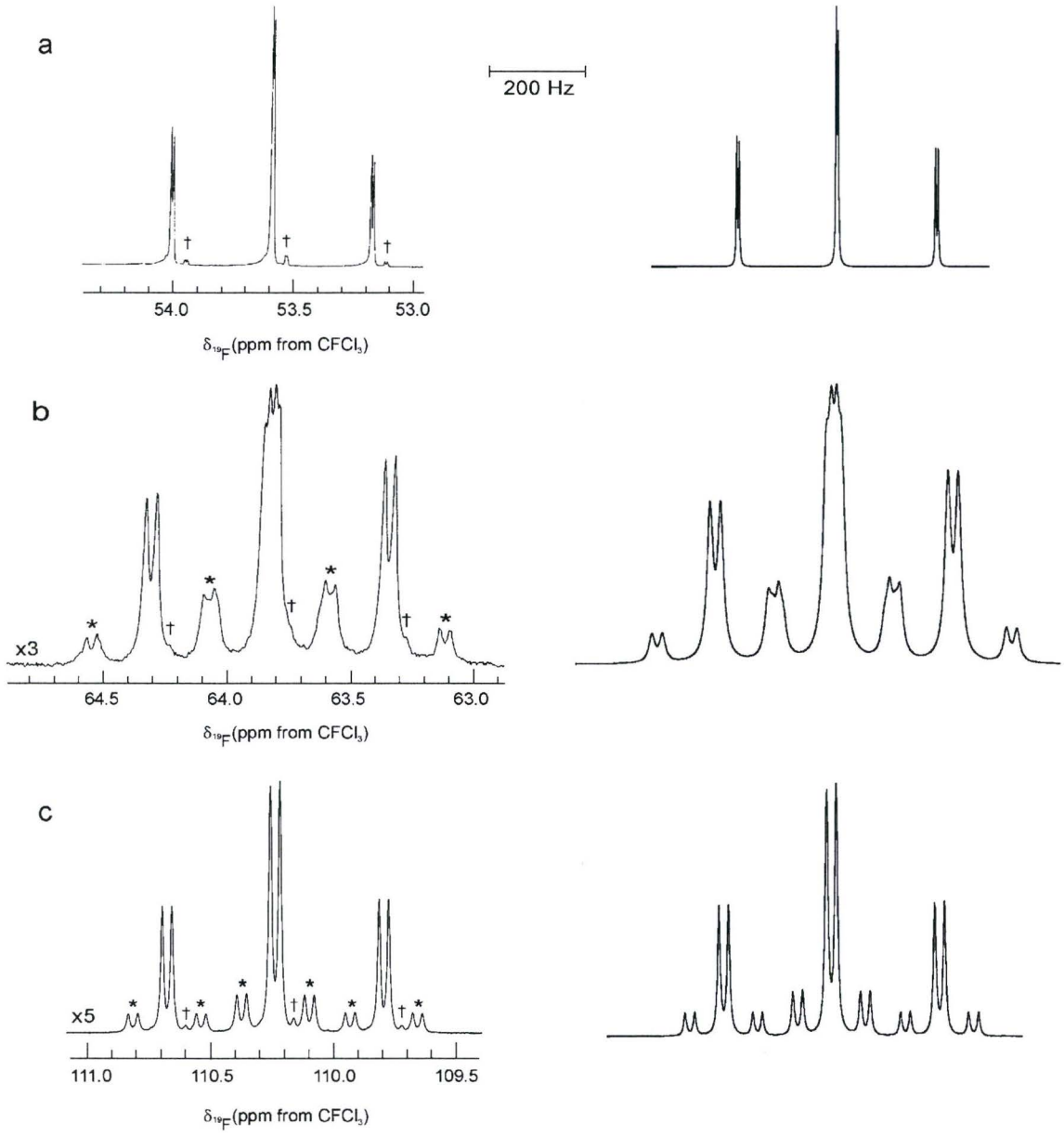

Figure 5.3. The ^{19}F NMR spectrum (470.592 MHz) of $F_4S{=}NXe^+$ in HF solvent at –20 ^oC (left-hand traces) and simulated spectrum (right-hand traces) depicting (a) F_A, (b) F_B, and (c) F_X; symbols denote the $^1\Delta^{19}F(^{34/32}S)$ secondary isotope shifts (†) and ^{129}Xe satellites (*) in the experimental spectrum.

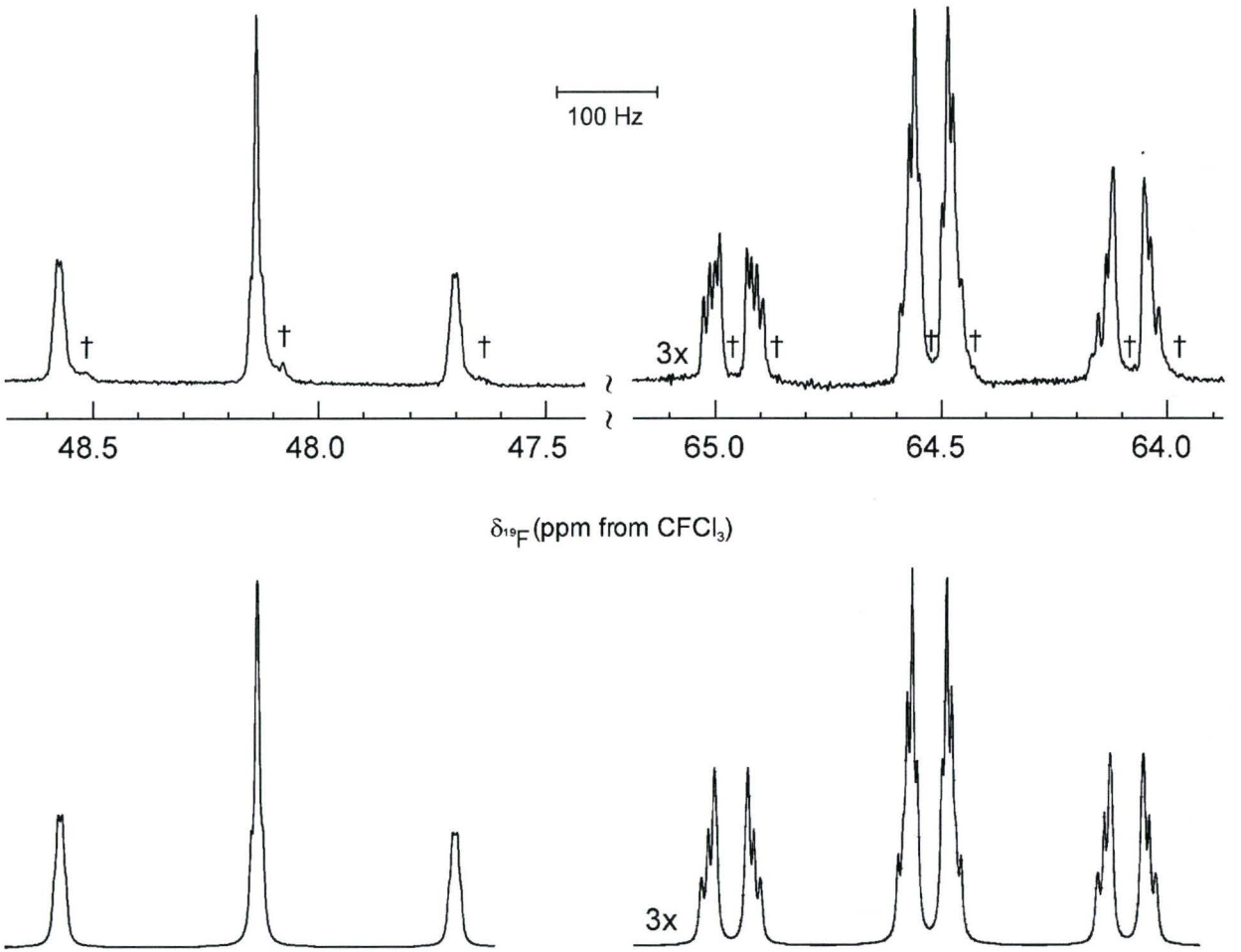

Figure 5.4. The experimental ^{19}F NMR spectrum (470.592 MHz) of $F_4S{=}NH_2^+$ in HF solvent at –20 °C (top traces) and simulated spectrum (bottom traces). The daggers (†) in the experimental spectrum denote the $^{1}\Delta^{19}F(^{34/32}S)$ secondary isotope shifts.

5.2.2.1. $[F_4S{=}NXe][AsF_6]$

The ^{19}F NMR spectrum of the $F_4S{=}NXe^+$ cation (Figure 5.3) is a superimposition of an A_2BX spin-coupling pattern (chemical shifts 53.6 (A_2), 63.8 (B), and 110.2 (X) ppm) that arises from the $F_4S{=}N$-group (C_s symmetry), and satellite spectra arising from an $A_2BX\Omega$ spin system that results from coupling to natural abundance ^{129}Xe (26.44%, indicated by Ω). Xenon-129 satellites are only observed on the B and X fluorine resonances. The ^{19}F chemical shifts of the F_4S-group of $F_4S{=}NXe^+$ have chemical shift ranges and trends similar to those of $F_4S{=}NCF_2CF_3$ (66.7, 77.2, and 98.5 ppm, respectively),[166] whereas in the case of $F_4S{=}NCH_3$ (68.2, 73.9, and 76.3 ppm, respectively),[99] the trend is maintained but F_X is significantly more shielded. The F_4S-group chemical shift trend is, however, reversed for $F_4S{=}NF$ (52.7, 45.0, and 13.2 ppm, respectively).[74] The pseudo-triplet corresponding to the equatorial F_A environment of $F_4S{=}NXe^+$ arises from a doublet of doublets that results from the two nearly equal couplings, $^2J(^{19}F_A{-}^{19}F_B)$ = 206.8 Hz and $^2J(^{19}F_A{-}^{19}F_X)$ = 206.5 Hz, which are similar to those of related species, e.g., $F_4S{=}NF$ (213.9 and 194.0 Hz),[74] $F_4S{=}NCH_3$ (201 and 194.0 Hz),[99] and $F_4S{=}NCF_2CF_3$ (208.0 and 210.6 Hz).[166] The F_B and F_X multiplets are each comprised of a doublet of triplets, with the triplet arising from $^2J(^{19}F_A{-}^{19}F_{B/X})$ (vide supra), and the doublets arising from $^2J(^{19}F_B{-}^{19}F_X)$ = 18.2 Hz. The multiplets are accompanied by natural abundance ^{129}Xe satellites resulting from $^3J(^{129}Xe{-}^{19}F_B)$ = 203.6 Hz and $^3J(^{129}Xe{-}^{19}F_X)$ = 129.7 Hz, respectively, with the satellites of the central peak of the F_B multiplet overlapping with the inner satellites of the outer multiplet lines. In $N{\equiv}SF_3$ solvent, the F_B multiplet could not be observed because it overlapped with the solvent peak, however, the $^3J(^{129}Xe{-}^{19}F_B)$ coupling that is reported for this solvent was

obtained from the ^{129}Xe spectrum (vide infra). The additional fine structure that is manifested in the small unequal doublet splittings on each of the F_A triplet transitions, the additional transitions in the central peak of the F_B multiplet, and the broadenings of the F_B and, to a lesser degree, the F_X resonances are due to second-order effects which were confirmed by spectral simulation. Quadrupolar relaxation resulting from ^{14}N and partially quadrupole collapsed ^{19}F–^{14}N coupling are not significant contributors to the ^{19}F line widths because the simulated ^{19}F spectra account for the spectral line widths without invoking quadrupolar relaxation and/or ^{19}F–^{14}N coupling.

The ^{129}Xe NMR spectrum of $F_4S{=}NXe^+$ (Figure 5.2) consists of a doublet of doublets, resulting from $^3J(^{129}Xe–^{19}F_B)$ and $^3J(^{129}Xe–^{19}F_X)$ (vide supra), centered at –2674 ppm. No $^3J(^{129}Xe–^{19}F_A)$ coupling could be resolved (vide infra). Failure to observe $^1J(^{129}Xe–^{14}N)$ likely results from the low symmetry and associated significant electric field gradient at nitrogen that results in quadrupolar relaxation and collapse of this coupling. The ^{129}Xe NMR chemical shift is consistent with that expected for xenon bound to an sp^2-hybridized nitrogen, but is considerably more shielded than the ^{129}Xe resonances of $Xe[N(SO_2CF_3)_2]_2$ (–2444 ppm in SO_2ClF at 8 °C),[47] $Xe[N(SO_2F)_2]_2$ (–2257 ppm in SO_2ClF at –40 °C),[47] $FXeN(SO_2F)_2$ (–2009 ppm in SO_2ClF at –40 °C),[47] $XeN(SO_2F)_2^+$ (–1943 ppm in SbF_5 at 25 °C),[49] and $F[XeN(SO_2F)_2]_2^+$ (–1933 ppm in BrF_5 at –5 °C).[45] The relatively high ^{129}Xe shielding of $F_4S{=}NXe^+$ is consistent with a Xe–N bond that is significantly more covalent than those of the aforementioned species[19] (also see section 5.3.). The ^{129}Xe chemical shift is most similar to those of xenon bound to sp^3-hybridized nitrogen in $F_5SN(H)Xe^+$ (–2897 ppm in HF at –20 °C)[118] and $F_5TeN(H)Xe^+$ (–2841 ppm in HF at –45 °C).[50] It has

been shown that the ^{129}Xe shielding may be correlated with the L-group electronegativity and Xe–E bond covalency, where L is an electronegative ligand and E is a second-row ligand atom.[50,118] Accordingly, shielding generally increases with increasing Xe–E bond covalency for the series of LXe^+ cations, i.e., Xe–F < Xe–O < Xe–N < Xe–C. It is noteworthy that the $^3J(^{129}Xe–^{19}F_X)$ coupling in $N{\equiv}SF_3$ solvent (102.0 Hz) is significantly less than in aHF or BrF_5 solvents (129.7 and 126.7 Hz, respectively), whereas the remaining coupling constants are very similar irrespective of solvent. This is likely a consequence of coordination of $N{\equiv}SF_3$ to the xenon atom of the cation.

The $^3J(^{19}F_A–^{129}Xe)$ coupling could not be resolved in either the ^{19}F or the ^{129}Xe NMR spectrum when recorded in aHF, BrF_5, or $N{\equiv}SF_3$ solvents. The small absolute to near-zero value of $^3J(^{19}F_A–^{129}Xe)$ may stem from a Karplus-type dependence,[174] where the absolute three-bond coupling constant is a minimum when the dihedral angle between the planes occupied by the coupled nuclei is 90°. In the present instance, the minimum is achieved when F_A–S–N–Xe is 90°. This finding is also consistent with $F_4S{=}NF$, for which the $^3J(^{19}F_N–^{19}F_A)$ coupling (F_N is F-on-N) is an order of magnitude smaller than $^3J(^{19}F_N–^{19}F_B)$ or $^3J(^{19}F_N–^{19}F_X)$.[73] In the structurally related compound, $F_4P^VN(H)P^{III}F_2$,[175] the coupling constants between P(III) and the *cis*- and *trans*-axial fluorines are 209.2 and 14.7 Hz, respectively, and are of opposite sign, whereas the coupling between P(III) and the equatorial fluorines was not resolved (< 0.2 Hz). The $F_A–P^V–N–P^{III}$ dihedral angle is expected to be 90°, however, this structural detail has not been confirmed.

5.2.2.2. $[F_4S{=}NH_2][AsF_6]$

The ^{19}F NMR spectrum of $F_4S{=}NH_2^+$ (Figure 5.4) is an $A_2BB'XX'$ spin pattern with ^{19}F NMR parameters that are in a range similar to those of isoelectronic $F_4S{=}CH_2$,[176] but have chemical shifts that exhibit the opposite trend (NMR parameters for neat $F_4S{=}CH_2$ at –150 °C appear in square brackets in the ensuing discussion). Chemical shifts at 48.1 [59.0] (A_2) and 64.5 [53.6] (BB') ppm arise from the $F_4S{=}N$-group (local C_{2v} symmetry), with additional fine structure on F_B arising from the protons (XX') bonded to nitrogen. As previously observed for $F_4S{=}CH_2$[176] and other C-substituted derivatives, $F_4S{=}CHR$,[177] two coupling paths between the F_B and H nuclei result from the high barrier to rotation about the S=N double bond. Although these ^{19}F chemical shifts are comparable to those of the $F_4S{-}N(CH_3)_2^+$ cation (63.8 and 61.6 ppm, SO_2, –55 °C),[178] the low-temperature NMR study shows no evidence for hindered rotation about the S–N bond, ruling out the iminium valence isomer, $F_4S{=}N(CH_3)_2^+$. Unfortunately, the ^1H NMR spectrum of the $F_4S{=}NH_2^+$ cation was almost entirely obscured by overlap with the broad HF doublet (HF/BrF_5 solvent; –70 °C; $\delta(^1H)$, 7.44 ppm; $^1J(^1H{-}^{19}F)$ = 470 Hz; $\Delta\nu_{1/2}$ = 700 Hz). Only two weak transitions that may be attributable to $F_4S{=}NH_2^+$ were observed that appeared as shoulders to high frequency of the high-frequency branch of the HF doublet (8.32 and 8.72 ppm), which may be compared with the chemical shift of $F_5SNH_3^+$ (7.74 ppm)[118] under the same experimental conditions. The ^{19}F spectral features arising from two $^{19}F{-}^1H$ coupling pathways were also apparent in the ^{19}F NMR spectrum and were confirmed by simulation (Figure 5.4). The F_A and F_B multiplets in the ^{19}F spectrum consist of triplets that arise from $^2J(^{19}F_A{-}^{19}F_B)$ = 205.5 [154.4] Hz with the F_A resonance being further split by $^3J(^{19}F_A{-}^1H)$ = –3.6 [10.5] Hz and the

F_B resonance being further split by coupling with the *syn*- and *anti*-hydrogen environments, i.e., $^3J(^{19}F_B–^1H)_{syn}$ = 42.5 [58.1] Hz and $^3J(^{19}F_B–^1H)_{anti}$ = –1.1 [9.7] Hz. Both resonances are also influenced by $^2J(^1H–^1H)$ = 14.9 Hz. A minor feature not reproduced by spectral simulation is the asymmetry of the outer transitions of the F_B multiplet. In the experimental spectrum, eight transitions of the high-frequency branch of the multiplet are resolved, whereas its lower frequency counterpart has only six transitions resolved due to overlap of the inner transitions.

5.2.3. X-ray Crystal Structures of $[F_4S{=}NXe][AsF_6]$ and $[F_4S{=}NH_2][AsF_6]$

Summaries of the refinement results and other crystallographic information are provided in Table 5.2. Important bond lengths and angles for $[F_4S{=}NXe][AsF_6]$ and $[F_4S{=}NH_2][AsF_6]$ are listed in Table 5.3 along with the calculated gas-phase geometries of the $F_4S{=}NXe^+$ and $F_4S{=}NH_2^+$ cations. Experimental and calculated geometric parameters for the $[F_4S{=}NXe][AsF_6]$ ion pair are compared in Table 5.4 and the experimental geometric parameters for the AsF_6^- anions in $[F_4S{=}NH_2][AsF_6]$ are provided in Table 5.5. Both cation geometries are derived from trigonal bipyramidal VSEPR arrangements of bonding pairs about sulfur, with the nitrogen and two fluorine atoms in the equatorial plane and two fluorine atoms in axial positions.

5.2.3.1. $[F_4S{=}NXe][AsF_6]$

In the crystal packing diagram of $[F_4S{=}NXe][AsF_6]$ (Figure 5.5), the structural units are stacked, without alternation of the cation and anion positions, along the *b*-axis,

Table 5.2. Summary of Crystal Data and Refinement Results for $[F_4S{=}NXe][AsF_6]$ and $[F_4S{=}NH_2][AsF_6]$

	$[F_4S{=}NXe][AsF_6]$	$[F_4S{=}NH_2][AsF_6]$
empirical formula	$F_{10}NSXeAs$	$F_{10}NSH_2As$
space group (No.)	$C2/c$ (15)	$P\bar{1}$ (2)
a (Å)	25.930(1)	5.4447(6)
b (Å)	5.0875(3)	6.6457(7)
c (Å)	14.8171(8)	10.306(1)
α (deg)	90	89.484(9)
β (deg)	119.549(1)	87.479(7)
γ (deg)	90	74.955(7)
V (Å^3)	1700.4(4)	359.79(9)
molecules/unit cell	8	2
mol wt (g mol^{-1})	442.29	313.00
calcd density (g cm^{-3})	3.455	2.889
T (°C)	−173	−173
μ (mm^{-1})	8.29	5.16
R_1 [a]	0.0224	0.0855
wR_2 [b]	0.0524	0.1725

[a] R_1 is defined as $\Sigma||F_o|-|F_c||/\Sigma|F_o|$ for $I > 2\sigma(I)$.

[b] wR_2 is defined as $[\Sigma[w(F_o^2 - F_c^2)^2]/\Sigma w(F_o^2)^2]^{1/2}$ for $I > 2\sigma(I)$.

Table 5.3. Experimental Geometries for $[F_4S{=}NXe][AsF_6]$ and $[F_4S{=}NH_2][AsF_6]$ and Calculated Geometries for $F_4S{=}NXe^+$ and $F_4S{=}NH_2^+$ [a]

	bond lengths (Å)							
	$F_4S{=}NXe^+$				$F_4S{=}NH_2^+$			
		calcd (C_1)[b]				calcd (C_s)[c]		
	Exptl	MP2	PBE1PBE	B3LYP	exptl	MP2	PBE1PBE	B3LYP
Xe(1)–N(1)	2.084(3)	2.063	2.120	2.183				
N(1)–S(1)	1.556(3)	1.583	1.582	1.595	1.511(6)	1.558	1.558	1.567
N(1)–H(1)					1.011[d]	1.013	1.013	1.014
N(1)–H(2)					1.012[d]	1.013	1.013	1.014
S(1)–F(1)	1.576(2)	1.573	1.576	1.594	1.564(5)	1.569	1.568	1.581
S(1)–F(2)	1.518(2)	1.536	1.534	1.547	1.511(5)	1.521	1.523	1.536
S(1)–F(3)	1.529(2)	1.536	1.534	1.547	1.526(5)	1.521	1.523	1.536
S(1)–F(4)	1.588(2)	1.604	1.592	1.605	1.558(5)	1.569	1.568	1.581
Xe(1)--F(5)	2.618(2)							
As(1)–F(5)	1.758(2)							

	bond angles (°)							
	$F_4S{=}NXe^+$				$F_4S{=}NH_2^+$			
		calcd (C_1)[b]				calcd (C_s)[c]		
	exptl	MP2	PBE1PBE	B3LYP	exptl	MP2	PBE1PBE	B3LYP
Xe(1)–N(1)–S(1)	118.0(2)	118.6	117.9	119.1				
S(1)–N(1)–H(1)					105.8[d]	119.0	119.1	119.1
S(1)–N(1)–H(2)					128.6[d]	119.0	119.1	119.1
H(1)–N(1)–H(2)					122.3[d]	122.0	121.7	121.8
N(1)–S(1)–F(1)	86.4(2)	85.7	84.4	83.9	92.6(3)	90.7	90.8	90.9
N(1)–S(1)–F(2)	127.3(2)	126.7	126.5	126.8	125.2(3)	125.3	125.2	125.2
N(1)–S(1)–F(3)	127.8(2)	126.7	126.5	126.8	126.3(3)	125.3	125.2	125.2
N(1)–S(1)–F(4)	100.1(2)	98.6	99.1	99.0	91.9(3)	90.7	90.8	90.9
F(1)–S(1)–F(2)	88.6(1)	89.4	89.4	89.5	88.7(3)	89.6	89.6	89.5
F(1)–S(1)–F(3)	87.9(1)	89.4	89.4	89.5	88.3(3)	89.6	89.6	89.5
F(1)–S(1)–F(4)	173.5(1)	175.7	176.5	177.1	175.5(3)	178.6	178.5	178.2
F(2)–S(1)–F(3)	104.3(1)	106.2	106.4	105.7	108.5(3)	109.4	109.5	109.5
F(2)–S(1)–F(4)	88.1(1)	88.0	88.5	88.8	88.9(3)	89.6	89.6	89.5
F(3)–S(1)–F(4)	87.5(1)	88.0	88.5	88.8	88.8(3)	89.6	89.6	89.5
N(1)–Xe(1)--F(5)	172.2(1)							
Xe(1)--F(5) –As(1)	148.6(1)							

[a] The labels correspond to those used in Figures 5.6 and 5.8. Geometric parameters for the AsF_6^- anions of $[F_4S{=}NXe][AsF_6]$ and $[F_4S{=}NH_2][AsF_6]$ are found in Tables 5.4 and 5.5, respectively. [b] aug-cc-pVTZ(-PP) basis set. [c] aug-cc-pVTZ basis set. [d] The hydrogen atom positions were calculated using a riding model, therefore no estimated standard deviations are provided.

Table 5.4. Experimental and Calculated (C_1) Geometries for the $[F_4S{=}NXe][AsF_6]$ Ion Pair[a]

Bond Lengths (Å)

		calcd[b]					calcd[b]		
	exptl	MP2	PBE1PBE	B3LYP		exptl	MP2	PBE1PBE	B3LYP
Xe(1)–N(1)	2.084(2)	2.072	2.078	2.122	As(1)–F(5)	1.758(2)	1.867	1.904	1.933
N(1)–S(1)	1.556(2)	1.545	1.535	1.545	As(1)–F(6)	1.702(2)	1.681	1.696	1.708
S(1)–F(1)	1.576(2)	1.586	1.591	1.608	As(1)–F(7)	1.715(2)	1.723	1.734	1.747
S(1)–F(2)	1.518(2)	1.553	1.557	1.573	As(1)–F(8)	1.717(2)	1.690	1.707	1.720
S(1)–F(3)	1.529(2)	1.553	1.557	1.573	As(1)–F(9)	1.718(2)	1.723	1.734	1.747
S(1)–F(4)	1.588(2)	1.613	1.613	1.631	As(1)–F(10)	1.716(2)	1.690	1.707	1.720
Xe(1)--F(5)	2.618(2)	2.309	2.273	2.293					

Bond Angles (°)

		calcd[b]					calcd[b]		
	exptl	MP2	PBE1PBE	B3LYP		exptl	MP2	PBE1PBE	B3LYP
Xe(1)–N(1)–S(1)	118.0(2)	119.9	120.5	120.7	F(5)–As(1)–F(6)	179.6(1)	177.1	177.7	177.9
N(1)–S(1)–F(1)	86.4(2)	89.5	90.0	89.9	F(5)–As(1)–F(7)	89.0(1)	84.6	84.5	84.4
N(1)–S(1)–F(2)	127.3(2)	127.5	127.3	127.6	F(5)–As(1)–F(8)	89.0(1)	87.2	86.4	86.2
N(1)–S(1)–F(3)	127.8(2)	127.5	127.3	127.5	F(5)–As(1)–F(9)	88.4(1)	84.6	84.5	84.4
N(1)–S(1)–F(4)	100.1(2)	99.7	99.9	100.0	F(5)–As(1)–F(10)	88.3(1)	87.2	86.4	86.2
F(1)–S(1)–F(2)	88.6(1)	87.7	87.4	87.4	F(6)–As(1)–F(7)	91.4(1)	93.3	93.9	94.1
F(1)–S(1)–F(3)	87.9(1)	87.7	87.4	87.4	F(6)–As(1)–F(8)	91.1(1)	94.9	95.2	95.3
F(1)–S(1)–F(4)	173.5(1)	170.9	170.1	170.1	F(6)–As(1)–F(9)	91.4(1)	93.3	93.9	94.1
F(2)–S(1)–F(3)	104.3(1)	104.7	105.2	104.6	F(6)–As(1)–F(10)	91.3(1)	94.9	95.2	95.3
F(2)–S(1)–F(4)	88.1(1)	86.7	86.6	86.6	F(7)–As(1)–F(8)	89.6(1)	89.9	89.8	89.8
F(3)–S(1)–F(4)	87.5(1)	86.7	86.6	86.6	F(7)–As(1)–F(9)	90.2(1)	87.6	87.8	87.9
N(1)–Xe(1)--F(5)	172.2(1)	171.3	171.3	171.0	F(7)–As(1)–F(10)	177.3(1)	171.6	170.8	170.5
Xe(1)--F(5)–As(1)	148.5(1)	116.2	117.8	119.2	F(8)–As(1)–F(9)	177.5(1)	171.6	170.8	170.5
					F(8)–As(1)–F(10)	90.3(1)	91.4	91.1	91.0
					F(9)–As(1)–F(10)	89.8(1)	89.9	89.8	89.8

[a] The labels correspond to those used in Figure 5.6. [b] MP2 with (SDB-)cc-pVTZ basis set, PBE1PBE and B3LYP with aug-cc-pVTZ(-PP) basis set.

Table 5.5. Experimental Geometric Parameters for the Two Crystallographically Independent AsF_6^- Anions in $[F_4S{=}NH_2][AsF_6]$ [a]

Bond Lengths (Å)			
As(1)–F(5)	1.705(5)	As(2)–F(8)	1.704(4)
As(1)–F(6)	1.726(4)	As(2)–F(9)	1.715(4)
As(1)–F(7)	1.709(4)	As(2)–F(10)	1.728(4)
Bond Angles (°)			
F(5)–As(1)–F(6)	91.1(2)	F(8)–As(2)–F(9)	89.8(2)
F(5)–As(1)–F(6A)	88.9(2)	F(8)–As(2)–F(9A)	90.2(2)
F(5)–As(1)–F(7)	90.1(2)	F(8)–As(2)–F(9)	89.2(2)
F(5)–As(1)–F(7A)	89.9(2)	F(8)–As(2)–F(9A)	90.8(2)
F(6)–As(1)–F(7)	90.0(2)	F(9)–As(2)–F(10)	89.9(2)
F(6)–As(1)–F(7A)	90.0(2)	F(9)–As(2)–F(10A)	90.1(2)

[a] The atom labels correspond to those used in Figure 5.8.

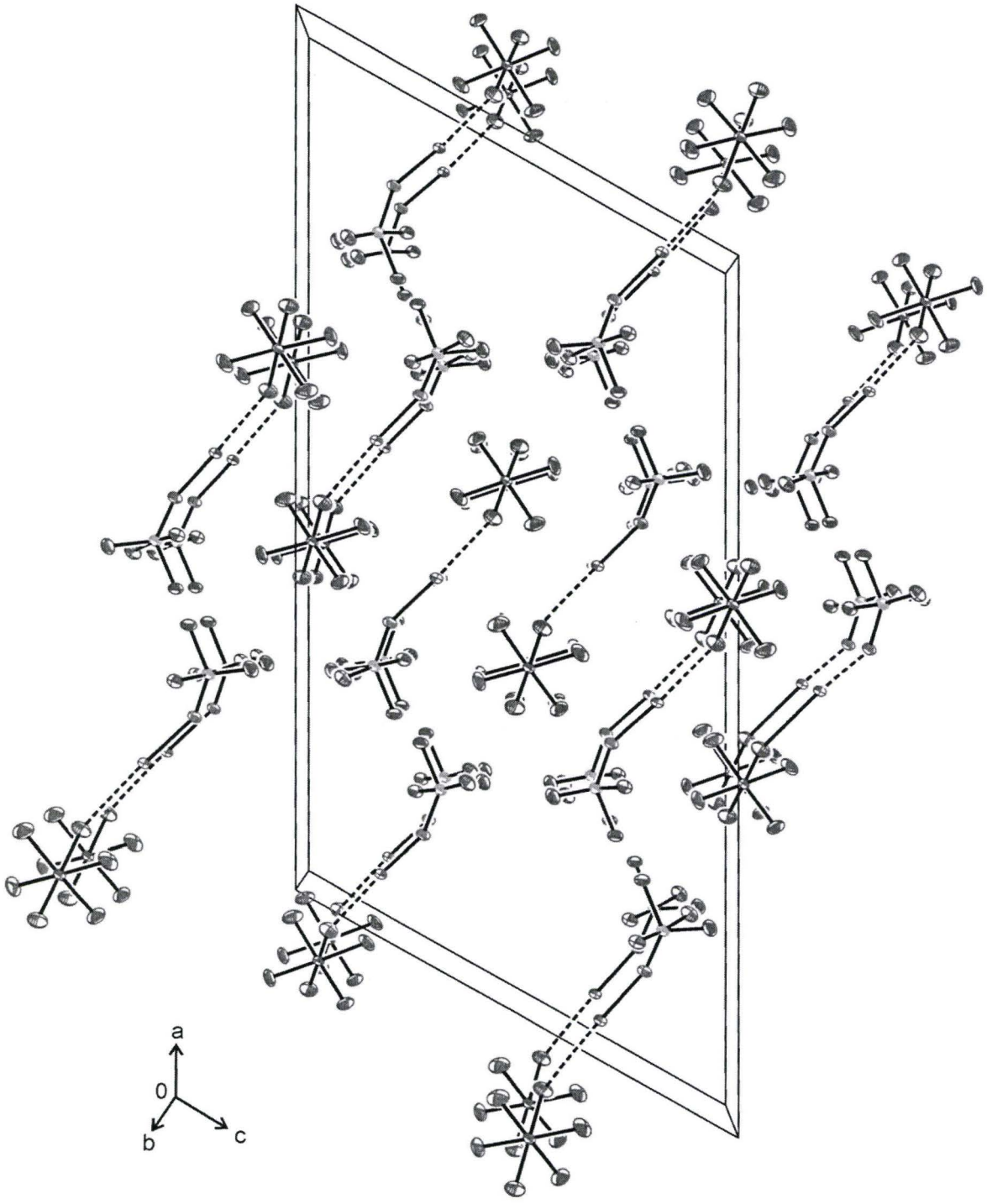

Figure 5.5. Packing diagram for the X-ray crystal structure of $[F_4S{=}NXe][AsF_6]$ viewed along the *b*-axis. Thermal ellipsoids are shown at the 50% probability level

but the cation and anion positions alternate along the *a*- and *c*-axes so that the ion pairs align in a head-to-tail fashion in the *ac*-plane. The $F_4S{=}NXe^+$ cation and the AsF_6^- anion form an ion pair by interaction through a Xe---F–As fluorine bridge (Figure 5.6). The symmetry lowering experienced by the anion is shown in the crystal structure to be essentially an axial distortion of its O_h symmetry in which the four equatorial As–F bonds and the As–F bond trans to the elongated bridging As–F bond are equal to within $\pm 3\sigma$, giving approximate local C_{4v} symmetry.

The Xe–N bond length (2.084(3) Å) is similar to that of $[F_5SN(H)Xe][AsF_6]$ (2.069(4) Å)[118] and is only slightly longer than the Xe–N bond in $[F_5TeN(H)Xe][AsF_6]$ (2.044(4) Å).[50] The xenon atom lies in the N(1), S(1), F(1), F(4)-plane and the bent S–N–Xe angle (118.0(2)°) is attributed to the stereochemically active valence electron lone pair on nitrogen. The S=N bond length (1.556(3) Å) is significantly longer than those of $F_4S{=}NF$ (1.520(9) Å)[74] and $F_4S{=}NCH_3$ (1.480(6) Å).[100] The axial S–F(1) bond (1.576(2) Å) anti to xenon is longer than those in $F_4S{=}NCH_3$ (1.546(7) Å)[100] and $F_4S{=}NF$ (1.535(12) Å),[74] while the *syn*-axial S–F(4) bond length (1.588(2) Å) is shorter than the corresponding bonds in $F_4S{=}NCH_3$ (1.643(4) Å)[100] and $F_4S{=}NF$ (1.615(7) Å).[74] The equatorial S–F(2) and S–F(3) bond lengths (1.518(2) and 1.529(2) Å) are also significantly shorter than those of $F_4S{=}NCH_3$ (1.567(4) Å)[100] and $F_4S{=}NF$ (1.564(5) Å).[74]

The long contacts to xenon in the crystal structure may be grouped into three categories that are significantly less than the sum of the Xe and F van der Waals radii (3.63 Å):[31] (1) the short ion-pair contact, Xe---F (2.618(2) Å), which is trans to the Xe–N bond and very similar to the corresponding contacts in $[F_5SN(H)Xe][AsF_6]$ (2.634(3)

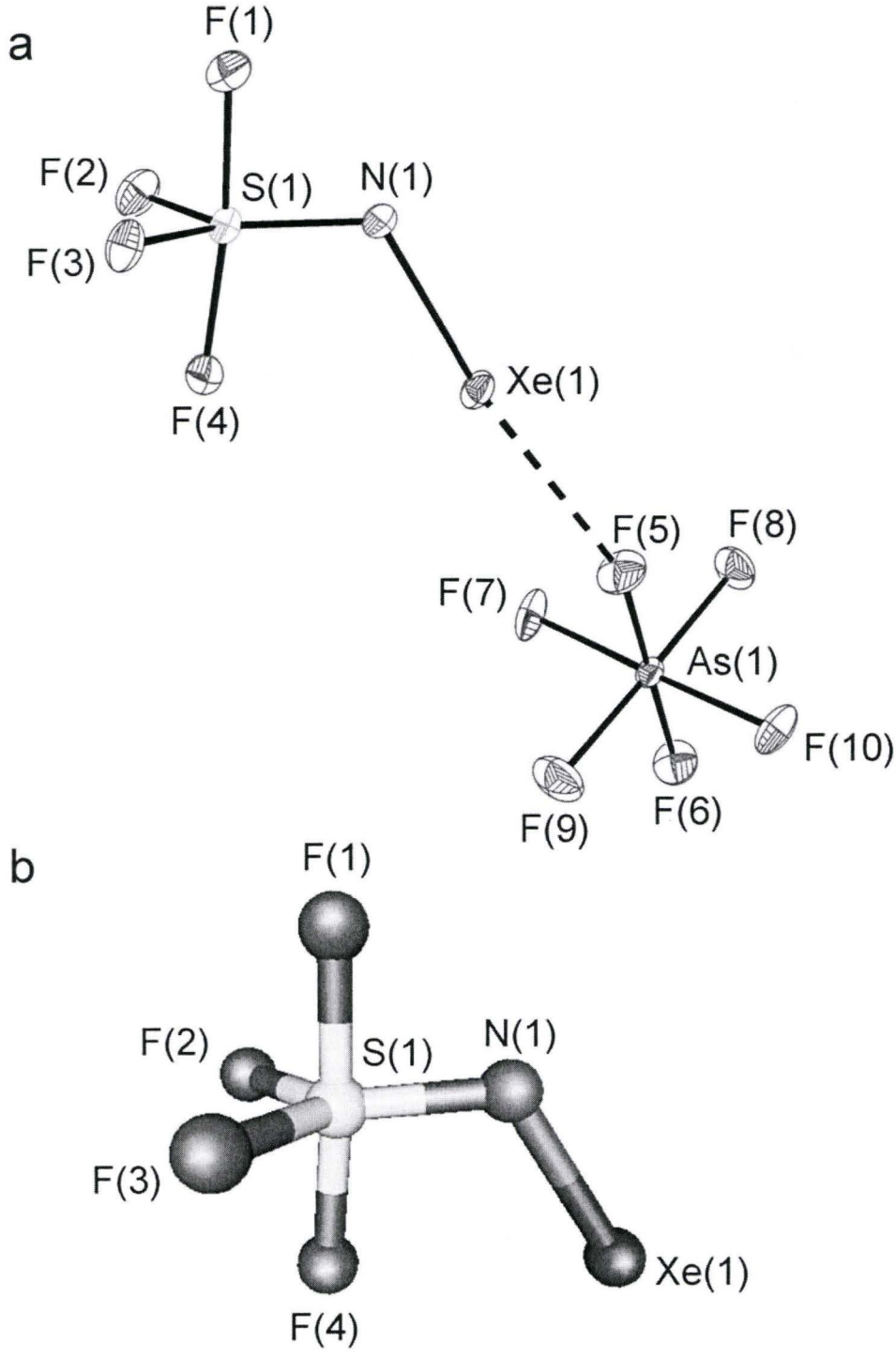

Figure 5.6. (a) The structural unit in the X-ray crystal structure of $[F_4S{=}NXe][AsF_6]$; thermal ellipsoids are shown at the 50% probability level. (b) Calculated geometry (MP2/aug-cc-pVTZ(-PP)) of the $F_4S{=}NXe^+$ cation.

Å)[118] and $[F_5TeN(H)Xe][AsF_6]$ (2.580(3) Å);[50] (2) three very similar contacts between fluorine atoms of the anion and xenon (F7A, 3.226(3); F9A, 3.226(3); F8A, 3.232(3) Å); and (3) three longer interionic contacts between xenon and fluorine atoms of the anion (F10A, 3.410(3); F7B, 3.452(3); F5A, 3.459(3) Å). The three contacts at 3.23 Å, when considered with the Xe–N bond and Xe---F ion pair contact, form a distorted trigonal bipyramidal arrangement about Xe. The three equatorial fluorine contacts are not coplanar with Xe, which is displaced 1.226(2) Å out of the F7A, F8A, F9A-plane towards the nitrogen atom (Figure 5.7). Thus, the three F-contacts avoid the torus of xenon valence electron density that results from its three valence electron lone pairs.[40]

5.2.3.2. $[F_4S{=}NH_2][AsF_6]$

The structure of $[F_4S{=}NH_2][AsF_6]$ consists of well-separated $F_4S{=}NH_2^+$ cations and AsF_6^- anions (Figure 5.8). There are two crystallographically independent anions which show little distortion from octahedral geometry, with As–F bonds ranging from 1.704(4) to 1.728(4) Å, in good agreement with previously reported values.[50,146] In the asymmetric unit, two half-occupancy arsenic atoms lie on inversion centers, with three fluorines defined on general positions for each arsenic atom, and the remaining three fluorines of each anion generated by symmetry. All atoms of the cation are on general positions. A distorted square planar arrangement of four fluorines from four different anions have close cation-anion N---F contacts (F10A, 2.824(3); F6, 2.841(3); F8, 2.916(3); F5A, 2.925(3) Å), which are less than the sum of the nitrogen and fluorine van der Waals radii (3.02 Å),[31] and result in a distorted square pyramidal arrangement with

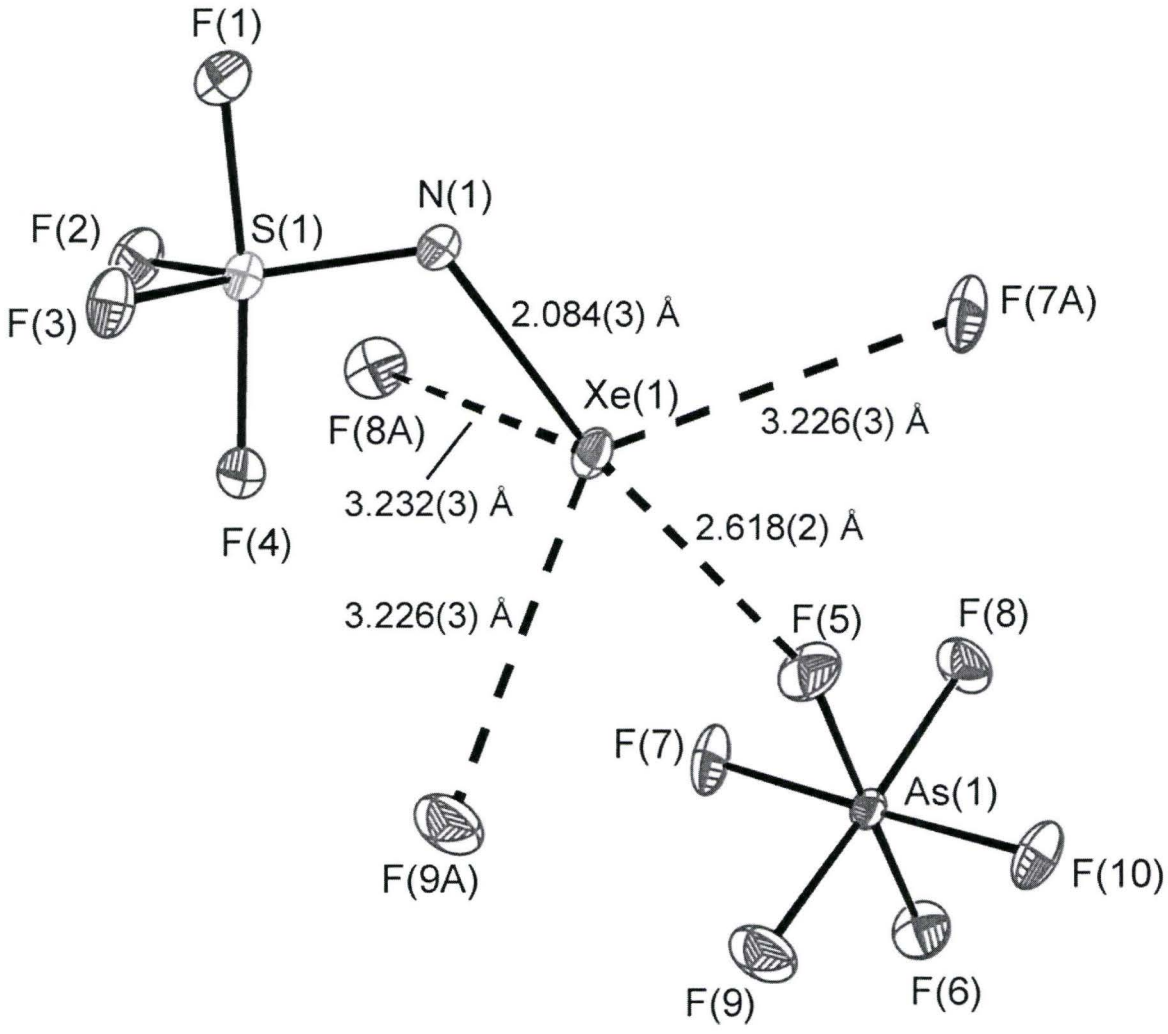

Figure 5.7. The structural unit in the X-ray crystal structure of $[F_4S{=}NXe][AsF_6]$ showing the closest contacts to xenon; thermal ellipsoids are shown at the 50% probability level.

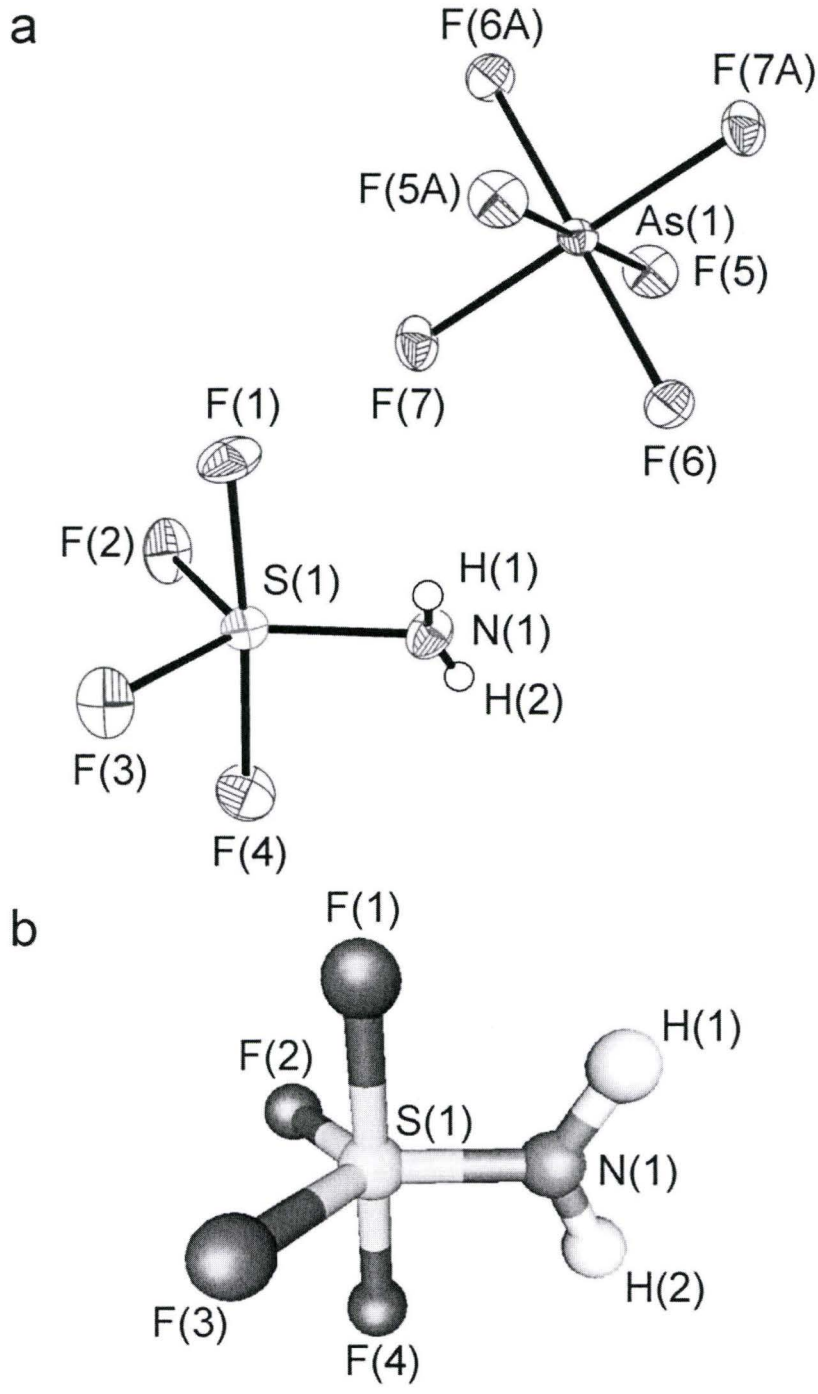

Figure 5.8. (a) The structural unit in the X-ray crystal structure of $[F_4S{=}NH_2][AsF_6]$; the hydrogen atom positions are calculated and the thermal ellipsoids of the non-hydrogen atoms are shown at the 50% probability level. (b) Calculated geometry (MP2/aug-cc-pVTZ) of the $F_4S{=}NH_2^+$ cation.

nitrogen at the apex and at a distance of 1.770(5) Å for its normal to the F10A, F6, F8, F5A-plane.

Although the electron densities and the three equatorial bond lengths were similar, the S=N bond could be differentiated on the basis of the three equatorial bond angles; i.e., two F–S–N angles were equal within experimental error, with the third smaller angle corresponding to the F–S–F angle. The crystallographic positions of the hydrogen atoms were calculated and therefore are not discussed.

The S=N bond length (1.511(6) Å) of $F_4S{=}NH_2^+$ is bracketed by those of $F_4S{=}NCH_3$ (1.480(6) Å)[100] and $F_4S{=}NF$ (1.520(9) Å)[74] and is significantly shorter than that of $F_4S{=}NXe^+$ (vide supra). The axial S–F(1) and S–F(4) bond lengths (1.564(5) and 1.558(5) Å) of $F_4S{=}NH_2^+$ are the same within experimental error and are significantly shorter than those in $F_4S{=}NXe^+$ (vide supra) and in isoelectronic $F_4S{=}CH_2$ (1.595(2) and 1.592(2) Å),[179] and $F_4S{=}O$ (1.596(4) Å).[180] Similarly, the equatorial S–F(2) and S–F(3) bond lengths (1.511(5) and 1.526(5) Å) are the same, within experimental error, and comparable to those in $F_4S{=}NXe^+$ (vide supra) and $F_4S{=}O$ (1.533(4) Å),[180] while they are significantly shorter than those of $F_4S{=}CH_2$ (1.560(2) and 1.561(2) Å).[179]

5.2.4. Raman Spectroscopy

The Raman spectrum of $[F_4S{=}NXe][AsF_6]$ (Figure 5.9) was assigned by comparison with those of $F_4S{=}NF$ (Table 5.6) and AsF_6^-,[6] and with those calculated for the gas-phase $F_4S{=}NXe^+$ cation (Table 5.7 and section 5.3) and the gas-phase $[F_4S{=}NXe][AsF_6]$ ion pair (Table 5.8) at several levels of theory. Calculated frequencies at

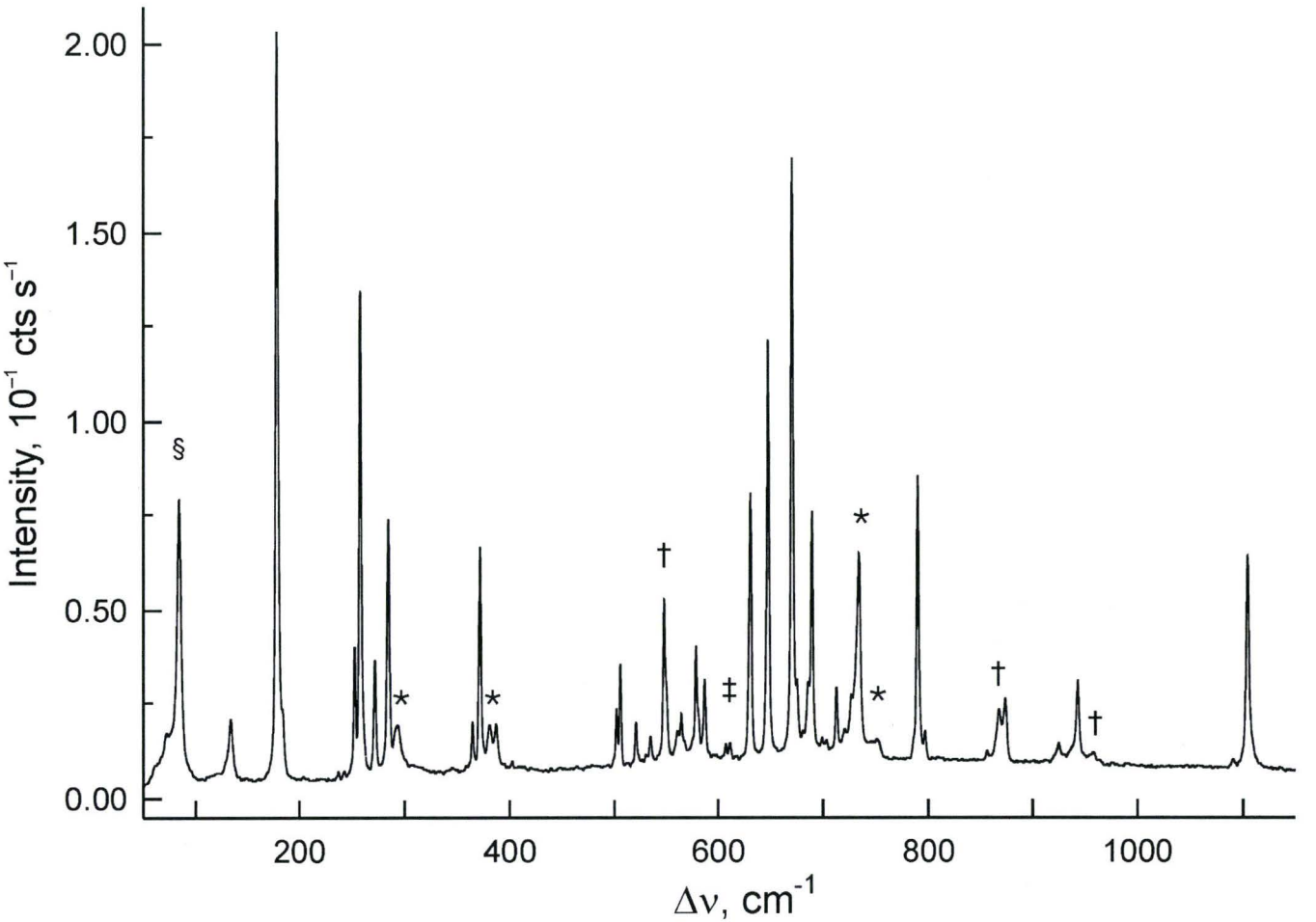

Figure 5.9. Raman spectrum of $[F_4S{=}NXe][AsF_6]$ formed by solid-state rearrangement of $[F_3S{\equiv}NXeF][AsF_6]$ after 70 min at 22 °C and recorded at –160 °C using 1064-nm excitation. Symbols denote peaks from unreacted $[F_3S{\equiv}NXeF][AsF_6]$ (†), ν(XeF) of unreacted $[XeF][AsF_6]$ (‡), an instrumental artifact (§), and FEP sample tube bands (*).

Table 5.6. Experimental Raman and Calculated Vibrational Frequencies, Intensities, and Assignments; Geometrical Parameters; and Natural Bond Orbital (NBO) Analyses for $F_4S{=}NF$

freq, cm^{-1}				
	calcd[b]			assgnts[c]
exptl[a]	MP2	PBE1PBE	B3LYP	
1125 m	1173 (6) [52]	1168 (5) [40]	1093 (5) [40]	ν(S=N – NF5)
933 sh	955 (3) [260]	962 (2) [322]	913 (2) [310]	ν(S=N + NF5)
870 sh	877 (2) [312]	882 (2) [322]	838 (3) [313]	ν(SF1 – SF4)
850 m	854 (3) [198]	854 (3) [200]	809 (4) [198]	ν(SF2 – SF3)
754 s	759 (31) [100]	758 (27) [81]	718 (28) [96]	ν(SF2 + SF3 + SF4) + ν(S=N)
697 w	647 (6) [14]	649 (6) [12]	620 (9) [10]	ν(SF1 + SF4)
644 s	586 (2) [13]	586 (3) [11]	562 (3) [7]	δ(NSF2F3) o.o.p.
591 w	559 (1) [24]	554 (1) [21]	535 (1) [18]	δ(NSF4) + ρ_w(F2SF3)
569 w	492 (4) [3]	495 (4) [4]	476 (5) [3]	δ(NSF1)
491 s	489 (1) [<1]	484 (1) [<1]	467 (1) [<1]	δ(F1SF2) + δ(F3SF4)
476 m	467 (4) [8]	464 (4) [8]	442 (4) [6]	δ(NSF1F4) o.o.p. + ρ_r(F2SF3)
341 w	337 (1) [2]	333 (1) [2]	323 (1) [2]	δ(SNF5) i.p. + δ(NSF4)
316 w	320 (1) [<1]	320 (1) [<1]	306 (1) [<1]	δ(SNF5) o.o.p.
271 m	267 (2) [2]	264 (2) [2]	254 (2) [2]	δ(F1SF4) – δ(F2SF3)
140 m	132 (1) [<1]	130 (1) [<1]	121 (2) [<1]	δ(NSF2) – δ(NSF3) + ρ_t(SNF5)

Table 5.6. (continued...)

calcd bond lengths (Å)

	MP2	PBE1PBE	B3LYP
S–N	1.570	1.566	1.581
S–F1	1.591	1.590	1.606
S–F2	1.568	1.569	1.586
S–F3	1.568	1.569	1.586
S–F4	1.598	1.597	1.614
N–F5	1.391	1.373	1.392

charges / valencies

atom	MP2	PBE1PBE	B3LYP	MP2	PBE1PBE	B3LYP
S	2.38	2.37	2.35	3.90	4.05	3.99
N	–0.37	–0.37	–0.35	1.70	1.79	1.76
F1	–0.45	–0.45	–0.45	0.59	0.65	0.63
F2	–0.43	–0.43	–0.43	0.59	0.63	0.64
F3	–0.43	–0.43	–0.43	0.59	0.63	0.64
F4	–0.47	–0.47	–0.47	0.56	0.62	0.60
F5	–0.22	–0.22	–0.23	0.58	0.61	0.60

calcd bond angles (°)

	MP2	PBE1PBE	B3LYP
S–N–F5	111.9	112.4	112.1
N–S–F1	87.7	87.9	87.8
N–S–F2	129.7	129.5	129.6
N–S–F3	129.7	129.5	129.6
N–S–F4	98.6	98.7	98.9
F1–S–F2	88.1	88.0	88.0
F1–S–F3	88.1	88.0	88.0
F1–S–F4	173.7	173.5	173.4
F2–S–F3	100.3	100.5	100.3
F2–S–F4	87.9	87.8	87.8
F3–S–F4	87.9	87.8	87.8

bond orders

bond	MP2	PBE1PBE	B3LYP
S–N	1.20	1.23	1.22
S–F1	0.66	0.70	0.68
S–F2	0.70	0.72	0.72
S–F3	0.70	0.72	0.72
S–F4	0.66	0.70	0.68
N–F5	0.60	0.64	0.62

[a] Experimental values from ref 14; abbreviations denote strong (s), medium (m), weak (w), and shoulder (sh). [b] aug-cc-pVTZ basis set. The calculated infrared intensities (in km mol^{-1}) are given in square brackets and calculated Raman intensities (in $Å^4$ amu^{-1}) are given in parentheses. [c] Abbreviations denote out-of-plane (o.o.p.), in-plane (i.p.) (planes are defined by the atoms they contain), wag (ρ_w), rock (ρ_r), and twist (ρ_t).

Table 5.7. Raman Frequencies and Intensities for $[F_4S{=}NXe][AsF_6]$ and Calculated Vibrational Frequencies, Intensities, and Assignments for $F_4S{=}NXe^+$

freq, cm^{-1}					
	calcd[b]			assgnts[c]	
exptl[a]	MP2	PBE1PBE	B3LYP	$F_4S{=}NXe^+$ (C_1)	AsF_6^- (C_{4v})
1104 (29) 1097 (1)	1102 (5) [322]	1077 (15) [297]	1020 (19) [283]	ν(S=N)	
943 (11) 924 (2)	958 (2) [173]	962 (3) [173]	919 (3) [169]	ν(SF2 – SF3)	
874 (8) 857 (1)	903 (8) [286]	908 (11) [285]	863 (13) [279]	ν(SF1 – SF4)	
796 (4) 789 (38)	806 (12) [82]	789 (12) [52]	744 (13) [47]	ν(SF2 + SF3 + SF4) + ν(S=N)	
726 sh 712 (9)					ν_8 (E)
689 (32)					ν_1 (A_1)
675 sh 670 (79)	664 (17) [23]	614 (16) [36]	588 (16) [30]	δ(NSF2F3) o.o.p.	
647 (55) 630 (35)	645 (8) [7]	658 (5) [2]	632 (5) [3]	ν(SF1 + SF4)	
587 (11)					ν_2 (A_1)
579 (15)					ν_5 (B_1)
565 (6) 561 (3)	578 (1) [30]	565 (3) [33]	545 (3) [26]	δ(NSF1) – δ(NSF4) + ρ_w(F2SF3)[d]	
535 (3) 530 sh	554 (1) [65]	546 (3) [11]	525 (4) [124]	δ(F1SF4) + δ(F2SF3)	
521 (5)	508 (1) [<1]	502 (1) [1]	483 (1) [1]	δ(F1SF2) + δ(F3SF4)	
506 (13) 502 (7)	497 (2) [17]	494 (2) [17]	474 (2) [15]	δ(NSF1F4) o.o.p. + ρ_r(F2SF3)	
402 (1)					ν_4 (A_1)
387 (6)					ν_3 (A_1)

Table 5.7. (continued…)

371 (30)					ν_7 (B_2)
364 (7)					ν_9 (E)
346 (1) br	450 (4) [20][e,f]	424 (2) [82] [e]	400 (3) [46] [e]	ν(As–F5) [e]	
	441 (1) [129][e,f]	416 (4) [76] [e]	411 (6) [104] [e]	ν(Xe--F5) [e]	
285 (35)	256 (2) [1]	272 (2) [1]	263 (1) [<1]	δ(F1SF4) + δ(F2SF3)[d]	
273 (16)	255 (1) [1]	259 (1) [1]	251 (1) [1]	δ(XeNS) o.o.p. + δ(NSF2) – δ(NSF3)	
259 (65)	288 (3) [<1]	245 (4) [5]	226 (4) [6]	ν(XeN)	
253 (18)					
184 sh	166 (5) [<1]	149 (7) [1]	135 (9) [2]	δ(XeNS) i.p.	
178 (100)					
134 (8)	97 (1) [<1]	94 (1) [<1]	90 (1) [<1]	torsion about Xe–N bond	

[a] Values in parentheses denote experimental Raman intensities and abbreviations denote shoulder (sh) and broad (br). [b] aug-cc-pVTZ(-PP) basis set. Calculated Raman intensities (Å^4 amu^{-1}) are given in parentheses and calculated infrared intensities (km mol^{-1}) are given in square brackets. [c] Abbreviations denote out of plane (o.o.p.), in plane (i.p.) (planes are defined by the atoms they contain), wag (ρ_w), and rock (ρ_r). [d] The coupled δ(NSF4) bend calculated at the MP2 level does not contribute to the split band at 561, 565 cm^{-1}, but it does contribute to the band at 285 cm^{-1}. [e] Values and mode descriptions are for the calculated ion pair; see Table 5.8 for a full frequency listing and assignments. [f] (SDB-)cc-pVTZ basis set.

Table 5.8. Experimental and Calculated Vibrational Frequencies, Intensities, and Assignments for the $[F_4S{=}NXe][AsF_6]$ Ion Pair

freq, cm^{-1}					
	calcd[b]			assgnts[c]	
exptl[a]	MP2[d]	PBE1PBE[e]	B3LYP[e]	$[F_4S{=}NXe][AsF_6]$ (C_1)	AsF_6^- (C_{4v})
1104 (29) 1097 (1)	1169 (29) [526]	1154 (44) [567]	1094 (62) [559]	ν(S=N)	
943 (11) 924 (2)	911 (3) [195]	899 (3) [189]	852 (4) [187]	ν(SF2 – SF3)	
874 (8) 857 (1)	880 (10) [316]	863 (15) [309]	817 (21) [302]	ν(SF1 – SF4)	
796 (4) 789 (38)	807 (10) [138]	796 (12) [131]	751 (14) [141]	ν(SF2 + SF3 + SF4) + ν(S=N)	
726 sh 712 (9)	776 (4) [196]	753 (7) [190]	728 (9) [184]	ν(AsF8 – AsF9) + ν(AsF7 – AsF10) + ν(AsF6)	
	774 (1) [158]	751 (1) [157]	726 (2) [155]	ν(AsF8 – AsF9) + ν(AsF10 – AsF7)	ν_8 (E)
	765 (3) [143]	745 (4) [139]	722 (5) [142]	ν(AsF6)	ν_1 (A_1)
689 (32)	684 (14) [62]	676 (18) [57]	652 (21) [49]	$\nu(AsF_{4eq})$	ν_2 (A_1)
675 sh 670 (79)	667 (35) [10]	658 (57) [14]	637 (50) [10]	δ(NSF2F3) o.o.p.	
647 (55) 630 (35)	626 (9) [8]	617 (14) [4]	587 (26) [6]	ν(SF1 + SF4)	
587 (11) 579 (15)	606 (1) [6]	596 (2) [4]	579 (2) [4]	ν(AsF8 + AsF9) – ν(AsF7 + AsF10)	ν_5 (B_1)
565 (6) 561 (3)	584 (2) [19]	574 (4) [17]	553 (3) [13]	δ(NSF1) – δ(NSF4) + ρ_w(F2SF3)	
535 (3) 530 sh	565 (2) [37]	556 (2) [34]	537 (2) [33]	δ(F1SF4) + δ(F2SF3)	
521 (5)	518 (1) [<1]	510 (1) [<1]	492 (1) [<1]	δ(F1SF2) + δ(F3SF4)	
506 (13) 502 (7)	503 (3) [14]	498 (3) [14]	476 (3) [11]	δ(NSF1F4) o.o.p. + ρ_r(F2SF3)	
402 (1) 387 (6)	414 (<1) [58]	385 (<1) [50]	376 (<1) [48]	AsF_6^- deformation modes	
	404 (3) [81]	379 (1) [35]	370 (2) [8]		
	398 (1) [21]	372 (1) [45]	362 (1) [31]		
371 (30) 364 (7)	370 (5) [211]	345 (<1) [236]	328 (<1) [296]	AsF_6^- deformation modes	
	365 (1) [<1]	336 (1) [<1]	326 (1) [<1]		
	275 (17) [120]	266 (3) [51]	261 (1) [121]		

Table 5.8. (continued…)

346 (1) br	450 (4) [20]	424 (2) [82]	400 (3) [46]	ν(As–F5)
	441 (1) [129]	416 (4) [76]	411 (6) [104]	ν(Xe--F5)
285 (35)	251 (4) [<1]	240 (4) [3]	232 (8) [1]	δ(F1SF4) – δ(F2SF3)
273 (16)	269 (1) [1]	268 (1) [1]	258 (1) [1]	δ(XeNS) o.o.p. + δ(NSF2) – δ(NSF3)
259 (65)	282 (9) [1]	273 (27) [70]	255 (30) [14]	ν(XeN)
253 (18)				
n.o.	248 (<1) [<1]	231 (<1) [<1]	224 (<1) [<1]	coupled deformation modes of $F_4S{=}NXe^+$ and AsF_6^-
n.o.	229 (<1) [<1]	208 (<1) [<1]	201 (<1) [<1]	
184 sh	180 (7) [31]	175 (5) [25]	168 (5) [27]	δ(XeNS) i.p.
178 (100)				
n.o.	135 (1) [29]	132 (6) [18]	126 (9) [15]	coupled deformation mode of $F_4S{=}NXe^+$ and AsF_6^-
134 (8)	121 (1) [1]	121 (1) [1]	116 (1) [1]	torsion about Xe–N bond
n.o.	85 (<1) [1]	78 (<1) [1]	74 (<1) [1]	δ(Xe--F–As) i.p.
n.o.	62 (<1) [1]	58 (<1) [1]	55 (<1) [1]	δ(Xe--F–As) o.o.p.
n.o.	33 (<1) [1]	32 (1) [1]	31 (1) [1]	coupled deformation modes of $F_4S{=}NXe^+$ and AsF_6^-
n.o.	32 (<1) [<1]	28 (<1) [<1]	24 (<1) [<1]	
n.o.	5 (<1) [<1]	3 (<1) [<1]	7 (<1) [<1]	

[a] Values in parentheses denote experimental Raman intensities, abbreviations denote shoulder (sh), broad (br) and not observed (n.o.). [b] Calculated Raman intensities (in $Å^4$ amu^{-1}) are given in parentheses and calculated infrared intensities (in km mol^{-1}) are given in square brackets. [c] Abbreviations denote out of plane (o.o.p.), in plane (i.p.) (planes are defined by the atoms they contain), four equatorial fluorines (F_{4eq}), wag (ρ_w), and rock (ρ_r). The anion mode symmetry assignments are made under C_1 symmetry and are also correlated to C_{4v} symmetry (in square brackets). [d] (SDB-)cc-pVTZ basis set. [e] aug-cc-pVTZ(-PP) basis set.

the MP2/aug-cc-pVTZ(-PP) level provided the best overall agreement with the experimental values (see section 5.3) and are considered in the ensuing discussion (indicated in square brackets). The $[F_4S{=}NXe][AsF_6]$ ion pair geometry and vibrational frequencies were calculated at the MP2/(SDB-)cc-pVTZ level.

The 15 vibrational modes of $F_4S{=}NXe^+$ have been assigned under C_1 symmetry, in accord with the energy-minimized geometry, rather than the ideal C_s symmetry expected for the gas-phase cation (see section 5.3). Accordingly, all modes belong to A irreducible representations and are both Raman- and infrared-active. The fluorine bridge between the cation and anion (see section 5.2.3.1) lowers the anion symmetry, giving rise to additional lines in the vibrational spectrum. Symmetry lowering of the anion can be approximated by local C_{4v} symmetry,[65] and the vibrational spectra can be assigned under this or a lower symmetry (C_{2v}, C_s, or C_1). In the present study, the anion modes have been assigned under local C_{4v} symmetry, which is expected to result in 15 fundamental vibrational modes belonging to the irreducible representations $4A_1 + 2B_1 + B_2 + 4E$, all of which are Raman-active, with the A_1 and E modes also infrared active. In practice, 8 of the 11 predicted vibrational bands were observed in the Raman spectrum (correlations with O_h symmetry are given in square brackets): 689 (A_1) and 712, 726 (E) [T_{1u}], 579 (B_1) and 587 (A_1) [E_g], 387 (A_1) and 402 (A_1) [T_{1u}], and 364 (E) and 371 (B_2) [T_{2g}] cm^{-1}. Factor-group analyses correlating the free cation (C_s) and distorted local anion (C_{4v}) symmetries to their crystal site symmetries (C_1) and to the unit cell symmetry (C_{2h}) are provided in Table 5.9. The A' and A" irreducible representations of the C_s gas-phase cation correlate to A irreducible representations under C_1 site symmetry, while the doubly-degenerate E-modes of the anion

Table 5.9. Correlation Diagrams for the Vibrational Modes of $[F_4S{=}NXe][AsF_6]$[a]

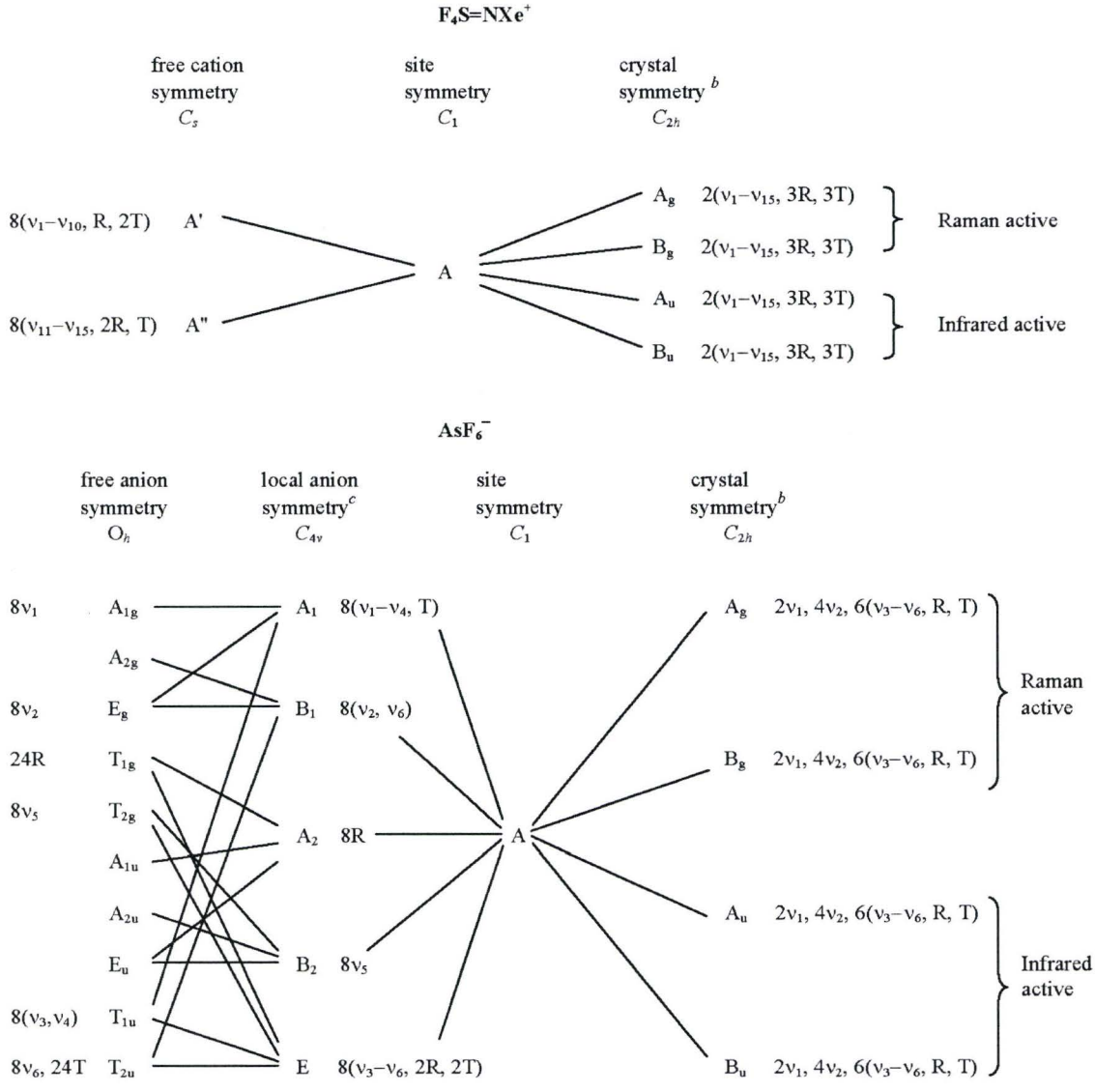

[a] The bending and torsional modes associated with the Xe---F–As bridge interaction are not accounted for in the above analysis. The irreducible representations are $\Gamma = 15A$ for the $F_4S{=}NXe^+$ cation and $\Gamma = 4A_1 + 2B_1 + B_2 + 4E$ for the AsF_6^- anion. [b] The crystallographic space group is $C2/c$ with $Z = 8$. [c] The local anion symmetry (C_{4v}) is only approximate and refers to AsF_6^- in the ion pair. The lower symmetry results from elongation of an As–F bond by formation of a fluorine bridge to xenon in $F_4S{=}NXe^+$.

are split due to site symmetry lowering. Both the cation and anion bands are split into Raman-active A_g and B_g components and infrared-active A_u and B_u components under C_{2h} crystal symmetry, giving the potential to observe a total of 30 bands for the cation and 30 bands for the anion. It proved possible to resolve this splitting in the Raman spectrum for 11 of the 15 observed cation bands and for one anion band.

The ν(XeN) stretching frequency at 253, 259 [288] cm^{-1} is similar to that observed in $F_5SN(H)Xe^+$ (224 cm^{-1}).[118] The most intense band in the Raman spectrum of $[F_4S{=}NXe][AsF_6]$ occurs at 178, 184 [166] cm^{-1} and is assigned to the in-plane Xe–N–S bend, which compares well with the strong band observed at 150 cm^{-1} for $F_5SN(H)Xe^+$.[118] The out-of-plane Xe–N–S bend at 273 [255] cm^{-1} and the in-plane bend bracket the Xe–N–S bends reported for $XeN(SO_2F)_2^+$ (226, 241, 251, 259, 267 cm^{-1})[49] and $F[XeN(SO_2F)_2]_2^+$ (208, 224, 231, 240, 247, 260, 264 cm^{-1})[49] which are all higher in frequency than those for $FXeN(SO_2F)_2$ (96, 111, 116, 119 cm^{-1}).[46] Although no ν(XeN) stretch was reported for $XeN(SO_2F)_2^+$,[49] it now appears likely, based on the assigned frequencies of $F_4S{=}NXe^+$ and $F_5SN(H)Xe^+$ [118] that at least one of the bands previously assigned to δ(XeNS) in $XeN(SO_2F)_2^+$ is, in fact, the ν(XeN) stretch, namely, the band at 251 cm^{-1}. The S=N stretch at 1097, 1104 [1102] cm^{-1} is in good agreement with that of $F_4S{=}NF$ (1125 cm^{-1}),[74] and is lower in frequency than those of $F_4S{=}NSF_5$ (1299 cm^{-1})[167] and $F_4S{=}NCF_3$ (1343 cm^{-1}).[163] The broad, low-intensity band at 346 cm^{-1} could not be assigned by comparison with the modes calculated for the $F_4S{=}NXe^+$ cation, and was assigned to ν(Xe---F) by comparison with its counterparts in $[XeN(SO_2F)_2][AsF_6]$ (317 cm^{-1}),[49] $[XeOTeF_5][AsF_6]$ (365 cm^{-1}),[40,150] and $[XeF][AsF_6]$ (417 cm^{-1}).[112] The ν(Xe---F)

stretching frequency calculated for the $[F_4S{=}NXe][AsF_6]$ ion pair [441 cm^{-1}] was significantly higher, which is in accordance with the underestimated Xe---F distance obtained for the calculated geometry (vide supra; also see Table 5.4). The experimental SF_4 stretches (670–958 cm^{-1}) and bends (285–647 cm^{-1}) fall into ranges that are similar to those of the benchmark, $F_4S{=}NF$.[74] The low-intensity band at 134 [97] cm^{-1} is assigned to the torsional motion of the $F_4S{=}N$-group about the Xe–N bond. No other calculated low-frequency anion bands or coupled deformation bands of the cation could be observed in the experimental spectrum.

5.3. Computational Results

Quantum-chemical calculations were carried out for $F_4S{=}NH_2^+$, $F_4S{=}NXe^+$, and the $[F_4S{=}NXe][AsF_6]$ ion pair, using B3LYP, PBE1PBE, and MP2 methods, to support the vibrational assignments (see section 5.2.4) and to gain insight into their structures and bonding (Tables 5.3 and 5.4). Comparison of the calculated and experimental frequencies for the benchmark, $F_4S{=}NF$, showed that the B3LYP calculations provided vibrational frequencies that were in better agreement for the S–N stretches, while the MP2 frequencies were in better agreement for the S–F stretching and F–S–F bending frequencies (Table 5.6). Assignments of the $F_4S{=}N$-group modes in $F_4S{=}NXe^+$ were made taking these trends into account. The best overall agreement (geometric parameters and vibrational frequencies) for the species discussed in this work was obtained for the MP2 calculations, using the aug-cc-pVTZ(-PP) basis set for the cations, and (SDB-)cc-

pVTZ for the ion pair. These values are referred to in the subsequent discussion and appear in square brackets.

5.3.1. Calculated Geometries

Although very close to C_s symmetry, the MP2, PBE1PBE, and B3LYP energy-minimized geometries of the $F_4S{=}NH_2^+$ and $F_4S{=}NXe^+$ cations and the $[F_4S{=}NXe][AsF_6]$ ion pair optimized to C_1 symmetry. For $[F_4S{=}NXe][AsF_6]$, the largest discrepancies occurred for the fluorine bridge, Xe---F–As. The calculated Xe---F and As–F fluorine-bridge bond lengths [2.309 and 1.867 Å] are under- and overestimated when compared with their respective experimental values, 2.618(2) and 1.758(2) Å. The calculated Xe---F bond order [0.11] is consistent with weak covalent bonding when compared with the bond order [0.53] of the Xe–N bond. The Xe---F–As angle, found to be bent in the low-temperature X-ray crystal structure (148.5(1)°), differs significantly from that of the calculated geometry [116.2°]. This is expected because this angle is very deformable and easily influenced by crystal packing. The deformability of this angle is supported by the calculated δ(Xe---F–As) frequencies which occur at very low values [62, 85 cm^{-1}]. Similar discrepancies have been found between the Xe---F–As angles for the calculated ion pairs, $[F_5SN(H)Xe][AsF_6]$[118] and $[F_5TeN(H)Xe][AsF_6]$,[50] and those in their crystal structures. It is noteworthy that the calculated local symmetry of AsF_6^- in $[F_4S{=}NXe][AsF_6]$ is better approximated by C_{2v} symmetry than by the local C_{4v} symmetry used to assign the vibrational frequencies of AsF_6^- in the ion pair. Local C_{4v} symmetry was employed for vibrational assignments because the AsF_6^- anion closely approximates this symmetry in the

X-ray crystal structure (see sections 5.2.3.1 and 5.2.4). In general, calculated S=N bond lengths were longer, and calculated S–F bond lengths were longer or the same within the error limits of the experimental bond lengths for $F_4S{=}NF$ and the $F_4S{=}NXe^+$ and $F_4S{=}NH_2^+$ cations (see section 5.3.2). In the calculated $F_4S{=}NH_2^+$ geometry, the hydrogen atoms are in the plane of the N, S, and axial F atoms, in agreement with the ^{19}F NMR spectrum (see section 5.2.2.2), establishing that the $F_4S{=}NH_2^+$ cation is isostructural with the isoelectronic $F_4S{=}CH_2$ molecule. The hydrogen positions of $F_4S{=}NH_2^+$ could not, however, be determined by single-crystal X-ray diffraction where a riding model was used to calculate their crystallographic positions.

The S=N bond length in $F_4S{=}NXe^+$ is predicted to be 0.025 Å longer than that of $F_4S{=}NH_2^+$, and the S–F bond lengths are also predicted to be longer, i.e., S–F(1) 0.004, S–F(2) 0.015, S–F(3) 0.015, S–F(4) 0.035 Å. This trend is in agreement with the experimental S=N bond length of $F_4S{=}NXe^+$, which is 0.045(9) Å longer than that of $F_4S{=}NH_2^+$, and with the experimental S–F(4) bond length, which is longer by 0.030(7) Å. These longer bond lengths are attributed to the steric effect of the xenon atom (see section 5.3.4). The experimental trends for $F_4S{=}NXe^+$ and $F_4S{=}NH_2^+$cannot be commented upon for S–F(1), S–F(2), and S–F(3) bond lengths because they are the same within $\pm 3\sigma$.

5.3.2. Calculated Frequencies

The calculated vibrational frequencies and intensities of $F_4S{=}NXe^+$ were used to assist in the assignment of the experimental Raman frequencies (see Table 5.7 and section 5.2.4), and although the Raman spectrum of $[F_4S{=}NH_2][AsF_6]$ could not be recorded (see

section 5.2.1) the vibrational frequencies were calculated (Table 5.10) and compared with the calculated frequencies of $F_4S{=}NXe^+$. All calculated stretching frequencies of the $F_4S{=}NH_2^+$ cation are shifted to significantly higher frequencies than the corresponding frequencies of $F_4S{=}NXe^+$: ν(S=N), [+69 cm^{-1}]; ν(SF2 – SF3), [+53 cm^{-1}]; ν(SF1 – SF4), [+29 cm^{-1}]; ν(SF2 + SF3 + SF4) + ν(S=N), [+31 cm^{-1}]; and ν(SF1 + SF4), [+40 cm^{-1}]. In contrast, there is no single trend for the calculated bending modes, i.e., the in-phase F–S–F bends are shifted to higher frequency (δ(F1SF4) + δ(F2SF3), [+26 cm^{-1}]; δ(F1SF2) + δ(F3SF4), [+6 cm^{-1}]) and the out-of-phase bend is effectively unshifted (δ(F1SF4) – δ(F2SF3), [+1 cm^{-1}]). In addition, modes involving N are shifted to lower frequency (δ(NSF2F3) o.o.p., [–82 cm^{-1}]; δ(F1SN) – δ(F4SN), [–43 cm^{-1}]) except for δ(NSF1F4) o.o.p., [–1 cm^{-1}], which is essentially unshifted.

5.3.3. Comparison of Charges, Valencies, and Bond Orders Among the $F_4S{=}NXe^+$, $F_4S{=}NH_2^+$, $F_5SN(H)Xe^+$, and $F_5TeN(H)Xe^+$ Cations

The natural bond orbital (NBO) charges, valencies, and bond orders calculated by the MP2, PBE1PBE, and B3LYP methods (MP2 values are reported in square brackets) for $F_4S{=}NXe^+$ and $F_4S{=}NH_2^+$ are listed in Table 5.11, and for $F_5SN(H)Xe^+$ and $F_5TeN(H)Xe^+$ are listed in Table 5.12. Positive charges in both $F_4S{=}NXe^+$ and $F_4S{=}NH_2^+$ reside on S, H, and Xe, with the positive charge on S [2.50] in $F_4S{=}NXe^+$ being slightly less than that in $F_4S{=}NH_2^+$ [2.61]. The Xe–N bond order of the $F_4S{=}NXe^+$ cation [0.59] is significantly greater than that of $F_3S{\equiv}NXeF^+$ [0.29], and essentially the same as those calculated for $F_5SN(H)Xe^+$ [0.60] and $F_5TeN(H)Xe^+$ [0.62], indicating considerable and comparable

Table 5.10. Calculated Vibrational Frequencies, Intensities and Assignments for $F_4S{=}NH_2^+$

calcd freq, cm^{-1} [a]			assgnts[b]
MP2	PBE1PBE	B3LYP	
3659 (24) [258]	3655 (26) [238]	3618 (28) [235]	ν(NH1 – NH2)
3516 (69) [229]	3519 (69) [214]	3848 (72) [213]	ν(NH1 + NH2)
1591 (1) [104]	1579 (2) [106]	1576 (2) [94]	δ(H1NH2)
1171 (4) [197]	1157 (3) [200]	1118 (3) [201]	ν(S=N)
1157 (1) [112]	1153 (<1) [119]	1149 (1) [103]	δ(SNH1) – δ(SNH2)
1011 (1) [198]	1005 (2) [199]	963 (2) [196]	ν(SF2 – SF3)
932 (<1) [249]	932 (<1) [243]	895 (<1) [253]	ν(SF1 – SF4)
837 (24) [41]	830 (23) [37]	794 (25) [39]	ν(NSF_4)
685 (4) [3]	684 (4) [3]	657 (4) [3]	ν(SF1 + SF4) – ν(SF2 + SF3 + S=N)
681 (<1) [0]	661 (<1) [0]	648 (<1) [0]	ρ_t(H1NH2)
582 (<1) [23]	575 (<1) [22]	562 (<1) [22]	δ(NSF2F3) o.o.p.
580 (1) [67]	574 (1) [63]	560 (1) [60]	δ(F1SF4) + δ(F2SF3)
562 (1) [36]	565 (<1) [70]	553 (<1) [68]	ρ_w(H1NH2)
540 (1) [<1]	532 (1) [<1]	522 (1) [<1]	δ(NSF1) – δ(NSF4)
514 (1) [0]	509 (1) [<1]	496 (1) [0]	δ(F1SF2) + δ(F3SF4)
496 (1) [196]	507 (1) [135]	488 (1) [134]	δ(NSF1F4) o.o.p. + ρ_r(F2SF3) + ρ_w(H1NH2)
257 (1) [1]	251 (1) [1]	243 (1) [1]	δ(F1SF4) – δ(F2SF3)
212 (1) [3]	210 (1) [4]	203 (2) [3]	δ(NSF2) – δ(NSF3)

[a] Values in parentheses denote experimental Raman intensities, abbreviations denote shoulder (sh), broad (br) and not observed (n.o.). [b] Calculated Raman intensities (in $Å^4$ amu^{-1}) are given in parentheses and calculated infrared intensities (in km mol^{-1}) are given in square brackets. [c] Abbreviations denote out of plane (o.o.p.), in plane (i.p.) (planes are defined by the atoms they contain), four equatorial fluorines (F_{4eq}), wag (ρ_w), and rock (ρ_r). The anion mode symmetry assignments are made under C_1 symmetry and are also correlated to C_{4v} symmetry (in square brackets). [d] (SDB-)cc-pVTZ basis set. [e] aug-cc-pVTZ(-PP) basis set.

Table 5.11. Natural Bond Orbital (NBO) Charges, Valencies, and Bond Orders for $F_4S{=}NXe^{+}$ [a] and $F_4S{=}NH_2^{+}$ [b]

atom	$F_4S{=}NXe^{+}$						$F_4S{=}NH_2^{+}$					
	charges			valencies			charges			valencies		
	MP2	PBE1PBE	B3LYP	MP2	PBE1PBE	B3LYP	MP2	PBE1PBE	B3LYP	MP2	PBE1PBE	B3LYP
Xe	1.01	0.92	0.87	0.62	0.57	0.53						
H							0.47	0.47	0.47	0.66	0.65	0.65
N	–0.87	–0.79	–0.73	1.67	1.60	1.56	–0.96	–0.95	–0.94	2.23	2.28	2.27
S	2.50	2.51	2.48	4.07	3.71	3.66	2.61	2.60	2.60	3.52	3.73	3.67
F1	–0.40	–0.40	–0.39	0.62	0.60	0.59	–0.43	–0.43	–0.44	0.51	0.56	0.55
F2	–0.38	–0.39	–0.38	0.65	0.60	0.59	–0.36	–0.36	–0.36	0.55	0.61	0.60
F3	–0.38	–0.39	–0.38	0.65	0.60	0.59	–0.36	–0.36	–0.36	0.55	0.61	0.60
F4	–0.47	–0.47	–0.46	0.56	0.52	0.53	–0.43	–0.43	–0.44	0.51	0.56	0.55

bond	bond orders					
	$F_4S{=}NXe^{+}$			$F_4S{=}NH_2^{+}$		
	MP2	PBE1PBE	B3LYP	MP2	PBE1PBE	B3LYP
Xe–N	0.59	0.55	0.52			
N–H				0.67	0.67	0.67
S–N	1.18	1.11	1.11	0.99	1.03	1.03
S–F1	0.69	0.62	0.60	0.61	0.65	0.64
S–F2	0.76	0.68	0.67	0.67	0.70	0.69
S–F3	0.76	0.68	0.67	0.67	0.70	0.69
S–F4	0.66	0.61	0.61	0.61	0.65	0.64

[a] aug-cc-pVTZ(-PP) basis set. [b] aug-cc-pVTZ basis set.

Table 5.12. Natural Bond Orbital (NBO) Charges, Valencies, and Bond Orders for $F_5SN(H)Xe^+$ and $F_5TeN(H)Xe^+$ [a]

	$F_5SN(H)Xe^+$				$F_5TeN(H)Xe^+$			
atom	charges		valencies		charges		valencies	
	MP2	PBE1PBE	MP2	PBE1PBE	MP2	PBE1PBE	MP2	PBE1PBE
Xe	1.03	1.16	0.62	0.26	1.05	0.99	0.64	0.64
H	0.41	0.25	0.71	0.65	0.42	0.42	0.71	0.71
N	–0.82	–0.90	1.87	1.16	–1.02	–0.96	1.81	1.84
S	2.56	2.36	4.13	3.44				
Te					3.35	3.29	3.09	3.24
F1	–0.41	–0.34	0.63	0.53	–0.53	–0.52	0.47	0.51
F2	–0.43	–0.36	0.58	0.43	–0.56	–0.53	0.44	0.50
F3	–0.45	–0.48	0.57	0.57	–0.58	–0.57	0.43	0.47
F4	–0.46	–0.39	0.56	0.60	–0.58	–0.55	0.42	0.48
F5	–0.42	–0.31	0.60	0.46	–0.55	–0.57	0.45	0.46

	bond orders			
bond	$F_5SN(H)Xe^+$		$F_5TeN(H)Xe^+$	
	MP2	PBE1PBE	MP2	PBE1PBE
Xe–N	0.60	0.08	0.62	0.61
N–H	0.71	0.61	0.71	0.71
S/Te–N	0.67	0.53	0.57	0.57
S/Te–F1	0.74	0.61	0.53	0.56
S/Te–F2	0.68	0.57	0.50	0.54
S/Te–F3	0.67	0.60	0.49	0.52
S/Te–F4	0.66	0.58	0.49	0.53
S/Te–F5	0.70	0.57	0.51	0.51

[a] aug-cc-pVTZ(-PP) basis set.

covalent bonding between xenon and nitrogen, which is in agreement with the Xe–N bond covalency trend inferred from the ^{129}Xe NMR chemical shifts for these species (see section 5.2.2.1). Although not reflected in the calculated or experimental bond lengths, a decrease in the charge difference for sulfur and nitrogen in $F_4S{=}NXe^+$ is consistent with the greater S–N bond covalency and higher bond order of this bond [1.18] compared to that of $F_4S{=}NH_2^+$ [0.99].

Higher negative charges and lower valencies for the fluorine ligands of $F_4S{=}NXe^+$ are consistent with the lower S–F bond orders when compared with those of $F_4S{=}NH_2^+$. The charges, valencies, and bond orders for the benchmark, $F_4S{=}NF$, are in better agreement with those of $F_4S{=}NXe^+$ than with those of $F_4S{=}NH_2^+$, which is consistent with the presence of strongly electron-withdrawing substituents at N in the former cases.

5.3.4. Comparison of $F_4S{=}NXe^+$ and $F_4S{=}NH_2^+$ with Related $F_4S{=}ERR'$ Derivatives and SF_4

The experimental and calculated geometries of $F_4S{=}NXe^+$, $F_4S{=}NH_2^+$, $F_4S{=}CH_2$, $F_4S{=}NCH_3$, $F_4S{=}NF$, $F_4S{=}O$, and SF_4 are compared in Table 5.13 along with their NBO charges, valencies, and bond orders. There is overall very good agreement between the calculated geometrical parameters, with all trends within the series being reproduced. The natural population analyses (NPA) reveal that the sulfur d orbital population ranges from 0.22 to 0.24 e for the $F_4S{=}ERR'$ species and is 0.17 for SF_4, so that the S–E bonds may be regarded as essentially $p\pi$–$p\pi$ bonds.

Although the $F_4S{=}NXe^+$ cation may be expected to exhibit shorter, more covalent bonds than its neutral homologues, this is only apparent within the margins of

Table 5.13. Geometrical Parameters and Natural Bond Orbital (NBO) Charge, Valencies, and Bond Orders for the $F_4S{=}E{-}$ moieties of $F_4S{=}CH_2$, $F_4S{=}NH_2^+$, $F_4S{=}NXe^+$, $F_4S{=}NCH_3$, $F_4S{=}NF$, and $F_4S{=}O$, and for SF_4 [a]

	$F_4S{=}CH_2$		$F_4S{=}NH_2^+$		$F_4S{=}NXe^+$		$F_4S{=}NCH_3$		$F_4S{=}NF$		$F_4S{=}O$		SF_4	
parameter	exptl[179]	calcd	exptl[b]	calcd	exptl[b]	calcd	exptl[100]	calcd	exptl[74]	calcd	exptl[180]	calcd	exptl[181]	calcd
$S{-}F_B$ (Å)	1.595(2)	1.617	1.564(5)	1.569	1.576(2)	1.573	1.546(7)	1.599	1.535(12)	1.591	1.596(4)	1.614	1.646(3)	1.664
$S{-}F_X$ (Å)	1.592(2)		1.558(5)		1.588(2)	1.604	1.643(4)	1.648	1.615(7)	1.598				
$S{-}F_A$ (Å)	1.561(2)	1.582	1.511(5)	1.521	1.518(2)	1.536	1.567(4)	1.578	1.564(5)	1.568	1.533(4)	1.558	1.545(3)	1.561
	1.560(2)		1.526(5)		1.529(2)									
S=E (Å)	1.554(4)	1.586	1.511(6)	1.558	1.556(3)	1.583	1.480(6)	1.505	1.520(9)	1.570	1.405(4)	1.425		
$F_A{-}S{-}F_A$ (°)	96.8(1)	97.2	108.5(3)	109.4	104.3(1)	106.2	102.6(2)	102.6	99.8(3)	100.3	114.9(34)	111.9	101.5(5)	101.5
$F_B{-}S{-}F_X$ (°)	170.5(1)	171.7	175.5(3)	178.6	173.5(1)	175.7	167.0(6)	167.0	172.5(7)	173.7	164.4(6)	164.5	173.1(5)	172.2
$E{=}S{-}F_A$ (°)	131.4(2)	131.4	125.2(3)	125.3	127.3(2)	126.7	128.7(4)	128.7	130.1(6)	129.7	122.5(17)	124.1	129.3(5)	129.3
	131.7(2)		126.3(3)		127.8(2)									
$E{=}S{-}F_X$ (°)	94.7(2)	94.1	91.9(3)	90.7	100.1(2)	98.6	98.4(4)	99.3	96.9(4)	98.6	97.8(3)	97.7	93.4(5)	93.9
$E{=}S{-}F_B$ (°)	94.9(2)	94.1	92.6(3)	90.7	86.4(2)	85.7	94.6(4)	93.8	90.6(5)	87.7	97.8(3)	97.7	93.4(5)	93.9
$E{=}S{-}F_X$ – $E{=}S{-}F_B$ (°)	–0.2(4)	0	–0.7(6)	0	13.7(4)	12.9	3.8(8)	5.5	6.3(9)	10.9	0	0	0	0
$QA_{\angle E=S-F}$ (°)	113.2(4)	112.8	109.0(6)	108.0	110.4(4)	109.4	112.6(7)	112.6	111.9(9)	111.4	110.2(18)	110.9	111.4(9)	111.6
NBO Analysis														
atom	charge	val	charge	val	charge	val	charge	val	charge	val	charge	val	charge	val
F_B	–0.49	0.52	–0.43	0.51	–0.40	0.62	–0.47	0.55	–0.45	0.59	–0.48	0.43	–0.55	0.41
F_A	–0.45	0.53	–0.36	0.55	–0.38	0.65	–0.44	0.56	–0.43	0.59	–0.42	0.50	–0.45	0.54
F_X	–0.49	0.52	–0.43	0.51	–0.47	0.56	–0.51	0.49	–0.47	0.56	–0.48	0.43	–0.55	0.41
S	2.27	3.81	2.61	3.52	2.50	4.07	2.47	3.92	2.38	3.90	2.62	3.47	2.00	2.16
E	–0.86	2.73	–0.96	2.23	–0.87	1.67	–0.83	1.90	–0.37	1.70	–0.81	1.00		
bond	bond order													
S=E	1.28		0.99		1.18		1.15		1.31		1.20			
$S{-}F_B$	0.61		0.61		0.69		0.55		0.65		0.66		0.46	
$S{-}F_A$	0.65		0.67		0.76		0.61		0.68		0.70		0.62	
$S{-}F_X$	0.61		0.61		0.66		0.55		0.60		0.66		0.46	

[a] Where E = C, N, O. All calculations at the MP2/aug-cc-pVTZ(-PP) level of theory. The fluorine atom labeling schemes are given by Structures I and II. $QA_{\angle E=S-F}$ is the quadruple average angle (see ref. 181), defined as the average of the four possible E=S–F (:–S–F, in the case of the SF_4) angles. [b] This work.

experimental error for axial S–F_X and equatorial S–F_A bond length comparisons. Moreover, the S=N bond is longer and more polar than in F_4S=NF, which is in accordance with the smaller negative charge on nitrogen in F_4S=NF than in F_4S=NXe^+ and correspondingly greater difference in sulfur and nitrogen charges for F_4S=NXe^+. The F_4S=NXe^+ cation follows the axial bond length trend of F_4S=NF and F_4S=NCH_3, i.e., S–F_B < S–F_X. The S–F_B and S–F_X bond lengths are nearly equal, within experimental error for F_4S=NXe^+, but the S–F_X bond is significantly longer and the S–F_B bond is significantly shorter in F_4S=NCH_3 and F_4S=NF (vide infra).

Comparison of F_4S=NXe^+ and F_4S=NH_2^+ reveals that the F_A–S–F_A and F_B–S–F_X angles are more compressed in F_4S=NXe^+ than in their F_4S=NH_2^+ counterparts. More insight is gained when the component angles N=S–F_X (100.1(2)°) and N=S–F_B (86.4(2)°) are considered for F_4S=NXe^+ and their difference, Δ(N=S–F_{axial}) = ∠N=S–F_X – ∠N=S–F_B (13.7(4)°), is considered. There is a significant interaction between the Xe and F_X atoms, with a Xe---F_X contact (2.824(8) Å) that is significantly less than the sum of the Xe and F van der Waals radii (3.63 Å),[31] causing ∠N=S–F_X to be more open and ∠N=S–F_B to be more closed. Interestingly, the NBO analysis provides a negligible bond order (0.01) in this case; thus, the interaction is essentially Coulombic in nature, and the short contact is presumably a partial consequence of the nonspherical (toroidal) distribution of the valence electron density arising from the three valence electron lone pairs of xenon.[40] The slight lengthening of the S–F_X bond with respect to the S–F_B bond, which is also observed for the calculated geometry, is also consistent with a weak Coulombic interaction between F_X and the positive xenon center.

A steric interaction also occurs between F_X and the fluorine bonded to nitrogen in $F_4S{=}NF$ ($F_N{---}F_X$, 2.377(9) Å; sum of the fluorine van der Waals radii, 2.94 Å[31]) with $\Delta(N{=}S{-}F_{axial})$ = 6.3(9)° and $\angle N{=}S{-}F_X$ (96.9(4)°) again being more open than $\angle N{=}S{-}F_B$ (90.6(5)°). The $F_A{-}S{-}F_A$ and $F_B{-}S{-}F_X$ angles of $F_4S{=}NF$ are more compressed than those of either $F_4S{=}NXe^+$ or $F_4S{=}NH_2^+$, with the $F_A{-}S{-}F_A$ angle showing the greater compression. This is consistent with a higher π-electron density in the equatorial $F_2S{=}N$-plane of $F_4S{=}NF$ and a higher S–N bond covalency that is corroborated by the S–N bond order (1.31) and a correspondingly lower charge difference between sulfur and nitrogen (2.75 e) when compared with those of $F_4S{=}NXe^+$ (S–N b.o., 1.18; c.d., 3.37 e) and $F_4S{=}NH_2^+$ (S–N b.o., 0.99; c.d., 3.57 e). Comparisons with $F_4S{=}NF$ and $F_4S{=}CH_2$ show that the latter molecules exhibit the greatest $F_A{-}S{-}F_A$ angle compressions within the series considered. The angle compressions and high S=N and S=C bond orders are again consistent with their charge differences and bond orders, S–C (b.o., 1.28; c.d., 3.13 e) and S–N (b.o., 1.31; c.d., 2.75 e) and with greater π S–E density in the equatorial $F_2S{=}E$-plane.

Although $\Delta(N{=}S{-}F_{axial})$ for $F_4S{=}NCH_3$ is considerably less than those for $F_4S{=}NXe^+$ and $F_4S{=}NF$, the difference is significant and is likely a consequence of the $F_X{---}CH_3$ steric interaction. The axial bond length differences for $F_4S{=}NF$ and $F_4S{=}NCH_3$ are significantly greater than that of $F_4S{=}NXe^+$, which is consistent with the strongly repulsive natures of the former steric interactions.

The $F_4S{=}CH_2$ molecule exhibits one of the most open $F_B{-}S{-}F_B$ angles and, at the same time, one of the most compressed $F_A{-}S{-}F_A$ angles among the $F_4S{=}ERR'$ (where R = R′) species considered in Table 5.13. The asymmetries of the S=C[179] and S=N bonds place

most of the π-bond electron density in the equatorial plane, which results in greater compression of the F_A–S–F_A angle than of the axial F_B–S–F_B angle. The greater degree of bond angle compression for both F–S–F angles in $F_4S{=}CH_2$ is presumably a consequence of the greater covalent character of the S=C bond (b.o. 1.28, compared to 0.99 for isoelectronic $F_4S{=}NH_2^+$), which results in greater double bond domain-single bond domain repulsions.

Following Hargittai,[181] the quadrupule averages of angles E=S–F_A (2×), E=S–F_B, and E=S–F_X (where ∠E=S–F_B = ∠E=S–F_X for $F_4S{=}CH_2$, $F_4S{=}NH_2^+$, $F_4S{=}O$, and SF_4) were evaluated and are compared in Table 5.13. The parameter, $QA_{\angle E=S-F}$, serves as a relative measure of the average spatial requirements of the double bond domains among the $F_4S{=}ERR'$ series and the lone pair domain of SF_4. The VSEPR rule-of-thumb, which states that a double bond domain and a lone pair domain have very similar spatial requirements,[182] is supported by the series under consideration, with the SF_4 value occurring approximately midway in the range and with a quadruple average E=S–F angle that is very similar to that of $F_4S{=}NF$. As expected for cations in a closely related series the $QA_{\angle E=S-F}$ values and spatial requirements of the S–N double bond domains of $F_4S{=}NXe^+$ and $F_4S{=}NH_2^+$, which are most similar to that of $F_4S{=}O$, are significantly less than those of the neutral molecules $F_4S{=}CH_2$, $F_4S{=}NCH_3$, and $F_4S{=}NF$.

5.4. Conclusions

The $F_4S{=}NXe^+$ cation has been synthesized by both solid-state rearrangement and HF solvolysis of the $F_3S{\equiv}NXeF^+$ cation. The discovery of the $F_4S{=}NXe^+$ cation as an intermediate in the HF solvolysis of the $F_3S{\equiv}NXeF^+$ cation en route to $F_5SN(H)Xe^+$ has

served to significantly enhance our understanding of the reaction pathways that lead to $F_4S{=}NXe^+$ and $F_5SN(H)Xe^+$. Two synthetic pathways, both starting from $F_3S{\equiv}NXeF^+$, have been shown to lead to the to $F_4S{=}NXe^+$ cation, namely, solvolysis of $[F_3S{\equiv}NXeF][AsF_6]$ in aHF, and solid-state rearrangement of $[F_3S{\equiv}NXeF][AsF_6]$ at ambient temperatures. Structural characterization of the $F_4S{=}NXe^+$ cation has revealed a rare example of xenon bonded to sp^2-hybridized nitrogen, providing the first example of the $F_4S{=}N$-group bonded to a noble gas. The $F_4S{=}NH_2^+$ cation was also formed in the course of HF solvolysis of $F_3S{\equiv}NXeF^+$. The $F_4S{=}NXe^+$ and $F_4S{=}NH_2^+$ cations significantly expand the chemistry of species containing the $F_4S{=}N$-group and represent the only known examples of cations containing this group. The calculated Xe–N bond order of $F_4S{=}NXe^+$ derived from the NBO analyses is consistent with the short Xe–N bond length and high shielding of the ^{129}Xe resonance of $F_4S{=}NXe^+$, which places it, along with the sp^3-hybridized nitrogen cations $F_5SN(H)Xe^+$ and $F_5TeN(H)Xe^+$, among the most covalent Xe–N bonds presently known.

CHAPTER 6

ON THE REACTIVITY OF $F_3S{\equiv}NXeF^+$; SYNTHESES AND STRUCTURAL CHARACTERIZATIONS OF $[F_4S{=}N{-}Xe{---}N{\equiv}SF_3][AsF_6]$, A RARE EXAMPLE OF AN N–Xe–N LINKAGE, AND $[F_3S(N{\equiv}SF_3)_2][AsF_6]$

6.1. Introduction

Until recently, the only xenon-nitrogen bonded species having formally sp^2-hybridized nitrogen bonded to xenon were the XeF^+ adducts of *s*-trifluorotriazine[36] and several perfluoropyridines;[37] the μ-imidobis(sulfurylfluoride) ($-N(SO_2F)_2$) derivatives of xenon(II), $FXeN(SO_2F)_2$,[44-46] $Xe[N(SO_2F)_2]_2$,[45,47] $F[XeN(SO_2F)_2]_2^+$,[45,47,49] and $XeN(SO_2F)_2^+$;[49] and the related trifluoromethyl derivative, $Xe[N(SO_2CF_3)_2]_2$.[48] The pentacoordinated sulfur(VI) cations, $F_4S{-}N(CH_3)_2^+$,[178] $F_4S{-}N(CH_2CH_3)_2^+$,[183] and $F_4S{-}NC_5H_{10}^+$,[183] have been structurally characterized by ^{19}F NMR spectroscopy, which showed that rotation about their S–N bonds was rapid on the NMR timescale. Most recently, the $F_4S{=}NXe^+$ and $F_4S{=}NH_2^+$ cations[184] were reported from this laboratory, which represent the only known cationic derivatives of the $F_4S{=}N$-group and the first sp^2-hybridized imido species in which the nitrogen bonded to xenon is doubly bonded to sulfur. Neither $F_4S{=}NXe^+$ nor $F_4S{=}NH_2^+$ exhibited rotation about their S=N bonds on the NMR time scale.

The basicity of thiazyl trifluoride, $N{\equiv}SF_3$, has been demonstrated by its reactions with BF_3, AsF_5, and SbF_5 in SO_2 to form the Lewis acid-base adducts, $F_3S{\equiv}NBF_3$,[82,87]

$F_3S{\equiv}NAsF_5$,[78,88] and $F_3S{\equiv}NSbF_5$;[88] by the formation of transition-metal complexes such as $[M(N{\equiv}SF_3)_4(AsF_6)_2]$ (M = Mn,[90] Zn[92]), $[Re(CO)_5N{\equiv}SF_3][AsF_6]$,[91] and $[CpFe(CO)_2N{\equiv}SF_3][AsF_6]$;[91] and more recently by the synthesis and structural characterization of the noble-gas-containing Lewis acid-base adduct $F_3S{\equiv}NXeF^+$.[146]

The present work investigates the reactivities of the $F_3S{\equiv}NXeF^+$ and $F_4S{=}NXe^+$ cations in $N{\equiv}SF_3$ solvent. The synthesis and detailed structural characterization of $[F_4S{=}N{-}Xe{---}N{\equiv}SF_3][AsF_6]$, a rare example of xenon bonded to an imido-nitrogen and of a N–Xe–N linkage, is reported along with that of $[F_3S(N{\equiv}SF_3)_2][AsF_6]$, a reduction product resulting from the reaction of $[F_4S{=}N{-}Xe{---}N{\equiv}SF_3][AsF_6]$ with $N{\equiv}SF_3$.

6.2. Results and Discussion

6.2.1. Reactions of $[F_3S{\equiv}NXeF][AsF_6]$ in $N{\equiv}SF_3$ Solvent

6.2.1.1. Synthesis of $[F_4S{=}N{-}Xe{---}N{\equiv}SF_3][AsF_6]$

The salt $[F_3S{\equiv}NXeF][AsF_6]$ was prepared as previously described[146] by reaction of $[XeF][AsF_6]$ with $N{\equiv}SF_3$ in neat $N{\equiv}SF_3$ at –20 °C for ca. 6 h to give a white solid, corresponding to $[F_3S{\equiv}NXeF][AsF_6]$, and a colourless supernatant. When the reaction mixture was warmed from –20 to 0 °C over ca. 15 h, the solid dissolved and the solution turned deep yellow, coinciding with the formation of $[F_4S{=}N{-}Xe{---}N{\equiv}SF_3][AsF_6]$ (eq 6.1). The removal of excess $N{\equiv}SF_3$ under dynamic vacuum at –50 °C yielded a deep

$$[F_3S{\equiv}NXeF][AsF_6] + N{\equiv}SF_3 \xrightarrow[N{\equiv}SF_3]{0\ ^\circ C} [F_4S{=}N{-}Xe{---}N{\equiv}SF_3][AsF_6] \quad (6.1)$$

yellow solid which was characterized by Raman spectroscopy at –160 °C. A prior study reported the ^{19}F parameters for the $F_4S{=}NXe^+$ cation in $N{\equiv}SF_3$ solvent at 0 °C,[184] however, a separate ^{19}F resonance corresponding to coordinated $N{\equiv}SF_3$ was not observed. It may be concluded that $N{\equiv}SF_3$ ligand exchange with the solvent occurs and that the donor-acceptor bond is labile under these conditions.

The solid-state rearrangement of $F_3S{\equiv}NXeF^+$ to $F_4S{=}NXe^+$ is known to occur at 22 °C over a period of ca. 70 min.[184] The X-ray crystal structure of $[F_3S{\equiv}NXeF][AsF_6]$[146] reveals that a fluorine ligand of AsF_6^- has a short contact (2.871(5) Å) with the sulfur atom of an adjacent $F_3S{\equiv}NXeF^+$ cation that is significantly less than the sum of the sulfur and fluorine van der Waals radii (3.27 Å).[31] In the proposed rearrangement mechanism, the short F---S contact leads to fluoride ion transfer and formation of the $[F_4S{=}NXe][AsF_6]$ ion-pair.[184] As the rearrangement proceeds, solid-state dilution of $[F_3S{\equiv}NXeF][AsF_6]$ and breakdown of the crystal lattice prevent complete conversion to $[F_4S{=}NXe][AsF_6]$. In the present solution study, the rearrangement proceeds at 0 °C with complete conversion to $[F_4S{=}N{-}Xe{---}N{\equiv}SF_3][AsF_6]$. In both cases, the reactions were monitored by Raman spectroscopy (vide infra). Solvent induced rearrangement of $F_3S{\equiv}NXeF^+$ to $F_4S{=}NXe^+$ in anhydrous HF (aHF) solution also occurs at lower temperature (–20 °C) with complete conversion.[184] Unlike the solid state rearrangement of $[F_3S{\equiv}NXeF][AsF_6]$,[184] rearrangements of the $F_3S{\equiv}NXeF^+$ in $N{\equiv}SF_3$ and aHF solutions do not suffer from solid state dilution effects, and proceed to completion.

Thiazyl trifluoride solvent likely promotes rearrangement at lower temperatures by means of solvent-induced S_N2 displacement of fluoride ion from the Xe–F group, and

concomittant fluoride ion coordination to sulfur (Scheme 6.1). An alternative mechanism in which $N{\equiv}SF_3$ accepts fluoride ion from the Xe–F group of $F_3S{\equiv}NXeF^+$ to generate

Scheme 6.1. Proposed Mechanism for the $N{\equiv}SF_3$ Promoted Fluoride Rearrangement of $F_3S{\equiv}NXeF^+$

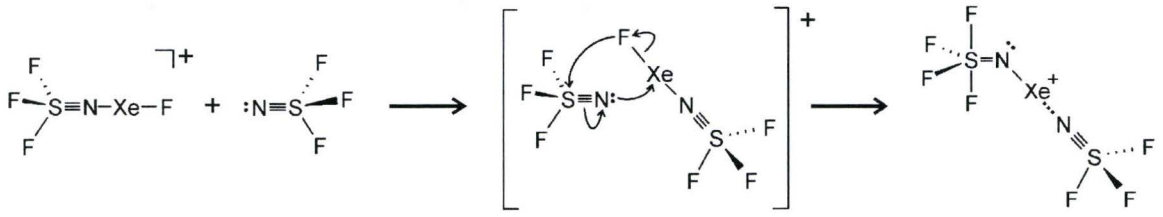

$F_4S{=}N^-$ as an intermediate seems less likely because this anion has not been experimentally observed. In the proposed solid-state and HF solution rearrangement mechanisms of $[F_3S{\equiv}NXeF][AsF_6]$ to $[F_4S{=}NXe][AsF_6]$,[184] the sulfur center is initially attacked by coordination of fluoride from AsF_6^- and HF, respectively, followed by fluoride ion abstraction from the Xe–F group by AsF_5 and HF, respectively.

6.2.1.2. Synthesis of $[F_3S(N{\equiv}SF_3)_2][AsF_6]$

In the course of growing single crystals of $[F_4S{=}N{-}Xe{---}N{\equiv}SF_3][AsF_6]$ from $N{\equiv}SF_3$ solution for an X-ray structure determination, colourless $[F_3S(N{\equiv}SF_3)_2][AsF_6]$ crystals were also obtained and characterized by single-crystal X-ray diffraction. The latter salt resulted from redox decomposition of the $F_4S{=}NXe^+$ cation at 0 °C (eq 6.2), and liberated Xe and N_2F_2 exclusively as the *cis*-isomer. The synthesis of pure $[F_3S(N{\equiv}SF_3)_2][AsF_6]$ was accomplished by allowing a $N{\equiv}SF_3$ solution of $[F_4S{=}N{-}Xe{---}$

$$[F_4S{=}N{-}Xe{-}{-}{-}N{\equiv}SF_3][AsF_6] + N{\equiv}SF_3 \xrightarrow[N{\equiv}SF_3]{0\ ^{\circ}C} [F_3S(N{\equiv}SF_3)_2][AsF_6] + Xe + \tfrac{1}{2}\ cis\text{-}N_2F_2 \qquad (6.2)$$

$N{\equiv}SF_3][AsF_6]$ (vide supra) to stand at 0 °C for 6 h. Over this period of time, the solution changed from yellow to colourless, accompanied by slow gas evolution. Removal of excess $N{\equiv}SF_3$ by brief pumping under dynamic vacuum at –50 °C yielded a friable white solid, comprised of $[F_3S(N{\equiv}SF_3)_2][AsF_6]$ and *cis*-N_2F_2, which were characterized by Raman spectroscopy at –160 °C. The Raman bands assigned to *cis*-N_2F_2 are in excellent agreement with previously reported values.[185] Continued pumping at –45 °C for 15 min resulted in complete removal of *cis*-N_2F_2 and $N{\equiv}SF_3$, and formation of $[SF_3][AsF_6]$ which was confirmed by Raman Spectroscopy (see Section 6.2.3.2).

The presence of *cis*-N_2F_2 was also established in the solution ^{19}F NMR spectrum of the decomposition mixture (vide infra). The ^{19}F NMR spectrum of a $[F_3S{\equiv}NXeF][AsF_6]$ sample that had been allowed to react to completion in liquid $N{\equiv}SF_3$ solvent at 0 °C (eqs 6.1 and 6.2) showed a broad ($\Delta\nu_{1/2}$ = 500 Hz) resonance at 38.6 ppm assigned to SF_3^+, in agreement with the reported value of 30.5 ppm in aHF at 25 °C.[186] The ^{19}F NMR spectrum also confirmed the formation of *cis*-N_2F_2 (singlet, 137.6 ppm, $\Delta\nu_{1/2}$ = 30 Hz), in agreement with the previously reported chemical shift (broad triplet at 133.7 ppm, $^1J(^{19}F{-}^{14}N)$ = 145 Hz, 25 °C, $CFCl_3$ solvent).[187] Failure to observe the $^1J(^{19}F{-}^{14}N)$ coupling in the present study is likely a consequence of quadrupolar relaxation resulting from a higher solvent viscosity and lower temperature. No *trans*-N_2F_2 was observed in the sample (broad triplet at 94.9 ppm, $^1J(^{19}F{-}^{14}N)$ = 136 Hz, 25 °C, $CFCl_3$ solvent).[187] Nitrogen trifluoride was

also observed by ^{19}F NMR spectroscopy (20 mol% when compared with the total molar amounts of NF_3 and *cis*-N_2F_2 soluble in the sample at 0 °C).

The proposed decomposition of $[F_4S{=}NXe{---}N{\equiv}SF_3][AsF_6]$ involves 2e reductions of xenon (+II to 0) and sulfur (+VI to +IV), and a 4e oxidation of nitrogen (–III to +I), that give Xe gas, SF_3^+, and ·NF radicals that combine to form *cis*-N_2F_2.[188] The series of reactions responsible for these products may be initiated by fluoride ion transfer from an AsF_6^- anion to the xenon atom of $F_4S{=}NXe^+$, forming $F_4S{=}NXeF$ as an intermediate (eq 6.3) which decomposes to Xe, *cis*-N_2F_2, and SF_4 (eqs 6.4 and 6.5). Fluoride ion abstraction by AsF_5 generated in eq 6.3 leads to SF_3^+ (eq 6.6). Nitrogen trifluoride may result from oxidation of *cis*-N_2F_2 by $F_4S{=}NXe^+$ according to eq 6.7.

$$F_4S{=}NXe^+ + AsF_6^- \xrightarrow[N{\equiv}SF_3]{0\ ^\circ C} [F_4S{=}NXeF] + AsF_5 \qquad (6.3)$$

$$[F_4S{=}NXeF] \xrightarrow[N{\equiv}SF_3]{0\ ^\circ C} \cdot NF + Xe + SF_4 \qquad (6.4)$$

$$2 \cdot NF \xrightarrow[N{\equiv}SF_3]{0\ ^\circ C} \textit{cis}\text{-}N_2F_2 \qquad (6.5)$$

$$SF_4 + AsF_5 \xrightarrow[N{\equiv}SF_3]{0\ ^\circ C} SF_3^+ + AsF_6^- \qquad (6.6)$$

$$F_4S{=}NXe^+ + \textit{cis}\text{-}N_2F_2 \xrightarrow[N{\equiv}SF_3]{0\ ^\circ C} NF_3 + N_2 + SF_3^+ + Xe \qquad (6.7)$$

6.2.2. X-ray Crystal Structures of $[F_4S{=}N{-}Xe{-}{-}{-}N{\equiv}SF_3][AsF_6]$ and $[F_3S(N{\equiv}SF_3)_2][AsF_6]$

A summary of the refinement results and other crystallographic information are provided in Table 6.1. Important bond lengths and angles for $[F_4S{=}N{-}Xe{-}{-}{-}N{\equiv}SF_3][AsF_6]$ and $[F_3S(N{\equiv}SF_3)_2][AsF_6]$, along with calculated values (see section 6.3), are listed in Tables 6.2 and 6.3, respectively.

6.2.2.1. $[F_4S{=}N{-}Xe{-}{-}{-}N{\equiv}SF_3][AsF_6]$

The crystal structure of $[F_4S{=}N{-}Xe{-}{-}{-}N{\equiv}SF_3][AsF_6]$ consists of well-separated $F_4S{=}N{-}Xe{-}{-}{-}N{\equiv}SF_3^+$ cations and AsF_6^- anions, with closest cation-anion contacts occurring between the equatorial fluorine F(3) of the cation and F(12) and F(14) of the anion (F(3)---F(12), 2.755(4) Å; and F(3)---F(14), 2.757(4) Å), which are somewhat less than the sum of the fluorine van der Waals radii (2.94 Å).[31] The AsF_6^- anion shows little distortion from octahedral symmetry, with As–F bonds ranging from 1.713(2) to 1.735(2) Å and F–As–F bond angles ranging from 89.3(1) to 91.0(1)° and 178.8(1) to 179.2(1)°, in good agreement with previously reported values.[50,146] The ligand arrangement at the sulfur atom of the cation is a distorted trigonal bipyramid, with the nitrogen and two fluorine atoms occupying the equatorial plane and two axial fluorine atoms approximately perpendicular to that plane (Figure 6.1a). The xenon atom is coplanar with the orthogonal plane defined by the N, S, and axial F atoms, and the Xe–N=S angle is bent (119.8(2)°) as a result of the sterically active valence electron lone pair on nitrogen.

The Xe–N(1) bond length (2.079(3) Å) is equal, within $\pm 3\sigma$, to those of

Table 6.1. Summary of Crystal Data and Refinement Results for $[F_4S{=}N{-}Xe{---}N{\equiv}SF_3][AsF_6]$ and $[F_3S(N{\equiv}SF_3)_2][AsF_6]$

	$[F_4S{=}N{-}Xe{---}N{\equiv}SF_3][AsF_6]$	$[F_3S(N{\equiv}SF_3)_2][AsF_6]$
empirical formula	$F_{13}N_2S_2XeAs$	$F_{15}N_2S_3As$
space group (No.)	$P2_1/n$ (14)	$P2_1/n$ (14)
a (Å)	7.3107(5)	7.4722(5)
b (Å)	12.0219(8)	16.264(1)
c (Å)	13.5626(9)	10.4247(7)
β (deg)	94.647(1)	97.919(1)
V (Å^3)	1188.08(1)	1254.84(3)
molecules/unit cell	4	4
mol. wt. (g mol^{-1})	545.36	484.12
calcd. density (g cm^{-3})	3.049	2.563
T (°C)	−173	−173
μ (mm^{-1})	6.17	3.39
R_1 [a]	0.0294	0.0324
wR_2 [b]	0.0709	0.0633

[a] R_1 is defined as $\Sigma||F_o|-|F_c||/\Sigma|F_o|$ for $I > 2\sigma(I)$.
[b] wR_2 is defined as $[\Sigma[w(F_o^2 - F_c^2)^2]/\Sigma w(F_o^2)^2]^{1/2}$ for $I > 2\sigma(I)$.

Table 6.2. Experimental Geometry for $[F_4S{=}N{-}Xe{---}N{\equiv}SF_3][AsF_6]$ and Calculated Geometries for $F_4S{=}N{-}Xe{---}N{\equiv}SF_3^+$ [a]

	Bond Lengths (Å)					
		calcd[b]				
	exptl	MP2	PBE1PBE	B3LYP		exptl
Xe(1)–N(1)	2.079(3)	2.062	2.079	2.131	As(1)–F(8)	1.726(2)
N(1)=S(1)	1.539(3)	1.563	1.557	1.573	As(1)–F(9)	1.714(2)
S(1)–F(1)	1.586(3)	1.576	1.577	1.593	As(1)–F(10)	1.722(2)
S(1)–F(2)	1.520(3)	1.545	1.544	1.558	As(1)–F(11)	1.721(2)
S(1)–F(3)	1.529(3)	1.545	1.544	1.558	As(1)–F(12)	1.718(2)
S(1)–F(4)	1.577(3)	1.619	1.611	1.625	As(1)–F(13)	1.735(2)
Xe(1)---N(2)	2.583(3)	2.524	2.547	2.623		
N(2)≡S(2)	1.398(3)	1.428	1.413	1.417		
S(2)–F(5)	1.524(3)	1.545	1.541	1.558		
S(2)–F(6)	1.521(3)	1.545	1.541	1.558		
S(2)–F(7)	1.526(3)	1.545	1.541	1.559		

	Bond Angles (°)					
		calcd[b]				
	exptl	MP2	PBE1PBE	B3LYP		exptl
Xe(1)–N(1)=S(1)	119.8(2)	119.3	119.8	119.8	F(8)–As(1)–F(9)	179.0(1)
N(1)=S(1)–F(1)	87.6(2)	88.1	87.9	87.3	F(8)–As(1)–F(10)	89.6(1)
N(1)=S(1)–F(2)	126.4(2)	127.1	126.8	127.0	F(8)–As(1)–F(11)	89.7(1)
N(1)=S(1)–F(3)	128.2(2)	127.1	126.8	127.0	F(8)–As(1)–F(12)	90.4(1)
N(1)=S(1)–F(4)	99.7(1)	98.8	99.1	99.1	F(8)–As(1)–F(13)	89.3(1)
F(1)–S(1)–F(2)	88.0(2)	88.7	88.6	88.7	F(9)–As(1)–F(10)	90.3(1)
F(1)–S(1)–F(3)	87.2(1)	88.7	88.6	88.7	F(9)–As(1)–F(11)	90.4(1)
F(1)–S(1)–F(4)	172.7(1)	173.1	173.0	173.6	F(9)–As(1)–F(12)	90.6(1)
F(2)–S(1)–F(3)	104.9(1)	105.7	106.1	105.6	F(9)–As(1)–F(13)	89.8(1)
F(2)–S(1)–F(4)	88.2(1)	87.1	87.2	87.4	F(10)–As(1)–F(11)	178.8(1)
F(3)–S(1)–F(4)	87.7(1)	87.1	87.2	87.4	F(10)–As(1)–F(12)	91.0(1)
N(1)–Xe(1)---N(2)	168.4(1)	173.2	173.5	173.1	F(10)–As(1)–F(13)	89.7(1)
Xe(1)---N(2)≡S(2)	148.0(2)	178.6	178.3	178.6	F(11)–As(1)–F(12)	90.0(1)
N(2)≡S(2)–F(5)	120.4(2)	121.1	120.9	121.1	F(11)–As(1)–F(13)	89.4(1)
N(2)≡S(2)–F(6)	122.8(2)	121.2	121.1	121.3	F(12)–As(1)–F(13)	179.2(1)
N(2)≡S(2)–F(7)	120.9(2)	121.3	121.1	121.3		
F(5)–S(2)–F(6)	95.5(2)	95.6	95.8	95.5		
F(5)–S(2)–F(7)	95.2(2)	95.6	95.8	95.5		
F(6)–S(2)–F(7)	95.5(2)	95.6	95.8	95.6		

[a] The atom labels correspond to those used in Figure 6.1. [b] aug-cc-pVTZ(-PP) basis set.

Table 6.3. Experimental and Calculated Geometries for $[F_3S(N{\equiv}SF_3)_2][AsF_6]$ [a]

Bond Lengths (Å)							
		calcd[b]				calcd[b]	
	exptl	PBE1PBE	B3LYP		exptl	PBE1PBE	B3LYP
S(3)–F(7)	1.511(1)	1.557	1.573	S(3)--N(1)	2.554(2)	2.610	2.689
S(3)–F(8)	1.519(1)	1.544	1.555	N(1)–S(1)	1.384(2)	1.416	1.421
S(3)–F(9)	1.520(1)	1.544	1.555	S(1)–F(1)	1.518(2)	1.562	1.580
S(3)--F(10)	2.558(2)	2.223	2.217	S(1)–F(2)	1.521(1)	1.545	1.566
As(1)–F(10)	1.745(1)	1.832	1.863	S(1)–F(3)	1.518(2)	1.552	1.570
As(1)–F(11)	1.723(1)	1.743	1.756	S(3)--N(2)	2.511(2)	2.610	2.689
As(1)–F(12)	1.708(2)	1.728	1.741	N(2)–S(2)	1.392(2)	1.416	1.421
As(1)–F(13)	1.684(2)	1.705	1.717	S(2)–F(4)	1.516(2)	1.552	1.570
As(1)–F(14)	1.706(1)	1.706	1.719	S(2)–F(5)	1.525(2)	1.562	1.580
As(1)–F(15)	1.714(2)	1.728	1.741	S(2)–F(6)	1.525(2)	1.548	1.566

Table 6.3. (continued…)

Bond Angles (°)							
		calcd[b]				calcd[b]	
	exptl	PBE1PBE	B3LYP		exptl	PBE1PBE	B3LYP
F(7)–S(3)–F(8)	96.2(1)	94.5	94.4	F(10)–As(1)–F(11)	88.2(1)	86.6	86.3
F(7)–S(3)–F(9)	96.8(1)	94.5	94.4	F(10)–As(1)–F(12)	87.9(1)	87.1	86.9
F(8)–S(3)–F(9)	96.3(1)	95.0	95.5	F(10)–As(1)–F(13)	179.0(1)	178.6	178.6
F(7)–S(3)--F(10)	174.3(1)	174.9	175.4	F(10)–As(1)–F(14)	89.7(1)	87.6	87.3
F(7)–S(3)--N(1)	83.1(1)	83.9	84.5	F(10)–As(1)–F(15)	87.4(1)	87.1	86.9
F(7)–S(3)--N(2)	81.1(1)	83.9	84.4	F(11)–As(1)–F(12)	89.8(1)	88.4	88.4
F(8)–S(3)--F(10)	78.4(1)	82.1	82.5	F(11)–As(1)–F(13)	91.1(1)	92.0	92.3
F(8)–S(3)--N(1)	83.2(1)	79.4	79.2	F(11)–As(1)–F(14)	177.8(1)	174.2	173.5
F(8)–S(3)--N(2)	177.3(1)	174.0	174.5	F(11)–As(1)–F(15)	89.2(1)	88.4	88.4
F(9)–S(3)--F(10)	82.3(1)	82.1	82.5	F(12)–As(1)–F(13)	92.9(1)	92.9	93.1
F(9)–S(3)--N(1)	179.5(1)	174.0	174.5	F(12)–As(1)–F(14)	89.8(1)	91.3	91.2
F(9)–S(3)--N(2)	84.2(1)	79.4	79.2	F(12)–As(1)–F(15)	175.2(1)	173.4	173.1
F(10)--S(3)--N(1)	97.7(1)	99.1	98.3	F(13)–As(1)–F(14)	91.0(1)	93.8	94.1
F(10)--S(3)--N(2)	104.4(1)	99.1	98.3	F(13)–As(1)–F(15)	91.9(1)	92.9	93.1
N(1)--S(3)--N(2)	96.3(1)	106.1	106.0	F(14)–As(1)–F(15)	91.0(1)	91.3	91.2
S(3)--N(1)–S(1)	158.3(1)	141.5	142.7	S(3)--N(2)–S(2)	132.2(1)	141.6	142.7
N(1)–S(1)–F(1)	121.7(1)	119.4	119.7	N(2)–S(2)–F(4)	121.8(1)	122.8	122.9
N(1)–S(1)–F(2)	121.9(1)	123.6	123.7	N(2)–S(2)–F(5)	120.2(1)	119.4	119.7
N(1)–S(1)–F(3)	120.9(1)	122.8	122.9	N(2)–S(2)–F(6)	122.2(1)	123.6	123.7
F(1)–S(1)–F(2)	95.3(1)	94.2	94.0	F(4)–S(2)–F(5)	95.2(1)	94.3	94.1
F(1)–S(1)–F(3)	95.3(1)	94.3	94.1	F(4)–S(2)–F(6)	95.2(1)	95.2	95.0
F(2)–S(1)–F(3)	94.8(1)	95.2	95.0	F(5)–S(2)–F(6)	95.5(1)	94.2	94.0

[a] The atom labels correspond to those used in Figure 6.2. [b] Calculated for the gas-phase ion-pair using the aug-cc-pVTZ (-PP) basis set.

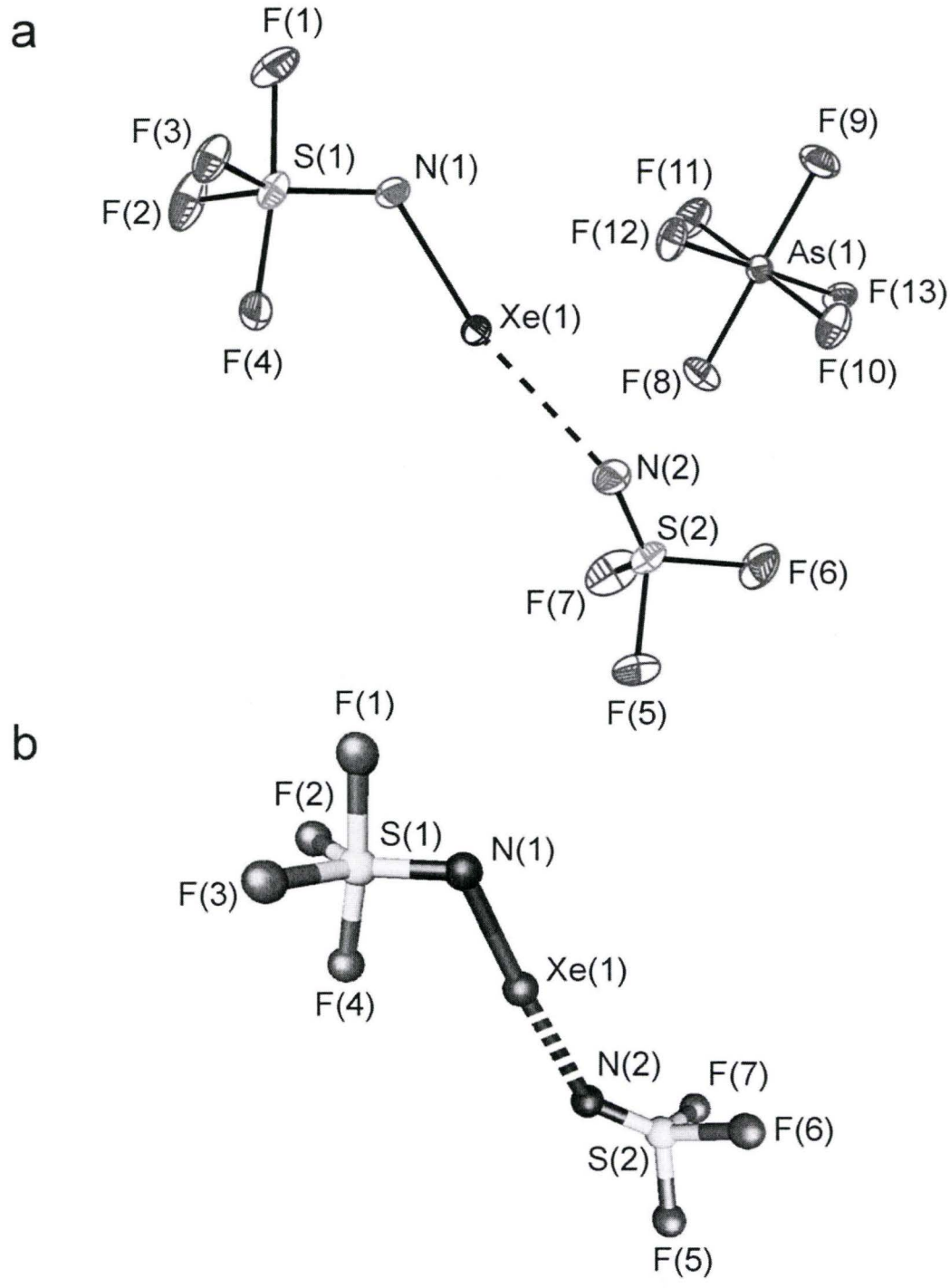

Figure 6.1. (a) The structural unit in the X-ray crystal structure of $[F_4S{=}N{-}Xe{---}N{\equiv}SF_3][AsF_6]$; thermal ellipsoids are shown at the 50% probability level. (b) The gas-phase geometry of the $F_4S{=}N{-}Xe{---}N{\equiv}SF_3^+$ cation calculated at the MP2/aug-cc-pVTZ level of theory (Table 6.2).

$[F_4S{=}NXe][AsF_6]$ (2.083(3) Å)[184] and $[F_5SN(H)Xe][AsF_6]$ (2.069(4) Å),[118] somewhat longer than the Xe–N bond of $[F_5TeN(H)Xe][AsF_6]$ (2.044(4) Å),[50] but considerably shorter than the Xe–N bonds of nitrogen base adducts of XeF^+ (vide infra). The S=N bond length of $F_4S{=}N{-}Xe{---}N{\equiv}SF_3^+$ (1.539(3) Å) is also equal, within experimental error, to those of $[F_4S{=}NXe][AsF_6]$ (1.556(3) Å)[184] and $F_4S{=}NF$ (1.520(9) Å),[74] but is longer than those of $F_4S{=}NH_2^+$ (1.511(6) Å)[184] and $F_4S{=}NCH_3$ (1.480(6) Å).[100] All of the SF_4-group bond lengths of $F_4S{=}N{-}Xe{---}N{\equiv}SF_3^+$ are the same within $\pm3\sigma$ as those of $[F_4S{=}NXe][AsF_6]$.[184] The Xe–N(1)=S(1) and N(1)=S(1)–F(1) angles of $F_4S{=}N{-}Xe{---}N{\equiv}SF_3^+$ (119.8(2) and 87.6(2)°) are slightly greater than those of $[F_4S{=}NXe][AsF_6]$ (118.0(2) and 86.4(2)°).[184] All other angles that are in common with the two structures are equal within ±0.9°. Comparisons of $F_4S{=}NXe^+$ with $F_4S{=}NH_2^+$, $F_4S{=}NCH_3$, and $F_4S{=}NF$ have been discussed in detail in ref 184.

The short Xe---N(2) contact (2.583(3) Å) is well within the sum of the nitrogen and xenon van der Waals radii (3.71 Å)[31] but considerably longer than the Xe–N bond lengths of the related cations $[F_3S{\equiv}NXeF][AsF_6]$ (2.236(4) Å),[146] $[HC{\equiv}NXeF][AsF_6]$ (2.235(3) Å),[38] $[(CH_3)_3C{\equiv}NXeF][AsF_6]$ (2.212(4) Å),[38] and $[CH_3C{\equiv}NXeF][AsF_6]{\cdot}HF$ (2.179(7) Å),[38] while somewhat shorter than the Xe---N contacts in the $CH_3C{\equiv}N$ solvated salts of the more weakly acidic $C_6F_5Xe^+$ cation, $[C_6F_5Xe{---}N{\equiv}CCH_3][B(C_6F_5)_4]$ (2.610(11) Å),[42] $[C_6F_5Xe{---}N{\equiv}CCH_3][B(CF_3)_4]$ (2.640(6) Å),[42] $[C_6F_5Xe{---}N{\equiv}CCH_3][(C_6F_5)_2BF_2]$ (2.681(8) Å),[41] and $[C_6F_5Xe{---}NC_5H_3F_2][AsF_6]$ (2.694(5) Å).[43] The donor-acceptor bond length trends are in accordance with the gas-phase donor-acceptor dissociation energies calculated for $F_3S{\equiv}NXeF^+$, $HC{\equiv}NXeF^+$, $F_4S{=}N{-}Xe{---}N{\equiv}SF_3^+$, and $F_3S{\equiv}NAsF_5$ (see section 6.3).

The bent Xe---N≡S angle (148.0(2)°) is similar to that of $[F_3S{\equiv}NXeF][AsF_6]$ (142.6(3)°)[146] and to the Xe---N≡C angles in $[C_6F_5Xe{---}N{\equiv}CCH_3][B(C_6F_5)_4]$ (150.3(9)°),[42] and $[C_6F_5Xe{---}N{\equiv}CCH_3][B(CF_3)_4]$ (155.0(7)°),[42] but contrasts with the nearly linear Xe---N≡C angles in $[HC{\equiv}NXeF][AsF_6]$ (177.7(3)°),[38] $[CH_3C{\equiv}NXeF][AsF_6]{\cdot}HF$ (175.0(8)°),[38] and $[(CH_3)_3C{\equiv}NXeF][AsF_6]$ (166.9(4)°),[38] and with the near-linear gas-phase geometries predicted by quantum-chemical calculations (MP2/aug-cc-pVTZ(-PP)) for the gas-phase ions. The N–Xe---N angle (168.4(1)°) deviates somewhat more from linearity than the C–Xe---N angles of $[C_6F_5Xe{---}N{\equiv}CCH_3][(C_6F_5)_2BF_2]$ (174.5(3)°),[41] $[C_6F_5Xe{---}N{\equiv}CCH_3][B(CF_3)_4]$ (174.9(2)°),[42] and $[C_6F_5Xe{---}N{\equiv}CCH_3][B(C_6F_5)_4]$ (176.9(3)°).[42] The out-of-plane and in-plane N–Xe---N bending frequencies are assigned at 144 and 255 cm^{-1}, respectively, and the Xe---N≡S bends, which were too low in frequency to be observed in the Raman spectrum, were calculated at 64 and 72 cm^{-1}, respectively, showing that both angles are highly deformable and that their non-linearities likely arise from crystal packing (see section 6.3.).

The bond lengths of adducted $N{\equiv}SF_3$ in $F_4S{=}N{-}Xe{---}N{\equiv}SF_3^+$ (S≡N, 1.398(3) and S–F, av., 1.524(3) Å) are shorter than those in free $N{\equiv}SF_3$ (S≡N, 1.415(3) and S–F, av., 1.547(1) Å).[85,86] Similar S≡N and S–F bond length contractions have been observed in other main-group adducts,[78] namely, $F_3S{\equiv}NAsF_5$ (1.383 and 1.439 Å)[78] and $[F_3S{\equiv}NXeF][AsF_6]$ (1.397(5) and 1.503(3) Å),[146] and in the transition metal adducts $[Mn(N{\equiv}SF_3)_4][AsF_6]_2$ (1.365(11) and 1.506(5) Å)[90] and $[Re(CO)_5N{\equiv}SF_3][AsF_6]$ (1.384(14) and 1.499(10) Å)[93] (see section 6.3.).

The N≡S–F and F–S–F angles in the adducted $N{\equiv}SF_3$ molecule average 121.4(2)° and 95.4(2)°, respectively, comprising a distorted tetrahedral arrangement about sulfur that is similar to those of free $N{\equiv}SF_3$ (av., 122.2(2)° and 94.2(1)°),[86] and of adducted $N{\equiv}SF_3$, as in $F_3S{\equiv}NAsF_5$ (122.2° and 94.3°)[78] and $[F_3S{\equiv}NXeF][AsF_6]$ (av., 119.8(2) and 97.4(2) Å)[146] (also see section 6.3.).

6.2.2.2. $[F_3S(N{\equiv}SF_3)_2][AsF_6]$

The SF_3^+ cation has been previously characterized as its AsF_6^-,[186,189-192] SbF_6^-,[186,189] PF_6^-,[186,191] BF_4^-,[186,189-191] and GeF_6^{2-} [193] salts. A series of mixed CF_3/F adduct-cations, $[(CF_3)_n(F)_{3-n}S{-}{-}{-}N{\equiv}SF_3][AsF_6]$ (n = 0–2), has been studied by ^{19}F NMR in SO_2 solvent at temperatures below –30 °C where the cations corresponding to n = 0 or 1 are labile and weakly coordinated.[89] In contrast, the $(CF_3)_2FS{-}{-}{-}N{\equiv}SF_3^+$ cation is non-labile and pentacoordinate at sulfur in SO_2 solvent at temperatures below –30 °C.[89]

The crystal structure of $[F_3S(N{\equiv}SF_3)_2][AsF_6]$ consists of an SF_3^+ cation having three long contacts to S(IV), one to a fluorine atom of a neighboring AsF_6^- anion and two to the nitrogen atoms of the $N{\equiv}SF_3$ molecules (Figure 6.2). Ignoring the S---N and S---F contacts, the SF_3^+ cation is very close to C_{3v} symmetry, as has been observed for $[SF_3][BF_4]$[190] and $[SF_3]_2[GeF_6]$,[193] the only other SF_3^+ salts to have been structurally characterized by single-crystal X-ray diffraction. In the latter salts, the S(IV) coordination sphere includes three long contacts to fluorine ligands of their anions. As in the

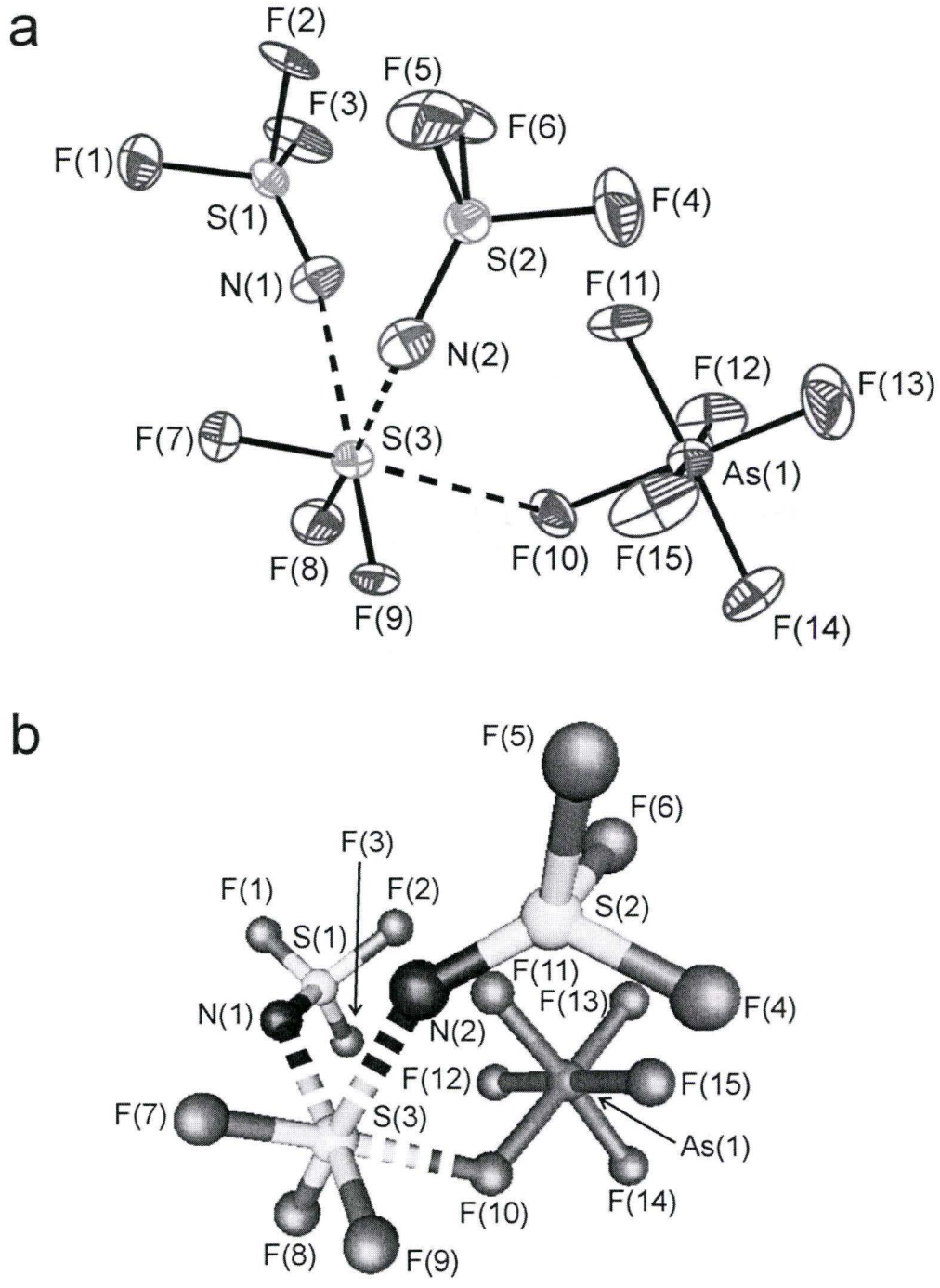

Figure 6.2. (a) The structural unit in the X-ray crystal structure of $[F_3S(N{\equiv}SF_3)_2][AsF_6]$; thermal ellipsoids are shown at the 50% probability level. (b) The gas-phase geometry of $[F_3S(N{\equiv}SF_3)_2][AsF_6]$ calculated at the PBE1PBE/aug-cc-pVTZ level of theory (Table 6.3).

$[SF_3][BF_4]$ and $[SF_3]_2[GeF_6]$ salts, the arrangement of long contacts in the present structure avoids, to the maximum extent, the F atoms and the nonbonding electron pair situated on the pseudo three-fold axis opposite the F ligands of SF_3^+, providing distorted octahedral coordination at the S(IV) atom.

The S–F bond lengths of SF_3^+ (1.511(1), 1.519(1), 1.520(1) Å) in $[F_3S(N{\equiv}SF_3)_2][AsF_6]$ are equal, within experimental error, to those in $[SF_3]_2[GeF_6]$ (1.515(2), 1.519(2), 1.519(2) Å)[193] and are somewhat longer than those in $[SF_3][BF_4]$ (1.495(2), 1.495(2), 1.499(2) Å, but are within $\pm 3\sigma$ for the thermally corrected values of the latter salt (1.518, 1.518, 1.514 Å).[190] The F–S–F bond angles of the cation (96.2(1)°, 96.3(1)°, 96.8(1)°) are in agreement with those in $[SF_3]_2[GeF_6]$ (96.2(1)°)[193] and $[SF_3][BF_4]$ (97.62(7)°, 97.62(7)°, 97.39(12)°),[190] and are significantly greater than 90°, as is predicted for the gas-phase cation (94.5°, 94.5°, 95.0°; also see section 6.3.). The short S---F contact between the cation and a fluorine of AsF_6^- (2.558(2) Å) of $[F_3S(N{\equiv}SF_3)_2][AsF_6]$ is well within the sum of the sulfur and fluorine van der Waals radii (3.27 Å)[31] and is bracketed by the S---F contact distances reported for $[SF_3]_2[GeF_6]$ (2.367(2) and 2.420(1) Å)[193] and for $[SF_3][BF_4]$ (2.593(3) and 2.624(2) Å).[190] The short S---N contacts between SF_3^+ and the nitrogen atoms of the $N{\equiv}SF_3$ molecules (2.511(2) and 2.554(2) Å) are significantly less than the sum of the sulfur and nitrogen van der Waals radii (3.35 Å)[31] and are similar to the S---F contact distances. The N---S---N (96.3(1)°), and F---S---N (97.7(1) and 104.4°) angles are significantly greater than 90°, forming a distorted octahedral geometry about sulfur such that the contacts to $N{\equiv}SF_3$ and AsF_6^- avoid the stereochemically active valence electron lone pair and fluorine ligands of SF_3^+

to the maximum extent, and are similar to the long contacts observed in the X-ray crystal structures of $[SF_3][BF_4]$[190] and $[SF_3]_2[GeF_6]$.[193]

The bond lengths and angles of the adducted $N{\equiv}SF_3$ molecules (S≡N; 1.384(2), and 1.392(2), S–F; av., 1.520(2) Å, N–S–F; av., 121.4(1)°, F–S–F; av., 95.2(1)° show the expected contractions[78] relative to those of free $N{\equiv}SF_3$ (S≡N; 1.415(3), S–F; av., 1.547(1) Å, N–S–F; 122.2(1)°, F–S–F; 94.2(1)°)[86] and are very similar to those of adducted $N{\equiv}SF_3$ in $F_4S{=}N{-}Xe{-}{-}{-}N{\equiv}SF_3^+$ and in related adducts (vide supra).

6.2.3. Raman Spectroscopy

6.2.3.1. $[F_4S{=}N{-}Xe{-}{-}{-}N{\equiv}SF_3][AsF_6]$

The Raman spectrum of the $F_4S{=}N{-}Xe{-}{-}{-}N{\equiv}SF_3^+$ cation in its AsF_6^- salt (Figure 6.3) was assigned by comparison with those of $[F_4S{=}NXe][AsF_6]$,[184] $N{\equiv}SF_3$,[146] and $[F_3S{\equiv}NXeF][AsF_6]$,[146] as well as by comparison with the calculated frequencies for the gas-phase energy-minimized geometries of $F_4S{=}NXe^+$,[184] $F_4S{=}NF$,[184] $F_3S{\equiv}NXeF^+$,[146] $N{\equiv}SF_3$,[146] and $F_4S{=}N{-}Xe{-}{-}{-}N{\equiv}SF_3^+$ (see Table 6.4, section 6.3.). The vibrational modes of the uncoordinated AsF_6^- anion were assigned by comparison with those of $[O_2][AsF_6]$,[160] $[HC{\equiv}NXeF][AsF_6]$,[35] $[F_3S{\equiv}NXeF][AsF_6]$,[146] $[F_5TeNH_3][AsF_6]$,[50] and $[F_5SNH_3][AsF_6]$.[118] Calculated frequencies at the MP2/aug-cc-pVTZ(-PP) level of theory provided the best overall agreement with experimental values (see section 6.3.) and are considered in the ensuing discussion (indicated in square brackets).

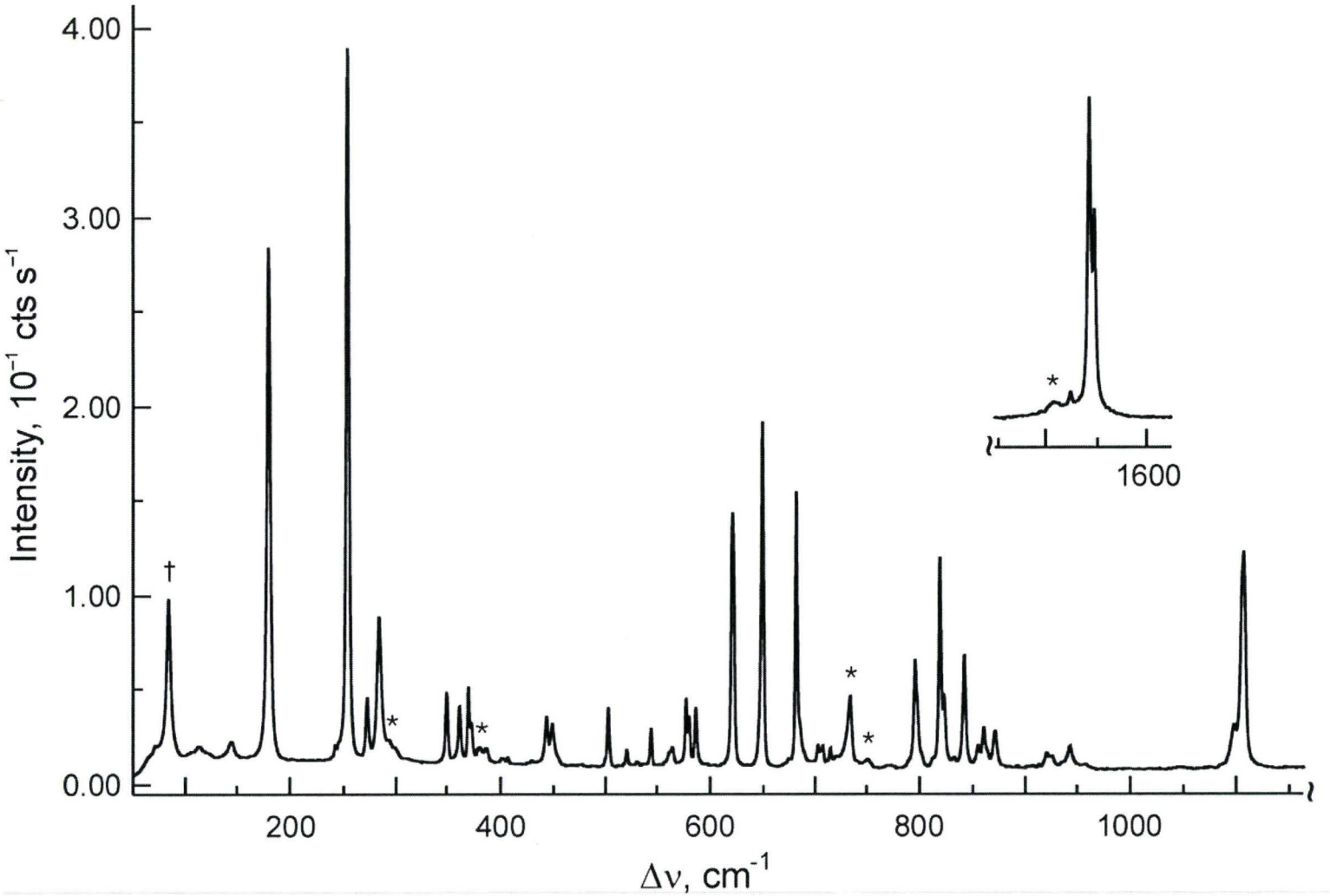

Figure 6.3. The Raman spectrum of $[F_4S{=}N{-}Xe{-}{-}{-}N{\equiv}SF_3][AsF_6]$ recorded at –160 °C using 1064-nm excitation; symbols denote FEP sample tube lines (*) and an instrumental artifact (†).

Table 6.4. Experimental Raman Vibrational Frequencies and Intensities for $[F_4S{=}N{-}Xe{---}N{\equiv}SF_3][AsF_6]$ and Calculated Vibrational Frequencies, Intensities, and Assignments for $F_4S{=}N{-}Xe{---}N{\equiv}SF_3^+$

freq, cm^{-1}					
	calcd[b]			assgnts[c]	
exptl[a]	MP2	PBE1PBE1	B3LYP	$F_4S{=}NXe{---}N{\equiv}SF_3^+$ (C_1)	AsF_6^- (O_h)
1548 (29) 1543 (45)	1546 [350]	1601 (166) [460]	1560 (180) [408]	ν(S≡N)	
1109 (30) 1099 (6)	1132 [558]	1112 (104) [571]	1044 (145) [523]	ν(S=N)	
943 (3)	932 [181]	935 (3) [184]	893 (4) [179]	ν(S1F2 – S1F3)	
926 (2) 921 (2)	885 [303]	898 (5) [199]	848 (8) [282]	ν(S2F5 + S2F6) – ν(S2F7) + ν(S1F1) – ν(S1F4)	
872 (5)	885 [182]	897 (5) [177]	848 (6) [179]	ν(S2F5 – S2F6) + ν(S2F7)	
862 (5) 856 (3)	884 [170]	889 (19) [274]	846 (21) [185]	ν(S1F1 – S1F4) + ν(S2F7)	
824 (10) 819 (29)	823 [143]	840 (59) [151]	794 (59) [164]	ν(S2F5 + S2F6 + S2F7) + ν(S≡N)	
798 sh 796 (15)	805 [121]	799 (16) [106]	753 (18) [101]	ν(S1F2 + S1F3 + S1F4) + ν(S=N)	
720 (2) 714 (3) 707 (3) 702 (3)					ν_3 (T_{1u})
685 (6) 682 (38)					ν_1 (A_{1g})
650 (48)	659 [15]	645 (60) [37]	624 (31) [39]	δ(N=SF2F3) o.o.p.	
622 (32)	624 [6]	632 (20) [2]	604 (48) [6]	ν(S1F1 + S1F4)	
586 (8) 580 (7)					ν_2 (E_g)
577 (10)	578 [31]	572 (8) [44]	552 (7) [40]	δ(N=SF1) – δ(N=SF4) + ρ_w(F2S1F3)	
564 (3) 561 (2)	556 [67]	555 (1) [74]	535 (1) [87]	δ(F1S1F4) + δ(F2S1F3)	

Table 6.4. (continued…)

544 (5)	527 [8]	525 (3) [7]	508 (2) [7]	$\delta(S2F_3)$	
531 (1) 521 (2)	511 [<1]	508 (1) [<1]	489 (1) [<1]	$\delta(F1S1F2) + \delta(F3S1F4)$	
503 (8)	496 [15]	498 (3) [16]	478 (3) [15]	$\delta(N{\equiv}SF1F4)$ o.o.p. + $\rho_r(F2S1F3)$	
450 (6)	432 [13]	439 (4) [16]	419 (4) [14]	$\delta(N{\equiv}SF5F7)$	
444 (7)	431 [13]	439 (4) [16]	419 (4) [13]	$\delta(N{\equiv}SF5F6)$	
407 (1) 403 (1) 401 (1)					ν_4 (T_{1u})
373 sh 370 (11)					ν_5 (T_{2g})
362 (8)	342 [3]	341 (2) [2]	329 (2) [2]	$\delta(N{\equiv}SF5) + \delta(F6S2F7)$	
349 (10)	341 [2]	341 (2) [2]	328 (2) [2]	$\delta(N{\equiv}SF7) + \delta(F5S2F6)$	
284 (20)	282 [11]	275 (36) [8]	259 (25) [4]	ν(XeN1)	
273 (9)	264 [1]	265 (1) [1]	255 (1) [1]	$\delta(XeN{=}S)$ o.o.p. + $\delta(N{=}SF2) - \delta(N{=}SF3)$	
255 (100)	251 [<1]	247 (8) [<1]	237 (23) [<1]	δ(N1XeN2) i.p.	
246 sh 243 (2)					ν_6 (T_{2u})
180 (71)	180 [21]	175 (17) [18]	164 (14) [25]	$\delta(XeN{=}S)$ i.p.	
144 (2)	119 [1]	116 (1) [1]	107 (1) [1]	δ(N1XeN2) o.o.p.	
113 (2)	103 [33]	96 (<1) [34]	86 (<1) [31]	ν(XeN2)	
n.o.	72 [2]	68 (<1) [2]	60 (<1) [2]	$\delta(XeN{\equiv}S)$ i.p.	
n.o.	64 [1]	60 (<1) [1]	55 (<1) [1]	$\delta(XeN{\equiv}S)$ o.o.p.	
n.o.	20 [<1]	18 (<1) [<1]	18 (<1) [<1]	$\rho_w(N{\equiv}SF_3)$ o.o.p.[d]	
n.o.	19 [<1]	17 (<1) [<1]	16 (<1) [<1]	$\rho_w(N{\equiv}SF_3)$ i.p.[d]	
n.o.	2 [<1]	2 (<1) [<1]	6 (<1) [<1]	$N{\equiv}SF_3$ torsion about Xe---N bond	

[a] Values in parentheses denote experimental Raman intensities, abbreviations denote shoulder (sh) and not observed (n.o.). [b] aug-cc-pVTZ(-PP) basis set. Calculated Raman intensities (in $Å^4$ amu^{-1}) are given in parentheses and calculated infrared intensities (in km mol^{-1}) are given in brackets. Calculated Raman intensities at the MP2 level were not possible given the presently available computing resources [c] The atom numbering corresponds to that given in Figure 1. Abbreviations denote out of plane (o.o.p.) and in plane (i.p.), where the planes are defined by the atoms they contain, unless otherwise specified; inversion (inv); wag (ρ_w); and rock (ρ_r). [d] The plane is defined by the S1, N1, and Xe1 atoms.

The $F_4S{=}N{-}Xe{---}N{\equiv}SF_3^+$ cation possesses C_1 symmetry for the calculated gas-phase and X-ray structures which is predicted to give rise to 30 Raman- and infrared-active fundamental vibrational modes belonging to A irreducible representations. The AsF_6^- anion possesses 15 fundamental vibrational modes which were assigned under O_h symmetry and belong to the irreducible representations $A_{1g} + E_g + T_{2g} + 2T_{1u} + T_{2u}$, where the A_{1g}, E_g, and T_{2g} modes are Raman-active and the T_{1u} modes are infrared-active. The formally Raman-inactive T_{1u} modes were, however, observed as weak bands at 702, 707, 714, and 720 cm^{-1} and at 401, 403, and 407 cm^{-1}, and the formally Raman-inactive T_{2u} mode was observed as a pair of weak bands at 243 and 246 cm^{-1} (vide infra), which are accounted for in the factor-group analysis of this salt. Factor-group analyses correlating the cation (C_1) and anion (O_h) symmetries to their crystal site symmetries (C_1) and to the unit cell symmetry (C_{2h}) are provided in Table 6.5. The A irreducible representations of the cation are maintained under C_1 site symmetry, but the doubly and triply degenerate E- and T-modes of the anion are split because their degeneracies are removed as a result of site-symmetry lowering. Both the cation and anion modes are further split into Raman-active A_g and B_g, and infrared-active A_u and B_u components under C_{2h} crystal symmetry, giving the potential to observe 60 bands for the cation and 30 bands for the anion in both the Raman and infrared spectra. Although several of the cation bands are split into two components in the Raman spectrum and the $\nu_3(T_{1u})$ band of the 15 observed anion bands is also split in the Raman spectrum, the coupling within the crystallographic unit cell is deemed to be weak and is not otherwise manifested for the cation or the anion.

Table 6.5. Correlation Diagrams and Selection Rules for the Vibrational Modes of $[F_4S{=}NXe{---}N{\equiv}SF_3][AsF_6]$

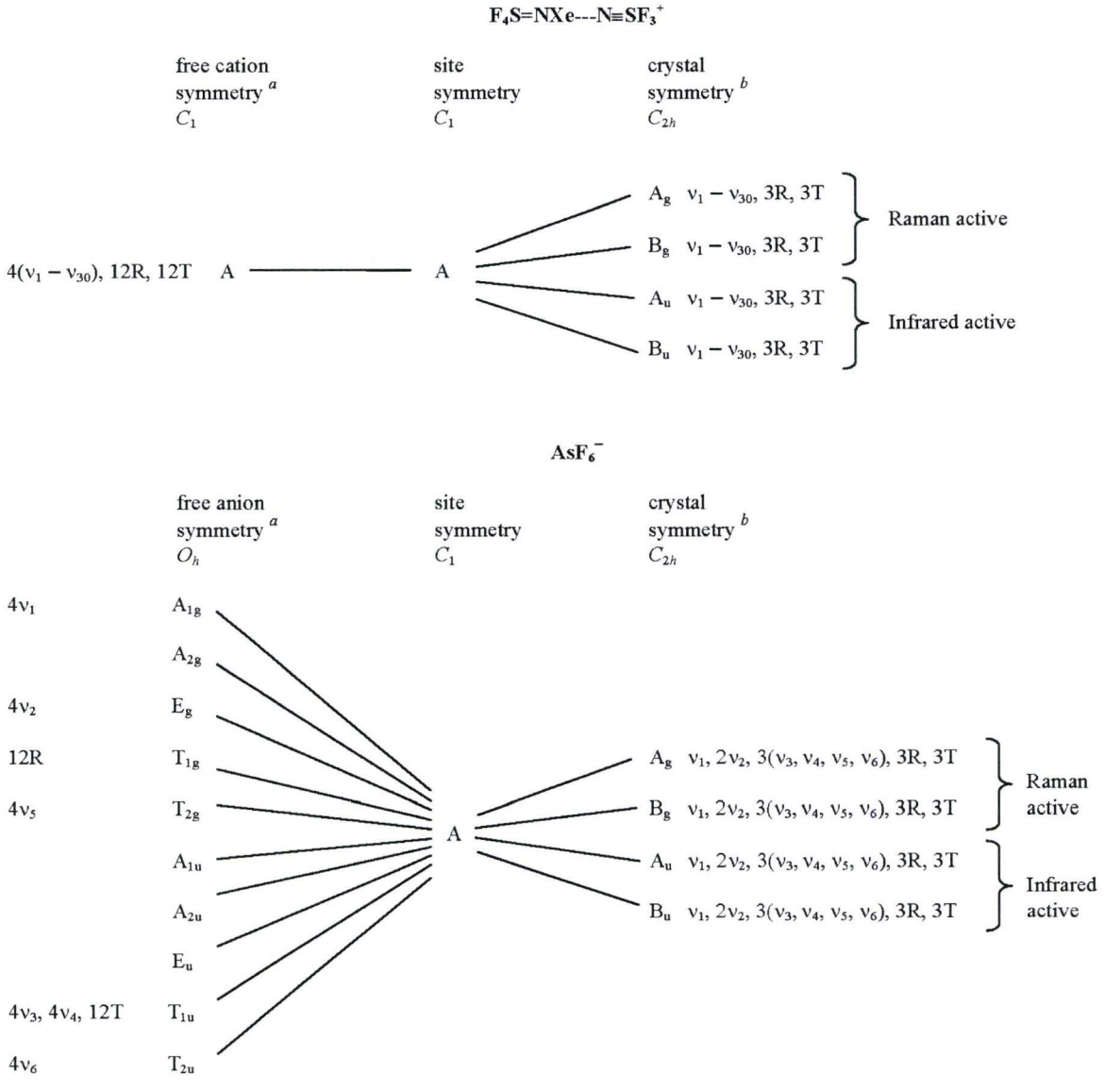

[a] The irreducible representations are $\Gamma = 30A$ (C_1) for the $F_4S{=}NXe{---}N{\equiv}SF_3^+$ adduct cation and $\Gamma = A_{1g} + E_g + T_{2g} + 2T_{1u} + T_{2u}$ (O_h) for the AsF_6^- anion in the gas phase. [b] The crystallographic space group is $P2_1/n$ with $Z = 4$ structural units per unit cell

The calculated vibrational frequencies for the $F_4S{=}N{-}Xe{---}N{\equiv}SF_3^+$ adduct cation are in good agreement with the experimental frequencies. The ν(Xe–N) stretch at 284 [282] cm^{-1} is slightly higher in frequency than the terminal ν(Xe–N) stretches observed for $F_4S{=}NXe^+$ (253, 259 cm^{-1})[184] and $F_5SN(H)Xe^+$ (224 cm^{-1}),[118] and the ν(Xe–N) stretch in $[F_3S{\equiv}NXeF][AsF_6]$ (194 cm^{-1}).[146] The ν(Xe---N) stretch at 113 [103] cm^{-1} is considerably lower than those mentioned above but is most similar to that in $F_3S{\equiv}NXeF^+$, affirming the highly ionic character of the Xe---N donor-acceptor bond. These ν(Xe–N) and ν(Xe---N) stretching frequencies are considerably lower than the coupled ν(Xe–N) + ν(Xe–N) and ν(Xe–N) – ν(Xe–N) stretches in $Xe[N(SO_2F)_2]_2$, (413, 406 and 386, 380 cm^{-1}, respectively).[47] The latter modes occur at higher frequencies due to the greater covalent characters of the Xe–N bonds. The in-plane and out-of-plane N–Xe---N bends in the Raman spectrum of $[F_4S{=}N{-}Xe{---}N{\equiv}SF_3][AsF_6]$ occur at 255 [251] and 144 [119] cm^{-1}, respectively, compared with bands observed at 201 and 161 cm^{-1} for δ(N–Xe–N) in $Xe[N(SO_2F)_2]_2$.[47] The in-plane N–Xe–N and N–Xe---N bends are the most intense bands in their respective Raman spectra. The out-of-plane and in-plane Xe–N=S bends of the $F_4S{=}NXe{-}$ moiety of $F_4S{=}N{-}Xe{---}N{\equiv}SF_3^+$ at 273 [264] and 180 [180] cm^{-1}, respectively, are in good agreement with the corresponding frequencies observed for $[F_4S{=}NXe][AsF_6]$[184] at 273, 178, and 184 cm^{-1}. Together, these values bracket the Xe–N–S bending frequencies reported for $XeN(SO_2F)_2^+$ (226, 241, 251, 259, 267 cm^{-1})[49] and $F[XeN(SO_2F)_2]_2^+$ (208, 224, 231, 240, 247, 260, 264 cm^{-1})[49] and are higher in frequency than those in $FXeN(SO_2F)_2$ (96, 111, 116, 119 cm^{-1}).[46] The S=N stretch at 1099, 1109

[1132] cm^{-1} compares well with the S=N stretching frequencies of other imido species ($[F_4S{=}NXe][AsF_6]$ 1097, 1104 cm^{-1};[184] $F_4S{=}NF$ 1125 cm^{-1};[74] $F_4S{=}NSF_5$ 1299 cm^{-1} [167]). The experimental SF_4 stretching (622–943 cm^{-1}) and bending (503–577 cm^{-1}) frequencies fall into ranges that are similar to those of $[F_4S{=}NXe][AsF_6]$[184] and the benchmark, $F_4S{=}NF$[74,184] (see section 6.3.).

All $N{\equiv}SF_3$ modes of $[F_4S{=}N{-}Xe{---}N{\equiv}SF_3][AsF_6]$ exhibit high-frequency shifts relative to those of $N{\equiv}SF_3$. The S≡N stretching mode occurs at 1543 and 1548 [1546] cm^{-1} compared to that of $N{\equiv}SF_3$ (solid, 1503, 1519, 1524 cm^{-1};[146] liquid, 1517 cm^{-1} [144]) and is comparable to that of $[F_3S{\equiv}NXeF][AsF_6]$ (1527, 1542, 1548 cm^{-1});[146] however, a larger complexation shift [43 cm^{-1}] is calculated for the gas-phase species. The average out-of-phase and in-phase $\nu(SF_3)$ frequencies increase by 66 [95] cm^{-1} and 43 [78] cm^{-1}, respectively, upon complexation, and the average in-phase and out-of-phase bending frequencies shift to higher frequency by 16, 5, and 4 [24, 18, 10] cm^{-1}, which are less than or similar to the complexation shifts observed for $[F_3S{\equiv}NXeF][AsF_6]$.[146] These high-frequency shifts are in accord with the N≡S and S–F bond length contractions that result from adduct formation with the $F_4S{=}NXe^+$ cation (see section 6.2.2.1.). Complexation shifts for $F_4S{=}N{-}Xe{---}N{\equiv}SF_3^+$ are less than those of $F_3S{\equiv}NXeF^+$ because $F_4S{=}N{-}Xe^+$ is a weaker Lewis acid than XeF^+ (see calculated donor-acceptor adduct dissociation energies; section 6.3.4.), and are in accordance with the longer Xe---N distance in $F_4S{=}N{-}Xe{---}N{\equiv}SF_3^+$ (2.583(3) Å), than in $F_3S{\equiv}NXeF^+$ (2.236(4) Å).[146]

6.2.3.2. $[F_3S(N{\equiv}SF_3)_2][AsF_6]$

The Raman spectrum of $[F_3S(N{\equiv}SF_3)_2][AsF_6]$ (Figure 6.4) was assigned by comparison with those of SF_3^+ in its AsF_6^-,[186,191] SbF_6^-,[186] PF_6^-,[186,191] and BF_4^-,[186,189,191] salts and by comparison with free $N{\equiv}SF_3$,[146] adducted $N{\equiv}SF_3$ in $[F_3S{\equiv}NXeF][AsF_6]$,[146] and $F_4S{=}N{-}Xe{---}N{\equiv}SF_3^+$ (vide supra) as well as by comparison with the calculated frequencies derived for the gas-phase energy-minimized geometry of the $[F_3S(N{\equiv}SF_3)_2][AsF_6]$ ion-pair (see Table 6.6, section 6.3.). The vibrational modes of AsF_6^- in the ion pair were assigned by comparison with those of $[F_4S{=}NXe][AsF_6]$,[184] $[F_5SN(H)Xe][AsF_6]$,[118] $[F_5TeN(H)Xe][AsF_6]$,[50] $[F_5TeOXe][AsF_6]$,[156] $[XeF][AsF_6]$,[112] and $[KrF][AsF_6]$.[109] Calculated frequencies for the PBE1PBE/aug-ccpVTZ(-PP) level of theory, the highest level of theory available for the ion-pair in this work, appear in square brackets in the following discussion.

The 57 vibrational modes of the $[F_3S(N{\equiv}SF_3)_2][AsF_6]$ ion-pair under C_1 symmetry (see section 6.3.) belong to A irreducible representations, which are both Raman- and infrared-active. The cation-anion fluorine bridge interaction lowers the O_h symmetry of the anion (see sections 6.2.2.1. and 6.2.2.2.), and additional lines in the vibrational spectrum were consequently observed. The vibrational bands of the anion were also assigned under C_1 symmetry of the ion-pair. A total of 17 vibrational bands were observed that are derived from their counterparts under O_h symmetry. The anion assignments are correlated to the irreducible representations $A_{1g} + E_g + 2T_{1u} + T_{2g} + T_{2u}$ under O_h symmetry, with only three bands being further split by symmetry-lowering of the anion [E_g and one T_{1u}], for a total of 17 observed bands (correlations with O_h symmetry are given in square brackets), namely,

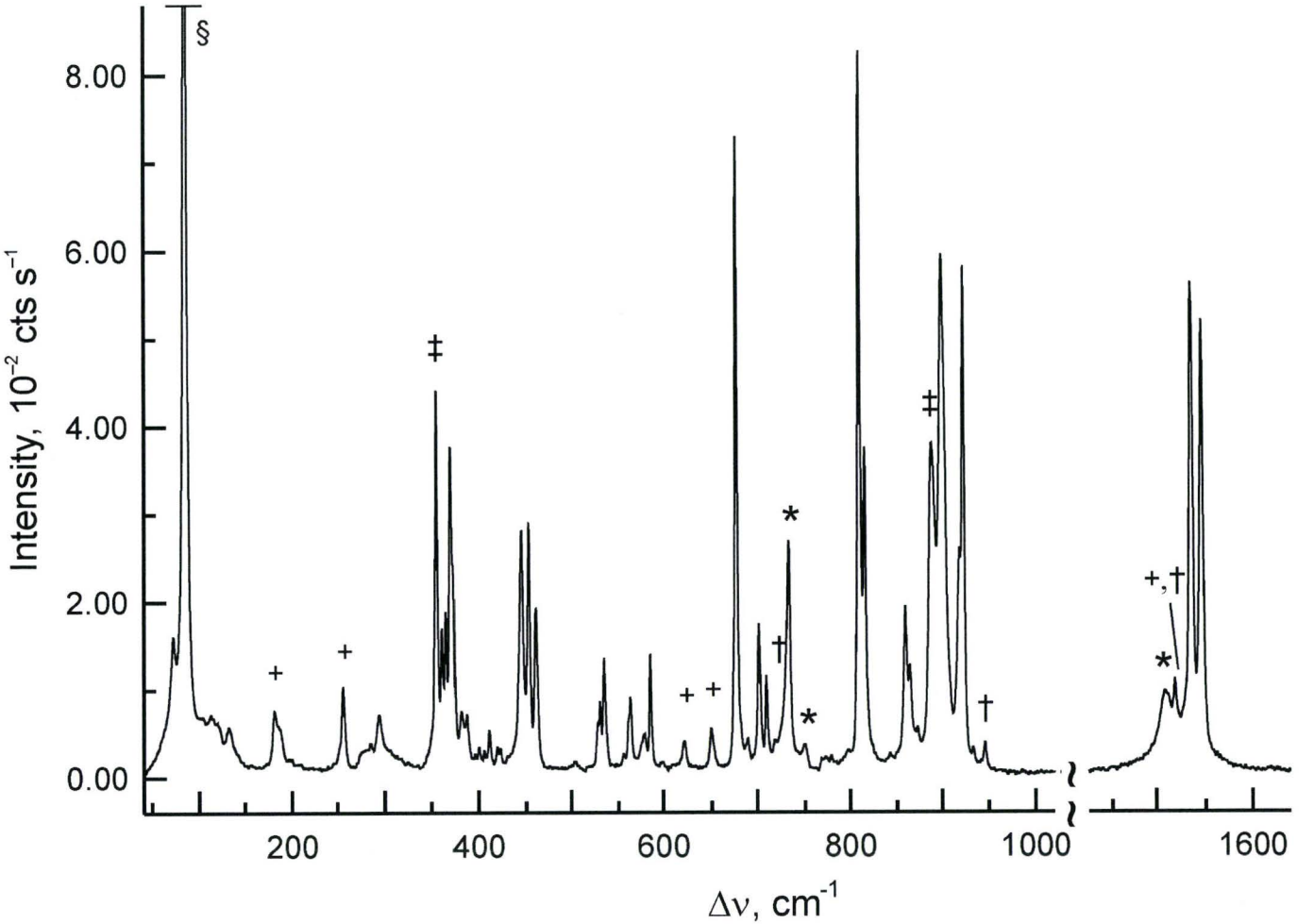

Figure 6.4. The Raman spectrum of $[F_3S(N{\equiv}SF_3)_2][AsF_6]$ recorded at –160 °C using 1064-nm excitation. Symbols denote bands from unreacted $[F_4S{=}N{-}Xe{---}N{\equiv}SF_3][AsF_6]$ (+); *cis*-N_2F_2 (†); coincidence of $F_3S(N{\equiv}SF_3)_2^+$ and *cis*-N_2F_2 bands (‡); FEP sample tube lines (*); and an instrumental artifact (§).

Table 6.6. Experimental Raman Frequencies and Intensities, and Calculated Vibrational Frequencies, Intensities, and Assignments for the $[F_3S(N{\equiv}SF_3)_2][AsF_6]$ ion-pair

freq, cm^{-1}			assgnts[c]	
	calcd[b]			
exptl[a]	PBE1PBE	B3LYP	$[F_3S(N{\equiv}SF_3)_2][AsF_6]$ (C_1)	AsF_6^- (O_h)
1546 (63)	1574 (95) [198]	1535 (98) [182]	ν(N1S1 + N2S2)	
1535 (68)	1569 (37) [290]	1530 (40) [255]	ν(N1S1 – N2S2)	
922 (70) 919 (31)	903 (100) [236]	872 (109) [209]	ν(S3F8 + S3F9)	
899 (72)	883 (22) [350]	851 (25) [298]	ν(S3F8 – S3F9)	
888 (46)	871 (6) [159]	822 (6) [178]	ν(S1F2 – S1F3) + ν(S2F6 – S2F4)	
881 sh	865 (3) [50]	816 (2) [101]	ν(S1F2 – S1F3) + ν(S2F4 – S2F6)	
873 (6)	862 (9) [509]	819 (12) [469]	ν(S3F7)	
864 (15)	845 (9) [15]	797 (9) [13]	ν(S1F2 + S1F3) – ν(S1F1) + ν(S2F4 + S2F6) – ν(S2F5)	
859 (23)	843 (8) [88]	796 (7) [135]	ν(S1F2 + S1F3) – ν(S1F1) – ν(S2F4 + S2F6) + ν(S2F5) + ν(S3F7)	
815 (45) 809 (100)	810 (50) [105]	767 (53) [109]	ν(N1S1) + ν($S1F_3$) + ν(N2S2) + ν($S2F_3$)	
798 (3)	804 (3) [289]	761 (3) [278]	ν(N1S1) + ν($S1F_3$) – ν(N2S2) – ν($S2F_3$)	
719 (4)	742 (2) [171]	716 (2) [167]	ν(As1F11 – As1F14)	ν_3 (T_{1u})
710 (13)	724 (4) [119]	700 (3) [122]	ν(As1F13)	
702 (20)	722 (1) [153]	698 (1) [151]	ν(As1F12 – As1F15)	
690 (4)				
677 (88)	665 (15) [60]	641 (17) [52]	ν(As1F11 + As1F14) + ν(As1F12 + As1F15)	ν_1 (A_{1g})
586 (16) 580 (5)	584 (1) [2]	567 (1) [2]	ν(As1F11 + As1F14) – ν(As1F12 + As1F15)	ν_2 (E_g)
564 (10) 557 (2)	527 (1) [31]	512 (1) [31]	δ(S3F7F8F9) o.o.p.	
536 (15)	518 (1) [24]	500 (1) [21]	δ(S1F1F2F3) o.o.p. + δ(S2F4F5F6) o.o.p.	
531 (9) 529 (6)	517 (2) [15]	500 (2) [14]	δ(S1F1F2F3) o.o.p. – δ(S2F4F5F6) o.o.p.	
504 (1) br	487 (2) [62]	460 (2) [52]	ν(As1F10)	
462 (22)	443 (2) [29]	422 (2) [26]	δ(N1S1F2F3) o.o.p. + δ(N2S2F5F6) o.o.p.	
454 (34)	443 (6) [5]	422 (7) [4]	δ(N1S1F2F3) o.o.p. – δ(N2S2F5F6) o.o.p.	

Table 6.6. (continued…)

446 (33)	438 (6) [10]	418 (6) [8]	δ(N1S1F1F3) o.o.p. + δ(N2S2F4F5) o.o.p.	
424 (3)	437 (<1) [19]	417 (<1) [15]	δ(N1S1F1F3) o.o.p. – δ(N2S2F4F5) o.o.p.	
420 (3)	419 (<1) [54]	409 (<1) [48]	ν(S3---F10)	
412 (5)	402 (<1) [23]	388 (<1) [19]	δ(F7S3F8) – δ(F7S3F9)	
406 (3)	395 (<1) [28]	383 (<1) [42]	δ(As1F10F12F13F15) o.o.p.[d] – δ(F8S3F9)	ν_4 (T_{1u})
400 (3)	392 (<1) [52]	382 (<1) [52]	δ(As1F10F11F13F14) o.o.p.[e]	
396 (3)	379 (1) [108]	362 (1) [78]	δ(As1F11F12F14F15) o.o.p.[f] + δ(F8S3F9)	
387 (8)	371 (1) [2]	362 (1) [2]	δ(F12As1F14) + δ(F13As1F15)	
381 (8)	359 (1) [39]	346 (1) [76]	δ(F10As1F11) + δ(F13As1F14)	
372 sh	349 (<1) [<1]	338 (<1) [<1]	δ(F12As1F13) + δ(F10As1F15) + δ(N1S1F3) + δ(F1S1F2) + δ(N2S2F4) + δ(F5S2F6)	ν_5 (T_{2g})
370 (44)	348 (4) [11]	335 (5) [14]	δ(N1S1F1) + δ(F2S1F3) + δ(N2S2F5) + δ(F6S2F7)	
365 (22)	348 (1) [2]	335 (<1) [2]	δ(F10As1F12) + δ(F13As1F15) + δ(N1S1F1) + δ(F2S1F3) + δ(N2S2F5) + δ(F4S2F6)	
361 (19)	343 (<1) [1]	330 (<1) [1]	δ(N1S1F2) + δ(F1S1F3) – δ(N2S2F6) – δ(F4S2F5)	
354 (53)	343 (4) [<1]	330 (4) [<1]	δ(N1S1F2) + δ(F1S1F3) + δ(N2S2F6) + δ(F4S2F5)	
294 (7)	256 (<1) [21]	251 (<1) [26]	δ(F10As1F13) – δ(F12As1F15) o.o.p.[d]	ν_6 (T_{2u})
285 (3)	243 (<1) [1]	237 (<1) [1]	δ(F10As1F13) – δ(F11As1F14) o.o.p.[e]	
278 (2) br	224 (<1) [<1]	216 (<1) [<1]	δ(F11As1F14) – δ(F12As1F15) o.o.p.[f]	
187 sh	193 (<1) [11]	181 (<1) [7]	ρ_t(F8S3F9)	
	191 (<1) [6]	181 (<1) [11]	ρ_w(F8S3F9) + ρ_r(F7S3F8)	
n.o.	145 (<1) [<1]	132 (<1) [<1]	SF_3^+ torsion about its own C_3-axis	
132 (6)	137 (1) [24]	135 (1) [23]	ν(N1S3 + N2S3)	
n.o.	95 (<1) [<1]	86 (<1) [<1]	δ(S1N1S3) o.o.p. + δ(S2N2S3) o.o.p.	
119 (6)	90 (1) [10]	84 (1) [8]	δ(S1N1S3) i.p. + δ(S2N2S3) i.p.	
112 (8)	87 (1) [7]	82 (1) [7]	δ(S1N1S3) i.p. – δ(S2N2S3) i.p.	
n.o.	77 (<1) [1]	69 (<1) [<1]	δ(S3F10As1) i.p.	
101 (7)	72 (1) [9]	66 (1) [7]	ν(N1S3 – N2S3)	
n.o.	58 (<1) [4]	50 (<1) [3]	coupled deformation mode	
n.o.	50 (<1) [<1]	45 (<1) [<1]	δ(N1S3N2) i.p.	
n.o.	49 (<1) [<1]	41 (<1) [<1]	coupled deformation mode	
n.o.	43 (<1) [2]	39 (<1) [2]	δ(N1S3N2) o.o.p.	
n.o.	41 (<1) [<1]	33 (<1) [<1]	N≡SF_3 torsions about N≡S bond	

Table 6.6. (continued…)

n.o.	37 (<1) [<1]	32 (<1) [<1]	coupled deformation modes
n.o.	32 (<1) [<1]	29 (<1) [<1]	
n.o.	18 (<1) [1]	15 (<1) [1]	
n.o.	12 (<1) [<1]	15 (<1) [<1]	δ(S3F10As1) o.o.p.

[a] Values in parentheses denote experimental Raman intensities, abbreviations denote shoulder (sh), broad (br) and not observed (n.o.). [b] aug-cc-pVTZ basis set. Calculated Raman intensities (in $Å^4$ amu^{-1}) are given in parentheses, calculated infrared intensities (in km mol^{-1}) are given in brackets. Bands corresponding to residual *cis*-N_2F_2 appear at 354,* 729,* 888,* 946 (5), and 1519† cm^{-1}, where * denotes coincidence with $F_3S(N{\equiv}SF_3)_2^+$ bands, and † denotes coincidence with ν(S≡N) of unreacted $F_4S{=}NXe{-}{-}{-}N{\equiv}SF_3^+$. [b] Abbreviations denote twist (ρ_t), wag (ρ_w), rock (ρ_r), out-of-plane (o.o.p.) and in-plane (i.p.), where the planes are defined by the atoms they contain, unless otherwise specified. [d] Plane defined by As1, F10, F12, F13, F15. [e] Plane defined by As1, F10, F11, F13, F14. [f] Plane defined by As1, F11, F12, F14, F15.

690, 702, 710, and 719 [T_{1u}]; 677 [A_{1g}]; 504, 580, and 586 [E_g]; 396, 400, and 406 [T_{1u}]; 372, 381 and 387 [T_{2g}]; and 278, 285, and 294 [T_{2u}] cm^{-1}.

A factor-group analysis correlating the ion-pair symmetry (C_1) to the crystal site symmetry (C_1) and to the unit cell symmetry (C_{2h}) is provided in Table 6.7. The A irreducible representations of the ion pair are maintained under C_1 site symmetry, and are split into Raman-active A_g and B_g components and infrared-active A_u and B_u components under C_{2h} crystal symmetry, giving the potential to observe a total of 114 bands for the ion-pair in both the Raman and infrared spectra. Only four cation and two anion bands of the 57 observed Raman bands, however, were further split under the crystal symmetry.

The calculated vibrational frequencies for $[F_3S(N{\equiv}SF_3)_2][AsF_6]$ are in good agreement with the experimental frequencies. The ν(S–F) stretches of SF_3^+ at 859, 873 [843, 862], 899 [883], and 919, 922 [903] cm^{-1} occur at lower frequencies than the ν(S–F) stretches of the BF_4^- (911, 914, 937 cm^{-1}),[191] AsF_6^- (926, 945, 960 cm^{-1}),[191] and PF_6^- (929, 954, 964 cm^{-1})[191] salts, but the δ(F–S–F) bends at 396 [379], 406 [395], 412 [402], 529, 531 [517], 536 [518], 557, and 564 [527] cm^{-1} are in better agreement with those of the BF_4^- (409, 526 cm^{-1}),[191] AsF_6^- (411, 530 cm^{-1}),[191] and PF_6^- (408, 531 cm^{-1})[191] salts. The intense high-frequency bands at 1535 [1569] and 1546 [1574] cm^{-1} are assigned to the coupled ν(N1≡S1) – ν(N2≡S2) and ν(N1≡S1) + ν(N2≡S2) stretches, respectively, and are consistent with the two adducted $N{\equiv}SF_3$ molecules of the $F_3S(N{\equiv}SF_3)_2^+$ cation. The ν(N≡S) stretching bands of the adducted $N{\equiv}SF_3$ molecules occur at higher frequencies relative to those of $N{\equiv}SF_3$ [1503] (liquid, 1517;[144] solid, 1503, 1519, 1524 cm^{-1} [146]) and are in close agreement with those of $F_3S{\equiv}NXeF^+$ (1527, 1542, 1548 cm^{-1})[146] and $F_4S{=}N{-}Xe{-}{-}{-}N{\equiv}SF_3^+$

Table 6.7. Correlation Diagram and Selection Rules for the Vibrational Modes of the $[F_3S(N{\equiv}SF_3)_2][AsF_6]$ Ion Pair

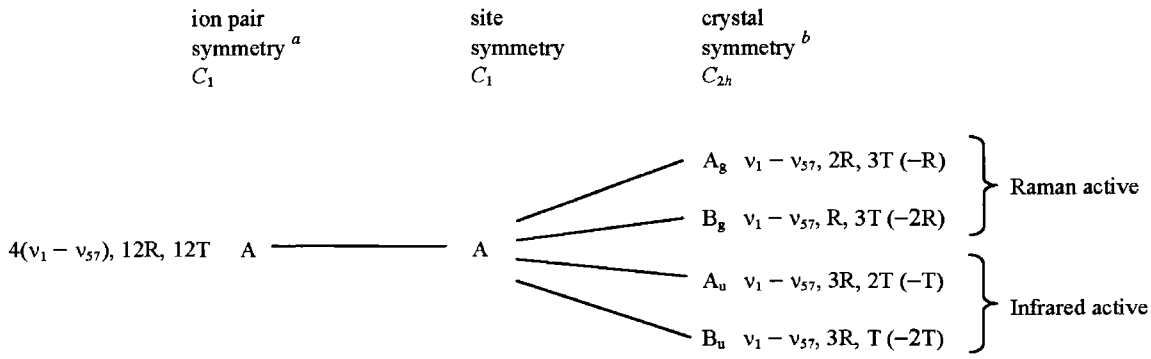

[a] The irreducible representations are Γ = 57A (C_1) for the $[F_3S(N{\equiv}SF_3)_2][AsF_6]$ ion-pair in the gas phase. [b] The crystallographic space group is $P2_1/n$ with Z = 4 structural units per unit cell.

(1543, 1548 cm^{-1}) (vide supra). The average out-of-phase and in-phase $\nu(SF_3)$ frequencies, all of which are coupled for the two adducted $N{\equiv}SF_3$ molecules, increase by 55 (liquid) and 42 (solid) [47] cm^{-1} and by 34 (liquid) and 28 (solid) [48] cm^{-1}, respectively, upon complexation. The average in-phase and out-of-phase $N{\equiv}SF_3$-group bending frequencies, all of which are coupled as above, exhibit complexation shifts that are less than or equal to those observed in $F_3S{\equiv}NXeF^+$ [146] and $F_4S{=}N{-}Xe{---}N{\equiv}SF_3^+$ (vide supra). These high-frequency shifts are in accord with the N≡S and S–F bond length contractions that result from adduct formation with the SF_3^+ cation (see sections 6.2.2.2. and 6.3).

The presence of *cis*-N_2F_2 (see eq 6.2.) was established from its Raman bands at 354(co), 729(sh), 888(co), 946(5), and 1519(co) cm^{-1},[194] where the abbreviations denote coincidence (co) and shoulder (sh). The bands at 354 and 888 cm^{-1} are coincident with the [δ(N1S1F2) + δ(F1S1F3) + δ(N2S2F6) + δ(F4S2F5)] and [δ(S1F2 – S1F3) + δ(S2F6 – S2F4)] bands of $F_3S(N{\equiv}SF_3)_2^+$, and the band at 1519 cm^{-1} is coincident with the ν(S≡N) band of unreacted $F_4S{=}N{-}Xe{---}N{\equiv}SF_3^+$. The presence of *cis*-$N_2F_2$ after pumping at –50 °C was surprising in view of the vapour-pressure of *cis*-N_2F_2 at –50 °C (1.19 x 104 mmHg), suggesting it may be adducted to unreacted $F_4S{=}N{-}Xe^+$ remaining in the product mixture. Further confirmation of the $[F_3S(N{\equiv}SF_3)_2][AsF_6]$ salt was achieved by pumping on the sample with dynamic vacuum at –45 °C for 15 min which resulted in complete removal of *cis*-N_2F_2 and the adducted $N{\equiv}SF_3$ forming $[SF_3][AsF_6]$, which was confirmed by Raman Spectroscopy (Table 6.8 and Figure 6.5).

Table 6.8. Experimental Raman Frequencies and Intensities for $[SF_3][AsF_6]$

freq, cm^{-1} [a]		assgnts
[b]	[c]	
957 (18)	960 (sh)	$\nu_1, \nu_3 (SF_3^+)$
944 (71)	945 (100)	
926 (17)	926 (19)	
685 (100)	686 (76)	$\nu_1 (AsF_6^-)$
586 (18)	587 (10)	$\nu_2 (AsF_6^-)$
561 (27)	563 (35)	
532 (3)	530 (7)	$\nu_2 (SF_3^+)$
408 (7)	411 (11)	$\nu_4 (SF_3^+)$
379 (30)	379 (36)	$\nu_5 (AsF_6^-)$
374 (34)		

[a] The abbreviation denotes shoulder (sh). [b] This work, see Figure 6.5. The peaks at 120 (19), 721 (sh), 771 (5), and 844 (5) cm^{-1} are attributed to one or more unidentified species, and are unassigned, while all other unassigned peaks are from unreacted $[F_4S{=}N{-}Xe{---}N{\equiv}SF_3][AsF_6]$. [c] Frequencies and assignments are from ref 186.

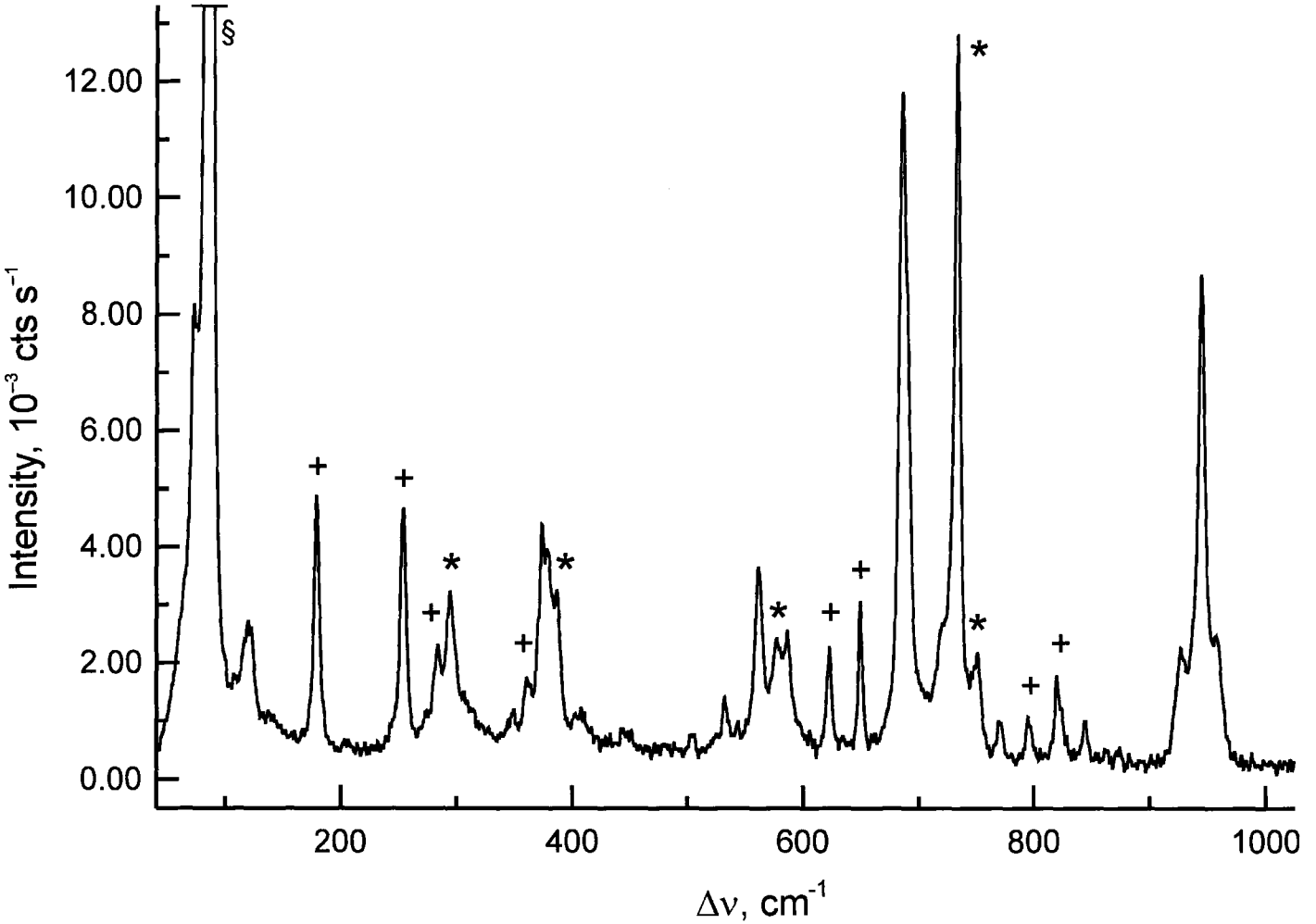

Figure 6.5. The Raman spectrum of $[SF_3][AsF_6]$ recorded at –160 °C using 1064-nm excitation; symbols denote peaks from unreacted $[F_4S{=}N{-}Xe{-}{-}{-}N{\equiv}SF_3][AsF_6]$ (+), FEP sample tube lines (*), and an instrumental artifact (§).

6.3. Computational Results

Quantum-chemical calculations were carried out at the MP2, B3LYP, and PBE1PBE levels for $F_4S{=}N{-}Xe{---}N{\equiv}SF_3^+$ and at the B3LYP and PBE1PBE levels only for the ion pair, $[F_3S(N{\equiv}SF_3)_2][AsF_6]$, due to computational constraints. All levels employed aug-cc-pVTZ(-PP) basis sets. The calculations were used to aid in the vibrational assignments (see section 6.2.3.2.) and to gain insight into the structure and bonding of these cations. Comparisons of the calculated and experimental geometrical parameters and vibrational frequencies with those of the benchmarks, $[F_4S{=}NXe][AsF_6]$[184] and $F_4S{=}NF$,[74,184] showed that the MP2 calculations provided the best overall agreement. Therefore, the vibrational assignments for $F_4S{=}N{-}Xe{---}N{\equiv}SF_3^+$ are based on the MP2 results (Table 6.4), which are reported in square brackets in the ensuing discussion. For $[F_3S(N{\equiv}SF_3)_2][AsF_6]$, the PBE1PBE level provided better overall agreement with the experimental geometry and vibrational frequencies (Table 6.6). The PBE1PBE values referred to in the ensuing discussion of the ion pair appear in parentheses.

6.3.1. Calculated Geometries

6.3.1.1. $F_4S{=}N{-}Xe{---}N{\equiv}SF_3^+$

Although close to C_s symmetry, the MP2, PBE1PBE, and B3LYP energy-minimized structures of $F_4S{=}N{-}Xe{---}N{\equiv}SF_3^+$ optimized to C_1 symmetry with all vibrational frequencies real. These calculations well-reproduced the experimental geometric parameters of the coordinated $F_4S{=}NXe^+$ cation, with the largest discrepancies occurring for the Xe---N≡S interaction in the adduct-cation. The calculated Xe---N [2.524

Å] and N≡S [1.428 Å] bond lengths are in very good agreement with the experimental values (2.583(3) and 1.398(3) Å). The calculated Xe---N≡S angle was less distorted from linearity [178.6°] than the experimental angle, 148.0(2)°, which is undoubtedly influenced by crystal packing (see section 6.2.2.). The energy difference between the bent and near-linear geometries is small [7.4 kJ mol^{-1}], as was the case for the $F_3S{\equiv}NXeF^+$ cation [7.9 kJ mol^{-1}],[146] showing the Xe---N≡S angle to be very deformable. The torsional angle defined by N1, Xe, N2, and S2 is substantially different in the experimental (–117.0(3)°) and calculated [–30.1°] geometries. The torsional angle is also very deformable (the calculated torsional frequency is 2 cm^{-1}), and again the difference is most likely a consequence of crystal packing.

6.3.1.2. $[F_3S(N{\equiv}SF_3)_2][AsF_6]$

The SF_3^+ cation of the energy-minimized structure of $[F_3S(N{\equiv}SF_3)_2][AsF_6]$ optimized to C_1 symmetry at the B3LYP and PBE1PBE levels using the aug-cc-pVTZ(-PP) basis sets, and was very near C_s symmetry. While the gross features of the cation, bridging anion, and adducted $N{\equiv}SF_3$ molecules were well-reproduced, the S–F, S≡N, and bridging As–F bonds were overestimated, and the S---F and S---N contacts were underestimated, with the S---F–As bridge bonds showing the greatest discrepancy. In the energy-minimized gas-phase SF_3^+ cation (C_{3v} symmetry), the S–F bond length [1.514 Å] is the same, within ±3σ, as that observed for $[F_3S(N{\equiv}SF_3)_2][AsF_6]$ (av., 1.517(2) Å), but the calculated F–S–F bond angles [99.5°] are greater than in the experimental structure (av.,

96.4(2)°), which may result from steric effects of the adducted N≡SF_3 molecules and the AsF_6^- anion of the ion pair.

6.3.2. Effect of Adduct Formation on the Geometry of N≡SF_3

Upon coordination of N≡SF_3, the valence electron lone pair on the nitrogen atom changes from predominantly s character to sp hybrid character, leading to strengthening and contraction of the S–N σ-bond.[78] This also removes charge-density from the S atom and results in more covalent and shorter S–F bonds. This bonding model is in accordance with the trend in the calculated bond lengths for free N≡SF_3,[146] and adducted N≡SF_3 in F_4S=N–Xe---N≡SF_3^+ and [F_3S(N≡SF_3)$_2$][AsF_6], where the S≡N bonds shorten by 0.017 and 0.023/0.023 Å, respectively, and the S–F bonds (average) shorten by 0.029 and 0.073/0.056 Å, respectively. The calculated trends agree with the experimental trends; that is, upon adduct formation, the S≡N bonds shorten by 0.017(4) and 0.031(4)/0.023(4) Å, respectively, and the S–F bonds (average) shorten by 0.026(3) and 0.031(3)/0.028(3) Å, respectively. This trend is also observed for F_3S≡NXeF^+, where the experimental S≡N and S–F (average) bonds shorten by 0.018(4) and 0.049(4) Å,[146] and the calculated bond lengths shorten by 0.019 and 0.047 Å.[144] The increased degree of sp mixing that is postulated to occur upon coordination not only results in S–N bond shortening, but apparently also influences the degree of sp^3 hybridization at sulfur, with decreasing p character leading to somewhat greater s character and somewhat more open F–S–F angles. The latter increase by 3.2(3)° (F_3S≡NXeF^+),[146] 1.2(3)° (F_4S=NXe---N≡SF_3^+),[144] 0.9(2) and 1.1(2)° (F_3S(N≡SF_3)$_2^+$),[144] and 1.8(3)° ($CpFe(CO)_2$N≡SF_3)$^+$,[91] relative to N≡SF_3.[86]

6.3.3. Charges, Valencies, and Bond Orders

The natural bond orbital (NBO) charges, valencies, and bond orders calculated using MP2, PBE1PBE, and B3LYP methods for $F_4S{=}N{-}Xe{---}N{\equiv}SF_3^+$ are listed in Table 6.9. The $F_4S{=}N{-}Xe{---}N{\equiv}SF_3^+$ cation is compared with $F_4S{=}NXe^+$,[11] $F_3S{\equiv}NXeF^+$, and $F_5SN(H)Xe^+$,[27] and adducted $N{\equiv}SF_3$ is compared with $N{\equiv}SF_3$ and $F_3S{\equiv}NXeF^+$ (Table 6.10). The observed and calculated geometrical changes that occur upon coordination of $N{\equiv}SF_3$ are reflected in the NBO analyses. Only the MP2 values are referred to in the ensuing discussion, and these are summarized in Scheme 6.2.

6.3.3.1. $F_4S{=}N{-}Xe{---}N{\equiv}SF_3^+$

The NBO parameters for $F_4S{=}NXe^+$ do not exhibit large changes upon $N{\equiv}SF_3$ coordination. The positive charges of $F_4S{=}N{-}Xe{---}N{\equiv}SF_3^+$ reside on xenon and both sulfur atoms, with the charges on S1 [2.51] and the fluorines bonded to S1 [av., –0.43] remaining essentially unchanged with respect to those of $F_4S{=}NXe^+$ [2.50; av., –0.41]. Comparison of XeF^+ with $F_3S{\equiv}NXeF^+$ also shows little change in xenon charge upon coordination. Upon coordination of $N{\equiv}SF_3$, the absolute charges on Xe and N of $F_4S{=}NXe^+$ increase somewhat when compared with those of free $F_4S{=}NXe^+$. This is consistent with a more polar Xe–N bond in $F_4S{=}N{-}Xe{---}N{\equiv}SF_3^+$ which is corroborated by the somewhat lower Xe–N bond order of the adduct [0.54] when compared with that of $F_4S{=}NXe^+$ [0.59]. Both bond orders are, however, similar to that of $F_5SN(H)Xe^+$ [0.60], which are nearly double that of $F_3S{\equiv}NXeF^+$ [0.29] and are indicative of much stronger

Table 6.9. Natural Bond Orbital (NBO) Charges, Valencies, and Bond Orders for $F_4S{=}NXe^+$ and $F_4S{=}NXe{-}{-}{-}N{\equiv}SF_3^+$ [a]

atom	$F_4S{=}NXe^+$ [b] charges			$F_4S{=}NXe^+$ [b] valencies			$F_4S{=}NXe{-}{-}{-}N{\equiv}SF_3^+$ charges			$F_4S{=}NXe{-}{-}{-}N{\equiv}SF_3^+$ valencies		
	MP2	PBE1PBE	B3LYP	MP2	PBE1PBE	B3LYP	MP2	PBE1PBE	B3LYP	MP2	PBE1PBE	B3LYP
Xe	1.01	0.92	0.87	0.62	0.57	0.53	1.05	1.04	0.99	0.70	0.69	0.65
N1	–0.87	–0.79	–0.73	1.67	1.60	1.56	–0.93	–0.92	–0.87	1.64	1.63	1.61
S1	2.50	2.51	2.48	4.07	3.71	3.66	2.51	2.51	2.49	3.70	3.72	3.66
F1	–0.40	–0.40	–0.39	0.62	0.60	0.59	–0.42	–0.42	–0.42	0.58	0.58	0.57
F2	–0.38	–0.39	–0.38	0.65	0.60	0.59	–0.40	–0.40	–0.40	0.58	0.58	0.58
F3	–0.38	–0.39	–0.38	0.65	0.60	0.59	–0.40	–0.40	–0.40	0.58	0.58	0.58
F4	–0.47	–0.47	–0.46	0.56	0.52	0.53	–0.49	–0.49	–0.48	0.51	0.52	0.51
N2							–1.06	–1.07	–1.04	1.21	1.22	1.20
S2							2.40	2.41	2.38	2.52	2.54	2.52
F5							–0.42	–0.42	–0.42	0.38	0.38	0.37
F6							–0.42	–0.42	–0.42	0.38	0.38	0.37
F7							–0.42	–0.42	–0.42	0.38	0.38	0.37

bond	bond orders: $F_4S{=}NXe^+$ [b]			$F_4S{=}NXe{-}{-}{-}N{\equiv}SF_3^+$		
	MP2	PBE1PBE	B3LYP	MP2	PBE1PBE	B3LYP
Xe–N1	0.59	0.55	0.52	0.54	0.54	0.52
S1=N1	1.18	1.11	1.11	1.17	1.18	1.16
S1–F1	0.69	0.62	0.60	0.62	0.62	0.61
S1–F2	0.76	0.68	0.67	0.66	0.66	0.65
S1–F3	0.76	0.68	0.67	0.66	0.66	0.65
S1–F4	0.66	0.61	0.61	0.59	0.60	0.59
Xe---N2				0.14	0.13	0.11
N2≡S2				1.17	1.19	1.20
S2–F5				0.45	0.45	0.44
S2–F6				0.45	0.45	0.44
S2–F7				0.45	0.45	0.44

[a] aug-cc-pVTZ(-PP) basis set. [b] From ref 184.

Table 6.10. Natural Bond Orbital (NBO) Charges, Valencies, and Bond Orders for $F_3S{\equiv}NXeF^+$, $N{\equiv}SF_3$, and XeF^+ [a]

	$F_3S{\equiv}NXeF^+$						$N{\equiv}SF_3$						XeF^+					
atom	charges			valencies			charges			valencies			charges			valencies		
	MP2	PBE	B3L	MP2	PBE	B3L	MP2	PBE	B3L	MP2	PBE	B3L	MP2	PBE	B3L	MP2	PBE	B3L
F_{Xe}	–0.47	–0.48	–0.47	0.39	0.40	0.39							–0.34	–0.33	–0.33	0.46	0.50	0.48
Xe	1.30	1.29	1.28	0.68	0.70	0.67							1.34	1.33	1.33	0.46	0.50	0.48
N	–1.10	–1.11	–1.09	1.23	1.21	1.21	–0.81	–0.79	–0.81	1.01	1.06	0.95						
S	2.47	2.49	2.47	2.44	2.15	2.15	2.18	2.13	2.19	2.33	2.44	2.12						
F_S	–0.40	–0.39	–0.40	0.33	0.30	0.30	–0.46	–0.45	–0.45	0.26	0.30	0.25						

	bond orders								
bond	$F_3S{\equiv}NXeF^+$			$N{\equiv}SF_3$			XeF^+		
	MP2	PBE1PBE	B3LYP	MP2	PBE1PBE	B3LYP	MP2	PBE1PBE	B3LYP
F–Xe	0.38	0.40	0.39				0.46	0.50	0.48
Xe–N	0.29	0.29	0.28						
N–S	1.09	1.03	1.04	1.18	1.21	1.09			
S–F	0.45	0.37	0.37	0.38	0.41	0.34			

[a] Fluorine-on-xenon is denoted by F_{Xe} and fluorine-on-sulfur is denoted by F_S; PBE = PBE1PBE, B3L = B3LYP, all calculations use aug-cc-pVTZ(-PP) basis sets.

Scheme 6.2. Natural bond orbital (NBO) charges, valencies, and bond orders for selected atoms and bonds in $N{\equiv}SF_3$, XeF^+, $F_3S{\equiv}NXeF^+$, $F_4S{=}NXe^+$, and $F_4S{=}N{-}Xe{-}{-}{-}N{\equiv}SF_3^+$ calculated at the MP2/aug-cc-pVTZ(-PP) level of theory.

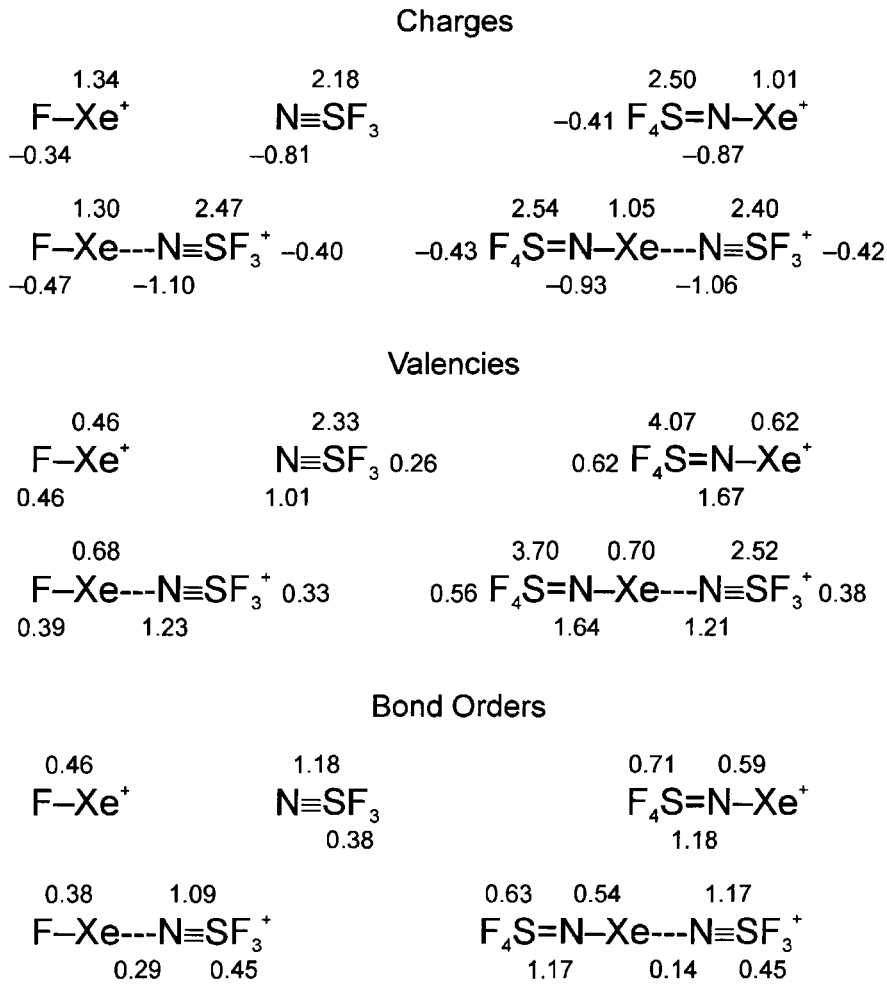

covalent bonding between xenon and nitrogen in $F_4S{=}NXe^+$, $F_4S{=}N{-}Xe{-}{-}{-}N{\equiv}SF_3^+$, and $F_5SN(H)Xe^+$. The lower S1 [3.70] and F-on-S1 [av., 0.56] valencies compared with those of the free cation [4.07; av., 0.62] are consistent with the lower S1–F bond orders in $F_4S{=}N{-}Xe{-}{-}{-}N{\equiv}SF_3^+$ [0.63] than in $F_4S{=}NXe^+$ [0.71]. The total NBO bond orders of the linear N---Xe–F and N–Xe---N moieties of $F_3S{\equiv}N{-}Xe{-}F^+$ and $F_4S{=}N{-}Xe{-}{-}{-}N{\equiv}SF_3^+$ are

nearly equal [0.67 and 0.68], but the Xe–F and Xe–N bond orders of their Lewis acid precursors, XeF^+ [0.46] and $F_4S{=}NXe^+$ [0.59], show that the Xe–N bond of $F_4S{=}NXe^+$ is more covalent.

The NBO parameters of coordinated $N{\equiv}SF_3$ display the most pronounced changes upon coordination to $F_4S{=}NXe^+$ and XeF^+, corroborating the experimental and calculated S–N and S–F bond length contractions. The increase in the valency of N upon adduct formation with $F_4S{=}NXe^+$ [0.20] is significantly greater than that of Xe [0.08], whereas the increases are equal for $F_3S{\equiv}NXeF^+$ [N, 0.22; Xe, 0.22]. The modest valency increase for Xe is corroborated by the low Xe---N bond order [0.14], which is half that of $F_3S{\equiv}NXeF^+$ [0.29]. Contraction of the S≡N and S–F bonds in $F_4S{=}N{-}Xe{-}{-}{-}N{\equiv}SF_3^+$ is in accord with increased N, S, and F valencies, and increased S–F bond orders. The negative charge drift to the N donor atom that occurs for $F_4S{=}N{-}Xe{-}{-}{-}N{\equiv}SF_3^+$ and $F_3S{\equiv}NXeF^+$ upon $N{\equiv}SF_3$ coordination is essentially matched by the increased positive charges on the S atoms of their $N{\equiv}SF_3$ donor molecules, leaving the Xe charges essentially unchanged. Thus, the Xe---N donor-acceptor bonds in these adduct cations are essentially polar interactions, which induce rehybridization of their nitrogen donor atom lone pairs upon adduct formation, providing the lone pairs and the N–S σ-bonds with enhanced sp characters. Although this results in shorter N–S bonds and greater N and S valencies for the adducted $N{\equiv}SF_3$ molecules, their total N–S bond orders remain essentially unchanged. No significant change in the S≡N bond order occurs upon adduct formation with $F_4S{=}NXe^+$, and a bond order decrease of only 0.09 occurs upon $F_3S{\equiv}NXeF^+$ formation with the stronger Lewis acid, XeF^+ (vide infra).

6.3.3.2. $[F_3S(N{\equiv}SF_3)_2][AsF_6]$

Only the adducted $N{\equiv}SF_3$ molecules in $F_3S{\equiv}NXeF^+$, $F_4S{=}N{-}Xe{---}N{\equiv}SF_3^+$, and the $[F_3S(N{\equiv}SF_3)_2][AsF_6]$ ion-pair are compared. The PBE1PBE/aug-cc-pVTZ(-PP) results (Table 6.11) are referred to in the ensuing discussion because they represent the highest level of theory available for the $[F_3S(N{\equiv}SF_3)_2][AsF_6]$ ion pair in the present study. As in the cases of $F_3S{\equiv}NXeF^+$ and $F_4S{=}N{-}Xe{---}N{\equiv}SF_3^+$, the experimental and calculated bond length contractions of the S–N and S–F bonds of coordinated $N{\equiv}SF_3$ are corroborated by the NBO analyses (Table 6.10.). Negative charge drifts to the N donor atoms (–0.79 to –0.99) occur upon $N{\equiv}SF_3$ coordination that are matched by the increased positive charges on the S atoms (2.13 to 2.33) of the donor $N{\equiv}SF_3$ molecules. The induced change in S–N bond polarization is similar to that in the XeF^+ and $F_4S{=}N{-}Xe^+$ adducts. The valency increases for N1 and N2 in $[F_3S(N{\equiv}SF_3)_2][AsF_6]$ that occur upon adduct formation (0.56) are, however, substantially greater than for $F_4S{=}N{-}Xe{---}N{\equiv}SF_3^+$ (0.16) and $F_3S{\equiv}NXeF^+$ (0.15). The Xe---N donor-acceptor bond orders are significantly greater than the S---N donor-acceptor bond orders (0.09) of the SF_3^+ adduct, but the S1–N1/S2–N2 bond orders increase by 0.44, which is substantially greater than for the xenon adducts calculated at the PBE1PBE level (cf. Scheme 6.2 and Tables 6.9 and 6.10). The greater experimental S–N and S–F bond length contractions observed for the adducted $N{\equiv}SF_3$ molecules in $F_3S(N{\equiv}SF_3)_2^+$ are also accompanied by significantly greater valency increases for S1 and S2 (1.15) and for F bonded to S1 and S2 (0.29), and by larger increases in the S1–F/S2–F bond orders (0.36). Despite the formation of a more weakly covalent donor-acceptor

Table 6.11. Natural Bond Orbital (NBO) Charges, Valencies, and Bond Orders for $[F_3S(N{\equiv}SF_3)_2][AsF_6]$[a]

	charges		valencies	
atom	B3LYP	PBE1PBE	B3LYP	PBE1PBE
S3	2.13	2.13	2.04	2.08
F7	–0.45	–0.45	0.53	0.54
F8	–0.43	–0.43	0.54	0.54
F9	–0.43	–0.43	0.54	0.54
N1	–0.97	–0.99	1.61	1.62
S1	2.30	2.33	3.59	3.64
F1	–0.45	–0.44	0.58	0.58
F2	–0.42	–0.43	0.60	0.60
F3	–0.43	–0.43	0.60	0.59
N2	–0.97	–0.99	1.61	1.62
S2	2.30	2.33	3.59	3.64
F4	–0.43	–0.43	0.60	0.59
F5	–0.45	–0.44	0.58	0.58
F6	–0.42	–0.43	0.60	0.60
As1	2.65	2.65	3.16	3.23
F10	–0.61	–0.61	0.45	0.46
F11	–0.61	–0.61	0.48	0.50
F12	–0.59	–0.59	0.49	0.50
F13	–0.57	–0.57	0.50	0.51
F14	–0.56	–0.56	0.50	0.51
F15	–0.59	–0.59	0.49	0.50

	bond orders	
bond	B3LYP	PBE1PBE
S3–F7	0.57	0.58
S3–F8	0.59	0.60
S3–F9	0.59	0.60
S3---N1	0.07	0.09
N1≡S1	1.64	1.65
S1–F1	0.64	0.65
S1–F2	0.66	0.67
S1–F3	0.65	0.67
S3---N2	0.07	0.09
N2≡S2	1.64	1.65
S2–F4	0.65	0.66
S2–F5	0.64	0.65
S2–F6	0.66	0.67
S3---F10	0.12	0.11
As1–F10	0.41	0.43
As1–F11	0.52	0.53
As1–F12	0.54	0.55
As1–F13	0.57	0.58
As1–F14	0.57	0.58
As1–F15	0.54	0.55

[a] Calculated for the gas-phase ion-pair using the aug-cc-pVTZ(-PP) basis sets.

bond and the similar S–N bond polarizations induced by the SF_3^+ cation, the latter cation apparently has more pronounced effects on the extent of sp hybridization of the S–N σ-bond and associated NBO parameters than do the XeF^+ and $F_4S{=}NXe^+$ cations.

6.3.4. Nature of the Xenon(II)-Nitrogen Adduct Bond

The gas-phase donor-acceptor dissociation energies for $F_4S{=}N{-}Xe{---}N{\equiv}SF_3^+$, $F_3S{\equiv}NXeF^+$, $F_3S{\equiv}NAsF_5$, and the related $HC{\equiv}NXeF^+$ cation were calculated at the MP2 level of theory and are listed in Scheme 6.3. The $F_4S{=}N{-}Xe{---}N{\equiv}SF_3^+$ dissociation energy

Scheme 6.3. Dissociation Energies (kJ mol^{-1}) for Selected Donor-Acceptor Adducts Calculated at the MP2/aug-cc-pVTZ(-PP) Level of Theory.

$F_3S{\equiv}NAsF_5 \rightarrow F_3S{\equiv}N: + AsF_5$	38.1
$F_4S{=}NXe{---}N{\equiv}SF_3^+ \rightarrow F_3S{\equiv}N: + F_4S{=}NXe^+$	85.2
$F_3S{\equiv}NXeF^+ \rightarrow F_3S{\equiv}N: + XeF^+$	173.2
$HC{\equiv}NXeF^+ \rightarrow HC{\equiv}N: + XeF^+$	180.9

is considerably less than that of the more covalent $F_3S{\equiv}NXeF^+$ and $HC{\equiv}NXeF^+$ cations, but significantly greater than the dissociation energy of $F_3S{\equiv}NAsF_5$. The NBO Xe---N bond order of $F_4S{=}N{-}Xe{---}N{\equiv}SF_3^+$ [0.14] is only half that of $F_3S{\equiv}NXeF^+$ [0.29] (Tables 6.9. and 6.10.), in accord with the calculated dissociation energies and the structural findings which show a significantly longer Xe---N bond for $F_4S{=}N{-}Xe{---}N{\equiv}SF_3^+$ (2.583(3) Å) than for $F_3S{\equiv}NXeF^+$ (2.236(4) Å)[146] and $HC{\equiv}NXeF^+$ (2.235(3)).[38]

As in the cases of $HC{\equiv}NNgF^+$ (Ng = Kr, Xe)[33] and $F_3S{\equiv}NXeF^+$,[146] the Xe---N bond of $F_4S{=}N{-}Xe{---}N{\equiv}SF_3^+$ may be regarded in terms of a mutual penetration of the outer diffuse non-bonded electron densities of Xe, a torus of three valence electron lone pairs,[40] and of the N, an electron lone pair. The torus of Xe valence density exposes the positive core charge of Xe, allowing the Xe atom to polarize the N donor atom. The highly polar nature of the interaction only produces a small shared density as reflected in the low Xe---N bond orders and small changes in Xe and N valencies (Scheme 6.2 and Tables 6.9 and 6.10). Although the negative charge drift to the N donor atom is essentially matched by the increased positive charge on the S atom of the donor molecule, little charge is actually transferred to the Xe acceptor atom. The interaction is primarily electrostatic, and its strength is determined by the extent of interpenetration of the closed shell densities of Xe and N, which leads to little modification of the Xe charge but significant polarization and negative charge increase on the N donor atom.

6.4. Conclusions

Both $F_4S{=}NXe^+$ and SF_3^+ have been shown to form Lewis acid-base adducts with $N{\equiv}SF_3$. The $[F_4S{=}N{-}Xe{---}N{\equiv}SF_3][AsF_6]$ salt has been synthesized by reaction of $[F_3S{\equiv}NXeF][AsF_6]$ with liquid $N{\equiv}SF_3$ solvent. The rearrangement is proposed to occur through an S_N2 mechanism involving fluoride ion displacement from the adducted XeF-group of $F_3S{\equiv}NXeF^+$ by $N{\equiv}SF_3$, followed by fluoride ion coordination to sulfur. The resulting $F_4S{=}N{-}Xe{---}N{\equiv}SF_3^+$ cation provides a rare example of xenon bound to nitrogen of an imido group and among the shortest Xe–N bonds presently known, as well as the first

example of an N–Xe–N linkage to be characterized by single-crystal X-ray diffraction. The reaction of $[F_4S{=}N{-}Xe{-}{-}{-}N{\equiv}SF_3][AsF_6]$ with $N{\equiv}SF_3$ resulted in the redox elimination of Xe and *cis*-N_2F_2 and formation of $[F_3S(N{\equiv}SF_3)_2][AsF_6]$, along with NF_3 as a minor byproduct. The latter salt is one of only a few main-group coordination compounds of $N{\equiv}SF_3$ to have been characterized by single-crystal X-ray diffraction, and the first definitively characterized example of the SF_3^+ cation coordinated to a ligand atom other than fluorine. The donor-acceptor interactions of both cations are highly polar in nature. The S≡N bonds of $F_4S{=}N{-}Xe{-}{-}{-}N{\equiv}SF_3^+$ and $F_3S(N{\equiv}SF_3)_2^+$ are shorter than that of the free $N{\equiv}SF_3$ molecule, in accord with the prevalent bonding description; that is, upon coordination, the nitrogen donor atom and its valence electron lone pair are polarized by the positive xenon Lewis acid center, inducing lone-pair rehybridization from predominantly s character to sp character, leading to strengthening and contraction of the S–N σ-bond of the $N{\equiv}SF_3$ ligand molecule.

CHAPTER 7

SYNTHESIS AND STRUCTURAL CHARACTERIZATION OF [FXeOXe---N≡SF_3][AsF_6]; A RARE EXAMPLE OF A XENON(II) OXIDE-FLUORIDE

7.1. Introduction

Oxide-fluorides of Xe(IV) ($XeOF_2$,[195-197] $XeOF_3^-$ [196]), Xe(VI) [$XeOF_4$,[7] $XeOF_3^+$,[52,198,199] $XeOF_5^-$,[200,201] $(XeOF_4)_3F^-$,[200] XeO_2F_2,[202] XeO_2F^+,[198,199,203,204] μ-$F(XeO_2F)_2^+$,[203,204] $XeO_2F_3^-$ [196]], and Xe(VIII) [XeO_3F_2,[205] $XeO_3F_3^-$,[206] XeO_2F_4,[207] *cis*-$XeO_4F_2^{2-}$,[206] *trans*-$XeO_4F_2^{2-}$ [206]] are known, however, until recently no examples of neutral or ionic Xe(II) oxide fluorides had been isolated or reported. The study of the reactions of [XeF][PnF_6] (Pn = As, Sb) with H_2O in HF solution resulted in the formation of two new xenon species, [Xe_3OF_3][PnF_6] and [H_3O][AsF_6]·2XeF_2.[117] The $Xe_3OF_3^+$ cation, with its $FXeOXe^+$---FXeF bonding model, can be considered as an XeF_2 adduct of the $FXeOXe^+$ cation, the first Xe(II) oxide-fluoride.

The basicity of thiazyl trifluoride, N≡SF_3, has been demonstrated by its reactions with BF_3, AsF_5, and SbF_5 in SO_2 to give the Lewis acid-base adducts, $F_3S{\equiv}NBF_3$,[82,87] $F_3S{\equiv}NAsF_5$,[78,88] and $F_3S{\equiv}NSbF_5$,[88] by the formation of other main-group adducts such as [$F(CF_3)_2S$---N≡SF_3][AsF_6],[89] and [$F_3S(N{\equiv}SF_3)_2$][AsF_6],[184] and by the formation of transition metal complexes such as ([$M(N{\equiv}SF_3)_4(AsF_6)_2$], M = Mn[90] and Zn[92]), [$Re(CO)_5N{\equiv}SF_3$][AsF_6],[91] and [$CpFe(CO)_2N{\equiv}SF_3$][AsF_6],[91] In addition, the synthesis and structural characterization of two noble-gas containing Lewis acid-base adducts of N≡SF_3

have been reported from this laboratory, namely, $F_3S{\equiv}NXeF^+$,[146] and $F_4S{=}NXe{---}N{\equiv}SF_3^+$.[184]

This work investigates the use of $N{\equiv}SF_3$ to displace XeF_2 from $Xe_3OF_3^+$ in the synthesis and detailed structural characterization of $[FXeOXe{---}N{\equiv}SF_3][AsF_6]$, providing rare examples of a xenon(II) oxide fluoride, an O–Xe–N linkage, and an inorganic Lewis acid-base adduct containing xenon bound to a formally sp^3-hybridized nitrogen.

7.2. Results and Discussion

7.2.1. Synthesis of $[FXeOXe{---}N{\equiv}SF_3][AsF_6]$

The synthesis of $[FXeOXe{---}N{\equiv}SF_3][AsF_6]$ was monitored by low-temperature Raman spectroscopy, and the salt was isolated as its natural abundance and ^{18}O-enriched (98.6 atom%) isotopomers. The salt $[Xe_3OF_3][AsF_6]$ was prepared as previously described,[117] by reaction of 2 M solutions of $[XeF][AsF_6]$ and H_2O in HF for 12 h at –78 °C. When $[Xe_3OF_3][AsF_6]$ was allowed to react with liquid $N{\equiv}SF_3$ at –60 °C for 6 h (eq 7.1), the deep red-orange solid slowly became a deep yellow-orange in colour while

$$[FXeOXeFXeF][AsF_6] + N{\equiv}SF_3 \xrightarrow[N{\equiv}SF_3]{-60\ ^\circ C} [FXeOXe{---}N{\equiv}SF_3][AsF_6] + XeF_2 \qquad (7.1)$$

the $N{\equiv}SF_3$ supernatant remained colorless. After removal of the $N{\equiv}SF_3$ by dynamic vacuum, yellow-orange solid remained. The adduct $[FXeOXe{---}N{\equiv}SF_3][AsF_6]$, was characterized by Raman spectroscopy at –160 °C. Because the $Xe_3OF_3^+$ cation can be thought of as an adduct of $FXeOXe^+$ and XeF_2, the reaction likely proceeds by a

mechanism whereby the more Lewis basic $N{\equiv}SF_3$ displaces XeF_2 as depicted in Scheme 7.1.

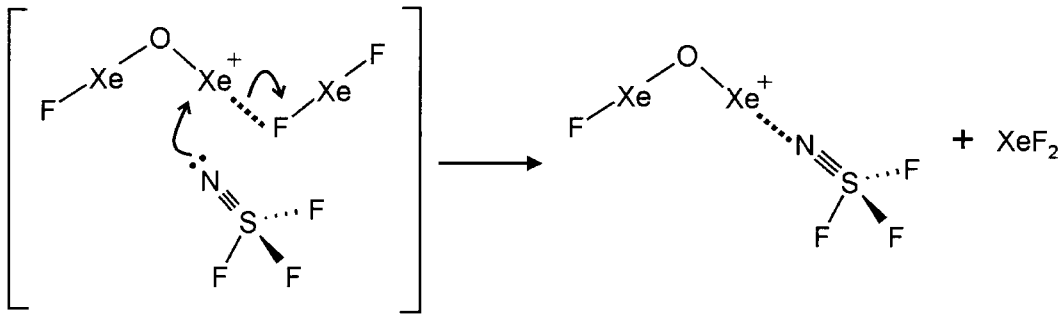

Scheme 7.1. Proposed mechanism for the displacement of XeF_2 from $Xe_3OF_3^+$ by $N{\equiv}SF_3$ to form the $FXeOXe{---}N{\equiv}SF_3^+$ adduct-cation.

7.2.2. Raman Spectroscopy

The Raman spectrum of $[FXe^{16,18}OXe{---}N{\equiv}SF_3][AsF_6]$ (Figure 7.1) was assigned by comparison with those of $[FXe^{16,18}OXe{---}FXeF][AsF_6]$,[117] $[F_4S{=}NXe{---}N{\equiv}SF_3][AsF_6]$,[184] $[F_3S{\equiv}NXeF][AsF_6]$,[146] and $N{\equiv}SF_3$,[146] (Table 7.1) and by comparison with the calculated frequencies derived for the gas-phase energy-minimized geometries of $FXe^{16,18}OXe{---}FXeF^+$,[117] $F_4S{=}NXe{---}N{\equiv}SF_3^+$,[184] $F_3S{\equiv}NXeF^+$,[146] $N{\equiv}SF_3$,[146] and $FXe^{16,18}OXe{---}N{\equiv}SF_3^+$ (see Computational Results). The vibrational modes of the uncoordinated AsF_6^- anion were assigned by comparison with those of $[O_2][AsF_6]$,[160] $[HC{\equiv}NXeF][AsF_6]$,[35] $[F_3S{\equiv}NXeF][AsF_6]$,[146] $[F_5TeNH_3][AsF_6]$,[50] and $[F_5SNH_3][AsF_6]$.[118] Calculated frequencies at the MP2/aug-cc-pVTZ level appear in square brackets.

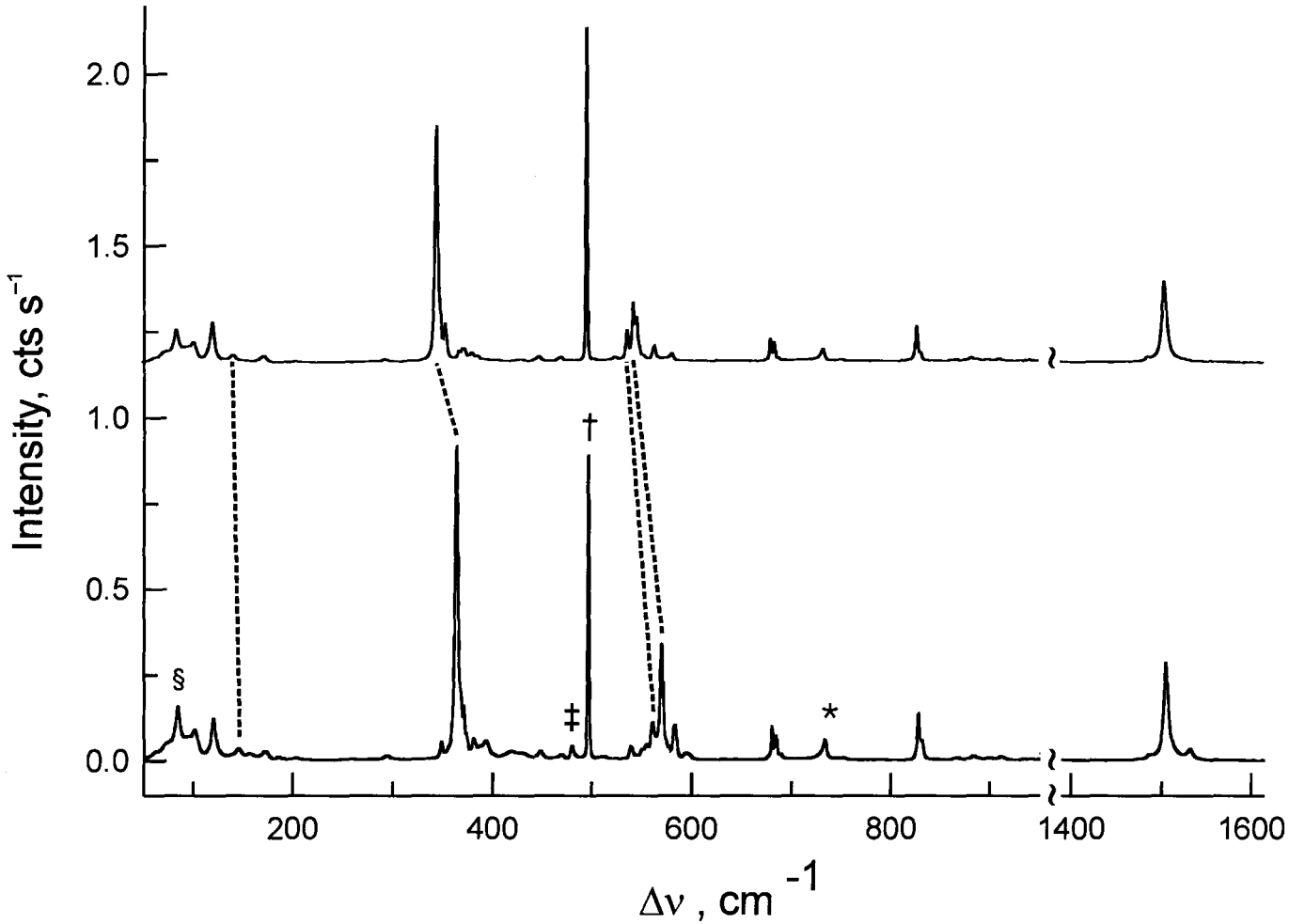

Figure 7.1. Raman spectra recorded at –160 °C using 1064-nm excitation for natural abundance (lower trace) and 98.6% ^{18}O-enriched (upper trace) $[FXeOXe{---}N{\equiv}SF_3][AsF_6]$; symbols denote bands from XeF_2 (†), unreacted $Xe_3OF_3^+$ (‡), an FEP sample tube line (*) and an instrumental artifact (§).

Table 7.1. Experimental Raman Frequencies and Intensities for [FXeOXe---N≡SF_3][AsF_6] and Calculated Vibrational Frequencies, Intensities, and Assignments for FXeOXe---N≡SF_3^+

freq, cm^{-1}											
			calcd								
exptl[a]			MP2			B3LYP			assgnts[c]		
^{16}O	^{18}O	Δν	^{16}O	^{18}O	Δν	^{16}O	^{18}O	Δν	FXeOXe---N≡SF_3^+ (C_1)	AsF_6^- (O_h)	
1531.0 (4)											
1504.6 (32)	1504.3 (34)	–0.3	1556.3 (206) [400]	1556.3 (206) [401]	0.0	1565.5 (206) [464]	1565.5 (206) [465]	0.0	ν(S≡N)		
1486.9 sh	1486.4 sh	–0.5									
	941.8 (<1)										
934.6 (<1)	931.8 (<1)	–2.8	892.2 (5) [178]	892.2 (5) [178]	0.0	853.9 (6) [178]	853.9 (6) [178]	0.0	ν(SF3 + SF4 – SF2)		
911.0 (1)	910.7 (1)	–0.3									
899.6 (1)	899.6 (1)	0.0									
888.9 sh	888.9 sh	0.0									
883.8 (1)	883.8 (1)	0.0	891.4 (5) [180]	891.4 (5) [180]	0.0	851.9 (6) [181]	851.9 (6) [181]	0.0	ν(SF3 – SF4)		
868.5 (1)	868.5 (1)	0.0									
864.0 sh	864.0 (<1)	0.0									
831.8 sh	832.4 sh	0.6	829.8 (76) [119]	829.8 (75) [121]	0.0	798.9 (71) [135]	798.9 (70) [136]	0.0	ν(SF2 + SF3 + SF4) + ν(S≡N)		
828.2 (14)	828.2 (14)	0.0									
689.0 sh	688.3 sh										
684.6 (8)	684.6 (8)										
680.5 (11)	680.5 (10)										
676.1 sh											
594.6 (2)											
584.3 (11)	582.6 (3)										
577.6 sh	574.8 sh										
	547.0 sh	–23.5									
570.5 (37)	543.8 (24)	–26.7	651.8 (18) [270]	618.6 (11) [201]	–33.2	587.4 (133) [99]	560.1 (50) [14]	–27.3	ν(Xe1F1 + Xe1O – Xe2O)		
564.8 (12)	561.7 (6)	–3.1	565.8 (77) [294]	563.7 (91) [326]	–2.1	547.7 (167) [270]	545.6 (237) [338]	–2.1	ν(Xe1F1 – Xe1O + Xe2O)		
555.5 (4)	554.2 sh	–1.3									
550.7 sh											
539.5 (4)	537.7 (13)	–1.8	529.0 (5) [8]	529.0 (3) [9]	0.0	509.4 (2) [12]	509.3 (1) [15]	–0.1	δ(SF_3)		
	525.6 (1)										
512.0 (1)											
469.3 (2)	470.4 (2)	1.1	431.7 (4) [12]	431.8 (4) [15]	0.1	419.7 (5) [15]	419.7 (5) [14]	0.0	δ(NSF3F4)		
448.0 (3)	448.0 (2)	0.0									
430.1 (4)	430.1 (1)	0.0	431.3 (4) [14]	431.3 (4) [14]	0.0	419.1 (4) [14]	419.1 (4) [14]	0.0	δ(NSF2) o.o.p.[d] + ρ_r(F3SF4)		
418.6 (3)											

Table 7.1. (continued…)

393.1 (6)									[ν_4 (T_{1u})]
374.2 sh	373.8 (5) 371.7 (5)	–0.4							[ν_5 (T_{2g})]
368.1 sh	368.5 (4)	0.4	341.7 (4) [12]	341.7 (4) [3]	0.0	329.2 (2) [2]	329.2 (2) [2]	0.0	δ(NSF4) + δ(F3SF4)
348.5 (6)	348.9 sh	0.4	340.6 (3) [2]	340.6 (2) [2]	0.0	328.2 (3) [1]	328.2 (2) [2]	–0.1	δ(NSF2) + δ(F3SF4)
371.3 (14) 363.9 (100)	354.5 (15) 345.6 (100)	–16.8 –18.3	442.4 (66) [12]	420.8 (60) [11]	–21.6	398.4 (14) [32]	378.9 (12) [30]	–19.5	ν(Xe1O) + ν(Xe2O)
203.7 (1)	204.7 (<1)	1.0	201.1 (1) [12]	195.7 (1) [12]	–5.4	179.8 (1) [12]	175.8 (1) [11]	–4.0	δ(F1Xe1O) o.o.p.
185.4 (1)									
172.3 (3)	172.3 (3)	0.0	185.2 (8) [4]	185.1 (9) [4]	–0.1	169.5 (6) [2]	170.6 (7) [2]	1.1	δ(F1Xe1O) i.p. – δ(Xe1OXe2) i.p.
156.6 (2)									
145.2 (4)	141.1 (3)	–4.1	120.4 (<1) [<1]	119.4 (<1) [<1]	–1.0	103.6 (<1) [1]	102.9 (<1) [1]	–0.7	δ(OXe2N) o.o.p.
120.7 (13)	120.7 (17)	0.0	122.9 (7) [38]	122.6 (7) [38]	–0.3	108.6 (8) [25]	108.8 (8) [24]	0.2	ν(Xe2N)
101.8 (10)	101.8 (8)	0.0	107.9 (1) [13]	107.9 (1) [13]	0.0	92.6 (1) [15]	93.0 (1) [16]	0.4	δ(OXe2N) i.p.
n.o.	n.o.		53.2 (2) [1]	53.1 (2) [1]	–0.1	48.0 (2) [2]	48.0 (2) [2]	0.0	
n.o.	n.o.		29.5 (<1) [<1]	29.2 (<1) [<1]	–0.3	24.4 (<1) [<1]	24.2 (<1) [<1]	–0.2	Coupled deformation modes
n.o.	n.o.		17.3 (1) [<1]	17.3 (1) [<1]	0.0	16.2 (1) [<1]	16.3 (1) [<1]	0.1	
n.o.	n.o.		2.7 (1) [<1]	2.7 (1) [<1]	0.0	1.4 (1) [<1]	1.5 (1) [<1]	0.1	N≡SF_3 torsion about Xe---N bond

[a] Values in parentheses denote relative Raman intensities; abbreviations denote shoulder (sh), broad (br), and not observed (n.o.). Bands corresponding to ν(XeF) of XeF_2 product (eq 7.1) appear at 496.6(97) and 496.6(140) cm^{-1}, and weak bands corresponding to $[\nu(Xe_3\text{-}F_2) - \nu(Xe_2\text{-}F_2)] + [\nu(Xe_1\text{-}O_1) - \nu(Xe_2\text{-}O_1)]$ of unreacted $Xe_3OF_3^+$ appear at 479.6(4) and 479.5(<1) cm^{-1} for the ^{16}O and ^{18}O salts, respectively. Bands appearing at 981.1, 1083.1, and 1141.5 cm^{-1} for the ^{16}O salt, and at 1029.5 and 1082.9 cm^{-1} for the ^{18}O salt, all with Raman intensities <1, are unassigned byproduct or combination bands. [b] The MP2/aug-cc-pVTZ(-PP) method. Calculated Raman [infrared] intensities, in $Å^4\ u^{-1}$ [km mol^{-1}] appear in parentheses [square brackets]. [c] The atom numbering corresponds to that given in Figure 7.2. Abbreviations denote out of plane (o.o.p.) and in plane (i.p.), where the plane is defined by the Xe1, O1, and Xe2 atoms unless otherwise specified, and rock (ρ_r). [d] The plane is defined by the N1, S1, and F2 atoms.

In the absence of a crystal structure, it was not possible to carry out a factor-group analysis, which would likely account for the splittings observed on the majority of the cation and anion Raman bands. The 21 fundamental vibrational modes of the FXeOXe---N≡SF_3^+ adduct-cation were assigned under the C_1 symmetry calculated for the gas-phase adduct cation. All 21 modes belong to A irreducible representations, which are both Raman- and infrared-active. The AsF_6^- anion possesses 15 fundamental vibrational modes which were assigned under O_h symmetry and belong to the irreducible representations, $A_{1g} + E_g + T_{2g} + 2T_{1u} + T_{2u}$, where the A_{1g}, E_g, and T_{2g} modes are Raman active and the T_{1u} modes are infrared active. The formally Raman inactive T_{1u} modes were, however, observed as weak bands at 684.6, 689.0, and 393.1 cm^{-1}.

The calculated vibrational frequencies for the FXeOXe---N≡SF_3^+ adduct-cation are in good agreement with the experimental frequencies, including those associated with the Xe---N bond. Unlike $Xe_3OF_3^+$,[117] but like other N≡SF_3 adducts such as F_4S=NXe---N≡SF_3^+ [184] and $F_3S(N{\equiv}SF_3)_2^+$,[184] the majority of the FXeOXe---N≡SF_3^+ vibrational modes do not exhibit coupling between the $FXeOXe^+$ cation and the adducted N≡SF_3 molecule. Moreover, all observed frequency trends and the $^{16/18}O$ isotopic frequency shifts are in good agreement with the calculations. The bands in the spectrum of natural abundance [FXeOXe---N≡SF_3][AsF_6] that are assigned to the Xe–O stretching modes exhibit a significant low-frequency isotopic shift upon ^{18}O substitution. Unlike in $Xe_3OF_3^+$, the antisymmetric ν(Xe1O) – ν(Xe2O) stretch in FXeOXe---N≡SF_3^+ is coupled with the ν(Xe1F1) stretch (see Figure 7.2 for the atom numbering scheme). The highest frequency band at 570.5 [651.8] cm^{-1} shows a large isotopic shift and splitting (–23.5,

–26.7 [–33.2] cm^{-1}) and is assigned to ν(Xe1F1 + Xe1O – Xe2O), while the band at 564.8 [565.8] cm^{-1} shows a much smaller isotopic shift and no splitting (–3.1 [–2.1] cm^{-1}) and is assigned to ν(Xe1F1 – Xe1O + Xe2O). These frequencies are slightly lower that that observed in $Xe_3OF_3^+$ (595.8 cm^{-1}), which is likely caused by the coupling to the ν(Xe1F1) stretch (511.9 cm^{-1} in $Xe_3OF_3^+$). The split bands at 363.9, 371.3 [442.4] cm^{-1} also show large isotopic shifts (–18.3, –16.8 [–21.6] cm^{-1}) and are assigned to ν(Xe1O + Xe2O). These bands are significantly higher in frequency than comparable modes in $Xe_3OF_3^+$ (418.7, 429.8, and 479.5 cm^{-1}), which are coupled to the coupled ν(Xe2F2) and ν(Xe3F2) stretches. The bands below 205 cm^{-1} are attributed to bending and deformation modes. The weak bands at 145.2 [120.4] and 203.7 [201.1] cm^{-1} are the only bands that exhibit significant isotopic dependencies (–4.1, +1.0 [–1.0, –5.4] cm^{-1}) and are assigned to the two out-of-plane bends, δ(OXe2N)o.o.p. and δ(F1Xe1O)o.o.p. As expected, the in-plane bends and ν(Xe2N) stretch are insensitive to ^{18}O substitution.

No $N{\equiv}SF_3$ modes of $[FXeOXe{---}N{\equiv}SF_3][AsF_6]$ exhibit significant $^{16/18}O$ isotopic dependencies, and they do not uniformly undergo high-frequency shifts relative to $N{\equiv}SF_3$ as is often observed.[146,184] The S≡N stretching mode appears as a split band at 1486.9, 1504.6, 1531.0 [1556.3] cm^{-1}, bracketing that of $N{\equiv}SF_3$ (solid; 1503, 1519, 1524 cm^{-1};[146] liquid; 1517 cm^{-1} [184]) and at lower frequency than those of $[F_3S{\equiv}NXeF][AsF_6]$ (1527, 1542, 1548 cm^{-1}),[146] and $[F_4S{=}NXe{---}N{\equiv}SF_3][AsF_6]$[184] (1543, 1548 [1546] cm^{-1}). The average out-of-phase and in-phase ν(SF_3) frequencies do increase, by 61.4 [82.8] cm^{-1} and 51.0 [70.8] cm^{-1}, respectively, upon complexation, and the average in-phase and out-

of-phase bending frequencies shift to higher frequency by 17.1, 0, and 6.3 [18.0, 12.5, 4.2] cm^{-1}, which are less than or similar to the complexation shifts observed for $[F_4S{=}NXe{-}{-}{-}N{\equiv}SF_3][AsF_6]$[184] and $[F_3S{\equiv}NXeF][AsF_6]$.[146] These high-frequency shifts are in accord with the N≡S and S–F bond length contractions that result from adduct formation with the $FXeOXe^+$ cation. Complexation shifts for $FXeOXe{-}{-}{-}N{\equiv}SF_3^+$, like those of $F_4S{=}N{-}Xe{-}{-}{-}N{\equiv}SF_3^+$, are less than those of $F_3S{\equiv}NXeF^+$ because $FXeOXe^+$ (like $F_4S{=}NXe^+$) is a weaker Lewis acid than XeF^+ (see calculated donor-acceptor adduct dissociation energies in Section 7.3.4., Nature of the Xenon-Nitrogen adduct bond), and are in accordance with the longer Xe---N distance calculated for $FXeOXe{-}{-}{-}N{\equiv}SF_3^+$ [2.458 Å] than for $F_3S{\equiv}NXeF^+$ [2.295 Å].[146]

7.3. Computational Results

Quantum-chemical calculations were carried out at the MP2 and B3LYP levels using aug-cc-pVTZ(-PP) basis sets for the $FXeOXe{-}{-}{-}N{\equiv}SF_3^+$ adduct-cation to aid in the vibrational assignments (see Section 7.2.2., Raman Spectroscopy). Comparisons of the calculated and experimental frequencies with those of $FXeOXe^+$ in $Xe_3OXeF_3^+$,[117] and of $N{\equiv}SF_3$ in $[F_3S{\equiv}NXeF][AsF_6]$,[146] and $[F_4S{=}NXe{-}{-}{-}N{\equiv}SF_3][AsF_6]$,[184] showed that the MP2 calculations provided vibrational frequencies that were in better agreement for the $N{\equiv}SF_3$ modes and $FXeOXe^+$ bending modes, while the B3LYP calculations were in better agreement for the $FXeOXe^+$ stretching modes. The assignments of the vibrational modes of the $FXeOXe{-}{-}{-}N{\equiv}SF_3^+$ cation were made taking these trends into consideration these trends (Table 7.1).

7.3.1. Calculated Geometry

Although close to C_s symmetry, each of the MP2, PBE1PBE and B3LYP energy-minimized structures of FXeOXe---N≡SF_3^+ optimized to C_1 symmetry (Figure 7.2). The calculated bond lengths and angles for the $FXeOXe^+$ and N≡SF_3 components of FXeOXe---N≡SF_3^+ (Table 7.2) are nearly identical to those of the $FXeOXe^+$ cation in FXeOXe---$FXeF^+$ [117] and the adducted N≡SF_3 molecule in F_4S=NXe---N≡SF_3^+.[184] The angles about Xe(1) and Xe(2) in FXeOXe---N≡SF_3^+ were found to be slightly less than 180° at all levels of theory, in agreement with the experimental and calculated geometries for FXeOXe---$FXeF^+$ [117] and $Xe_2F_3^+$.[28] The Xe---N–S angle [175.8°] was the most distorted from linearity, but this angle is expected to be more deformable, and can be quite bent, as found experimentally in [F_4S=NXe---N≡SF_3][AsF_6] (148.0(2)°).[184]

7.3.2. Effect of Adduct Formation on the Geometry of N≡SF_3

Upon coordination of N≡SF_3, the valence electron lone pair on the nitrogen atom changes from predominantly s character to sp hybrid character, leading to strengthening and contraction of the S–N σ-bond.[13] This also removes charge-density from the S atom and results in more covalent and shorter S–F bonds. This bonding model is in accordance with the trend in the calculated bond lengths for free N≡SF_3,[17] and adducted N≡SF_3 in FXeOXe---N≡SF_3^+, where the S≡N bonds shorten by 0.010 Å, and the average of the S–F bond lengths shortens by 0.031 Å. This agrees with the calculated and experimental trends observed for F_4S=NXe---N≡SF_3^+, F_3S≡$NXeF^+$, and $F_3S(N{\equiv}SF_3)_2^+$.[184]

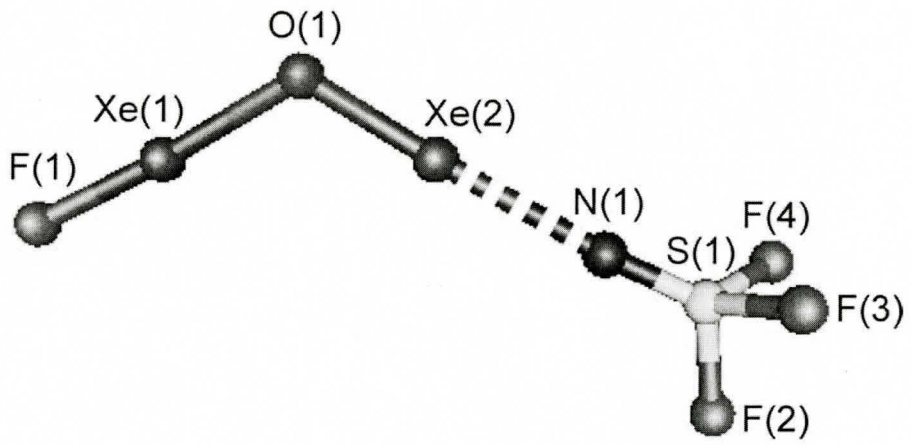

Figure 7.2 Calculated geometry (MP2/aug-cc-pVTZ(-PP)) of FXeOXe---N≡SF_3^+.

Table 7.2. Calculated Geometric Parameters for the FXeOXe---N≡SF_3^+ Cation [a]

	bond lengths (Å)		
	MP2	PBE1PBE	B3LYP
F(1)–Xe(1)	1.960	1.959	1.974
Xe(1)–O(1)	2.148	2.171	2.188
O(1)–Xe(2)	1.957	1.963	1.983
Xe(2)---N(1)	2.458	2.521	2.564
N(1)≡S(1)	1.427	1.412	1.417
S(1)–F(2)	1.543	1.537	1.556
S(1)–F(3)	1.543	1.538	1.557
S(1)–F(4)	1.543	1.538	1.557

	bond angles (°)		
	MP2	PBE1PBE	B3LYP
F(1)–Xe(1)–O(1)	176.6	175.8	175.4
Xe(1)–O(1)–Xe(2)	117.0	121.2	121.8
O(1)–Xe(2)---N(1)	177.2	177.0	177.0
Xe(2)---N(1)–S(1)	175.8	173.5	173.6
N(1)–S(1)–F(2)	120.8	120.5	120.7
N(1)–S(1)–F(3)	121.2	121.2	121.4
N(1)–S(1)–F(4)	121.2	121.1	121.3
F(2)–S(1)–F(3)	95.8	96.0	95.7
F(2)–S(1)–F(4)	95.8	95.9	95.7
F(3)–S(1)–F(4)	95.8	95.9	95.7

[a] The atom labels correspond to those used in Figure 7.2; the aug-cc-pVTZ basis set was used.

7.3.3. NBO Valencies, Bond Orders, and NPA Charges.

The NBO (Natural Bond Orbital) valencies, bond orders, and NPA (Natural Population Analysis) charges calculated using MP2, PBE1PBE, and B3LYP methods for FXeOXe---N≡SF_3^+ are listed in Table 7.3, along with those for $Xe_3OF_3^+$.[117] The FXeOXe---N≡SF_3^+ cation is also compared with F_4S=NXe---N≡SF_3^+, F_3S≡NXeF^+, and N≡SF_3.[184] The highest level of theory available for comparisons among the aforementioned species and FXeOXe---N≡SF_3^+ is PBE1PBE/aug-cc-pVTZ(-PP); these values are referred to in the ensuing discussion (values in square brackets). The NBO parameters for the FXeOXe^+ component of $Xe_3OF_3^+$ do not exhibit any significant changes upon displacement of XeF_2 to form the FXeOXe---N≡SF_3^+ adduct-cation. This is strong support for the argument that the correct bonding model for $Xe_3OF_3^+$ is the XeF_2 adduct, FXeOXe---FXe^+.[117] The positive charges of FXeOXe---N≡SF_3^+ reside on both xenon atoms and the sulfur atom, with the charges on Xe1 and Xe2 [1.21, 1.13] the same as those of $Xe_3OF_3^+$, and the charge on S1 [2.40] the same as that of the N≡SF_3-sulfur of F_4S=NXe---N≡SF_3^+. With regards to the Xe---N bond, similar charges and valencies in FXeOXe---N≡SF_3^+, when compared with those of F_4S=NXe---N≡SF_3^+, are consistent with their similar bond orders [0.17, 0.14]. These low bond orders are half that of F_3S≡NXeF^+ [0.29] and are significantly less than the Xe–N bond orders of F_4S=NXe^+ [0.59] and $F_5SN(H)Xe^+$ [0.60].

The NBO and NPA parameters for the adducted N≡SF_3 molecule in FXeOXe---N≡SF_3^+ are essentially the same as those in F_4S=NXe---N≡SF_3^+. Upon adduct formation, the valency at N increases, and the negative charge drift to the N donor atom is essentially

Table 7.3. Natural Bond Orbital (NBO) Valencies, Bond Orders, and NPA Charges for FXeOXe---N≡SF_3^+ and $Xe_3OF_3^+$ [a]

atom	FXeOXe---N≡SF_3^+ [b]						FXeOXe---$FXeF^+$ [c]			
	charges			valencies			charges		valencies	
	MP2	PBE1PBE	B3LYP	MP2	PBE1PBE	B3LYP	PBE1PBE	B3LYP	PBE1PBE	B3LYP
F1	–0.53	–0.53	–0.52	0.35	0.36	0.34	–0.53	–0.52	0.36	0.34
Xe1	1.19	1.21	1.20	0.67	0.66	0.63	1.21	1.20	0.66	0.64
O1	–0.91	–0.90	–0.86	0.85	0.88	0.83	–0.89	–0.86	0.88	0.86
Xe2	1.17	1.13	1.10	0.69	0.72	0.65	1.13	1.11	0.62	0.60
N1	–1.07	–1.08	–1.05	1.14	1.24	1.23				
S1	2.40	2.41	2.39	2.43	2.54	2.52				
F_S	–0.42	–0.41	–0.42	0.31	0.38	0.37				
F2							–0.69	–0.68	0.29	0.28
Xe3							1.27	1.26	0.56	0.54
F3							–0.51	–0.50	0.38	0.36

bond	bond orders				
	FXeOXe---N≡SF_3^+ [b]			FXeOXe---$FXeF^+$ [c]	
	MP2	PBE1PBE	B3LYP	PBE1PBE	B3LYP
F1–Xe1	0.34	0.34	0.33	0.34	0.33
Xe1–O1	0.33	0.32	0.31	0.32	0.32
O1–Xe2	0.51	0.54	0.51	0.54	0.53
Xe2---N1	0.17	0.17	0.15		
N1≡S1	1.13	1.18	1.19		
S1–F_S	0.43	0.45	0.44		
Xe2---F2				0.08	0.07
F2–Xe3				0.20	0.19
Xe3–F3				0.36	0.35

[a] The aug-cc-pVTZ(-PP) basis set was used. [b] The atom labeling corresponds to that used in Figure 7.2. [c] From ref 117.

matched by the increased positive charge on the S atom, while the charge at Xe is effectively unchanged. Thus, the Xe---N donor-acceptor bond of the adduct-cation is essentially a polar interaction, which induces rehybridization of the nitrogen donor atom lone pair upon adduct formation, providing the lone pair and the N–S σ-bond with enhanced sp character. Although this results in a shorter N–S bond and greater N and S valencies for the adducted $N{\equiv}SF_3$ molecule, the total N–S bond order remains essentially unchanged. No significant change in the S≡N bond order occurs upon adduct formation with $FXeOXe^+$, and a bond order decrease of only 0.09 occurs upon $F_3S{\equiv}NXeF^+$ formation with the stronger Lewis acid, XeF^+.

7.3.4. Nature of the Xenon-Nitrogen Adduct Bond

Gas-phase reaction energies corresponding to $N{\equiv}SF_3$ and XeF_2 donor-acceptor adduct dissociation were calculated at the MP2/aug-cc-pVTZ(-PP) level of theory for $FXeOXe{---}N{\equiv}SF_3^+$, $Xe_3OF_3^+$, $F_4S{=}NXe{---}N{\equiv}SF_3^+$, $F_3S{\equiv}NXeF^+$, and $F_3S{\equiv}NAsF_5$ and are listed in Scheme 7.2. This series shows that the dissociation energies of $FXeOXe{---}N{\equiv}SF_3^+$ and $FXeOXe{---}FXeF^+$ are similar, and of the same order of magnitude as that of $F_4S{=}N{-}Xe{---}N{\equiv}SF_3^+$. The dissociation energies are considerably less than that of $F_3S{\equiv}NXeF^+$, but significantly greater than the As–N dissociation energy of $F_3S{\equiv}NAsF_5$. Under gas-phase conditions, it is clear, however, that $N{\equiv}SF_3$ is a sufficiently strong Lewis base to displace XeF_2 from $FXeOXe{---}FXeF^+$, and these findings are consistent with the spectroscopic findings. As in the case of $F_3S{\equiv}NXeF^+$,[146] mutual penetration of outer

diffuse non-bonded densities of the Xe and N atoms, unlike a covalent interaction, produces no substantial shared density as reflected in the low Xe–N bond order and small changes in Xe and N valencies (Table 7.2). Instead, the final density and bond strength of the interaction are primarily determined by the extent of interpenetration of their closed shell densities, which leads to little modification of the Xe charge but polarization of, and increased negative charge on, the N donor atom.

$F_3S{\equiv}NAsF_5 \rightarrow F_3S{\equiv}N: + AsF_5$	38.1
$F_4S{=}NXe{-}{-}{-}N{\equiv}SF_3^+ \rightarrow F_3S{\equiv}N: + F_4S{=}NXe^+$	85.2
$FXeOXe{-}{-}{-}FXeF^+ \rightarrow XeF_2 + FXeOXe^+$	89.3
$FXeOXe{-}{-}{-}N{\equiv}SF_3^+ \rightarrow F_3S{\equiv}N: + FXeOXe^+$	97.0
$F_3S{\equiv}NXeF^+ \rightarrow F_3S{\equiv}N: + XeF^+$	173.2

Scheme 7.2. Dissociation Energies (kJ mol^{-1}) for Selected Donor-Acceptor Adducts of $N{\equiv}SF_3$ and XeF_2 Calculated at the MP2/aug-cc-pVTZ(-PP) Level of Theory.

7.4. Conclusions

The $[FXeOXe{-}{-}{-}N{\equiv}SF_3][AsF_6]$ salt has been synthesized by reaction of $[Xe_3OF_3][AsF_6]$ with $N{\equiv}SF_3$ in $N{\equiv}SF_3$ solvent. Thiazyl trifluoride is a sufficiently strong Lewis base to displace XeF_2 from $Xe_3OF_3^+$ to form the $FXeOXe{-}{-}{-}N{\equiv}SF_3^+$ cation, thereby supporting $FXeOXe{-}{-}{-}FXeF^+$ as an appropriate representation for the bonding in the $Xe_3OF_3^+$ cation. Characterization of natural abundance and ^{18}O-enriched salts by low-

temperature Raman spectroscopy confirms the structure of this rare example of a xenon(II) oxide fluoride, an O–Xe–N linkage, and xenon bound to an inorganic sp-hybridized nitrogen centre.

CHAPTER 8

CHARACTERIZATION AND REACTIVITY OF $F_5SNH_3^+$, PROTON SOURCE IN THE CYCLOTRIMERIZATION OF CH_3CN; SYNTHESES AND STRUCTURAL CHARACTERIZATIONS OF $[F_5SNH_3][AsF_6]\cdot 2N{\equiv}SF_3$, $F_5SNH_2\cdot 2[F_5SNH_3][AsF_6]\cdot 4HF$, AND $[s\text{-}C_3(CH_3)_3N_3H\text{---}NCCH_3][AsF_6]\cdot CH_3CN$

8.1. Introduction

Prior work has shown that $[F_5SNH_3][AsF_6]$ is formed by HF solvolysis of $N{\equiv}SF_3$ in the superacidic medium AsF_5/aHF,[101] whereas the neutral amine, F_5SNH_2, is formed by $N{\equiv}SF_3$ solvolysis in aHF in the absence of a Lewis acid.[96] Thus, $F_5SNH_3^+$ would be expected to be a reasonably strong acid, but there are no examples known which document this cation as a proton source. The structural characterization of $F_5SNH_3^+$ includes ^{19}F and ^1H NMR,[101,118] Raman,[118] and limited infrared spectroscopic[101] studies, but does not include a single-crystal X-ray structure despite several attempts.[116,118] The characterization of F_5SNH_2 is surprisingly sparse in the literature, and is limited to only infrared spectroscopy and mass spectrometry.[96]

Nitriles are known to cyclotrimerize to form symmetric 1,3,5-triazines through various synthetic routes including the use of high pressure and temperature, alcohol catalysis under basic conditions and hydrogen halide catalysis under acidic conditions, which have been thoroughly reviewed.[208,209] The use of trifluoromethanesulfonic acid has been shown to be effective for the synthesis of 2,4,6-trimethyl-1,3,5-triazine from CH_3CN.[210] An intermediate in this synthesis has been identified as the 1H-2,4,6-trimethyl-1,3,5-triazinium

cation, which has been partially characterized by elemental analysis, infrared and UV spectroscopies, and mass spectrometry.[210,211]

In the current work, $F_5SNH_3^+$ is shown to protonate CH_3CN to form CH_3CNH^+, which initiates the cyclotrimerization of CH_3CN to form the 1H-2,4,6-trimethyl-1,3,5-triazinium cation and F_5SNH_2 in CH_3CN solvent. This work represents the first characterization of protonated cyclic *sym*-2,4,6-trimethyl-1,3,5-triazine by multi-NMR spectroscopy and by single-crystal X-ray diffraction, and supports the proposal of such a species as an intermediate in the Brønsted acid catalyzed cyclotrimerizations of nitriles.[210] In addition, crystallization of $[F_5SNH_3][AsF_6]$ from liquid $N{\equiv}SF_3$ has made the characterization of $[F_5SNH_3][AsF_6]\cdot 2N{\equiv}SF_3$ by single-crystal X-ray diffraction possible, providing the first crystal structure of the $F_5SNH_3^+$ cation, and only the second of non-adducted $N{\equiv}SF_3$.[86] The conjugate base of $F_5SNH_3^+$, the amine, F_5SNH_2, is characterized by multi-NMR and Raman spectroscopy and both species are characterized by single-crystal X-ray diffraction in the salt $F_5SNH_2\cdot 2[F_5SNH_3][HF_2]\cdot 4HF$. This work, therefore, represents a significant expansion of the structural characterizations of two fundamental F_5SN- group precursors, F_5SNH_2 and $F_5SNH_3^+$.

8.2. Results and Discussion

8.2.1. Syntheses of F_5SNH_2, $[F_5SNH_3][AsF_6]\cdot 2N{\equiv}SF_3$, and $[s\text{-}C_3(CH_3)_3N_3H][AsF_6]$

8.2.1.1. Synthesis of F_5SNH_2

Pentafluorosulfanylamine, F_5SNH_2, was prepared by a method similar to that previously described[96] by reaction of $N{\equiv}SF_3$ with excess aHF at 0 °C for ca. 6 h (eq 8.1)

$$N{\equiv}SF_3 + 2HF \xrightarrow[HF]{0\ ^\circ C} F_5SNH_2 \qquad (8.1)$$

forming a colorless solution in aHF. Slow removal of HF by distillation under dynamic vacuum at –65 °C yielded a friable white powder of composition $F_5SNH_2{\cdot}n$HF, which was stored at –78 °C until characterized by Raman spectroscopy at –40 °C, or sublimed for crystal growth. Static sublimation under 1 atm of dry N_2 at –30 to –35 °C afforded single crystals of $F_5SNH_2{\cdot}2[F_5SNH_3][HF_2]{\cdot}4HF$. The formation of this compound is presumably driven by the lattice energy gained upon salt formation and hydrogen bond formation (eq 8.2). No evidence for $[F_5SNH_3][HF_2]$ was observed in the sample by Raman spectroscopy prior to sublimation.

$$3F_5SNH_2 + 8HF \xrightarrow{-30\ ^\circ C} F_5SNH_2{\cdot}2[F_5SNH_3][HF_2]{\cdot}4HF \qquad (8.2)$$

8.2.1.2. Synthesis of $[F_5SNH_3][AsF_6]{\cdot}2N{\equiv}SF_3$

The salt, $[F_5SNH_3][AsF_6]$, was prepared as previously described[101,146] by reaction of the donor-acceptor adduct $F_3S{\equiv}NAsF_5$,[88] with aHF at 0 °C for ca. 6 h (eq 8.3) forming colorless, featherlike crystals which were characterized by Raman spectroscopy at –160 °C.

$$F_3S{\equiv}NAsF_5 + 3HF \xrightarrow[HF]{0\ ^\circ C} [F_5SNH_3][AsF_6] \qquad (8.3)$$

Recrystallization from liquid $N{\equiv}SF_3$ at –70 °C produced crystals of $[F_5SNH_3][AsF_6]{\cdot}2N{\equiv}SF_3$ which were suitable for a single-crystal X-ray structure determination.

8.2.1.3. Synthesis of [*s*-$C_3(CH_3)_3N_3H$][AsF_6]

The *s*-$C_3(CH_3)_3N_3H^+$ cation was synthesized by reaction of [F_5SNH_3][AsF_6] (vide supra), with CH_3CN in CH_3CN solvent at –10 °C for ca. 30 min (eq 8.4), after which time

$$F_5SNH_3^+ + 3CH_3CN \xrightarrow[CH_3CN]{-10\,^\circ C} F_5SNH_2 + s\text{-}C_3(CH_3)_3N_3H^+ \qquad (8.4)$$

a yellow solution had formed that was characterized by ^1H, ^{13}C, and ^{19}F NMR spectroscopy in CH_3CN solution at –20 °C. Protonation of CH_3CN by $F_5SNH_3^+$ to form CH_3CNH^+ [212] initiates the cyclotrimerization which presumably proceeds by the mechanism outlined in Scheme 8.1. The CH_3CNH^+ cation interacts with CH_3CN to form protonated dimer and trimer cations, and the trimer cation undergoes cyclization to form the triazinium cation. This scheme is in accordance with the originally published mechanism which employed HCl as the proton source for the cyclization of alkyl nitriles (RCN).[213] The latter mechanism involved protonated CH_3CN dimer and trimer chloride salts, followed by cyclization and loss of HCl to generate the neutral triazine. A subsequent study demonstrated that the dimer halide is unreactive toward RCN,[208] which supported an alternate one-step, trimolecular, cyclic electron transfer mechanism in cases involving halides.[214] The absence of halides in the present case, coupled with the statistically unfavourable trimolecular mechanism, led to the present mechanistic proposal (Scheme 8.1). The protonation of CH_3CN by $F_5SNH_3^+$, and subsequent dimerization, trimerization, and ring closure reaction steps that generate the 1H-2,4,6-trimethyl-1,3,5-triazine cation are supported by quantum-chemical calculations (see Section 8.3.1., Computational Results).

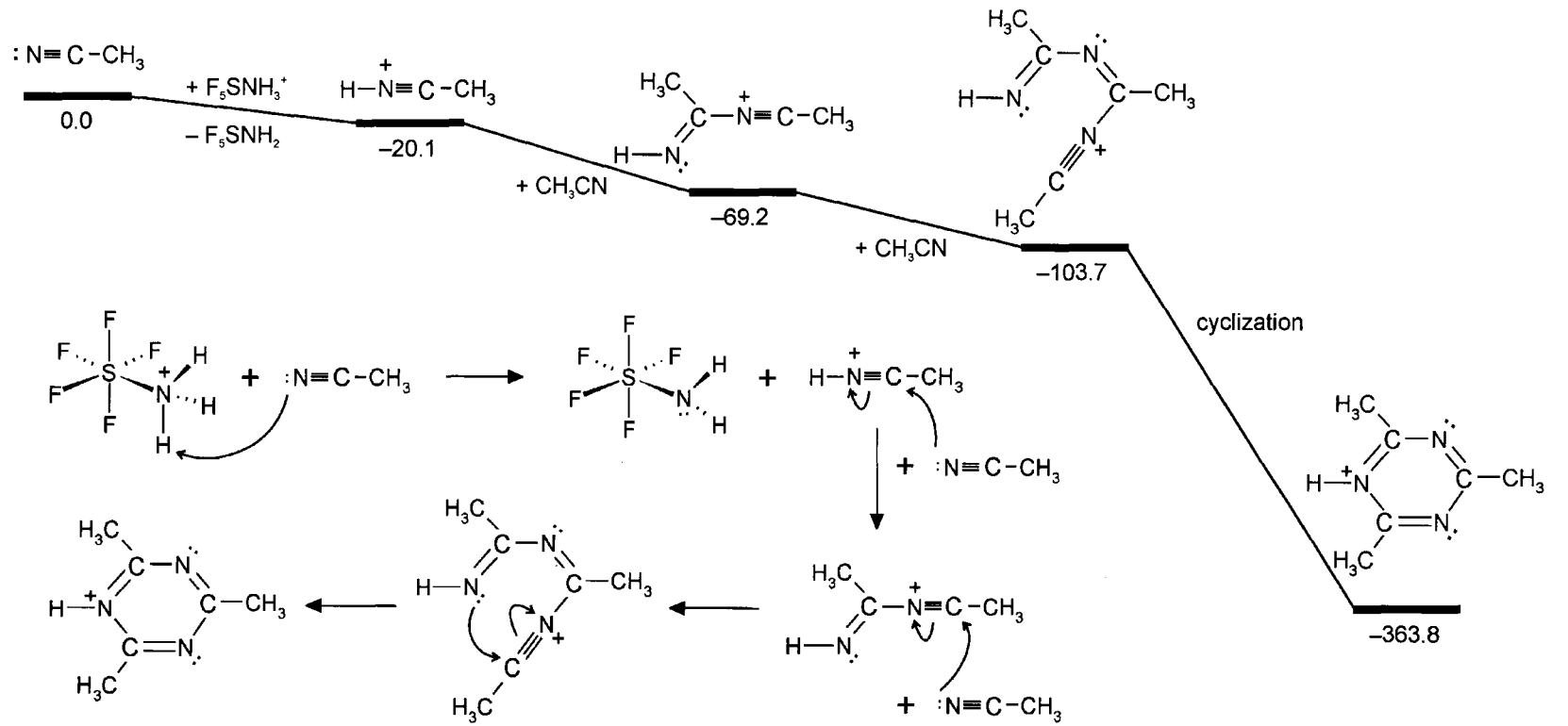

Scheme 8.1. Calculated Relative Gas-Phase Energies of Reagents, Intermediates, and Products in the Proposed $F_5SNH_3^+$-initiated Cyclotrimerization of CH_3CN to form *s*-$C_3(CH_3)_3N_3H^+$ (kJ mol^{-1}; PBE1PBE/aug-cc-pVTZ)

8.2.2. NMR Spectroscopy

The ^{1}H and ^{19}F NMR parameters for $[F_5SNH_3][AsF_6]$ and F_5SNH_2, and the ^{1}H and ^{13}C NMR parameters for the *s*-$C_3(CH_3)_3N_3H^+$ cation in CH_3CN solvent (–20 °C) are listed in Table 8.1. The ^{1}H and ^{13}C NMR spectra of a reaction mixture containing *s*-$C_3(CH_3)_3N_3H^+$, CH_3CNH^+, and F_5SNH_2 in CH_3CN solvent (–20 °C) are shown in Figures 8.1 and 8.2, and the ^{19}F spectrum of F_5SNH_2 is shown in Figure 8.3. Assignments of the chemical shifts and coupling constants were made by comparison with those of the parent triazine, 2,4,6-trimethyl-1,3,5-triazine,[215,216] CH_3CN, CH_3CNH^+,[212] $F_5SNH_3^+$,[101,118] and other F_5S– deivatives.[101,148]

8.2.2.1. $[F_5SNH_3][AsF_6]$

The ^{19}F and ^{1}H NMR spectra of the $F_5SNH_3^+$ cation have been well documented.[101,146] The NMR parameters in CH_3CN solvent at –20 °C [$\delta(^{19}F_{eq})$ = 72.1 ppm (doublet), $\delta(^{19}F_{ax})$ = 58.9 ppm (quintet), $^{2}J(^{19}F_{ax}–^{19}F_{eq})$ = 158.4 Hz and $\delta(^{1}H)$ = 10.25 ppm (singlet)] are in good agreement with the parameters previously reported in aHF at –20 °C and in BrF_5 supercooled to –70 °C (NMR parameters obtained in BrF_5 are given in parentheses): [$\delta(^{19}F_{eq})$ = 71.7 (73.8) ppm (doublet), $\delta(^{19}F_{ax})$ = 50.1 (50.0) ppm (quintet), $^{2}J(^{19}F_{ax}–^{19}F_{eq})$ = 152.6 (154.7) Hz, and $\delta(^{1}H)$ = 8.92 (7.74) ppm (singlet)].[146]

8.2.2.2. F_5SNH_2

Although F_5SNH_2 is known,[96] its NMR spectroscopic characterization is not to be found in the chemical literature. In the present study, the following NMR parameters for

Table 8.1. NMR Chemical Shifts and Spin-Spin Coupling Constants for [*s*-$C_3(CH_3)_3N_3H$][AsF_6], CH_3CNH^+, $F_5SNH_3^+$, and F_5SNH_2 in CH_3CN Solvent at –20 °C.[a]

species	chemical shifts, ppm									coupling constants, Hz
	$\delta(^{19}F_{ax})$	$\delta(^{19}F_{eq})$	$\delta(^{13}C_{n,o})$	$\delta(^{13}C_{n,p})$	$\delta(^{13}C_{m,o})$	$\delta(^{13}C_{m,p})$	$\delta(^{1}H_{n})$	$\delta(^{1}H_{m,o})$	$\delta(^{1}H_{m,p})$	$^{2}J(^{19}F_{ax}–^{19}F_{eq})$
s-$C_3(CH_3)_3N_3H^+$			166.1	129.0	17.9	22.8	11.89	2.63	3.08	
s-$C_3(CH_3)_3N_3$[b]			175.9		25.4			2.54		
CH_3CNH^+			90.1		n.o.[c]		12.30	4.93		
CH_3CN			117.7		0.9			2.14		
$F_5SNH_3^+$	58.9	72.1					10.25			158.4
F_5SNH_2[d]	65.4	72.9					9.71			156.1

[a] Subscripts indicate the following chemical environments: axial (ax), equatorial (eq), bound to nitrogen (n), methyl group carbon or hydrogen (m), *ortho-* to the protonated nitrogen (o), *para-* to the protonated nitrogen (p), where o and p only refer to the triazinium cation. The ^{19}F resonance of AsF_6^- was observed as a 1:1:1:1 quartet at $\delta(^{19}F) = 67.0$ ppm and $^{1}J(^{19}F–^{33}As) = 932.3$ Hz. [b] Data from refs 215 (^{13}C) and 216 (^{1}H). [c] The ^{13}C resonance of the methyl carbon was not observed, which is consistent with ref 212. [d] The secondary isotope effect arising from $^{34/32}S$ was observed in the ^{19}F spectrum; $^{1}\Delta^{19}F(^{34/32}S) = –0.061$ ppm.

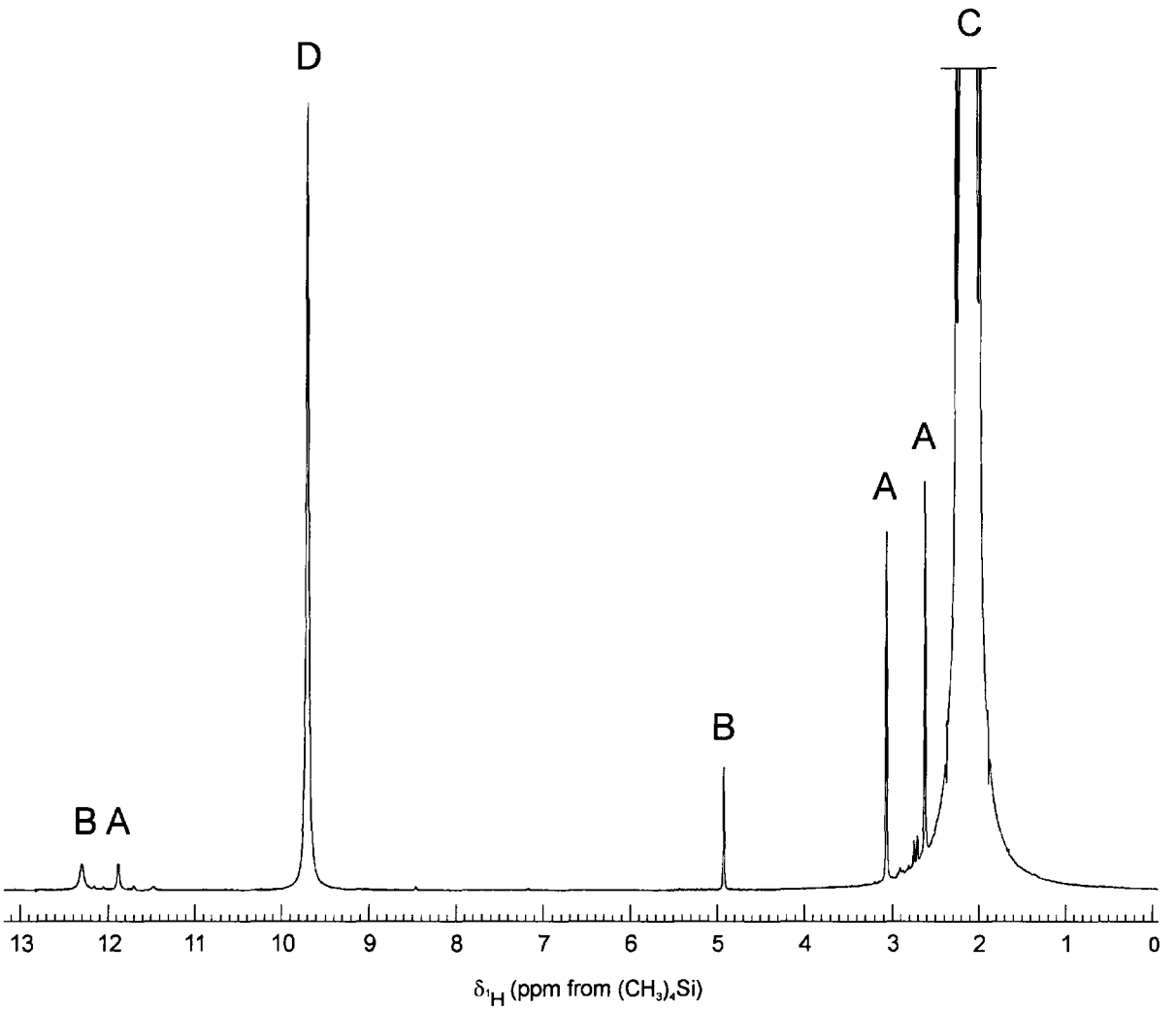

Figure 8.1. ^{1}H NMR spectrum (500.138 MHz) of *s*-$C_3(CH_3)_3N_3H^+$ in CH_3CN solvent at –20 °C; symbols denote *s*-$C_3(CH_3)_3N_3H^+$ (A), CH_3CNH^+ (B), CH_3CN (C), and F_5SNH_2 (D).

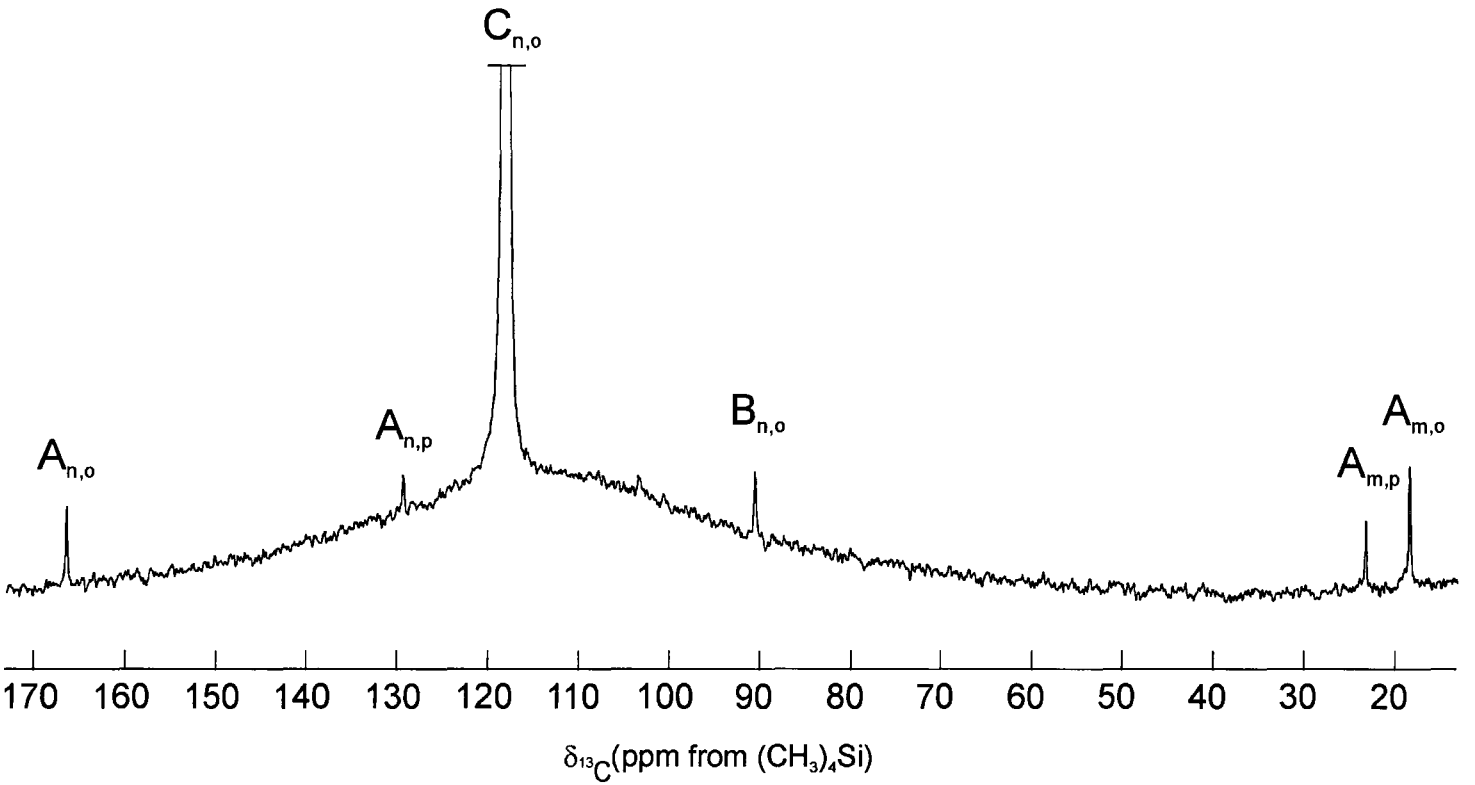

Figure 8.2. ^{13}C NMR spectrum (125.758 MHz) of *s*-$C_3(CH_3)_3N_3H^+$ in CH_3CN solvent at –20 °C; symbols denote *s*-$C_3(CH_3)_3N_3H^+$ (A), CH_3CNH^+ (B), and CH_3CN (C); subscripts defined in Table 8.1.

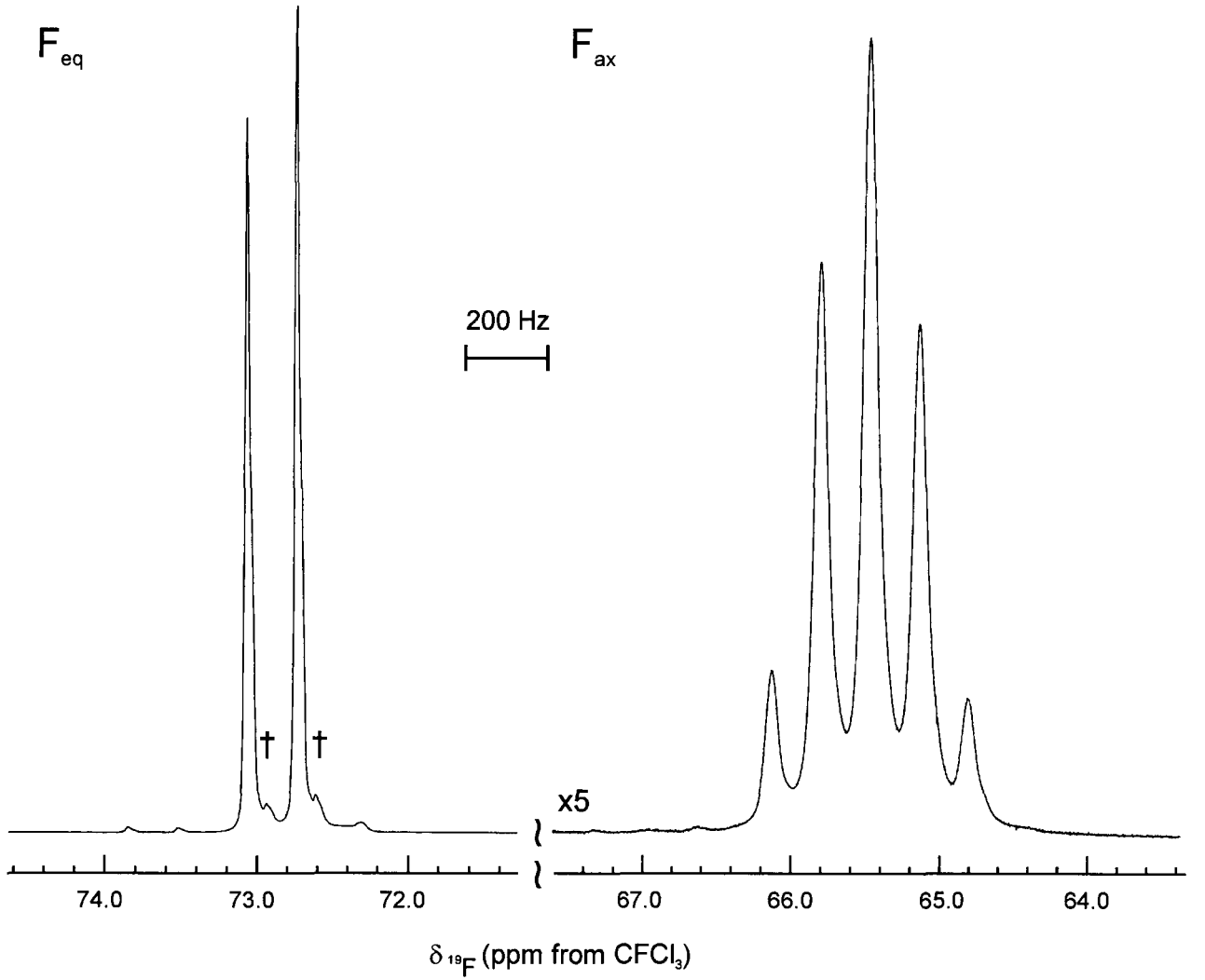

Figure 8.3. ^{19}F NMR spectrum (470.592 MHz) of F_5SNH_2 in CH_3CN solvent at –20 °C showing the F_{eq} environment, and the F_{ax} environment; daggers (†) denote the $^1\Delta^{19}F(^{34/32}S)$ secondary isotope shift.

parameters for F_5SNH_2 have been determined in CH_3CN solvent at –20 °C: $\delta(^{19}F_{eq})$ = 72.9 ppm (doublet), $\delta(^{19}F_{ax})$ = 65.4 ppm (quintet), $^2J(^{19}F_{ax}–^{19}F_{eq})$ = 156.1 Hz, and $\delta(^1H)$ = 9.71 ppm (singlet). The ^{19}F chemical shift values are comparable with, but slightly higher in frequency (more shielded) than those of $F_5SNH_3^+$ (vide supra).

8.2.2.3. [*s*-$C_3(CH_3)_3N_3H$][AsF_6]

The ^{13}C NMR spectrum of the *s*-$C_3(CH_3)_3N_3H^+$ cation shows four resonances attributable to the four carbon environments of the triazinium cation. The ring carbon atom that is *para-* to the protonated nitrogen atom (129.0 ppm) and the ring carbon atoms that are *ortho-* to the protonated nitrogen atom (166.1 ppm) are significantly more shielded than the ring carbons of neutral 2,4,6-trimethyl-1,3,5-triazine (175.9 ppm).[215,216] The chemical shift difference between the *ortho-* carbons going from unprotonated to protonated triazine (–9.8 ppm) is similar in magnitude to that for the carbon bound to nitrogen in CH_3CN/CH_3CNH^+ (–27.6 ppm),[144] and the chemical shift of the *para*-carbon is close to that of the nitrile carbon in CH_3CN (117.7 ppm). Similarly, the two methyl carbons that are *ortho-* to the protonated nitrogen atom (17.9 ppm) and *para-* to the protonated nitrogen atom (22.8 ppm) are more shielded than the methyl carbon resonance of neutral 2,4,6-trimethyl-1,3,5-triazine (25.4 ppm).[216] The shielding is likely due to the greater localization of electron density within the ring caused by protonation (see Sections 8.2.3.3., X-ray Crystallography and 8.3.1.4., Computational Results). The resonance at 90.1 ppm is assigned to the nitrile carbon of CH_3CNH^+, and is in reasonable agreement with the value (108 ppm) reported in SO_2

solution at –60 °C.[212] The methyl carbon of CH_3CNH^+ was not observed, nor was it reported in the prior study.

The ^1H NMR spectrum of the *s*-$C_3(CH_3)_3N_3H^+$ cation consists of three singlets. The resonances at 2.63 and 3.08 ppm correspond to the methyl groups which are *ortho*- and *para*- to the protonated nitrogen, respectively. Integration is not possible due to overlap with the solvent resonance. The *para*- methyl group resonance is somewhat more deshielded indicating some partial positive charge on the adjacent ring carbon atom, which is consistent with evidence for the electron localization found in the crystal structure (see Section 8.2.3.3., X-ray Crystallography). The proton bound to the ring appears as a broad singlet at 11.89 ppm, with the broadening and absence of resolved $^1J(^{14}N–^1H)$ couplings likely a result of quadrupolar relaxation by the directly bonded ^{14}N atom ($I = 1$), which results from the high electric field gradient at the ^{14}N nucleus caused by the low symmetry around nitrogen. The CH_3CNH^+ cation was also observed, with the methyl-group singlet appearing at 4.93 ppm, and the proton bound to nitrogen appearing as a broad ($\Delta\nu_{1/2} = 17.0$ Hz) singlet at 12.30 ppm, compared with the chemical shifts of 3.25 and 10.58 ppm, respectively, reported in SO_2 solution at –60 °C.[212] The broadening of the singlet corresponding to the N-H hydrogen presumably also results from unresolved $^1J(^{14}N–^1H)$ coupling and ^{14}N quadrupolar relaxation.

The low-intensity peaks observed in the ^1H spectrum were not assigned and likely arise from the protonated CH_3CN dimer and trimer intermediates (see Scheme 8.1) in the cyclotrimerization reaction pathway.

8.2.3. X-ray Crystal Structures of $F_5SNH_2 \cdot 2[F_5SNH_3][HF_2] \cdot 4HF$, $[F_5SNH_3][AsF_6] \cdot 2N{\equiv}SF_3$, and $[s\text{-}C_3(CH_3)_3N_3H\text{---}NCCH_3][AsF_6] \cdot CH_3CN$

A summary of the refinement results and other crystallographic information is provided in Table 8.2. Important bond lengths and angles for $F_5SNH_2 \cdot 2[F_5SNH_3][HF_2] \cdot 4HF$, $[F_5SNH_3][AsF_6] \cdot 2N{\equiv}SF_3$, and $[s\text{-}C_3(CH_3)_3N_3H\text{---}NCCH_3][AsF_6] \cdot CH_3CN$ are listed in Tables 8.3–8.6, respectively, along with their calculated geometric parameters (see Section 8.3.1., Computational Results). In the structures of F_5SNH_2 and $F_5SNH_3^+$ (Figures 8.4–8.6), both geometries are derived from octahedral VSEPR arrangements of bond pair domains at sulfur, and tetrahedral VSEPR arrangements of bonding and electron lone pair domains at nitrogen. In the structure of $[s\text{-}C_3(CH_3)_3N_3H\text{---}NCCH_3][AsF_6] \cdot CH_3CN$ (Figure 8.7), one CH_3CN molecule is hydrogen bonded through nitrogen to the triazinium ring proton, and a second CH_3CN molecule is co-crystallized and does not interact to any significant extent with the cation or anion of the structural unit.

8.2.3.1. $F_5SNH_2 \cdot 2[F_5SNH_3][HF_2] \cdot 4HF$

The crystal structure of $F_5SNH_2 \cdot 2[F_5SNH_3][HF_2] \cdot 4HF$ (Figure 8.4) consists of well separated F_5SNH_2 molecules and $F_5SNH_3^+$ cations which are linked by N–H---F hydrogen bonding interactions through HF molecules and HF_2^- anions. The atom numbering scheme appears in Figure 8.4 and Table 8.3. For each of the three distinct F_5SN– moieties present in the asymmetric unit, the N, S, F_{ax}, and two F_{eq} atoms (and one H atom of the $F_5SNH_3^+$ cation) are situated on mirror planes at half-occupancy, while one F_{eq} atom and one H atom are defined at full occupancy on general positions. The remaining F_{eq} and H atoms are defined by symmetry. Both bifluoride anions are defined by a half-occupancy H atom on a

Table 8.2. Summary of Crystal Data and Refinement Results for $F_5SNH_2 \cdot 2[F_5SNH_3][HF_2] \cdot 4HF$, $[F_5SNH_3][AsF_6] \cdot 2N{\equiv}SF_3$, and $[s\text{-}C_3(CH_3)_3N_3H\text{---}NCCH_3][AsF_6] \cdot CH_3CN$

	$F_5SNH_2 \cdot 2[F_5SNH_3][HF_2] \cdot 4HF$	$[F_5SNH_3][AsF_6] \cdot 2N{\equiv}SF_3$	$[s\text{-}C_3(CH_3)_3N_3H\text{---}NCCH_3][AsF_6] \cdot CH_3CN$
empirical formula	$F_{23}S_3N_3H_{14}$	$F_{17}S_3N_3H_3As$	$C_{10}H_{16}N_5AsF_6$
space group (No.)	$P2_1/m$ (No. 11)	$P\bar{1}$ (No. 2)	$P\bar{1}$ (No. 2)
a (Å)	12.4482(8)	5.8841(5)	8.606(3)
b (Å)	5.8432(4)	9.3276(7)	8.629(3)
c (Å)	13.470(1)	13.639(1)	11.798(4)
α (deg)	90	90.000(2)	71.84(2)
β (deg)	115.520(4)	90.011(2)	79.65(1)
γ (deg)	90	71.602(2)	78.47(1)
V (Å^3)	884.2(1)	710.3(1)	809.2(8)
molecules/unit cell	2	2	2
mol. wt. (g mol^{-1})	589.29	539.16	585.12
calcd. density (g cm^{-3})	2.514	2.521	2.401
T (°C)	−173	−173	−173
μ (mm^{-1})	6.53	3.03	6.51
R_1 [a]	0.0528	0.0635	0.0337
wR_2 [b]	0.1495	0.1856	0.0941

[a] R_1 is defined as $\Sigma||F_o| - |F_c||/\Sigma|F_o|$ for $I > 2\sigma(I)$.
[b] wR_2 is defined as $[\Sigma[w(F_o^2 - F_c^2)^2]/\Sigma w(F_o^2)^2]^{1/2}$ for $I > 2\sigma(I)$.

Table 8.3. Experimental Geometry for $F_5SNH_2 \cdot 2[F_5SNH_3][HF_2] \cdot 4HF$ and Calculated Geometries for F_5SNH_2 and the $F_5SNH_3^+$ Cation [a]

	bond lengths (Å)							
	F_5SNH_2				$F_5SNH_3^+$			
		calcd (C_1)[b]				calcd (C_1)[b]		
	exptl	MP2	PBE1PBE	B3LYP	exptl	MP2	PBE1PBE	B3LYP
N(1)–S(1)	1.716(8)	1.680	1.680	1.696	1.717(7) [1.739(7)]	1.848	1.859	1.891
N(1)–H(1)	0.852[c]	1.013	1.012	1.013	0.862 [0.877][c]	1.024	1.023	1.023
N(1)–H(1A)	0.852[c]	1.013	1.012	1.013	0.862 [0.877][c]	1.024	1.023	1.023
N(1)–H(10)					0.856 [0.883][c]	1.024	1.023	1.024
S(1)–F(1)	1.552(5)	1.592	1.593	1.608	1.559(5) [1.551(5)]	1.535	1.535	1.547
S(1)–F(2)	1.568(4)	1.595	1.595	1.611	1.557(3) [1.564(3)]	1.571	1.570	1.584
S(1)–F(2A)	1.568(4)	1.595	1.595	1.611	1.557(3) [1.564(3)]	1.571	1.570	1.583
S(1)–F(4)	1.579(5)	1.588	1.588	1.603	1.560(5) [1.550(5)]	1.571	1.570	1.583
S(1)–F(5)	1.560(5)	1.616	1.616	1.634	1.559(5) [1.558(5)]	1.571	1.569	1.584
F(6)---F(6A)					2.325(8) [2.329(8)]			

continued...

Table 8.3. (continued...)

	bond angles (°)							
	F_5SNH_2				$F_5SNH_3^+$			
		calcd (C_1)[b]				calcd (C_1)[b]		
	exptl	MP2	PBE1PBE	B3LYP	exptl	MP2	PBE1PBE	B3LYP
S(1)–N(1)–H(1)	114.1[c]	108.4	108.8	108.6	110.8 [107.0][c]	109.4	109.4	109.3
S(1)–N(1)–H(1A)	114.1[c]	108.4	108.8	108.6	110.8 [107.0][c]	109.0	109.1	109.0
S(1)–N(1)–H(10)					113.2 [97.5][c]	109.8	109.7	109.5
H(1)–N(1)–H(1A)	104.8[c]	109.6	110.1	110.2	102.3 [108.0][c]	109.5	109.5	109.7
H(1)–N(1)–H(10)					109.6 [117.8][c]	109.6	109.5	109.7
H(1A)–N(1)–H(10)					109.6 [117.8][c]	109.6	109.5	109.7
N(1)–S(1)–F(1)	178.4(3)	179.7	179.7	179.7	179.2(3) [179.7(3)]	179.2	179.3	179.3
N(1)–S(1)–F(2)	90.1(2)	90.8	90.9	90.9	90.3(1) [89.8(1)]	87.5	87.5	87.4
N(1)–S(1)–F(2A)	90.1(2)	90.8	90.9	90.9	90.3(1) [89.8(1)]	86.9	86.9	86.8
N(1)–S(1)–F(4)	89.2(3)	92.3	92.4	92.4	91.2(3) [91.0(3)]	88.0	87.9	87.8
N(1)–S(1)–F(5)	91.4(3)	93.8	93.8	93.8	89.4(3) [89.1(3)]	86.4	86.5	86.5
F(1)–S(1)–F(2)	89.9(2)	89.2	89.1	89.1	89.7(1) [90.2(1)]	92.8	92.8	92.9
F(1)–S(1)–F(2A)	89.9(2)	89.2	89.1	89.1	89.7(1) [90.2(1)]	92.8	92.8	92.9
F(1)–S(1)–F(4)	89.2(3)	87.4	87.3	87.3	89.6(3) [89.3(3)]	92.8	92.8	92.9
F(1)–S(1)–F(5)	90.2(3)	86.5	86.5	86.4	89.8(3) [90.7(3)]	92.8	92.8	92.9
F(2)–S(1)–F(2A)	179.6(3)	178.4	178.3	178.2	179.2(3) [179.2(3)]	174.4	174.4	174.3
F(2)–S(1)–F(4)	89.8(2)	90.1	90.1	90.1	89.7(2) [89.6(2)]	89.7	89.7	89.7
F(2)–S(1)–F(5)	90.2(2)	89.8	89.8	89.8	90.3(2) [90.4(2)]	89.9	89.9	89.9
F(2A)–S(1)–F(4)	89.8(2)	90.1	90.1	90.1	89.7(2) [89.6(2)]	89.8	89.8	89.8
F(2A)–S(1)–F(5)	90.2(2)	89.8	89.8	89.8	90.3(2) [90.4(2)]	90.1	90.0	90.0
F(4)–S(1)–F(5)	179.5(3)	173.9	173.8	173.8	179.5(3) [179.4(3)]	174.4	174.4	174.2
F(6)---H(6)---F(6A)					177.4 [172.7][c]			

[a] The atom labels correspond to those used in Figure 8.3; add 20 [30] to the numbering scheme shown above for the two crystallographically independent $F_5SNH_3^+$ cations and HF_2^- anions. [b] aug-cc-pVTZ basis set. [c] The hydrogen atom positions were calculated using a riding model, therefore no estimated standard deviations are provided.

Table 8.4. Experimental Geometry for $[F_5SNH_3][AsF_6]\cdot 2N{\equiv}SF_3$ (Preliminary) and Calculated Geometries for $F_5SNH_3^+$ and $N{\equiv}SF_3$ [a]

	bond lengths (Å)					
		calcd (C_1)[b]				
	exptl	MP2	PBE1PBE	B3LYP		exptl
N(1)–S(1)	1.673(14)	1.848	1.859	1.891	As(1)–F(11)	1.705(11)
N(1)–H(1)	0.900[c]	1.024	1.023	1.023	As(1)–F(12)	1.722(14)
N(1)–H(2)	0.900[c]	1.024	1.023	1.023	As(1)–F(13)	1.762(13)
N(1)–H(3)	0.900[c]	1.024	1.023	1.024	As(1)–F(14)	1.612(11)
S(1)–F(1)	1.522(12)	1.535	1.535	1.547	As(1)–F(15)	1.736(7)
S(1)–F(2)	1.546(9)	1.571	1.570	1.584	As(1)–F(16)	1.759(7)
S(1)–F(3)	1.543(4)	1.571	1.570	1.583		
S(1)–F(4)	1.552(4)	1.571	1.570	1.583		
S(1)–F(5)	1.586(12)	1.571	1.569	1.584		
N(2)≡S(2)	1.394(13)	1.439	1.418	1.424	N(3)≡S(3)	1.407(12)
S(2)–F(21)	1.511(10)	1.578	1.571	1.590	S(3)–F(31)	1.531(9)
S(2)–F(22)	1.515(13)	1.578	1.571	1.590	S(3)–F(32)	1.500(12)
S(2)–F(23)	1.444(16)	1.578	1.571	1.590	S(3)–F(33)	1.470(12)

	bond angles (°)					
		calcd (C_1)[b]				
	exptl	MP2	PBE1PBE	B3LYP		exptl
S(1)–N(1)–H(1)	109.5[c]	109.4	109.4	109.3	F(11)–As(1)–F(12)	88.2(5)
S(1)–N(1)–H(2)	109.5[c]	109.0	109.1	109.0	F(11)–As(1)–F(13)	172.1(5)
S(1)–N(1)–H(3)	109.5[c]	109.8	109.7	109.5	F(11)–As(1)–F(14)	90.1(5)
H(1)–N(1)–H(2)	109.5[c]	109.5	109.5	109.7	F(11)–As(1)–F(15)	87.8(6)
H(1)–N(1)–H(3)	109.5[c]	109.6	109.5	109.7	F(11)–As(1)–F(16)	94.8(6)
H(2)–N(1)–H(3)	109.5[c]	109.6	109.5	109.7	F(12)–As(1)–F(13)	84.0(4)
N(1)–S(1)–F(1)	178.4(7)	179.2	179.3	179.3	F(12)–As(1)–F(14)	178.2(5)
N(1)–S(1)–F(2)	88.4(6)	87.5	87.5	87.4	F(12)–As(1)–F(15)	82.8(6)
N(1)–S(1)–F(3)	90.9(5)	86.9	86.9	86.8	F(12)–As(1)–F(16)	92.4(6)
N(1)–S(1)–F(4)	90.5(5)	88.0	87.9	87.8	F(13)–As(1)–F(14)	97.7(5)
N(1)–S(1)–F(5)	90.1(3)	86.4	86.5	86.5	F(13)–As(1)–F(15)	87.3(7)
F(1)–S(1)–F(2)	90.6(4)	92.8	92.8	92.9	F(13)–As(1)–F(16)	94.2(7)
F(1)–S(1)–F(3)	87.9(6)	92.8	92.8	92.9	F(14)–As(1)–F(15)	97.2(6)
F(1)–S(1)–F(4)	90.8(6)	92.8	92.8	92.9	F(14)–As(1)–F(16)	87.7(6)
F(1)–S(1)–F(5)	90.8(7)	92.8	92.8	92.9	F(15)–As(1)–F(16)	178.3(6)
F(2)–S(1)–F(3)	178.5(7)	174.4	174.4	174.3		
F(2)–S(1)–F(4)	90.3(5)	89.7	89.7	89.7		
F(2)–S(1)–F(5)	91.2(5)	89.9	89.9	89.9		
F(3)–S(1)–F(4)	89.6(6)	89.8	89.8	89.8		
F(3)–S(1)–F(5)	88.9(6)	90.1	90.0	90.0		
F(4)–S(1)–F(5)	178.5(7)	174.4	174.4	174.2		
N(2)–S(2)–F(21)	110.5(10)	123.0	122.8	122.9	N(3)–S(3)–F(31)	101.0(7)
N(2)–S(2)–F(22)	117.0(8)	123.0	122.8	122.9	N(3)–S(3)–F(32)	112.6(9)
N(2)–S(2)–F(23)	118.9(13)	123.0	122.8	122.9	N(3)–S(3)–F(33)	138.3(10)
F(21)–S(2)–F(22)	96.6(7)	93.1	93.4	93.2	F(31)–S(3)–F(32)	95.4(7)
F(21)–S(2)–F(23)	109.3(10)	93.1	93.4	93.2	F(31)–S(3)–F(33)	100.8(6)
F(22)–S(2)–F(23)	102.1(10)	93.1	93.4	93.2	F(32)–S(3)–F(33)	100.2(8)

[a] The labels correspond to those used in Figure 8.6. [b] The aug-cc-pVTZ basis set was used. [c] The hydrogen atom positions were calculated using a riding model, therefore no estimated standard deviations are provided.

Table 8.5. Experimental Geometry for $[s\text{-}C_3(CH_3)_3N_3H\text{---}NCCH_3][AsF_6]\cdot CH_3CN$ and Calculated Geometry for the $s\text{-}C_3(CH_3)_3N_3H\text{---}NCCH_3^+$ Cation [a]

Bond Lengths (Å)					
		calcd[b]			
	exptl	PBE1PBE	B3LYP		exptl
N(1)–C(2)	1.346(4)	1.350	1.356	As(1)–F(1)	1.710(2)
N(1)–C(3)	1.346(4)	1.350	1.356	As(1)–F(2)	1.725(2)
N(2)–C(1)	1.348(4)	1.340	1.344	As(1)–F(3)	1.725(2)
N(2)–C(2)	1.323(4)	1.310	1.314	As(1)–F(4)	1.721(2)
N(3)–C(1)	1.346(3)	1.340	1.344	As(1)–F(5)	1.726(2)
N(3)–C(3)	1.318(4)	1.310	1.314	As(1)–F(6)	1.718(2)
C(1)–C(10)	1.485(4)	1.477	1.484		
C(2)–C(20)	1.478(4)	1.480	1.487		
C(3)–C(30)	1.479(4)	1.480	1.487		
N(1)–H(1)	0.806[c]	1.040	1.038		
H(1)---N(40)	2.038[c]	1.788	1.827		
N(1)---N(40)	2.844(5)	2.828	2.865		
N(40)–C(41)	1.135(4)	1.148	1.148	N(50)–C(51)	1.144(4)
C(41)–C(40)	1.451(4)	1.444	1.451	C(51)–C(50)	1.452(5)
Bond Angles (°)					
C(1)–N(2)–C(2)	116.6(2)	117.3	117.7	F(1)–As(1)–F(2)	90.46(8)
C(1)–N(3)–C(3)	116.7(2)	117.3	117.7	F(1)–As(1)–F(3)	90.45(9)
C(2)–N(1)–C(3)	120.9(2)	120.2	120.3	F(1)–As(1)–F(4)	90.46(8)
N(1)–C(2)–N(2)	120.4(2)	120.5	120.3	F(1)–As(1)–F(5)	179.48(8)
N(1)–C(3)–N(3)	120.6(2)	120.5	120.3	F(1)–As(1)–F(6)	90.20(9)
N(2)–C(1)–N(3)	124.7(2)	124.2	123.9	F(2)–As(1)–F(3)	89.84(8)
N(1)–C(2)–C(20)	118.6(2)	119.1	119.3	F(2)–As(1)–F(4)	178.95(7)
N(1)–C(3)–C(30)	118.2(2)	119.1	119.3	F(2)–As(1)–F(5)	89.02(8)
N(2)–C(2)–C(20)	121.0(2)	120.4	120.4	F(2)–As(1)–F(6)	90.04(9)
N(2)–C(1)–C(10)	118.0(2)	117.9	118.1	F(3)–As(1)–F(4)	89.66(9)
N(3)–C(3)–C(30)	121.2(2)	120.4	120.4	F(3)–As(1)–F(5)	89.54(9)
N(3)–C(1)–C(10)	117.4(2)	117.9	118.1	F(3)–As(1)–F(6)	179.33(8)
H(1)–N(1)–C(2)	120.1(2)	119.9	119.9	F(4)–As(1)–F(5)	90.06(8)
H(1)–N(1)–C(3)	119.1[c]	119.9	119.9	F(4)–As(1)–F(6)	90.45(9)
N(1)–H(1)---N(40)	172.2[c]	179.8	180.0	F(5)–As(1)–F(6)	89.81(9)
H(1)---N(40)–C(41)	165.8[c]	179.8	179.9		
N(40)–C(41)–C(40)	179.6(4)	180.0	180.0	N(50)–C(51)–C(50)	179.2(3)

[a] The labels correspond to those used in Figure 8.6; geometries for the methyl groups of the cation and CH_3CN molecules are given in Table 8.6. [b] The aug-cc-pVTZ basis set was used. [c] The hydrogen atom positions were calculated using a riding model, therefore no estimated standard deviations are provided.

Table 8.6. Experimental and Calculated Geometries for the Methyl Groups in the *s*-$C_3(CH_3)_3N_3H$---$NCCH_3^+$ Cation. [a]

Bond Lengths (Å)		
	calcd[b]	
	PBE1PBE	B3LYP
C(10)–H(10A)	1.096	1.095
C(10)–H(10B)	1.088	1.087
C(10)–H(10C)	1.088	1.087
C(20)–H(20A)	1.088	1.086
C(20)–H(20B)	1.092	1.091
C(20)–H(20C)	1.091	1.090
C(30)–H(30A)	1.088	1.086
C(30)–H(30B)	1.091	1.090
C(30)–H(30C)	1.092	1.091
C(40)–H(40A)	1.091	1.089
C(40)–H(40B)	1.091	1.089
C(40)–H(40C)	1.091	1.089
Bond Angles (°)		
C(1)–C(10)–H(10A)	108.2	108.4
C(1)–C(10)–H(10B)	110.8	110.7
C(1)–C(10)–H(10C)	110.8	110.8
H(10A)–C(10)–H(10B)	107.6	107.5
H(10A)–C(10)–H(10C)	107.6	107.6
H(10B)–C(10)–H(10C)	111.9	111.7
C(2)–C(20)–H(20A)	112.5	112.4
C(2)–C(20)–H(20B)	108.8	108.9
C(2)–C(20)–H(20C)	108.9	109.0
H(20A)–C(20)–H(20B)	109.6	109.7
H(20A)–C(20)–H(20C)	110.1	109.8
H(20B)–C(20)–H(20C)	106.7	106.8
C(3)–C(30)–H(30A)	112.4	112.4
C(3)–C(30)–H(30B)	108.9	109.0
C(3)–C(30)–H(30C)	108.8	108.9
H(30A)–C(30)–H(30B)	110.1	110.0
H(30A)–C(30)–H(30C)	109.6	109.6
H(30B)–C(30)–H(30C)	106.8	106.8
C(41)–C(40)–H(40A)	109.8	109.8
C(41)–C(40)–H(40B)	109.8	109.8
C(41)–C(40)–H(40C)	109.8	109.8
H(40A)–C(40)–H(40B)	109.2	109.1
H(40A)–C(40)–H(40C)	109.2	109.1
H(40B)–C(40)–H(40C)	109.2	109.1

[a] The labels correspond to those used in Figure 8.7. The experimental hydrogen positions of all CH_3-groups were calculated using a riding model, therefore, no error is given; all C–H bond lengths are 0.980 Å, and all C–C–H and H–C–H angles are 109.5°. [b] The aug-cc-pVTZ basis set was used.

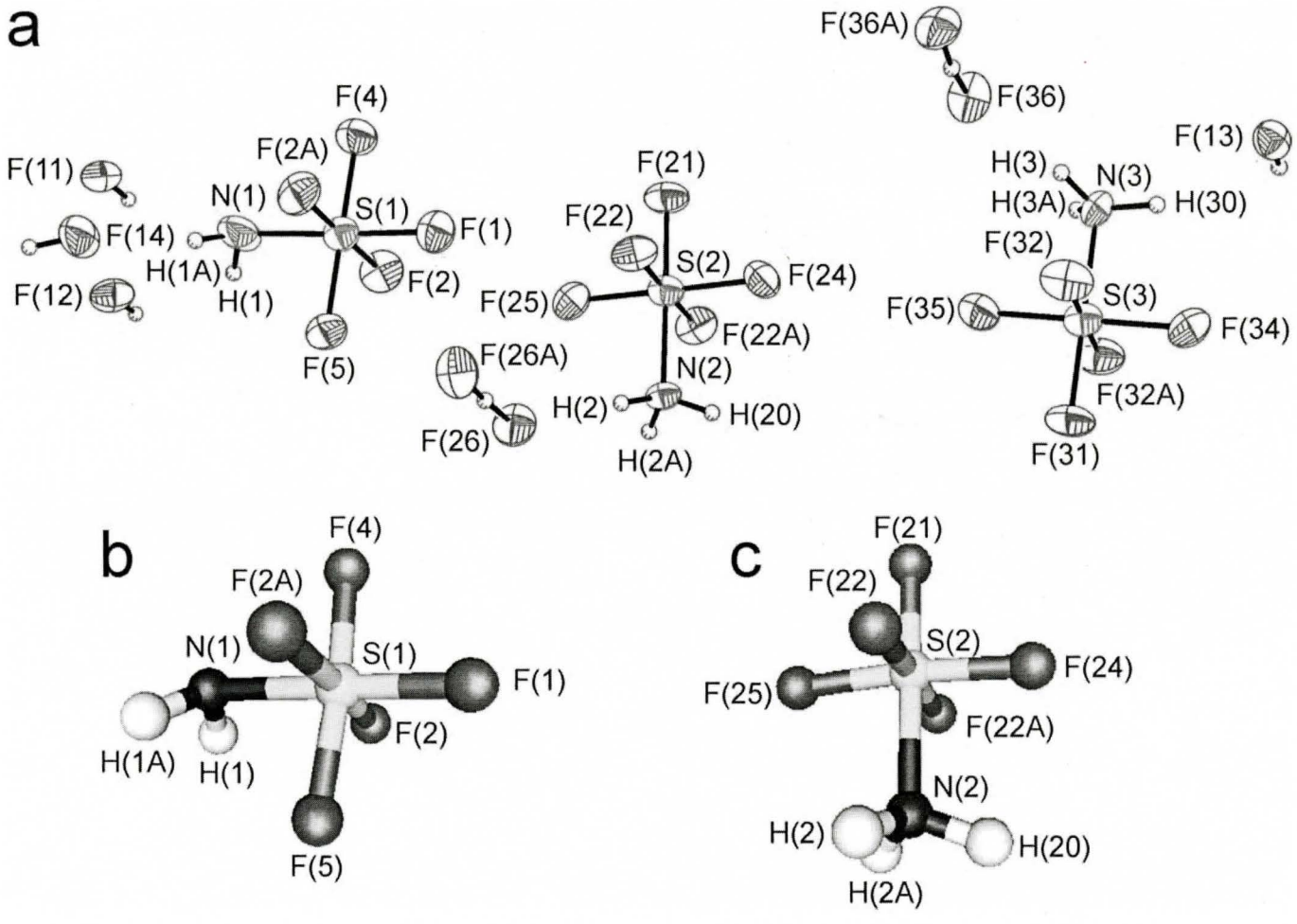

Figure 8.4. (a) Structural unit in the X-ray crystal structure of $F_5SNH_2 \cdot 2[F_5SNH_3][HF_2] \cdot 4HF$; thermal ellipsoids are shown at the 50% probability level. (b) Calculated geometry of F_5SNH_2. (c) Calculated geometry of the $F_5SNH_3^+$ cation. The atom numbering scheme corresponds to that used in Table 8.3; the HF and HF_2^- hydrogen atoms have the same numbering as the fluorine atom to which they are bonded.

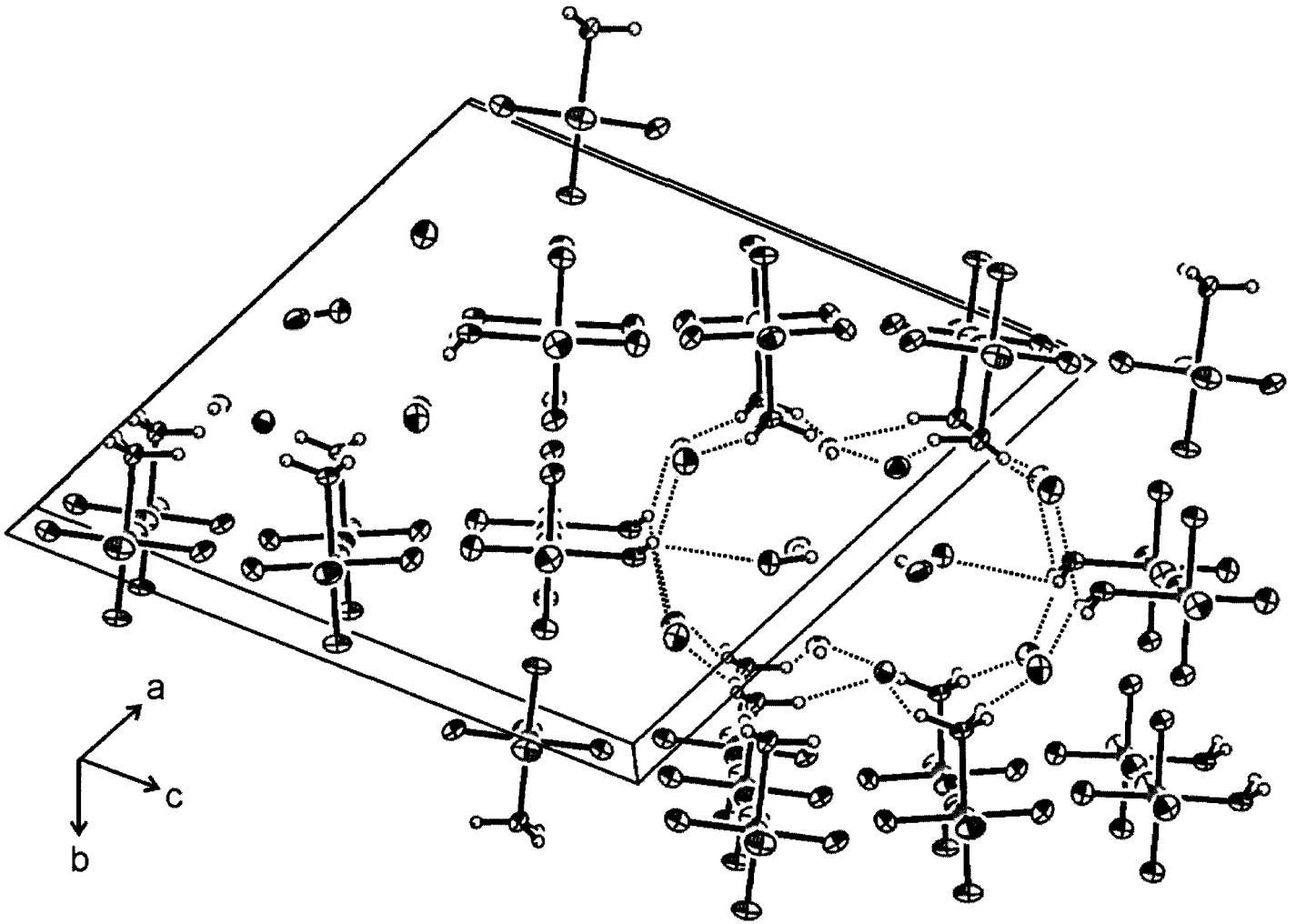

Figure 8.5. Packing diagram for the X-ray crystal structure of $F_5SNH_2 \cdot 2[F_5SNH_3][HF_2] \cdot 4HF$ viewed along the *b*-axis illustrating the hydrogen bonding present; thermal ellipsoids are shown at the 30% probability level for clarity.

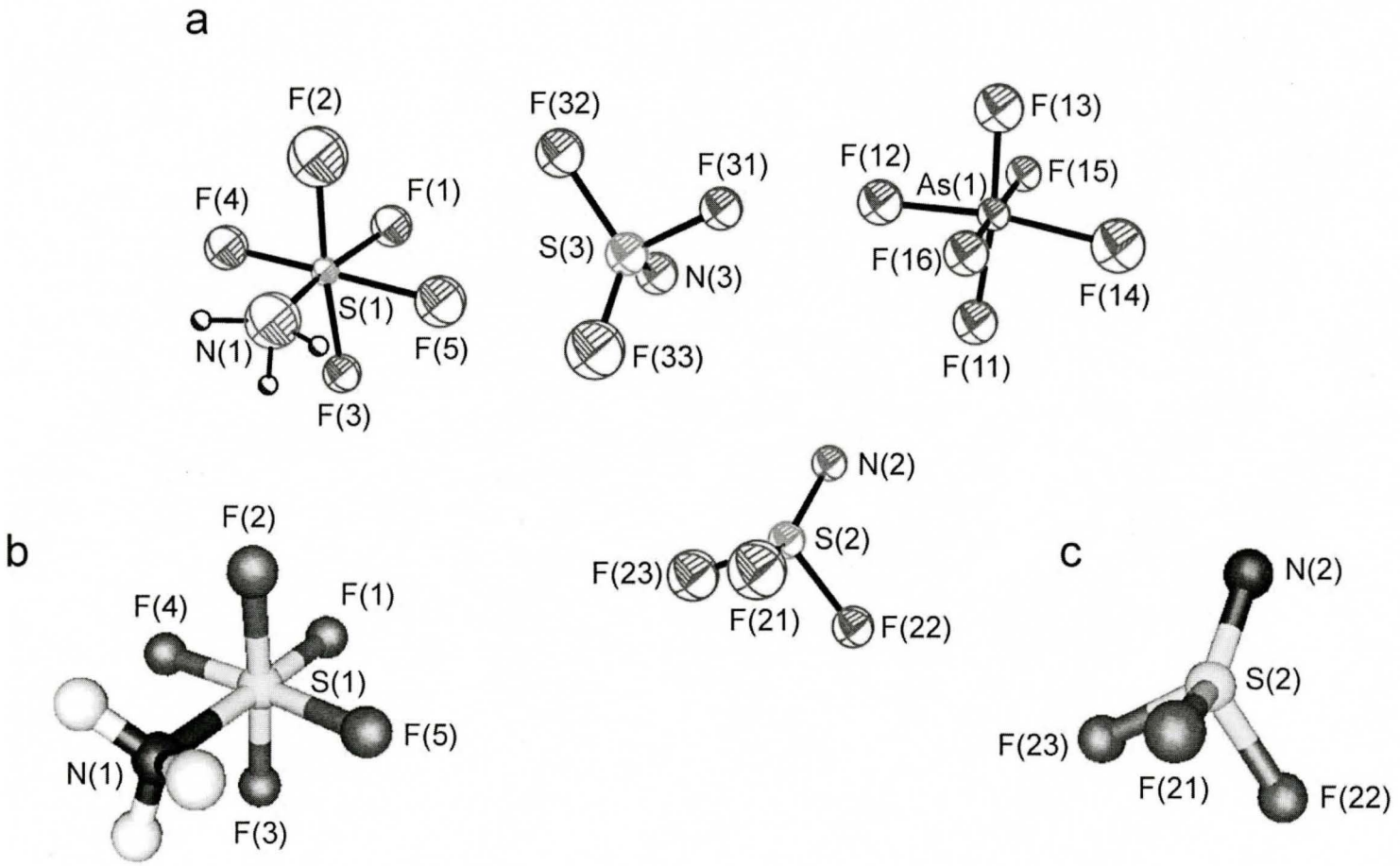

Figure 8.6. (a) Structural unit in the X-ray crystal structure of $[F_5SNH_3][AsF_6]\cdot 2N{\equiv}SF_3$ (preliminary); thermal ellipsoids are shown at the 50% probability level. (b) Calculated geometry of the $F_5SNH_3^+$ cation. (c) Calculated geometry of $N{\equiv}SF_3$. The atom numbering scheme corresponds to that used in Table 8.4.

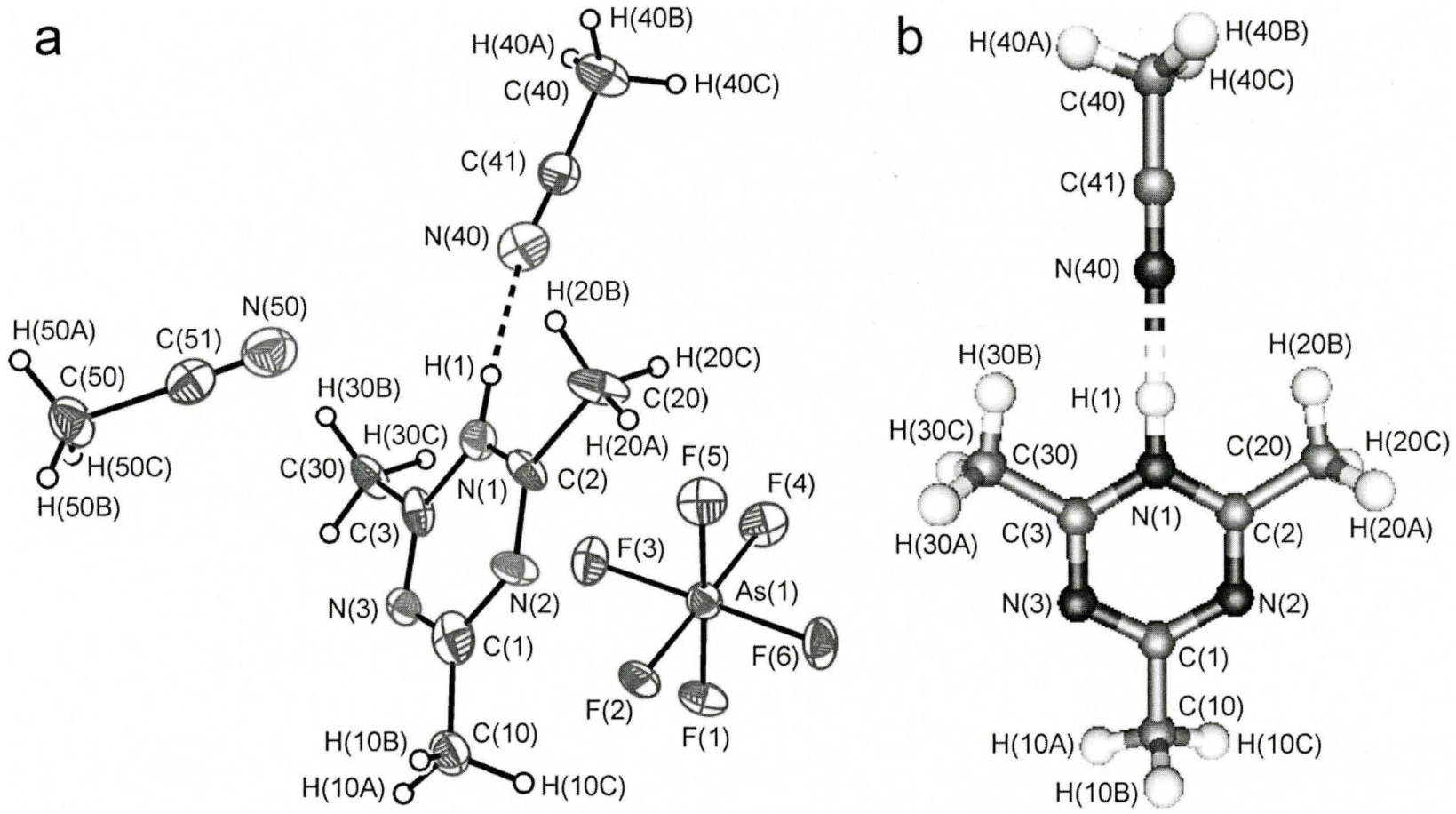

Figure 8.7. (a) Structural unit in the X-ray crystal structure of [*s*-$C_3(CH_3)_3N_3H$---$NCCH_3$][AsF_6]·CH_3CN; thermal ellipsoids are shown at the 50% probability level. (b) Calculated geometry of the *s*-$C_3(CH_3)_3N_3H$---$NCCH_3^+$ adduct cation. The atom numbering scheme corresponds to that used in Table 8.5.

mirror plane with the F atoms related by symmetry. Within the asymmetric unit, three HF molecules are disordered about a mirror plane, while one HF molecule lies in a mirror plane and is well defined. The HF_2^- anions show little distortion from linearity, with F---H---F bond angles of 172.7 and 177.4°, and F---F distances of 2.325(8) and 2.329(8) Å, in good agreement with previously reported values.[217-219]

In the F_5SNH_2 molecule and $F_5SNH_3^+$ cations, the N–S bond lengths 1.716(8), 1.717(7), and 1.739(7) Å, respectively, are the same within experimental error, and all S–F bond lengths (range, 1.550(5) to 1.579(5) Å) are the same within ±3σ. The N–S bond lengths are shorter, but the S–F bond lengths are similar to those of the $F_5SN(H)Xe^+$ cation in $[F_5SN(H)Xe][AsF_6]$ (1.761(4) Å, and range from 1.559(3) to 1.578(3) Å).[118] The N–S bond lengths are similar, but the S–F bond lengths are longer, compared to those of F_5SNC (N–S; 1.693(8), 1.710(7) Å, and S–F; range from 1.515(5) to 1.543(5) Å).[220]

Hydrogen bonding interactions involving the F_5SNH_2 and $F_5SNH_3^+$ components of the unit cell only occur between the hydrogen atoms bonded to nitrogen, and fluorine atoms of HF or HF_2^- (the sum of the H and F van der Waals radii is 2.67 Å).[31] The hydrogen atoms of F_5SNH_2 hydrogen bond to F(26) and F(36) of each HF_2^- anion [1.926 and 2.503 Å] and to F(14) of the ordered HF molecule [2.524 Å]. The H(20) and H(30) atoms of the two $F_5SNH_3^+$ cations, each interact with F(11) [1.916 and 2.595 Å] and F(13) [2.555 and 1.928 Å] of disordered HF molecules, while H(2) and H(2A) interact with F(26) [1.797 Å] and F(13) [2.574 Å], and H(3) and H(3A) interact with F(36) [1.781 Å] and F(11) [2.563 Å]. This results in a succession of large hydrogen-bonded rings in the extended crystal structure, that involve all of the nitrogen-bound hydrogen atoms, all of the bifluoride anions, and

several HF molecules (Figure 8.5). These rings lie in the *ac*-planes forming three dimensional channels along the *b*-axis. These channels are occupied by the more weakly-interacting [F(14)] and non-interacting [F(12)] HF molecules.

8.2.3.2. $[F_5SNH_3][AsF_6]\cdot 2N{\equiv}SF_3$

The crystal structure of $[F_5SNH_3][AsF_6]\cdot 2N{\equiv}SF_3$ (Figure 8.6) represents a preliminary solution that requires further refinement. The X-ray diffraction data is consistent with a multiple crystal, and multiple crystals of $[F_5SNH_3][AsF_6]$ have been reported previously.[116,118] In this preliminary solution, the gross structural features of the well-separated $F_5SNH_3^+$ cation, AsF_6^- anion, and two $N{\equiv}SF_3$ molecules are confirmed. The atom numbering scheme appears in Figure 8.6 and Table 8.4. The AsF_6^- anion is disordered (only one component is reported for clarity) and shows some distortion from octahedral symmetry, with As–F bond lengths ranging from 1.612(11) to 1.762(13) Å and F–As–F bond angles ranging from 82.8(6) to 97.7(5)° and 172.1(5) to 178.3(6)°, which bracket previously reported values.[50,146] The $F_5SNH_3^+$ cation exhibits the expected distorted octahedral geometry, with an S–N bond length (1.673(14) Å) that is significantly longer than the S–F bond lengths (range 1.522(12) to 1.586(12) Å), and all bond lengths comparable to those found in the crystal structure of $F_5SNH_2\cdot 2[F_5SNH_3][HF_2]\cdot 4HF$. The two crystallographically independent $N{\equiv}SF_3$ molecules are co-crystallized and are not adducted to any other species within the asymmetric unit. They exhibit the expected distorted tetrahedral geometry about sulfur, with short S–N bond lengths (1.394(13) and

1.407(12) Å) and S–F bond lengths (range 1.444(16) to 1.531(9) Å), which agree with, or are slightly shorter than, those recently reported in the X-ray crystal structure of $N{\equiv}SF_3$.[86]

8.2.3.3. [*s*-$C_3(CH_3)_3N_3H$---$NCCH_3$][AsF_6]·CH_3CN

The 1H-2,4,6-trimethyl-1,3,5-triazinium cation has been observed by ^1H NMR and UV spectroscopy in concentrated aqueous H_2SO_4 solution,[211] and the triflate salt of the 2,4,6-triisopropyl analogue, [*s*-$C_3(CH(CH_3)_2)_3N_3H$][O_3SCF_3], has been characterized by ^1H NMR, infrared spectroscopy, and mass spectrometry,[210] constituting the extent of characterization for monoprotonated 2,4,6-trialkyl-1,3,5-triazines. Oxidation of molecular bromine by UF_6 in CH_3CN solution generates the positive bromine-containing analogue [*s*-$C_3(CH_3)_3N_3Br$][UF_6].[221] The former salt and related *N*-fluoro-*sym*-triazinium salt [*s*-$C_3(Cl)_3N_3F$][BF_4] have been characterized by multi-NMR spectroscopy.[222] The crystal structure has been determined for the protonated analogue, [*s*-$C_3(Cl)_3N_3H$][$SbCl_6$],[223] and the only known crystal structure of a compound containing a *s*-$C_3(R)_3N_3H^+$ (R = any alkyl or aryl) substructure is the protonated *tert*-butylpyridine (LH^+) substituted 1H-2,4,6-tri-(LH^+)-1,3,5-triazine cation in [s-$C_3(LH^+)_3N_3H$][NO_3]$_3$[PF_6], which has a +4 charge due to the protonation of each of the four rings in the cation.[224] Several crystal structures are known for salts of the diamino analogue, the 1H-2,4-diamino-6-methyl-1,3,5-triazinium cation, e.g., [$C(CH_3)C_2(NH_2)_2N_3H$][$C_2F_3O_2$],[225] [$C(CH_3)C_2(NH_2)_2N_3H$][NO_3],[226] and [$C(CH_3)C_2(NH_2)_2N_3H$]$_2$[$C_4H_4O_4$],[227] and a number of crystal structures are known for salts of the triamino analogue, the 1H-2,4,6-triamino-1,3,5-triazinium cation, e.g., [s-$C_3(NH_2)_3N_3H$][Cl],[228] [s-$C_3(NH_2)_3N_3H$][Cl]·0.5H_2O,[229] and [s-$C_3(NH_2)_3N_3H$]

$[C_4H_3O_4]\cdot H_2O$.[230] Finally, examples of triazinium cations exhibiting hydrogen bonding to a nitrogen atom include $[s\text{-}C_3(NH_2)_3N_3H][C_3(NCN)_3N_3H]\cdot 2H_2O$,[228] $[s\text{-}C_3(NH_2)_3N_3H]$ $[N_3O_4]$,[229] and the $s\text{-}C_3(NH_2)_3N_3H^+$, $s\text{-}C_3(NH_2)_2(CH_3)N_3H^+$, and $s\text{-}C_3(NH_2)_2(C_6H_5)N_3H^+$ salts of the $N(SO_2CH_3)_2^-$ anion.[231] The present work provides the first definitive structural characterization of the $s\text{-}C_3(CH_3)_3N_3H^+$ cation.

The crystal structure of $[s\text{-}C_3(CH_3)_3N_3H\text{---}NCCH_3][AsF_6]\cdot CH_3CN$ consists of well separated $s\text{-}C_3(CH_3)_3N_3H^+$ cations and AsF_6^- anions, with one molecule of CH_3CN hydrogen bonded through nitrogen to the ring hydrogen of the cation, and one molecule of CH_3CN co-crystallized and not adducted to any other species within the crystallographic unit. The atom numbering scheme appears in Figure 8.7 and Tables 8.5 and 8.6. The AsF_6^- anions show little distortion from octahedral symmetry, with As–F bonds ranging from 1.710(2) to 1.726(2) Å and F–As–F bond angles ranging from 89.02(8) to 90.46(8)° and 178.95(7) to 179.48(8)°, in good agreement with previously reported values.[50,146]

The C–C bond lengths of the 1H-2,4,6-trimethyl-1,3,5-triazinium cation are equal, within experimental error, and range from 1.478(4) to 1.485(4) Å, however, the C–N bonds of the triazinium ring can be grouped into two classes. The four ring bonds adjacent to N(1) or C(1) range in length from 1.346(4) to 1.348(4) Å, and are therefore equal within experimental error, but the N(2)–C(2) and N(3)–C(3) bonds (both α, β- with respect to the protonated nitrogen atom) are 1.323(4) and 1.318(4) Å, respectively, and are at the 3σ limit of being significantly shorter than the other bonds. All of the ring bond lengths agree very well with those calculated (see Section 8.3.1.4., Computational Results) and these differing bond lengths confirm the expectation that triazine ring protonation is accompanied by

electron localization. Although there are no other examples of 1H-2,4,6-trimethyl-1,3,5-triazinium cations known, similar bond length differences are observed in the trichloro- and triamino- analogues, with the analogous N–C bond lengths ranging from 1.333(8) to 1.360(8) Å and 1.294(6) to 1.302(7) Å in [*s*-$C_3(Cl)_3N_3H$][$SbCl_6$],[223] and from 1.351(2) to 1.364(2) Å and 1.332(2) to 1.335(2) Å in [s-$C_3(NH_2)_3N_3H$][Cl].[228] The ring proton lies in the plane of the triazine ring and forms a short bond with nitrogen (0.806 Å).

The formally adducted CH_3CN molecule interacts with the cation through an N---H hydrogen bond (2.038 Å) with the ring proton of the triazinium cation, which is well within the sum of the nitrogen and hydrogen van der Waals radii (2.75 Å).[31] Addition of the hydrogen bond distance to the N(1)–H(1) bond length, 0.806 Å, gives an N(1)---N(40) distance of 2.844(5) Å. These three distances are similar to those found in the closely related examples [s-$C_3(NH_2)_2(C_6H_5)N_3H$][$N(SO_2CH_3)_2$] (2.04(3), 0.84(3), and 2.880(3), respectively),[231] and [4-C_6H_5N-C_6H_4NH][$Fe^{II}(CN)_4(CNH)_2$] (2.15(4), 0.83(4), and 2.889(3), respectively).[232] The N–H---N angle (172.2°) deviates more from linearity than the calculated value, 179.8°, but is expected to be very deformable and is likely to be bent due to crystal packing. Examples from among the above systems include 179(3)°,[231] and range from 104 to 178.4° for the series of protonated pyridine derivatives with cyanoferrates.[232] The bond lengths and angles of the adducted and non-adducted CH_3CN molecules are the same within ±3σ, indicating that the hydrogen-bonding interaction that one exhibits with the triazinium ring proton does not significantly alter the geometry of the CH_3CN molecule.

The co-crystallized CH_3CN molecule does not strongly interact with any other species within the crystal structure. The closest contact is between N(50) and N(1) (3.048(5)

Å). The three closest hydrogen contacts of the nitrogen atom are to H(40A) and H(30B) (3.077 and 3.086 Å), methyl-group hydrogen atoms of the adducted CH_3CN molecule and the triazinium cation, respectively, and to the ring proton H(1) (3.099 Å), all outside the sum of the nitrogen and hydrogen van der Waals radii (2.75 Å).[31] This CH_3CN molecule is situated above the triazinium ring, pointed towards H(1), with an N(50)---H(1)–N(1) angle of 78.9° and an N(50)---H(1)---N(40) angle of 108.9° with the adducted CH_3CN nitrogen atom.

8.2.4. Raman Spectroscopy of $F_5SNH_2 \cdot n$HF

The Raman spectrum of $F_5SNH_2 \cdot n$HF (Figure 8.8) was assigned by comparison with the spectra of $F_5SNH_3^+$,[118] $F_5SN(H)Xe^+$,[118] F_5TeNH_2,[50] $F_5TeNH_3^+$,[50] $F_5TeN(H)Xe^+$,[50] F_5SCl,[159] and SF_6,[157,158] (Table 8.7), and by comparison with the calculated frequencies derived for the gas-phase energy-minimized geometries of F_5SNH_2 (see Section 8.3., Computational Results). Calculated frequencies, appearing in parentheses, were obtained at the MP2/aug-cc-pVTZ level, and the vibrational frequencies of SF_6 and F_5SCl were chosen as benchmarks for the F_5S-group frequencies of F_5SNH_2 (Table 8.8 and Section 8.3., Computational Results). In the absence of a refined crystal structure, it was not possible to carry out a factor-group analysis which might account for the splittings observed on several of the Raman bands. The 21 vibrational modes of F_5SNH_2 were assigned under C_1 point symmetry and belong to the 21 A irreducible representations, all of which are Raman- and infrared-active. While some HF was present in the F_5SNH_2 (see Section 8.2.1.1., Results and Discussion), Raman spectra were obtained at –40 °C before the sample was warmed to

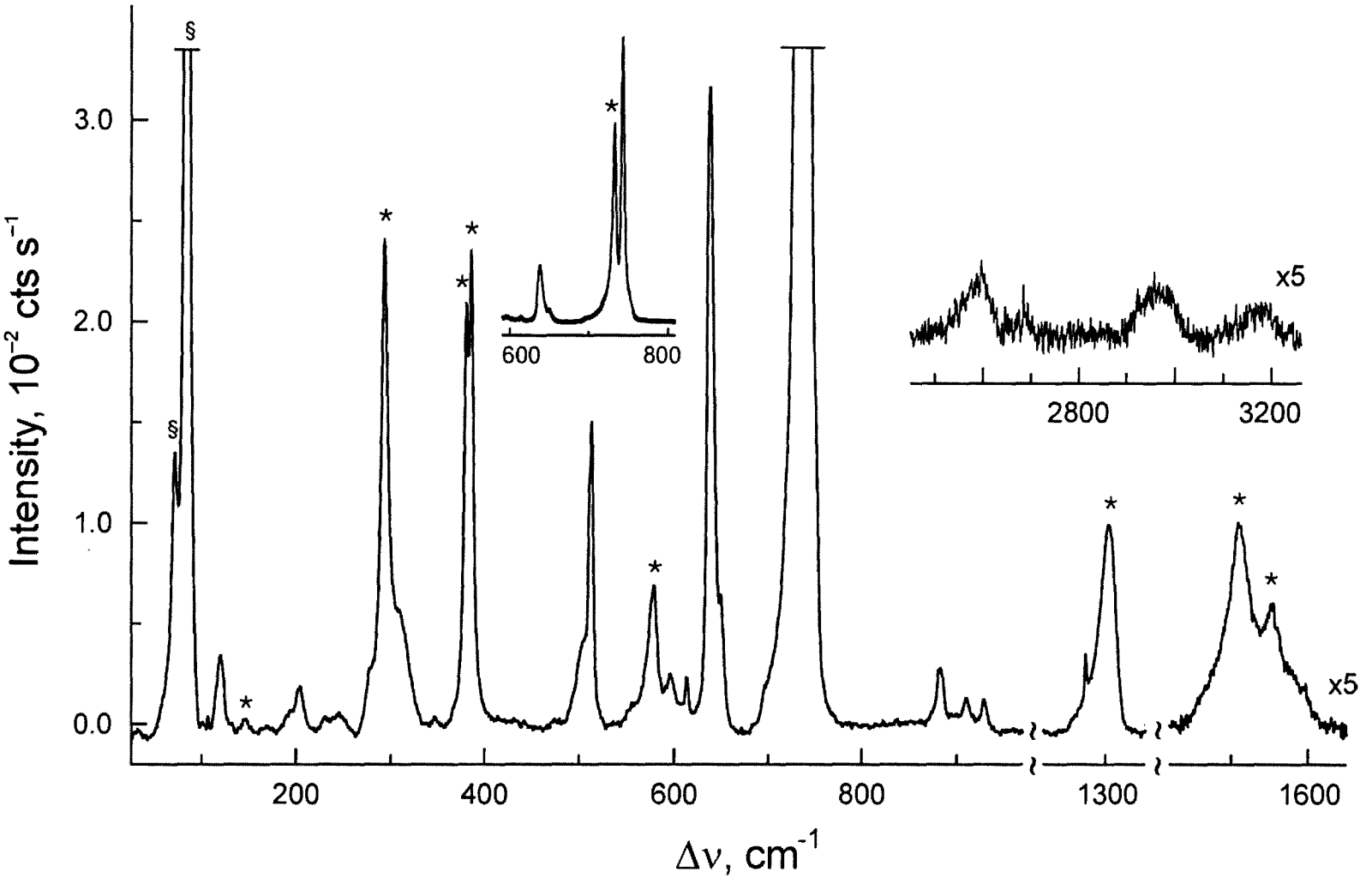

Figure 8.8. Raman spectrum of $F_5SNH_2 \cdot n$HF recorded at −35 °C using 1064-nm excitation; symbols denote FEP sample tube lines(*) and an instrumental artifact (§).

Table 8.7. Experimental and Calculated Vibrational Frequencies, Intensities, and Assignments for F_5SNH_2

freq, cm^{-1}						
	calcd[b]					assgnts[c]
exptl[a]	MP2		PBE1PBE		B3LYP	
3170 (<1) br 2957 (<1) br	3651	(28) [56]	3654	(30) [51]	3609	(32) [48]	ν(NH1 – NH2)
2684 (<1) br 2595 (1) br	3544	(83) [32]	3555	(84) [31]	3513	(86) [30]	ν(NH1 + NH2)
1597 (<1)	1620	(2) [46]	1609	(2) [47]	1608	(2) [41]	δ(H1NH2)
1281 (2)	1225	(1) [38]	1215	(1) [43]	1214	(1) [37]	ρ_t(H1NH2)
929 (1) 910 (1)	979	(1) [225]	972	(1) [240]	957	(1) [206]	δ(SNH1) + δ(SNH2)
883 (2)	888	(1) [443]	885	(1) [436]	843	(1) [424]	ν(SN – SF1) + ν(SF4 – SF5)
881 (2)	885	(1) [352]	883	(1) [351]	842	(1) [357]	ν(SF2 – SF3)
836 (<1)	812	(4) [211]	803	(5) [202]	783	(3) [233]	ρ_w(H1NH2)
742 (100)	717	(23) [9]	709	(22) [15]	672	(27) [12]	ν(SN + SF1 + SF2 + SF3 + SF4 + SF5)
649 (4) 638 (19)	626	(4) [3]	623	(4) [2]	595	(4) [1]	ν(SN + SF1) – ν(SF2 + SF3)
613 (1)	607	(1) [42]	600	(1) [40]	581	(1) [38]	δ(F2SF3) + δ(F4SF5)
596 (1)	598	(2) [14]	595	(2) [15]	568	(3) [12]	δ(F1SN) + δ(F2SF3) + ν(SF4 + SF5) – ν(SF1)
578 co	577	(<1) [9]	572	(<1) [8]	552	(1) [4]	δ(F1SN) + δ(F2SF3) [d]
555 sh	562	(<1) [14]	556	(<1) [13]	539	(<1) [10]	δ(F1SN) + δ(F4SF5)
513 (9) 511 sh	500	(1) [10]	494	(1) [11]	480	(2) [10]	δ(F1SF5) + δ(F4SN)
503 sh	491	(1) [<1]	484	(1) [<1]	471	(1) [<1]	δ(F1SF2) + δ(F3SN)
493 sh	481	(1) [<1]	475	(1) [<1]	460	(1) [<1]	δ(F2SF4) + δ(F3SF5)
347 (<1)	342	(<1) [1]	338	(<1) [1]	328	(<1) [1]	δ(F2SF3) – δ(F4SF5)
n.o.	330	(<1) [4]	326	(<1) [5]	316	(<1) [4]	δ(F1SN) – δ(F2SF3)
310 sh	317	(<1) [2]	312	(<1) [2]	302	(<1) [2]	δ(F1SN) – δ(F4SF5)
277 sh							
247 (1)							
204 (1) 120 (2)	210	(<1) [25]	192	(<1) [24]	190	(<1) [23]	NH_2 torsion

Table 8.7. (continued…)

[a] Values in parentheses denote experimental relative Raman intensities; abbreviations denote broad (br), shoulder (sh), coincident with an FEP sample tube line (co) and not observed (n.o.). [b] The aug-cc-pVTZ basis set was used. Calculated infrared intensities (in km mol^{-1}) are given in brackets, calculated Raman intensities (in $Å^4$ u^{-1}) are given in parentheses. [c] The atom numbering corresponds to that used in Figure 3, abbreviations denote twist (ρ_t) and wag (ρ_w). [d] This mode also contains a – ν(SF5) component in the B3LYP calculation only.

Table 8.8. Experimental and Calculated Geometrical Parameters, Vibrational Frequencies, NBO Valencies and Bond Orders, and NPA Charges for the Benchmarks, SF_6 (O_h) and F_5SCl (C_{4v})

SF_6	exptl	MP2[a]	PBE1PBE[a]	B3LYP[a]		
Bond Lengths (Å)[b]						
S–F	1.5622(7)	1.575	1.575	1.590		
Frequencies (cm^{-1})[c]					assgnts[d]	
	940 (n.o.) [n.o.]	951 (0) [406]	950 (0) [408]	908 (0) [402]	$\nu_{as}(SF - SF)$	(T_{1u})
	773.5 (vs) [n.o.]	768 (21) [0]	765 (21) [0]	730 (23) [0]	$\nu_s(SF_6)$	(A_{1g})
	641.7 (s) [n.o.]	643 (3) [0]	641 (3) [0]	613 (3) [0]	$\nu_{as}(SF_2) - \nu(SF_4)$	(E_g)
	615 (n.o.) [n.o.]	602 (0) [27]	596 (0) [26]	579 (0) [22]	$\nu(SF_4)_{o.o.p.}$	(T_{1u})
	525 (s) [n.o.]	511 (1) [0]	505 (1) [0]	491 (1) [0]	$\delta(SF_2) + \delta(SF_2)$	(T_{2g})
	347 (n.o.) [n.o.]	339 (0) [0]	335 (0) [0]	325 (0) [0]	$\rho_w(SF_2) - \rho_w(SF_2)$	(T_{2u})
Charges						
S		2.68	2.67	2.67		
F		–0.45	–0.44	–0.45		
Valencies						
S		3.58	3.92	3.84		
F		0.49	0.53	0.52		
Bond Orders						
S–F		0.60	0.65	0.64		

continued...

Table 8.8. (continued...)

F_5SCl	exptl	MP2 [a]	PBE1PBE[a]	B3LYP[a]		
Bond Lengths (Å)[e]						
$S–F_a$	1.588(9)	1.579	1.579	1.594		
$S–F_e$	1.566(3)	1.586	1.586	1.601		
S–Cl	2.047(3)	2.057	2.065	2.096		
Frequencies (cm^{-1})[e]					assgnts[d]	
	909.0	914 (1) [331]	914 (1) [333]	869 (1) [330]	$\nu_{as}(SF_{4eq})$	(E)
	854.6	854 (1) [425]	852 (1) [425]	814 (1) [417]	$\nu(SF_a)$	(A_1)
	707.1	704 (19) [17]	702 (19) [16]	667 (21) [16]	$\nu_s(SF_{4eq})$	(A_1)
	625	627 (3) [0]	626 (3) [<1]	596 (4) [0]	$\nu(SF_{4eq})$	(B_1)
	601.9	595 (1) [79]	589 (1) [80]	569 (1) [69]	$\delta(SF_{4eq})_{o.o.p.}$	(A_1)
	579.0	569 (<1) [14]	563 (<1) [14]	545 (<1) [11]	$\rho_w(SF_{4eq})$	(E)
	505	493 (1) [0]	488 (1) [0]	472 (1) [0]	$\delta(SF_{4eq})_{i.p.}$	(B_2)
	441.0	434 (1) [1]	428 (1) [1]	413 (1) [1]	$\rho(SF_{4eq})_{i.p.}$	(E)
	401.7	408 (11) [4]	399 (12) [4]	373 (14) [5]	$\nu(SCl)$	(A_1)
	n.o.	333 (<1) [0]	328 (<1) [0]	317 (<1) [0]	$\rho(SF_{4eq})_{o.o.p.}$	(B_1)
	271	265 (<1) [0]	260 (<1) [<1]	249 (1) [<1]	$\rho_w(SCl)$	(E)

continued...

Table 8.8. (continued...)

Charges			
S	2.39	2.40	2.39
F_a	–0.45	–0.45	–0.45
F_e	–0.45	–0.45	–0.45
Cl	–0.13	–0.14	–0.14
Valencies			
S	4.18	4.30	4.20
F_a	0.59	0.59	0.58
F_e	0.58	0.60	0.58
Cl	0.67	0.62	0.59
Bond Orders			
S–F_a	0.70	0.73	0.71
S–F_e	0.68	0.71	0.70
S–Cl	0.77	0.72	0.70

[a] The aug-cc-pVTZ basis set was used; calculated infrared intensities (in km mol^{-1}) are given in brackets; calculated Raman intensities (in $Å^4$ u^{-1}) are given in parentheses. [b] Experimental value from *J. Chem. Phys.* **1981**, *75*, 5326–5328. [c] Experimental values for the Raman data are from ref 157, and for infrared data, from ref 158, abbreviations denote very strong (vs), strong (s), and not observed (n.o.). [d] Abbreviations denote the four equatorial fluorine atoms (F_{4eq}); out of plane (o.o.p.) and in plane (i.p.), where the plane is defined by the four equatorial fluorine atoms; and wag (ρ_w). [e] Experimental values from ref 159.

–30 °C, and sublimation occurred over a period of ca. 6 h forming crystals of $F_5SNH_2 \cdot 2[F_5SNH_3][HF_2] \cdot 4HF$ (see Section 8.2.3.1., X-ray Crystallography). The Raman spectrum does not contain any bands attributable to the Raman spectra of $F_5SNH_3^+$ [118] or HF_2^-,[217] and the experimental vibrational frequencies are in very good agreement with the calculated frequencies for F_5SNH_2 (see Section 8.3., Computational Results).

The asymmetric NH_2 stretch at 3170, 2957 (3651) cm^{-1}, and the symmetric NH_2 stretch at 2595, 2684 (3544) cm^{-1} were overestimated by the calculations, which was also observed for $F_5SNH_3^+$,[118] $F_5TeNH_3^+$,[50] and F_5TeNH_2,[50] however, the NH_2 bend at 1597 (1620) and twist at 1281 (1225) cm^{-1} were in better agreement with the calculated values. The S–N stretch is coupled to the SF_5-group in-phase breathing mode at 742 (717) cm^{-1}, as in the case of $F_5SNH_3^+$,[118] and as in the analogous modes in F_5TeNH_2.[50] The S–N stretch also in-phase and out-of-phase couples with the ν(SF1) stretch, in combination with other trans equatorial SF_2 stretches, in the modes that occur at 638, 649 (626) and 883 (888) cm^{-1}, respectively. This contrasts with $F_5SNH_3^+$, for which the S–N stretch couples with the equatorial SF_4 out-of-phase, out-of-plane bend, the trans equatorial stretches are coupled to NH_3 rocking modes, and the axial S–F stretch is not coupled.[118] This, however, is similar to the coupling observed in F_5TeNH_2 and $F_5TeNH_3^+$.[50] All of the bands involving S–F stretches fall into the range 596–883 (598–888) cm^{-1} and those involving SF_5 bending modes occur in the range 310–613 (317–607) cm^{-1}, with frequencies similar to those of $F_5SNH_3^+$ (645–920 and 362–632 cm^{-1}),[118] SF_6 (615–940 and 347–525 cm^{-1}) and F_5SCl (602–909 and 271–579 cm^{-1}).[159] The NH_2 torsion, predicted at 210 cm^{-1}, was observed at 204 cm^{-1}.

8.3. Computational Results

Quantum-chemical calculations were carried out at the MP2, B3LYP, and PBE1PBE levels for F_5SNH_2, $F_5SNH_3^+$, and $N{\equiv}SF_3$, and at the B3LYP and PBE1PBE levels only for all of the CH_3CN cyclotrimerization reagents and intermediates, *s*-$C_3(CH_3)_3N_3H^+$, *s*-$C_3(CH_3)_3N_3H$---$NCCH_3^+$, and *s*-$C_3(CH_3)_3N_3H$---$NCCH_3^+{\cdot}CH_3CN$ due to computational constraints. All levels employed aug-cc-pVTZ basis sets. The calculations were used to aid in the vibrational assignments (see Raman Spectroscopy) and to gain insight into the structure and bonding of the triazinium adduct-cation. Comparisons of the calculated and experimental geometrical parameters and vibrational frequencies with those of the benchmarks, F_5SCl and SF_6, showed that the MP2 calculations provided the best overall agreement. Therefore, the vibrational assignments for F_5SNH_2 are based on the MP2 results (Table 8.8), which are reported in square brackets in the ensuing discussion.

8.3.1. Calculated Geometries

8.3.1.1. F_5SNH_2

Although close to C_s symmetry, the MP2, PBE1PBE, and B3LYP energy-minimized structures of F_5SNH_2 optimized to C_1 symmetry with all vibrational frequencies real. These calculations well reproduced the overall experimental geometric parameters of F_5SNH_2 in $F_5SNH_2{\cdot}2[F_5SNH_3][HF_2]{\cdot}4HF$, with the largest discrepancies occurring for the N–S bond length [1.680 Å] which was underestimated, and S–F(5) axial bond length [1.616 Å] which was overestimated, compared to the experimental

values (1.716(8) and 1.560(5) Å). The bond angles about sulfur were experimentally closer to an octahedral geometry [range 89.2(3) to 91.4(3)°] than predicted (range 86.5 to 93.8°). The calculations predict that the hydrogen atoms have a greater steric influence on the SF_5-group geometry than was observed in the crystal structure. The most significant example is the overestimated N(1)–S(1)–F(5) bond angle, which is calculated (93.8°) to be greater than what was found experimentally (91.4(3)°). This less significant intra-molecular interaction may be due to involvement of the hydrogen atoms in the extensive hydrogen bonding present in the extended crystal structure (see Section 8.2.3.1., X-ray Crystal Structure).

8.3.1.2. $F_5SNH_3^+$

Although close to C_s symmetry, the MP2, PBE1PBE, and B3LYP energy-minimized structures of the $F_5SNH_3^+$ cation optimized to C_1 symmetry with all vibrational frequencies real. These calculations well reproduced the overall experimental geometric parameters of the $F_5SNH_3^+$ cation in $F_5SNH_2{\cdot}2[F_5SNH_3][HF_2]{\cdot}4HF$ and $[F_5SNH_3][AsF_6]{\cdot}2N{\equiv}SF_3$, but all bond lengths were overestimated at all levels. The largest discrepancies occurred for the calculated N–S bond length [1.848 Å], compared to the experimental values (1.717(7), 1.739(7) and 1.673(14) Å). The bond angles about sulfur were within $\pm 3\sigma$ of an octahedral geometry except for one bond angle [range 89.4(3) to 91.2(3)°], but were significantly more distorted in the calculated geometry (range 86.9 to 92.8°). As seen for F_5SNH_2, the calculations appear to predict that the hydrogen atoms have a greater influence on the structure and bonding than was observed,

and the less significant effect experimentally may be due to the hydrogen atom's involvement in the extensive hydrogen bonding present in the crystal structure (see X-ray Crystal Structures).

8.3.1.3. $N{\equiv}SF_3$

The MP2, PBE1PBE, and B3LYP energy-minimized structures of $N{\equiv}SF_3$ optimized to C_{3v} symmetry with all vibrational frequencies real. These calculations well reproduced the experimental geometric parameters, but due to the preliminary nature of the solution to the X-ray crystal structure of $[F_5SNH_3][AsF_6]{\cdot}2N{\equiv}SF_3$, (see X-ray Crystal Structure of $[F_5SNH_3][AsF_6]{\cdot}2N{\equiv}SF_3$) a detailed comparison is not possible. The calculated geometry compares well to those determined experimentally for pure $N{\equiv}SF_3$ by single-crystal X-ray diffraction[86] and gas-phase microwave spectroscopy,[85] with the same bond angles, within experimental error, but slightly overestimated S–N and S–F bond lengths.

8.3.1.4. $[s\text{-}C_3(CH_3)_3N_3H{---}NCCH_3][AsF_6]{\cdot}CH_3CN$

The $s\text{-}C_3(CH_3)_3N_3H^+$ cation, whether calculated alone, or in the energy-minimized adduct-cation, $s\text{-}C_3(CH_3)_3N_3H{---}NCCH_3^+$, optimized to C_1 symmetry at the B3LYP and PBE1PBE levels using aug-cc-pVTZ basis sets, and was very near C_s symmetry. Although the gross features of the cation and the formally adducted (hydrogen bonded) CH_3CN molecule were well reproduced, the greatest differences occur for the hydrogen bonding interactions. The calculated N(40)---H(1) hydrogen bond [1.788 Å] was

underestimated, and the N(1)–H(1) bond [1.040 Å] was overestimated, compared to the experimental values (2.038 and 0.806 Å). The calculated N(40)---N(1) distance [2.828 Å], however, well reproduced the experimental distance (2.844(5) Å). The calculated N(1)–H(1)---N(40) and H(1)---N(40)–C(41) angles deviated less from linearity [both 179.8°] than the experimental angles, 172.2° and 165.8°, respectively, which are undoubtedly influenced by crystal packing (see X-ray Crystallography).

8.3.2. Comparison of NBO Valencies, Bond Orders, and NPA Charges

The natural bond orbital (NBO) valencies, bond orders, and natural population analysis (NPA) charges calculated using MP2, PBE1PBE, and B3LYP methods for F_5SNH_2 and $F_5SNH_3^+$ are listed in Table 8.9, and those calculated using PBE1PBE and B3LYP methods for *s*-$C_3(CH_3)_3N_3$, *s*-$C_3(CH_3)_3N_3H^+$, and *s*-$C_3(CH_3)_3N_3H$---$NCCH_3^+$ are listed in Table 8.10. Values appearing in square brackets in the ensuing discussion are MP2 for the F_5SN-species and PBE1PBE for the triazine species.

8.3.2.1. F_5SNH_2 and the $F_5SNH_3^+$ cation

Positive charges in both F_5SNH_2 and $F_5SNH_3^+$ reside on S and H, with the positive charge on S [2.55] and H [0.39] in F_5SNH_2 being less than that in $F_5SNH_3^+$ [2.81] and [0.46]. Although negatively charged, the charge on N [–0.99] is more negative in F_5SNH_2 than in $F_5SNH_3^+$ [–0.86], while the charges on the fluorine atoms of each species are essentially the same. The increase in the charge difference for sulfur and nitrogen in $F_5SNH_3^+$ is consistent with the lower S–N bond covalency and lower bond order of this

Table 8.9. Natural Bond Orbital (NBO) Valencies, Bond Orders and NPA Charges for $F_5SNH_3^+$ and F_5SNH_2 [a]

atom	$F_5SNH_3^+$						F_5SNH_2					
	charges			valencies			charges			valencies		
	MP2	PBE1PBE	B3LYP	MP2	PBE1PBE	B3LYP	MP2	PBE1PBE	B3LYP	MP2	PBE1PBE	B3LYP
H	0.46	0.46	0.46	0.65	0.64	0.64	0.39	0.40	0.39	0.73	0.74	0.72
N	–0.86	–0.86	–0.84	2.48	2.43	2.42	–0.99	–0.98	–0.96	2.15	2.17	2.16
S	2.81	2.59	2.59	4.19	3.50	3.86	2.55	2.54	2.52	4.15	3.85	3.77
F1	–0.43	–0.39	–0.39	0.65	0.51	0.59	–0.45	–0.45	–0.45	0.57	0.49	0.51
F2	–0.47	–0.43	–0.43	0.58	0.46	0.53	–0.47	–0.47	–0.47	0.56	0.49	0.50
F3	–0.47	–0.43	–0.43	0.58	0.46	0.53	–0.47	–0.47	–0.47	0.56	0.49	0.50
F4	–0.47	–0.43	–0.43	0.58	0.46	0.53	–0.46	–0.46	–0.46	0.56	0.49	0.49
F5	–0.47	–0.43	–0.43	0.58	0.46	0.53	–0.48	–0.48	–0.48	0.53	0.48	0.47

bond	bond orders					
	$F_5SNH_3^+$			F_5SNH_2		
	MP2	PBE1PBE	B3LYP	MP2	PBE1PBE	B3LYP
N–H	0.66	0.66	0.66	0.72	0.73	0.73
S–N	0.59	0.55	0.54	0.83	0.82	0.80
S–F1	0.76	0.63	0.70	0.67	0.62	0.61
S–F2	0.71	0.58	0.65	0.66	0.60	0.59
S–F3	0.71	0.58	0.65	0.66	0.60	0.59
S–F4	0.71	0.58	0.65	0.67	0.61	0.59
S–F5	0.71	0.58	0.65	0.64	0.59	0.57

[a] The aug-cc-pVTZ basis set was used.

Table 8.10. Natural Bond Orbital (NBO) Valencies, Bond Orders, and NPA Charges for *s*-$C_3(CH_3)_3N_3$, *s*-$C_3(CH_3)_3N_3H^+$ and *s*-$C_3(CH_3)_3N_3H^+$ in *s*-$C_3(CH_3)_3N_3H$---$NCCH_3^+$ [a]

	s-$C_3(CH_3)_3N_3$				*s*-$C_3(CH_3)_3N_3H^+$				*s*-$C_3(CH_3)_3N_3H$---$NCCH_3^+$			
atom	charges		valencies		charges		valencies		charges		valencies	
	PBE1	B3LYP	PBE1	B3LYP	PBE1	B3LYP	PBE1	B3LYP	PBE1	B3LYP	PBE1	B3LYP
H1					0.44	0.43	0.73	0.73	0.47	0.47	0.72	0.72
N1	–0.51	–0.51	2.17	2.16	–0.50	–0.50	2.62	2.60	–0.53	–0.53	2.45	2.44
N2	–0.51	–0.51	2.17	2.16	–0.45	–0.46	2.20	2.19	–0.46	–0.46	2.20	2.19
N3	–0.51	–0.51	2.17	2.16	–0.45	–0.46	2.20	2.19	–0.46	–0.46	2.20	2.19
C1	0.46	0.46	3.26	3.24	0.53	0.54	3.30	3.28	0.53	0.53	3.31	3.28
C2	0.46	0.46	3.26	3.24	0.53	0.53	3.23	3.21	0.52	0.53	3.21	3.19
C3	0.46	0.46	3.26	3.24	0.53	0.54	3.23	3.21	0.53	0.53	3.21	3.19
C10	–0.65	–0.63	3.28	3.28	–0.67	–0.65	3.29	3.29	–0.67	–0.64	3.29	3.29
C20	–0.65	–0.63	3.28	3.28	–0.68	–0.65	3.28	3.28	–0.67	–0.65	3.26	3.26
C30	–0.65	–0.63	3.28	3.28	–0.68	–0.65	3.28	3.28	–0.67	–0.65	3.26	3.26

	bond orders					
bond	*s*-$C_3(CH_3)_3N_3$		*s*-$C_3(CH_3)_3N_3H^+$		*s*-$C_3(CH_3)_3N_3H$---$NCCH_3^+$	
	PBE1	B3LYP	PBE1	B3LYP	PBE1	B3LYP
N1–H1			0.71	0.71	0.60	0.61
N1–C2	1.15	1.11	0.99	0.98	1.00	0.99
N1–C3	1.12	1.14	1.00	0.99	1.00	0.99
C1–N2	1.15	1.11	1.09	1.09	1.11	1.10
C1–N3	1.12	1.14	1.10	1.09	1.11	1.10
C2–N2	1.12	1.14	1.19	1.19	1.18	1.18
C3–N3	1.15	1.11	1.19	1.18	1.18	1.18
C1–C10	0.90	0.90	0.95	0.94	0.94	0.93
C2–C20	0.90	0.90	0.94	0.93	0.93	0.93
C3–C30	0.90	0.90	0.94	0.93	0.93	0.93

[a] The aug-cc-pVTZ basis set was used; for charges and valencies, PBE1PBE is abbreviated PBE1; the methyl-group hydrogen atoms are excluded.

bond [0.59] compared to that of F_5SNH_2 [0.83]. This is reflected in a longer calculated S–N bond length for $F_5SNH_3^+$, but experimentally, the $F_5SNH_3^+$ and F_5SNH_2 bond lengths are the same, within $\pm 3\sigma$. Greater valencies for the fluorine ligands of $F_5SNH_3^+$, and greater positive charge on sulfur is consistent with the greater S–F bond orders when compared with those of F_5SNH_2.

8.3.2.2. *s*-$C_3(CH_3)_3N_3$, *s*-$C_3(CH_3)_3N_3H^+$, and *s*-$C_3(CH_3)_3N_3H$---$NCCH_3^+$

The positive charges in *s*-$C_3(CH_3)_3N_3$ and in the free and CH_3CN-adducted *s*-$C_3(CH_3)_3N_3H^+$ cations reside on the ring carbon atoms and the hydrogen atoms. The positive charges on the ring C atoms in *s*-$C_3(CH_3)_3N_3$ [0.46] increase with protonation in both the free and adducted cations [av. 0.53]. The negative charge on N in *s*-$C_3(CH_3)_3N_3$ [–0.51] remains essentially unchanged [–0.50] for the protonated nitrogen in the cation, and becomes less negative for the other ring nitrogen atoms [–0.46]. In the adducted cation, the charges are similar [–0.53 and –0.46, respectively]. The increase in the charge difference between N1 and C2/C3 in *s*-$C_3(CH_3)_3N_3H$---$NCCH_3^+$ is consistent with the lower N1–C2/C3 bond covalency and lower bond order of this bond [1.00] compared to that of the neutral triazine [av. 1.14], and this is reflected in the calculated and experimental bond lengths. The greater valency of N1 in the cation is a result of the bond to hydrogen. The greater valencies for N2 and N3 in the cation coupled with the greater positive charges on C2 and C3 are consistent with the greater N2–C2 and N3–C3 bond orders [1.18] when compared with those of *s*-$C_3(CH_3)_3N_3$ [av. 1.14].

8.4. Conclusions

The pentafluorosulfanyl species F_5SNH_2 and $F_5SNH_3^+$ have been definitively characterized by multi-NMR and Raman spectroscopy, and by single-crystal X-ray diffraction in the structures of $F_5SNH_2 \cdot 2[F_5SNH_3][AsF_6] \cdot 4HF$ and $[F_5SNH_3][AsF_6] \cdot 2N{\equiv}SF_3$, significantly expanding the structural characterization of these fundamental inorganic species. The latter structure is the only known example that includes $N{\equiv}SF_3$ in a salt in which it is not adducted to a main-group or transition metal centre. Dissolution of $[F_5SNH_3][AsF_6]$ in CH_3CN at −10 °C yields the *s*-$C_3(CH_3)_3N_3H^+$ triazinium cation, which forms by trimerization of CH_3CN which is initiated by protonation of CH_3CN by $F_5SNH_3^+$. The proposed mechanism invokes protonated CH_3CN dimer and trimer intermediates which lead to cyclization. The CH_3CNH^+ and *s*-$C_3(CH_3)_3N_3H^+$ cations have been characterized by ^1H and ^{13}C NMR spectroscopy, and the salt of the CH_3CN adduct, [*s*-$C_3(CH_3)_3N_3H$---$NCCH_3$][AsF_6]·CH_3CN, was characterized by single-crystal X-ray diffraction. In the crystal structure, one molecule of CH_3CN is hydrogen-bonded through nitrogen to the hydrogen of the triazinium ring. This work represents the first definitive characterization of the 1H-2,4,6-trimethyl-1,3,5-triazinium cation, a rare example of a *sym*-2,4,6-trialkyl-1,3,5-triazinium cation. Proton transfer from $F_5SNH_3^+$ also generated F_5SNH_2, which was characterized by ^1H and ^{19}F NMR spectroscopy.

CHAPTER 9

CONCLUSIONS AND DIRECTIONS FOR FUTURE WORK

9.1. Conclusions

The chemistry of xenon(II) has been significantly extended by the syntheses and characterizations of new examples of xenon bound to nitrogen ligands derived from thiazyl trifluoride, $N{\equiv}SF_3$. The $F_3S{\equiv}NXeF^+$, $F_4S{=}NXe^+$, $F_4S{=}NXe{---}N{\equiv}SF_3^+$, and $F_5SN(H)Xe^+$ cations are examples of xenon bound to formally sp-, sp^2-, and sp^3-hybridized nitrogen centres, and have been thoroughly characterized by multi-NMR and Raman spectroscopy, and by single-crystal X-ray diffraction. The Lewis basicity of $N{\equiv}SF_3$ is sufficient to displace XeF_2 from $[FXeOXeFXeF][AsF_6]$ to form the $FXeOXe{---}N{\equiv}SF_3^+$ adduct-cation, which was characterized by Raman spectroscopy of natural abundance and ^{18}O-enriched salts, and represents only the third example of a xenon(II) oxide fluoride. The $FXeOXe{---}N{\equiv}SF_3^+$ and $F_4S{=}NXe{---}N{\equiv}SF_3^+$ adduct cations are rare examples of O–Xe–N and N–Xe–N linkages, and the latter is the first to have been definitively characterized by single-crystal X-ray diffraction.

The HF solvolysis pathway of $[F_3S{\equiv}NXeF][AsF_6]$ in aHF or BrF_5 solutions was investigated by multi-NMR spectroscopy, revealing that the $F_4S{=}NXe^+$, $F_4S{=}NH_2^+$, and $F_5SN(H)Xe^+$ cations are intermediates in two distinct solvolytic routes to $F_5SNH_3^+$, culminating in the formation of XeF_2, SF_6 and NH_4^+. The rearrangement of $[F_3S{\equiv}NXeF][AsF_6]$ in $N{\equiv}SF_3$ solution yielded $[F_4S{=}NXe{---}N{\equiv}SF_3][AsF_6]$. The $F_4S{=}NXe^+$ and $F_4S{=}NH_2^+$ cations, which exhibit high barriers to rotation about their S=N

double bonds, significantly extend the chemistry of the $F_4S{=}N$- group and are the first known cations to contain this group.

Solvolysis of $N{\equiv}SF_3$ in aHF led to isolation of $F_5SNH_2{\cdot}n$HF, which when sublimed, formed single crystals of $F_5SNH_2{\cdot}2[F_5SNH_3][HF_2]{\cdot}4HF$. Recrystallization of $[F_5SNH_3][AsF_6]$ from $N{\equiv}SF_3$ solution afforded crystalline $[F_5SNH_3][AsF_6]{\cdot}2N{\equiv}SF_3$. The redox decomposition of $[F_4S{=}NXe{---}N{\equiv}SF_3][AsF_6]$ in $N{\equiv}SF_3$ led to the formation of $[F_3S(N{\equiv}SF_3)_2][AsF_6]$. X-ray crystal structure determinations of these salts constitute a significant extension of structural sulfur-nitrogen-fluorine chemistry, providing the first definitive characterizations of F_5SNH_2 and $F_5SNH_3^+$, the second known example of a structure containing a non-adducted $N{\equiv}SF_3$ molecule, and rare examples of main-group coordination compounds of $N{\equiv}SF_3$. The $F_5SNH_3^+$ cation has been shown to be sufficiently acidic to protonate CH_3CN to form CH_3CNH^+, initiating the cyclotrimerization of CH_3CN, which generates F_5SNH_2 and $[s\text{-}C_3(CH_3)_3N_3H][AsF_6]$. Crystal growth from CH_3CN allowed for the determination of the first crystal structure of a *sym*-2,4,6-trialkyl-1,3,5-triazinium cation, namely, $[s\text{-}C_3(CH_3)_3N_3H{---}NCCH_3][AsF_6]{\cdot}CH_3CN$.

The extension of krypton-nitrogen chemistry was not achieved as no conclusive evidence for Kr–N bond formation was found in repeated low-temperature synthetic attempts to form $[F_3S{\equiv}NKrF][AsF_6]$ and $[F_5SN(H)Kr][AsF_6]$. In each case, the fluorination and oxidation products SF_6, NF_3, NF_4^+ and AsF_6^- were observed instead, supporting the trend that krypton compounds are less thermodynamically stable than their xenon analogues.

9.2. Directions for Future Work

The teflate group (-$OTeF_5$) is known to have a chemistry similar to that of the fluorine ligand in main-group chemistry.[233] The teflate analogue of XeF^+, $XeOTeF_5^+$, should be investigated as a Lewis acid for reaction with $N{\equiv}SF_3$ to yield the $F_3S{\equiv}NXeOTeF_5^+$ cation according to eq 9.1. The study of the HF solvolysis of the

$$N{\equiv}SF_3 + [XeOTeF_5][AsF_6] \xrightarrow{N{\equiv}SF_3} [F_3S{\equiv}NXeOTeF_5][AsF_6] \qquad (9.1)$$

$F_3S{\equiv}NXeOTeF_5^+$ cation, by analogy with that of $F_3S{\equiv}NXeF^+$ is not possible because of the HF solvolysis leading to the formation of $HOTeF_5$. However, the analogous solid-state rearrangement (see Scheme 6.1) may occur yielding $F_3(OTeF_5)S{=}NXe^+$, which could exist as a mixture of up to three isomers: the teflate group, bound to sulfur, may be in an equatorial position, or could be *syn-* or *anti*-axial with respect to the xenon atom. The isomers should be readily identifiable by ^{19}F and ^{129}Xe NMR spectroscopy, and should lead to a better understanding of the solid-state rearrangement mechanism.

Recrystallization of the $[F_5SN(H)Xe][AsF_6]$ salt from liquid $N{\equiv}SF_3$ could be expected to form single crystals of the donor-acceptor adduct $[F_5SN(H)Xe{---}N{\equiv}SF_3][AsF_6]$ (eq 9.2) by analogy with $[F_4S{=}NXe{---}N{\equiv}SF_3][AsF_6]$. This would provide

$$[F_5SN(H)Xe][AsF_6] + N{\equiv}SF_3 \xrightarrow{N{\equiv}SF_3} [F_5SN(H)Xe{---}N{\equiv}SF_3][AsF_6] \qquad (9.2)$$

only the second X-ray crystal structure of a compound containing an N–Xe–N linkage, and would be a rare example of xenon bound to an inorganic sp^3-hybridized nitrogen centre.

The synthesis of $[FXeOXe{-}{-}{-}N{\equiv}SF_3][AsF_6]$ from $[FXeOXe{-}{-}{-}FXeF][AsF_6]$ should be repeated, followed by continued pumping under dynamic vacuum, at warmer temperatures if necessary, to attempt to remove the $N{\equiv}SF_3$ from the salt, leaving $[FXeOXe][AsF_6]$ (eq 9.3), which would be the first example of a non-adducted xenon(II) oxide fluoride cation. Another approach would be to complex coordinated $N{\equiv}SF_3$ by addition of a Lewis acid. Based on calculated dissociation energies (see Scheme 7.2.), AsF_5 would not be strong enough, but XeF^+ should be able to adduct $N{\equiv}SF_3$ and displace the free $FXeOXe^+$ cation. This would result in a mixture of salts (eq 9.4), from which single crystal growth from a solvent other than $N{\equiv}SF_3$ (which would adduct to the

$$[FXeOXe{-}{-}{-}N{\equiv}SF_3][AsF_6] \xrightarrow{\text{vac.}} [FXeOXe][AsF_6] + N{\equiv}SF_3 \uparrow \qquad (9.3)$$

$$[FXeOXe{-}{-}{-}N{\equiv}SF_3][AsF_6] + [XeF][AsF_6] \xrightarrow[SO_2ClF]{BrF_5 \text{ or}} [FXeOXe][AsF_6] + [F_3S{\equiv}NXeF][AsF_6] \qquad (9.4)$$

available Lewis acid sites) or HF (which would solvolyse the S≡N triple bond), such as BrF_5 or SO_2ClF, should be attempted.

Attempts should also be made to extend the use of $N{\equiv}SF_3$ as a ligand to xenon in the +4 oxidation state. Reaction of a salt of XeF_3^+ with excess liquid $N{\equiv}SF_3$ would be expected to yield the xenon(IV) analogue of $F_3S{\equiv}NXeF^+$ (eq 9.5). If successful, the HF solvolysis of $F_3S{\equiv}NXeF_3^+$ should be investigated by ^{19}F NMR spectroscopy, which could lead to the $F_4S{=}NXeF_2^+$ and $F_5SN(H)XeF_2^+$ cations (eq 9.6 and 9.7), significantly

extending the known chemistry of xenon(IV) by providing the first strongly covalent Xe(IV)–N bonded species.

$$N{\equiv}SF_3 + [XeF_3][AsF_6] \xrightarrow{N{\equiv}SF_3} [F_3S{\equiv}NXeF_3][AsF_6] \quad (9.5)$$

$$[F_3S{\equiv}NXeF_3][AsF_6] + HF \xrightarrow[HF/BrF_5]{HF\ or} [F_4S{=}NXeF_2][AsF_6] \quad (9.6)$$

$$[F_4S{=}NXeF_2][AsF_6] + HF \xrightarrow[HF/BrF_5]{HF\ or} [F_5SN(H)XeF_2][AsF_6] \quad (9.7)$$

Isolation of HF-free F_5SNH_2 by distillation of $F_5SNH_2{\cdot}n$HF onto NaF to sequester the HF as HF_2^-, followed by redistillation of the purified F_5SNH_2, should allow for crystal growth by sublimation and for the X-ray structure determination of F_5SNH_2, and for confirmation of the Raman spectrum, thereby completing the structural characterization of this fundamental amine.

The fluoride ion acceptor properties of $N{\equiv}SF_3$ should also be investigated, by reaction of $N{\equiv}SF_3$ with $[N(CH_3)_4][F]$, to generate the $N{=}SF_4^-$ anion (eq 9.8). This anion

$$N{\equiv}SF_3 + [N(CH_3)_4][F] \xrightarrow{N{\equiv}SF_3} [N(CH_3)_4][N{=}SF_4] \quad (9.8)$$

is expected to be reasonably stable as it is isoelectronic with the well-known $O{=}SF_4$ molecule and would significantly extend the known chemistry of $N{\equiv}SF_3$, and of sulfur-nitrogen-fluorine chemistry in general.

REFERENCES

(1) Bartlett, N. *Proc. Chem. Soc.* **1962**, 218.

(2) Graham, L.; Graudejus, O.; Jha, N. K.; Bartlett, N. *Coord. Chem. Rev.* **2000**, *197*, 321-334.

(3) Hoppe, R.; Dähne, W.; Mattauch, H.; Rödder, K. *Angew. Chem. Int. Ed. Engl.* **1962**, *1*, 599.

(4) Claassen, H. H.; Selig, H.; Malm, J. G. *J. Am. Chem. Soc.* **1962**, *84*, 3593.

(5) Malm, J. G.; Sheft, I.; Chernick, C. L. *J. Am. Chem. Soc.* **1963**, *85*, 110-111.

(6) Smith, D. F. *J. Am. Chem. Soc.* **1963**, *85*, 816-817.

(7) Smith, D. F. *Science* **1963**, *140*, 899-900.

(8) Schreiner, F.; Malm, J. G.; Hindman, J. C. *J. Am. Chem. Soc.* **1965**, *87*, 25-28.

(9) Khriachtchev, L.; Pettersson, M.; Runeberg, N.; Lundell, J.; Räsänen, M. *Nature* **2000**, *406*, 874-876.

(10) Runeberg, N.; Pettersson, M.; Khriachtchev, L.; Lundell, J.; Räsänen, M. *J. Chem. Phys.* **2001**, *114*, 836-841.

(11) Berkowitz, J.; Chupka, W. A. *Chem. Phys. Lett.* **1970**, *7*, 447-450.

(12) Fields, P. R.; Stein, L.; Zirin, M. H. *J. Am. Chem. Soc.* **1962**, *84*, 4164-4165.

(13) Stein, L. *J. Am. Chem. Soc.* **1969**, *91*, 5396-5397.

(14) Stein, L. *Science* **1972**, *175*, 1463-1465.

(15) Selig, H.; Holloway, J. H. In *Topics in Current Chemistry*; Bosche, F. L., Ed.; Springer-Verlag: Berlin, 1984; Vol. 124, pp 33-90.

(16) Holloway, J. H. *J. Fluorine Chem.* **1986**, *33*, 149-158.

(17) Holloway, J. H.; Hope, E. G. *Adv. Inorg. Chem.* **1998**, *46*, 51-100.

(18) Schrobilgen, G. J. In *Synthetic Fluorine Chemistry*; Olah, G. A., Prakash, G. K. S., Chambers, R. D., Eds.; John Wiley & Sons, Inc.: New York, 1999, pp 31-42.

(19) Gerken, M.; Schrobilgen, G. J. *Coord. Chem. Rev.* **2000**, *197*, 335-395.

(20) Brel, V. K.; Pirkuliev, N. S.; Zefirov, N. S. *Russ. Chem. Rev. (Engl. Transl.)* **2001**, *70*, 231-264.

(21) Lehmann, J. F.; Mercier, H. P. A.; Schrobilgen, G. J. *Coord. Chem. Rev.* **2002**, *233-234*, 1-39.

(22) Laszlo, P.; Schrobilgen, G. J. *Angew. Chem. Int. Ed. Engl.* **1988**, *27*, 479-489.

(23) Malm, J. G.; Selig, H.; Jortner, J.; Rice, S. A. *Chem. Rev.* **1965**, *65*, 199-236.

(24) Falconer, W. E.; Sunder, W. A. *J. Inorg. Nucl. Chem.* **1967**, *29*, 1380-1381.

(25) Johnson, G. K.; Malm, J. G.; Hubbard, W. N. *J. Chem. Thermodyn.* **1972**, *4*, 879-891.

(26) Schreiner, F.; McDonald, G. N.; Chernick, C. L. *J. Phys. Chem.* **1968**, *72*, 1162-1166.

(27) Sladky, F. O.; Bulliner, P. A.; Bartlett, N.; DeBoer, B. G.; Zalkin, A. *Chem. Commun.* **1968**, 1048-1049.

(28) Fir, B. A.; Gerken, M.; Pointner, B. E.; Mercier, H. P. A.; Dixon, D. A.; Schrobilgen, G. J. *J. Fluorine Chem.* **2000**, *105*, 159-167.

(29) Bartlett, N. *Endeavour* **1972**, *31*, 107-112.

(30) Lehmann, J. F. Ph.D. Thesis, McMaster University, Hamilton, ON, 2004.

(31) Bondi, A. *J. Phys. Chem.* **1964**, *68*, 441-451.

(32) Schrobilgen, G. J. In *Synthetic Fluorine Chemistry*; Olah, G. A., Chambers, R. D., Prakash, G. K. S., Eds.; John Wiley & Sons: New York, 1992, pp 1-30.

(33) MacDougall, P. J.; Schrobilgen, G. J.; Bader, R. F. W. *Inorg. Chem.* **1989**, *28*, 763-769.

(34) Emara, A. A. A.; Schrobilgen, G. J. *J. Chem. Soc., Chem. Commun.* **1987**, 1644-1646.

(35) Emara, A. A. A.; Schrobilgen, G. J. *Inorg. Chem.* **1992**, *31*, 1323-1332.

(36) Schrobilgen, G. J. *J. Chem. Soc., Chem. Commun.* **1988**, 1506-1508.

(37) Emara, A. A. A.; Schrobilgen, G. J. *J. Chem. Soc., Chem. Commun.* **1988**, 257-259.

(38) Fir, B. A. M.Sc. Thesis, McMaster University, Hamilton, ON, 1999.

(39) Emara, A. A. A. Ph.D. Thesis, McMaster University, Hamiton, ON, 1991.

(40) Mercier, H. P. A.; Moran, M. D.; Sanders, J. C. P.; Schrobilgen, G. J.; Suontamo, R. J. *Inorg. Chem.* **2005**, *44*, 49-60.

(41) Frohn, H.-J.; Jakobs, S.; Henkel, G. *Angew. Chem., Int. Ed. Engl.* **1989**, *28*, 1506-1507.

(42) Koppe, K.; Frohn, H.-J.; Mercier, H. P. A.; Schrobilgen, G. J. *Inorg. Chem.* **2008**, *47*, 3205-3217.

(43) Frohn, H. J.; Schroer, T.; Henkel, G. *Z. Naturforsch.* **1995**, *50 b*, 1799-1810.

(44) LeBlond, R. D.; DesMarteau, D. D. *J. Chem. Soc., Chem. Commun.* **1974**, 555-556.

(45) DesMarteau, D. D.; LeBlond, R. D.; Hossain, S. F.; Nothe, D. *J. Am. Chem. Soc.* **1981**, *103*, 7734-7739.

(46) Sawyer, J. F.; Schrobilgen, G. J.; Sutherland, S. J. *Inorg. Chem.* **1982**, *21*, 4064-4072.

(47) Schumacher, G. A.; Schrobilgen, G. J. *Inorg. Chem.* **1983**, *22*, 2178-2183.

(48) Foropoulos, J. J.; DesMarteau, D. D. *J. Am. Chem. Soc.* **1982**, *104*, 4260-4261.

(49) Faggiani, R.; Kennepohl, D. K.; Lock, C. J. L.; Schrobilgen, G. J. *Inorg. Chem.* **1986**, *25*, 563-571.

(50) Fir, B. A.; Whalen, J. M.; Mercier, H. P. A.; Dixon, D. A.; Schrobilgen, G. J. *Inorg. Chem.* **2006**, *45*, 1978-1996.

(51) Colbourn, E. A.; Dagenais, M.; Douglas, A. E.; Raymonda, J. W. *Can. J. Phys.* **1976**, *54*, 1343-1359.

(52) Mercier, H. P. A.; Sanders, J. C. P.; Schrobilgen, G. J.; Tsai, S. S. *Inorg. Chem.* **1993**, *32*, 386-393.

(53) Gunn, S. R. *J. Am. Chem. Soc.* **1966**, *88*, 5924.

(54) Gunn, S. R. *J. Phys. Chem.* **1967**, *71*, 2934-2937.

(55) Sessa, P. A.; McGee, H. A. J. *J. Phys. Chem.* **1969**, *73*, 2078-2080.

(56) Frlec, B.; Holloway, J. H. *Inorg. Chem.* **1976**, *15*, 1263-1270.

(57) MacKenzie, D. R. *Science* **1963**, *141*, 1171.

(58) MacKenzie, D. R.; Fajer, J. *1966* **1966**, *5*, 699-700.

(59) Turner, J. J.; Pimentel, G. C. *Science* **1963**, *140*, 974-975.

(60) Streng, L. V.; Streng, A. G. *Inorg. Chem.* **1966**, *5*, 328-329.

(61) Slivnik, J.; Šmalc, A.; Lutar, K.; Žemva, B.; Frelc, B. *J. Fluorine Chem.* **1975**, *5*, 273-274.

(62) Šmalc, A.; Lutar, K.; Žemva, B. *Inorg. Synth.* **1992**, *29*, 11-14.

(63) Kinkead, S. A.; FitzPatrick, J. R.; Foropoulos, J. J.; Kissane, R. J.; Purson, J. D. *ACS Symp. Ser.* **1994**, *555*, 40-55.

(64) Bezmel'nitsyn, V. N.; Lagasov, V. A.; Chaivanov, B. B. *Dokl. Chem.* **1977**, *235*, 365-367.

(65) Lehmann, J. F.; Dixon, D. A.; Schrobilgen, G. J. *Inorg. Chem.* **2001**, *40*, 3002-3017.

(66) Schrobilgen, G. J. *J. Chem. Soc., Chem. Commun.* **1988**, 863-865.

(67) Glemser, O.; Schröder, H.; Haeseler, H. *Z. Anorg. Allg. Chem.* **1955**, *279*, 28-37.

(68) Glemser, O.; Schröder, H. *Z. Anorg. Allg. Chem.* **1956**, *284*, 97-100.

(69) Glemser, O.; Richert, H.; Rogowski, F. *Naturwissenschaften* **1960**, *47*, 94-95.

(70) Kirchhoff, W. H.; Wilson, E. B., Jr. *J. Am. Chem. Soc.* **1963**, *85*, 1726-1729.

(71) Glemser, O.; Mews, R.; Roesky, H. W. *J. Chem. Soc. D* **1969**, *16*, 914a.

(72) Kebabcioglu, R.; Mews, R.; Glemser, O. *Spectrochim. Acta, Part A* **1972**, *28A*, 1593-1599.

(73) DesMarteau, D. D.; Seppelt, K. *Angew. Chem., Int. Ed. Engl.* **1980**, *19*, 643.

(74) DesMarteau, D. D.; Eysel, H. H.; Oberhammer, H.; Günther, H. *Inorg. Chem.* **1982**, *21*, 1607-1616.

(75) Logothetis, A. L.; Sausen, G. N.; Shozda, R. J. *Inorg. Chem.* **1963**, *2*, 173-175.

(76) Cady, G. H.; Eggers, D. F.; Tittle, B. *Proc. Chem. Soc.* **1963**, 65-66.

(77) Stump, E. C., Jr.; Padgett, C. D.; Brey, W. S., Jr. *Inorg. Chem.* **1963**, *2*, 648-649.

(78) Glemser, O.; Mews, R. *Angew. Chem., Int. Ed. Engl.* **1980**, *19*, 883-899.

(79) Mews, R. *Adv. Inorg. Chem. Radiochem.* **1976**, *19*, 185-237.

(80) Glemser, O.; Mews, R. *Adv. Inorg. Chem. Radiochem.* **1972**, *14*, 333-390.

(81) Roesky, H. W. *J. Fluorine Chem.* **1999**, *100*, 217-226.

(82) Glemser, O.; Richert, H. *Z. Anorg. Allg. Chem.* **1961**, *307*, 313-327.

(83) Koeniger, F.; Muller, A.; Glemser, O. *J. Mol. Struct.* **1978**, *46*, 29-34.

(84) Muller, A.; Ruoff, A.; Krebs, B.; Glemser, O.; Koch, W. *Spectrochim. Acta, Part A* **1969**, *25*, 199-205.

(85) Kirchhoff, W. H.; Wilson, E. B., Jr. *J. Am. Chem. Soc.* **1962**, *84*, 334-336.

(86) Borrmann, T.; Lork, E.; Mews, R.; Parsons, S.; Petersen, J.; Stohrer, W.-D.; Watson, P., G. *Inorg. Chim. Acta* **2008**, *361*, 479-486.

(87) Muller, A.; Glemser, O.; Scherf, K. *Chem. Ber.* **1966**, *99*, 3568-3571.

(88) Glemser, O.; Koch, W. *Anales. Asoc. Quim. Argentina* **1971**, *59*, 143-148.

(89) Erhart, M.; Mews, R. *Z. Anorg. Allg. Chem.* **1992**, *615*, 117-122.

(90) Buss, B.; Clegg, W.; Hartmann, G.; Jones, P. G.; Mews, R.; Noltemeyer, M.; Sheldrick, G. M. *J. Chem. Soc., Dalton Trans.* **1981**, 61-63.

(91) Behrens, U.; Lork, E.; Petersen, J.; Waterfeld, A.; Mews, R. *Z. Anorg. Allg. Chem.* **1997**, *623*, 1518-1524.

(92) Behrens, U.; Hoppenheit, R.; Isenberg, W.; Lork, E.; Petersen, J.; Mews, R. *Z. Naturforsch.* **1994**, *49 b*, 238-242.

(93) Schnepel, F. M.; Mews, R.; Glemser, O. *J. Mol. Struct.* **1980**, *60*, 89-92.

(94) Mews, R. *J. Chem. Soc., Chem. Commun.* **1979**, 278-279.

(95) Mews, R.; Glemser, O. *Angew. Chem., Int. Ed. Engl.* **1975**, *14*, 186-187.

(96) Clifford, A. F.; Duncan, L. C. *Inorg. Chem.* **1966**, *5*, 692-693.

(97) Clifford, A. F.; Zeilenga, G. R. *Inorg. Chem.* **1969**, *8*, 1789-1791.

(98) Mews, R. *Angew. Chem., Int. Ed. Engl.* **1978**, *17*, 530.

(99) Bartsch, R.; Henle, H.; Meier, T.; Mews, R. *Chem. Ber.* **1988**, *121*, 451-456.

(100) Günther, H.; Oberhammer, H.; Mews, R.; Stahl, I. *Inorg. Chem.* **1982**, *21*, 1872-1875.

(101) Meier, T.; Hoppenheit, R.; Mews, R. *Z. Anorg. Allg. Chem.* **1993**, *619*, 1241-1246.

(102) Glemser, O.; Meyer, H.; Haas, A. *Chem. Ber.* **1965**, *98*, 2049-2050.

(103) Glemser, O.; Koch, W. *Z. Naturforsch.* **1968**, *B23*, 745.

(104) Clifford, A. F.; Harman, J. S. *J. Chem. Soc., Dalton Trans.* **1974**, 571-575.

(105) Waterfeld, A.; Bludssus, W.; Mews, R.; Glemser, O. *Z. Anorg. Allg. Chem.* **1980**, *464*, 268-272.

(106) Clifford, A. F.; Howell, J. L.; Wooton, D. L. *J. Fluorine Chem.* **1978**, *11*, 433-439.

(107) Roesky, H. W.; Glemser, O.; Hoff, A.; Koch, W. *Inorg. Nucl. Chem. Lett.* **1967**, *3*, 39-42.

(108) Mews, R.; Borrmann, T.; Hoppenheit, R.; Lork, E.; Parsons, S.; Petersen, J.; Schroter, M.; Stohrer, W.-D.; Waterfeld, A.; Watson, P., G. *J. Fluorine Chem.* **2004**, *125*, 1649-1655.

(109) Gillespie, R. J.; Schrobilgen, G. J. *Inorg. Chem.* **1976**, *15*, 22-31.

(110) Winfield, J. M. *J. Fluorine Chem.* **1984**, *25*, 91-98.

(111) Emara, A. A. A.; Lehmann, J. F.; Schrobilgen, G. J. *J. Fluorine Chem.* **2005**, *126*, 1373-1376.

(112) Gillespie, R. J.; Landa, B. *Inorg. Chem.* **1973**, *12*, 1383-1388.

(113) Thrasher, J. S. *Inorg. Synth.* **1986**, *24*, 99-101.

(114) Thrasher, J. S. *Inorg. Synth.* **1986**, *24*, 10-12.

(115) Mews, R.; Keller, K.; Glemser, O. *Inorg. Synth.* **1986**, *24*, 12-17.

(116) Private communications with R. Mews and B. Žemva.

(117) Gerken, M.; Moran, M. D.; Mercier, H. P. A.; Pointner, B. E.; Schrobilgen, G. J.; Hoge, B.; Christe, K. O.; Boatz, J. A. *J. Am. Chem. Soc.* **2009**, *131*, 13474-13489.

(118) Smith, G. L.; Mercier, H. P. A.; Schrobilgen, G. J. *Inorg. Chem.* **2008**, *47*, 4173-4184.

(119) Gerken, M.; Dixon, D. A.; Schrobilgen, G. J. *Inorg. Chem.* **2000**, *39*, 4244-4255.

(120) *SMART*, release 5.054, and *SAINT*, release 056.001; Siemens Energy and Automation Inc.; Madison, WI, 1999.

(121) Sheldrick, G. M. *SADABS (Siemens Area Detector Absorption Corrections)*, version 2.10; Siemens Analytical X-ray Instruments, Inc.: Madison, WI, 2004.

(122) *APEX2*, release 2.0-2; Bruker AXS Inc.: Madison, WI, 2005.

(123) Sheldrick, G. M. *SHELXTL-Plus*, release 6.14, Siemens Analytical X-ray Instruments, Inc.: Madison, WI, 2000-2003.

(124) Santry, D. P.; Mercier, H. P. A.; Schrobilgen, G. J., *ISOTOPOMER, A Multi-NMR Simulation Program, version 3.02NTF.*; Snowbird Software, Inc.: Hamilton, ON, 2000.

(125) Frisch, M. J.; Trucks, G. W.; Schlegel, H. B.; Scuseria, G. E.; Robb, M. A.; Cheeseman, J. R.; Zakrzewski, V. G.; Montgomery, J. A., Jr.; Stratmann, R. E.; Burant, J. C.; Dapprich, S.; Millam, J. M.; Daniels, A. D.; Kudin, K. N.; Strain, M. C.; Farkas, O.; Tomasi, J.; Barone, V.; Cossi, M.; Cammi, R.; Mennucci, B.; Pomelli, C.; Adamo, C.; Clifford, S.; Ochterski, J.; Petersson, G. A.; Ayala, P. Y.; Cui, Q.; Morokuma, K.; Salvador, P.; Dannenberg, J. J.; Malick, D. K.; Rabuck, A. D.; Raghavachari, K.; Foresman, J. B.; Cioslowski, J.; Ortiz, J. V.; Baboul, A. G.; Stefanov, B. B.; Liu, G.; Liashenko, A.; Piskorz, P.; Komaromi, I.; Gomperts, R.; Martin, R. L.; Fox, D. J.; Keith, T.; Al-Laham, M. A.; Peng, C. Y.; Nanayakkara, A.; Challacombe, M.; Gill, P. M. W.; Johnson, B.; Chen, W.; Wong, M. W.; Andres, J. L.; Gonzalez, C.; Head-Gordon, M.; Replogle, E. S.; Pople, J. A.; *Gaussian 98*, Revision A.11; Gaussian, Inc.: Pittsburgh, PA, 2003.

(126) Frisch, M. J.; Trucks, G. W.; Schlegel, H. B.; Scuseria, G. E.; Robb, M. A.; Cheeseman, J. R.; Scalmani, G.; Barone, V.; Mennucci, G. A.; Petersson, B.; Nakatsuji, H.; Caricato, M.; Li, X.; Hratchian, H. P.; Izmaylov, A. F.; Bloino, J.; Zheng, G.; Sonnenberg, J. L.; Hada, M.; Ehara, M.; Toyota, K.; Fukuda, R.; Hasegawa, J.; Ishida, M.; Nakajima, T.; Honda, Y.; Kitao, O.; Nakai, H.; Vreven, T.; Montgomery, J. A. Jr.; Peralta, J. E.; Ogliaro, F.; Bearpark, M. Heyd, J. J.; Brothers, E.; Kudin, K. N.; Staroverov, V. N.; Kobayashi, R.; Normand, J.; Raghavachari, K.; Rendell, A.; Burant, J. C.; Iyengar, S. S.; Tomasi, J.; Cossi, M.; Rega, N.; Millam, J. M.; Klene, M.; Knox, J. E.; Cross, J. B.; Bakken, V.; Adamo, C.; Jaramillo, J.; Gomperts, R.; Stratmann, R. E.; Yazyev, O.; Austin, A. J.; Cammi, R.; Pomelli, C.; Ochterski, J. W.; Martin, R. L.; Morokuma, K.; Zakrzewski, V. G.; Voth, G. A.; Salvador, P.; Dannenberg, J. J.; Dapprich, S.;

Daniels, A. D.; Farkas, O.; Foresman, J. B.; Ortiz, J. V.; Cioslowski, J.; and Fox, D. J. *Gaussian 09*, Revision A.02: Gaussian, Inc.; Wallingford CT, 2009.

(127) Basis sets were obtained from the Extensible Computational Chemistry Environment Basis set Database, version 2/25/04, as developed and distributed by the Molecular Science Computing Facility, Environmental and Molecular Science Laboratory, which is part of the Pacific Northwest Laboratory, P.O. Box 999, Richland, WA 99352.

(128) Feller, D. *J. Comp. Chem.* **1996**, *17*, 1571-1586.

(129) Schuchardt, K. L.; Didier, B. T.; Elsethagen, T.; Sun, L.; Gurumoorthi, V.; Chase, J.; Li, J.; Windus, T. L. *J. Chem. Inf. Model.* **2007**, *47*.

(130) *GaussView*, release 3.0; Gaussian Inc.: Pittsburgh, PA, 2003.

(131) Sawyer, J. F.; Schrobilgen, G. J.; Sutherland, S. J. *J. Chem. Soc., Chem. Commun.* **1982**, 210-211.

(132) Beach, D., B.; Jolly, W. L.; Mews, R.; Waterfeld, A. *Inorg. Chem.* **1984**, *23*, 4080-4084.

(133) Zalkin, A.; Ward, D. L.; Biagioni, R. N.; Templeton, D. H.; Bartlett, N. *Inorg. Chem.* **1978**, *17*, 1318-1322.

(134) Bartlett, N.; Gennis, M.; Gibler, D. D.; Morrell, B. K.; Zalkin, A. *Inorg. Chem.* **1973**, *12*, 1717-1721.

(135) Burns, J. H.; Ellison, R. D.; Levy, H. A. *Acta Crystallogr.* **1965**, *18*, 11-16.

(136) Gillespie, R. J.; Martin, D.; Schrobilgen, G. J. *J. Chem. Soc., Dalton Trans.* **1980**, 1898-1903.

(137) Bartlett, N.; DeBoer, B. G.; Hollander, F. J.; Sladky, F. O.; Templeton, D. H.; Zalkin, A. *Inorg. Chem.* **1974**, *13*, 780-785.

(138) Lu, J.; Harrison, W. T. A.; Jacobson, A. J. *Angew. Chem., Int. Ed. Engl.* **1995**, *34*, 2557-2559.

(139) Connelly, N. G.; Hicks, O. M.; Lewis, G. R.; Moreno, M. T.; Orpen, A. G. *J. Chem. Soc., Dalton Trans.* **1998**, 1913-1917.

(140) Werner, B.; Kräuter, T.; Neumüller, B. *Z. Anorg. Allg. Chem.* **1995**, *621*, 346-358.

(141) Behrens, U.; Brimah, A. K.; Soliman, T. M.; Fischer, R. D.; Apperly, D. C.; Davies, N. A.; Harris, R. K. *Organometallics* **1992**, *11*, 1718-1726.

(142) Sanders, J. C. P.; Schrobilgen, G. J. In *A Methodological Approach to Multinuclear NMR in Liquids and Solids-Chemical Applications; NATO Advanced Study Institute, Magnetic Resonance*; Granger, P., Harris, R. K., Eds.; Kluwer Academic Publishers: Dordrecht, 1990, pp Chapter 11, pp 157-186.

(143) Richert, H.; Glemser, O. *Z. Anorg. Allg. Chem.* **1961**, *307*, 328-344.

(144) This work

(145) Zirz, C.; Ahlrichs, R. *Inorg. Chem.* **1984**, *23*, 26-31.

(146) Smith, G. L.; Mercier, H. P. A.; Schrobilgen, G. J. *Inorg. Chem.* **2007**, *46*, 1369-1378.

(147) Christe, K. O. *Inorg. Chem.* **1975**, *14*, 2821-2824.

(148) Merrill, C. I.; Williamson, S. M.; Cady, G. H.; Eggers, D. F., Jr. *Inorg. Chem.* **1962**, *1*, 215-219.

(149) Koppe, K.; Bilir, V.; Frohn, H. J.; Mercier, H. P. A.; Schrobilgen, G. J. *Inorg. Chem.* **2007**, *46*, 9425-9437.

(150) Keller, N.; Schrobilgen, G. J. *Inorg. Chem.* **1981**, *20*, 2118-2129.

(151) Schrobilgen, G. J.; Holloway, J. H.; Granger, P.; Brevard, C. *Inorg. Chem.* **1978**, *17*, 980-987.

(152) Brown, I. D. *The Chemical Bond in Inorganic Chemistry*; Oxford University Press: Oxford, 2002.

(153) Brese, N. E.; O'Keeffe, M. *Acta. Crystallogr., Sect. B.* **1991**, *47*, 192-197.

(154) Turowsky, L.; Seppelt, K. *Inorg. Chem.* **1990**, *29*, 3226-3228.

(155) Frohn, H.-J.; Klose, A.; Schroer, T.; Henkel, G.; Buss, V.; Opitz, D.; Vahrenhorst, R. *Inorg. Chem.* **1998**, *37*, 4884-4890.

(156) Fir, B. A.; Mercier, H. P. A.; Sanders, J. C. P.; Dixon, D. A.; Schrobilgen, G. J. *J. Fluorine Chem.* **2001**, *110*, 89-107.

(157) Claassen, H. H.; Goodman, G. L.; Holloway, J. H.; Selig, H. *J. Chem. Phys.* **1970**, *53*, 341-348.

(158) Weinstock, B.; Goodman, G. L. *Adv. Chem. Phys.* **1965**, *9*, 169-316.

(159) Marsden, C. J.; Bartell, L. S. *Inorg. Chem.* **1976**, *15*, 3004-3009.

(160) Naulin, C.; Bougon, R. *J. Chem. Phys.* **1976**, *64*, 4155-4158.

(161) O'Brien, B. A.; DesMarteau, D. D. *Inorg. Chem.* **1984**, *23*, 2188-2195.

(162) DesMarteau, D. D.; Lam, W. Y.; O'Brien, B. A.; Chang, S.-C. *J. Fluorine Chem.* **1984**, *25*, 387-394.

(163) Tullock, C. W.; Coffman, D. D.; Muetterties, E. L. *J. Am. Chem. Soc.* **1964**, *1964*, 357-361.

(164) Muetterties, E. L.; Mahler, W.; Packer, K. J.; Schmutzler, R. *Inorg. Chem.* **1964**, *3*, 1298-1303.

(165) Walker, N.; Fox, W. B.; De Marco, R. A.; Moniz, W. B. *J. Mol. Spectrosc.* **1979**, *34*, 295-299.

(166) Stahl, I.; Mews, R.; Glemser, O. *Angew. Chem. Int. Ed. Engl.* **1980**, *19*, 408-409.

(167) Waterfeld, A.; Mews, R. *Angew. Chem. Int. Ed. Engl.* **1982**, *21*, 354.

(168) Waterfeld, A.; Oberhammer, H.; Mews, R. *Angew. Chem. Int. Ed. Engl.* **1982**, *21*, 355.

(169) Waterfeld, A.; Mews, R. *Chem. Ber.* **1983**, *116*, 1674-1677.

(170) Meier, T.; Mews, R. *J. Fluorine Chem.* **1989**, *42*, 81-85.

(171) Meier, T.; Mews, R. *Chem. Ber.* **1993**, *126*, 2437-2439.

(172) Clifford, A. F.; Howell, J. L. *J. Fluorine Chem.* **1977**, *10*, 431-432.

(173) Boate, A. R.; Morton, J. R.; Preston, K. F. *J. Phys. Chem.* **1976**, *80*, 409-412.

(174) Karplus, M. *J. Chem. Phys.* **1959**, *30*, 11-15.

(175) Rankin, D. W. H.; Wright, J. G. *J. Chem. Soc., Dalton Trans* **1979**, *6*, 1070-1074.

(176) Kleemann, G.; Seppelt, K. *Angew. Chem. Int. Ed. Engl.* **1978**, *17*, 516-518.

(177) Seppelt, K. In *Synthetic Fluorine Chemistry*; Olah, G. A., Chambers, R. D., Prakash, G. K. S., Eds.; John Wiley & Sons, Inc.: Toronto, 1992, pp 87-96.

(178) Meier, T.; Mews, R. *Angew. Chem., Int. Ed. Engl.* **1985**, *24*, 344-345.

(179) Simon, A.; Peters, E. M.; Lentz, D.; Seppelt, K. *Z. anorg. allg. Chem.* **1980**, *468*, 7-14.

(180) Gundersen, G.; Hedberg, K. *J. Chem. Phys.* **1969**, *51*, 2500-2507.

(181) Hargittai, I. *J. Mol. Struct.* **1979**, *56*, 301-303.

(182) Gillespie, R. J.; Hargittai, I. *The VSEPR Model of Molecular Geometry*; Allyn and Bacon: Toronto, 1991.

(183) Meier, T.; Mews, R. *J. Fluor. Chem.* **1994**, *66*, 141-146.

(184) Smith, G. L.; Schrobilgen, G. J. *Inorg. Chem.* **2009**, *48*, 7714-7728.

(185) King, S.-T.; Overend, J. *Spectrochim. Acta* **1967**, *23A*, 61-66.

(186) Azeem, M.; Brownstein, M.; Gillespie, R. J. *Can. J. Chem.* **1969**, *47*, 4159-4167.

(187) Noggle, J. H.; Baldeschwieler, J. D.; Colburn, C. B. *J. Chem. Phys.* **1962**, *37*, 182-189.

(188) Diesen, R. W. *J. Chem. Phys.* **1964**, *41*, 3256-3257.

(189) Bartlett, N.; Robinson, P. L. *J. Chem. Soc.* **1961**, 3417-3425.

(190) Gibler, D. D.; Adams, C. J.; Fischer, M.; Zalkin, A.; Bartlett, N. *Inorg. Chem.* **1972**, *11*, 2325-2329.

(191) Brownstein, M.; Shamir, J. *Appl. Spectrosc.* **1972**, *26*, 77-80.

(192) Barr, M. R.; Dunell, B. A. *Can. J. Chem.* **1970**, *48*, 895-903.

(193) Mallouk, T. E.; Rosenthal, G. R.; Müller, G.; Brusasco, R.; Bartlett, N. *Inorg. Chem.* **1984**, *23*, 3167-3173.

(194) Zaborowski, L. M.; De Marco, R. A.; Shreeve, J. n. M. *Inorg. Synth.* **1973**, *14*, 34-39.

(195) Ogden, J. S.; Turner, J. J. *Chem. Commun.* **1966**, 693-694.

(196) Gillespie, R. J.; Schrobilgen, G. J. *J. Chem. Soc., Chem Commun.* **1977**, 595-597.

(197) Brock, D. S.; Bilir, V.; Mercier, H. P. A.; Schrobilgen, G. J. *J. Am. Chem. Soc.* **2007**, *129*, 3598-3611.

(198) Gillespie, R. J.; Schrobilgen, G. J. *Inorg. Chem.* **1974**, *13*, 2370-2374.

(199) Gillespie, R. J.; Landa, B.; Schrobilgen, G. J. *Inorg. Chem.* **1976**, *15*, 1256-1263.

(200) Holloway, J. H.; Kaučič, V.; Martin-Rovet, D.; Russell, D. R.; Schrobilgen, G. J.; Selig, H. *Inorg. Chem.* **1985**, *24*, 678-683.

(201) Ellern, A.; Seppelt, K. *Angew. Chem. Int. Ed. Engl.* **1995**, *34*, 1586-1587.

(202) Peterson, S. W.; Willett, R. D.; Huston, J. L. *J. Chem. Phys.* **1973**, *59*, 453-459.

(203) Christe, K. O.; Wilson, W. W. *Inorg. Chem.* **1988**, *27*, 2714-2718.

(204) Pointner, B. E.; Suontamo, R. J.; Schrobilgen, G. J. *Inorg. Chem.* **2006**, *45*, 1517-1534.

(205) Claassen, H. H.; Huston, J. L. *J. Chem. Phys.* **1971**, *55*, 1505-1507.

(206) Gerken, M. Ph.D. Thesis, McMaster University, Hamilton, ON, 2000.

(207) Huston, J. L. *J. Am. Chem. Soc.* **1971**, *93*, 5255-5256.

(208) Martin, D.; Bauer, M.; Pankratov, V. A. *Russ. Chem. Rev. (Engl. Transl.)* **1978**, *47*, 975-990.

(209) Quirke, J. M. E. In *Comprehensive Heterocyclic Chemistry*; Katritzky, A. R., Rees, C. W., Eds.; Pergamon Press: Toronto, 1984; Vol. 3, pp 457-530.

(210) Amer, M. I.; Booth, B. L.; Noori, G. F. M.; Proença, M. F. J. R. P. *J. Chem. Soc., Perkin Trans. 1* **1983**, 1075-1082.

(211) Korolev, B. A.; Mal'tseva, M. A.; Andronova, N. A. *J. Gen. Chem. USSR* **1975**, *45*, 232-233.

(212) Olah, G. A.; Kiovsky, T. E. *J. Am. Chem. Soc.* **1968**, *90*, 4666-4672.

(213) Grunmann, C.; Weisse, G.; Seide, S. *Justus Liebigs Ann. Chem.* **1952**, *577*, 77-95.

(214) Zil'berman, E. N. *Russ. Chem. Rev. (Engl. Transl.)* **1962**, *31*, 615-633.

(215) Braun, S.; Frey, G. *Org. Magn. Reson.* **1975**, *7*, 194-198.

(216) Herrera, A.; Martínez-Alvarez, R.; Ramiro, P.; Chioua, M.; Chioua, R. *Synthesis* **2004**, 503-505.

(217) Wilson, W. W.; Christe, K. O.; Feng, J.-a.; Bau, R. *Can. J. Chem.* **1989**, *67*, 1898-1901.

(218) Whittlesey, M. K.; Perutz, R. N.; Greener, B.; Moore, M. H. *Chem. Commun.* **1997**, 187-188.

(219) Murphy, V. J.; Hascall, T.; Chen, J. Y.; Parkin, G. *J. Am. Chem. Soc.* **1996**, *118*, 7428-7429.

(220) Buschmann, J.; Lentz, D.; Luger, P.; Perpetuo, G.; Preugschat, D.; Thrasher, J. S.; Willner, H.; Wölk, H.-J. *Z. Anorg. Allg. Chem.* **2004**, *630*, 1136-1142.

(221) McGhee, L.; Rycroft, D. S.; Winfield, J. M. *J. Fluorine Chem.* **1987**, *36*, 351-359.

(222) Banks, R. E.; Besheesh, M. K.; Fraenk, W.; Klapötke, T. M. *J. Fluorine Chem.* **2003**, *124*, 229-232.

(223) Weller, F.; Schmock, F.; Dehnicke, K.; Findeisen, K. *Z. Naturforsch., B: Chem. Sci.* **1994**, *49*, 360-364.

(224) Chan, G. Y. S.; Drew, M. G. B.; Hudson, M. J.; Isaacs, N. S.; Byers, P.; Madic, C. *Polyhedron* **1996**, *15*, 3385-3398.

(225) Perpétuo, G. J.; Janczak, J. *Acta Crystallogr., Sect. C.* **2007**, *63*, o271-o273.

(226) Fan, Y.; You, W.; Qian, H.-F.; Liu, J.-L.; Huang, W. *Acta Crystallogr., Sect. E* **2009**, *65*, o494.

(227) Delori, A.; Suresh, E.; Pedireddi, V. R. *Chem. –Eur. J.* **2008**, *14*, 6967-6977.

(228) Jing, H.; Ströbele, M.; Weisser, M.; Meyer, H.-J. *Z. Anorg. Allg. Chem.* **2003**, *629*, 368-370.

(229) Athikomrattanakul, U.; Promptmas, C.; Katterle, M.; Schilde, U. *Acta Crystallogr., Sect. E.* **2007**, *63*, o2154-o2156.

(230) Janczak, J.; Perpétuo, G. J. *Acta Crystallogr., Sect. C.* **2004**, *60*, o211-o214.

(231) Wijaya, K.; Moers, O.; Henschel, D.; Blaschette, A.; Jones, P. G. *Z. Naturforsch., B: Chem. Sci.* **2004**, *59*, 747-756.

(232) Gorelsky, S. I.; Ilyukhin, A. B.; Kholin, P. V.; Kotov, V. Y.; Lokshin, B. V.; Sapoletova, N. V. *Inorg. Chim. Acta* **2007**, *360*, 2573-2582.

(233) Mercier, H. P. A.; Moran, M. D.; Schrobilgen, G. J.; Steinberg, C.; Suontamo, R. J. *J. Am. Chem. Soc.* **2004**, *126*, 5533-5548, and references therein.

APPENDIX A

ATTEMPTED SYNTHESES OF THE NEW Kr-N BONDED CATIONS $F_3S{\equiv}NKrF^+$ AND $F_5SN(H)Kr^+$

A.1. Introduction

The chemistry of krypton has been reviewed,[21] and in many ways is analogous to that of xenon, however, far fewer krypton compounds are known because of their lower thermodynamic stabilities and stronger oxidant properties. The only known neutral krypton fluoride, KrF_2, has an endothermic heat of formation, but can be produced in macroscopic quantities at low temperature (see Section 1.4., Krypton(II) Chemistry).

The known chemistry of krypton-nitrogen bonded compound is limited to the four cations generated by the low-temperature reaction of KrF_2 with the protonated hydrogen cyanide cation, $HC{\equiv}NH^+$ (eq A.1),[66] and the Lewis acid-base adducts, $R_FC{\equiv}NAsF_5$ (R_F = CF_3, C_2F_5, n-C_3F_7) (eq A.2)[36] in BrF_5 or aHF solvent at ca. –60 °C to give the

$$[HC{\equiv}NH][AsF_6] + KrF_2 \longrightarrow [HC{\equiv}NKrF][AsF_6] + HF \qquad (A.1)$$

$$R_FC{\equiv}NAsF_5 + KrF_2 \longrightarrow [R_FC{\equiv}NKrF][AsF_6] \qquad (A.2)$$

corresponding KrF^+ adducts. This synthetic strategy differs from the approach of directly reacting XeF^+ with a nitrile (eq. 1.6) that has been used to generate the analogous xenon cations. This is because the KrF^+ cation is a much more potent oxidizer than XeF^+, which results in oxidative attack and fluorination of the base with the rapid evolution of Kr, NF_3, and CF_4 gases at higher temperature. Such reactions are likely to be accompanied by

detonations. Although these cations were found to be far less stable than their xenon analogues, they have been unambiguously characterized by low-temperature multi-NMR spectroscopy despite their short (1–2 h) lifetimes at ca. –60 °C,[36,66] which precluded their study by other means.

The new xenon-nitrogen containing cations $F_3S{\equiv}NXeF^+$ and $F_5SN(H)Xe^+$ have been synthesized as their AsF_6^- salts by reaction of $[XeF][AsF_6]$ with the Lewis base $N{\equiv}SF_3$, and by the equilibrium reaction of XeF_2 with $[F_5SNH_3][AsF_6]$, respectively, in aHF and BrF_5 solvents (see Sections 3.2.1. and 4.2.1.2.).

The present work examines the possibility of synthesizing the krypton analogues of the above-mentioned xenon-nitrogen bonded cations. To avoid the use of the stronger oxidative fluorinating agent KrF^+, the reaction with $N{\equiv}SF_3$ was adapted as the reaction of KrF_2 with the donor-acceptor adduct $F_3S{\equiv}NAsF_5$.

A.2. Results and Discussion

A.2.1. Attempted Syntheses of $[F_3S{\equiv}NKrF][AsF_6]$ and $[F_5SN(H)Kr][AsF_6]$

In typical reactions, ca. 0.5 mL of BrF_5 was condensed onto $F_3S{\equiv}NAsF_5$ (ca. 0.41 g, 1.5 mmol; see Section 2.2.7) or $[F_5SNH_3][AsF_6]$ (ca. 0.23g, 1.5 mmol; see Section 2.4.2) which had been prepared in a 4-mm o.d. FEP NMR tube. A ca. 10 mol% excess of KrF_2 was distilled onto the frozen BrF_5 at –196 °C. The sample was not melted or mixed until immediately before analysis by low temperature ^{19}F NMR spectroscopy, at or below the freezing point of BrF_5 (ca. –65 to–70 °C). Immediately upon melting the BrF_5 and mixing the same, gas evolution was observed with both reactions which intensified with

warming. No krypton-containing reaction products were ever identified, however the fluorination products SF_6, NF_3, NF_4^+ and AsF_6^- were observed after both reactions.

It seems clear that rather than bond, krypton and nitrogen are involved in a redox process in which krypton is reduced (oxidation state +2 to 0) to krypton gas, and nitrogen is oxidatively fluorinated (+3 to +5) forming NF_4^+ in solution. While a preliminary quantum chemical investigation of these systems was begun, the lack of experimental evidence for $F_3S{\equiv}NKrF^+$ or $F_5SN(H)Kr^+$ meant that expensive supercomputer CPU time could be better spent on other projects.